Theoretical and experimental studies of large scale modes in Hall thrusters and methods of their control

A Thesis Submitted to the
College of Graduate and Postdoctoral Studies
in Partial Fulfillment of the Requirements
for the degree of Doctor of Philosophy
in the Department of Physics and Engineering Physics
University of Saskatchewan
Saskatoon

By

Ivan Romadanov

Permission to Use

In presenting this thesis in partial fulfilment of the requirements for a Postgraduate degree from the University of Saskatchewan, I agree that the Libraries of this University may make it freely available for inspection. I further agree that permission for copying of this thesis in any manner, in whole or in part, for scholarly purposes may be granted by the professor or professors who supervised my thesis work or, in their absence, by the Head of the Department or the Dean of the College in which my thesis work was done. It is understood that any copying or publication or use of this thesis or parts thereof for financial gain shall not be allowed without my written permission. It is also understood that due recognition shall be given to me and to the University of Saskatchewan in any scholarly use which may be made of any material in my thesis.

Requests for permission to copy or to make other use of material in this thesis in whole or part should be addressed to:

Head of the Department of Physics and Engineering Physics, University of Saskatchewan
Rm 163, 116 Science Place
Saskatoon, Saskatchewan
Canada
S7N 5E2
OR
Dean of College of Graduate and Postdoctoral Studies, University of Saskatchewan
116 Thorvaldson Building, 110 Science Place
Saskatoon, Saskatchewan
Canada
S7N 5C9

Abstract

Partially-magnetized plasmas with magnetized electrons and weakly-magnetized ions in crossed electric and magnetic fields are common in the nature and industrial devices, such as magnetrons, MHD generators, electric propulsion (ion/Hall thrusters, helicon thrusters), and Penning discharges. Such plasmas are usually in a strongly non-equilibrium state, exhibiting a variety of turbulent fluctuations. These fluctuations are responsible for anomalous transport phenomena and large-scale plasma structures. This study investigates one of the most known and pervasive examples: rotating spokes and breathing modes in Hall thrusters. Breathing mode is an $m = 0$ mode (here m is the azimuthal mode number), propagating in the axial direction and leading to strong oscillations of the discharge current, up to 100 % in amplitude. Spoke is an $m = 1, 2, ...$ mode rotating in an azimuthal direction and is thought to be responsible for a large part of the anomalous current in a system. These large-scale perturbations can critically affect the performance of Hall thrusters, but the exact nature of these modes is unknown. Both types of oscillations are believed to be induced and strongly affected by the equilibrium electron current due to $\mathbf{E} \times \mathbf{B}$ drift, plasma density gradients, and ionization. This thesis is devoted to theoretical and experimental studies of spoke and breathing mode mechanisms, their coupling, and methods of their control.

We have performed the theoretical study of the gradient-drift (collisionless Simon-Hoh) instability. This is a robust instability considered to be important for Hall plasma discharges supported by the electron current due to the $\mathbf{E} \times \mathbf{B}$ drift. Most of the previous studies of this mode were based on the local approximation. Here, we consider the nonlocal model which takes into account the electron inertia as well as the effects of the plasma profiles, such as the electric, magnetic fields and plasma density. Contrary to local models, nonlocal analysis predicts multiple unstable modes, existing in the regions where local instability criteria is not satisfied. This is especially pronounced for the long wavelength modes which are believed to lead to spokes.

Despite the long history of theoretical and experimental studies of breathing mode, the exact physical mechanism and conditions for the mode occurrence are not well understood. Therefore, new diagnostic methods are important, in order to provide better insights on physical processes during breathing oscillations. For this purpose, the time-resolved laser-induced fluorescence (LIF) diagnostic was developed and implemented for studying the effect of breathing modes on the ion velocity distribution function (IVDF) in the cylindrical Hall thruster (CHT). These intrinsic breathing oscillations were locked into the externally driven anode voltage modulations. It was shown that the commonly used LIF diagnostic of xenon IVDF can have large uncertainties when used in the regimes with significant oscillations of plasma parameters. Thus, these effects should be taken into account for proper experimental data interpretation.

We have studied the effect of the external modulations on the breathing mode, and linear and nonlinear regimes of the thruster response were identified. This manifest itself in the discharge and ion current measurements in the CHT during the external modulations. These measurements revealed that their amplitudes and root-mean-square (RMS) values increase with the magnitude of the modulation. The latter leads to an increase of the current utilization and the propellant utilization efficiencies, and total increase of the thruster efficiency up to 20%. The 1D fluid model of the intrinsic axial modes was developed to study the role of various effects: competition of the neutral and ion species depletion, the role of the self-consistent resistive axial current instabilities with effect of the electron diffusion. The experimental results were partially confirmed with these simulations performed in BOUT++ framework.

The final part of this thesis investigates the effect of the modulated breathing oscillations on azimuthally rotating spoke. This was done by means of a high speed camera, which recorded plasma emission intensity changes in the thruster channel during the external modulations of the breathing mode. This signal was processed with image analysis techniques; during this analysis spoke and breathing modes were identified. By varying the amplitude and frequency of the modulation, the suppression of the spoke mode was achieved. This shows that there exists an interaction between these two modes.

Acknowledgements

Over the course of the past five years I learned so many things and expanded my horizons so much, that looking back, it is hard to understand sometimes how I was even able to live before. The great part of this development happened because I was lucky to become a PhD student with the group of my professor, Andrei Smolyakov. Andrei Ivanovich, thank you a lot for your guidance, patience, and help over these years.

Another person whose contribution to my growth as a researcher is hard to estimate is Yevgeny Raitses. Thank you a lot, for your guidance during my visits to the Princeton Plasma Physics Laboratory. You taught me most of the things I know about experimental physics.

I would like to say thank you to Sergey V. Ryzhkov, from my home University, who introduced me to the field of plasma physics a long time ago. Becoming a plasma physicist was a long and not very straightforward path, but it all started because you agreed to take me as a student.

I want to thank my thesis committee: Professor Alexandre Koustov, Professor Michael Bradley, Professor Safa Kasap, Professor Chijin Xiao, and external exterminator Professor Richard Sydora for their comments, interesting questions, and important corrections to this dissertation.

I am grateful to the University of Saskatchewan for the opportunity to study here and for providing financial support. After these long five years, I can name it as my second home. Here I met a lot of wonderful and inspirational people: Oleksandr Koshkarov, Oleksandr Chapurin, Igor Voldiner, Jeffery Zielinski, Winston Frias, Vincent Morin, Salomon Janhunen. Thank you, guys!

I want to say thank you to the people I met at Princeton Plasma Physics Laboratory: Dr. Igor Kaganovich, for help with my papers and discussions; Dr. Ahmed Diallo, who let me borrow his equipment, and taught me useful things about plasma diagnostics; Dr. Alexandros Gerakis, for his help and advice about optics; Dr. Vladislav Vekselman, for numerous discussions and help; Dr. Panagiotis Svarnas (from the University of Parnas), who introduced me to laser-induced fluorescence diagnostic. This list would not be complete

without the engineers, postdocs, and students with whom I interacted there: thank you to Alex Merzhevsky, Jacob Simmonds, Valentin Skoutnev, Aleksandr Khrabry, Shurik Yatom, Andrew Tasman Powis, and Eduardo Rodriguez.

Making this path would be impossible without my family. Thanks a lot for your encouragement, advice, and support. Especially to my grandmother, I am very proud to continue your engineering legacy in our family.

Finally, I want to say thank you to Bryn Rees. You made my final year here way more enjoyable and fun. You became the very important part of my life, and this is unexpected, but very pleasant result of this journey.

Ivan Romadanov

Saskatoon, SK

2018.

To my parents and grandparents.

Contents

List of Tables

List of Figures

List of Abbreviations

AOM	Acousto-Optic Modulator
B.C.	Bounday Conditions
BS	Beam Splitter
CSD	Cross-Spectral Density
CHT	Cylindrical Hall Thruster
DAQ	Data Acquisition
EP	Electric Propulsion
FFT	Fast Fourier Transform
GEO	Geosynchronous Earth Orbit
HT	Hall Thruster
IVDF	Ion Velocity Distribution Function
RMS	Root-Mean Square
LIF	Laser-Induced Fluorescence
LEO	Low Earth Orbit
MHD	MagnetoHydroDynamic
PD	Photo Diode
PMT	Photo Multiplier Tube
RHS	Right Hand Side
sccm	Standard Cubic Centimeter per Minute
SHTF	Small Hall Thruster Facility
SPT	Stationary Plasma Thruster
TR-LIF	Time-Resolved Laser-Induced Fluorescence
TAL	Thruster with Anode Layer
VDF	Velocity Distribution Function

Chapter 1

Introduction

1.1 Problem statement

Plasmas with low degrees of ionization, magnetized electrons and weakly-magnetized ions, in crossed magnetic and electric fields (Hall plasmas) are usually in non-equilibrium state with complex nonlinear behavior. Practical applications of such plasmas include: advanced beam-plasma systems for material processing [4], magnetron sputter deposition sources [5,6], space plasma propulsion devices (Hall thrusters [7, 8], helicon thrusters [9, 10], etc.), and MHD generators. Despite the commercial success of some of these devices and long history of their applications, the unknown mechanism for large-scale oscillations and the nature of the anomalous current (when electron current across the magnetic field lines is much larger than predicted by classical [11] or Bohm [12, 13] diffusion) appears to be a key obstacle for future progress in these applied areas, especially when scaling of device parameters is required. The formation of large-scale coherent plasma structures is very common and can critically affect the performance, efficiency, and life-time of these devices. On a fundamental level, this requires a better understanding of turbulence and transport in these plasmas which are very different from typically studied cases of highly-ionized and fully-magnetized plasmas such as that in magnetic fusion or basic plasma science experiments in linear devices. For Hall thrusters, the most prominent coherent modes are breathing and spoke.

Breathing mode is an axially propagating mode with $m = 0$ (m is the azimuthal mode number) and has typical characteristic frequency of about tens of kilohertz. These modes manifest themselves in oscillations of the discharge (and ion) current, and their appearance is usually associated with plasma instability of the ionization region in the thruster channel. Spoke mode is an azimuthally propagating mode with $m = 1, 2, ...$, with a typical frequency

up to 100 kHz. Physical phenomena responsible for the spoke mode are largely unknown. Neither, the exact mechanisms leading to the formation of the breathing mode is well understood. Studying these modes requires an integrated approach that includes theoretical consideration and experimental investigation. The goal of the theoretical research is to develop the understanding of physical mechanisms responsible for the instabilities, formation of coherent structures and anomalous transport in partially-ionized $\mathbf{E} \times \mathbf{B}$ plasmas. Theoretical findings should be confirmed by experimental studies, which require development and application of advanced diagnostics. While full understanding of these phenomena is not yet achieved, methods to control large-scale coherent structures should be investigated and developed so negative effects from these structures can be minimized.

1.2 Research objectives and results

While the scope of the general problem is very broad, the objectives of this work include several narrower topics related to plasma with crossed electric and magnetic fields, and its application for space propulsion, namely Hall thrusters. Hall thruster is a device, where thrust is created by electrostatic acceleration of ions, while electrons are confined with the magnetic field. The magnetic field almost does not affect ion trajectories. Although Hall thrusters have been developed since the 1960s in Russia [14] and in the USA [15], and have been used for a number of successful missions [16], the understanding of fundamental plasma physics in such devices is still not complete. For instance, mechanisms responsible for various oscillations over a wide frequency range, and their effect on the thruster performance and life-time are not fully known. Breathing and spoke oscillations are the most prominent ones, and have the biggest impact on thruster operation.

The theoretical part of this thesis was devoted to the study of the instability mechanism, which appears in plasmas with stationary $\mathbf{E} \times \mathbf{B}$ flows and density gradients, which is a typical situation for all devices with Hall plasmas. This gradient-drift instability mechanism, namely Simon-Hoh [17, 18], is believed to be responsible for large-scale structure formation [19–21]. Previous works on this instability in $\mathbf{E} \times \mathbf{B}$ plasmas were done with the framework of local theory. In this thesis, the nonlocal model for the global instabilities in plasmas with inhomogeneous profiles of plasma density, temperature, electric and magnetic fields

was developed. The nonlocal consideration allows for an investigation of the global effect of profiles on instabilities, and determine the global stability criteria. Results of this research can be used for better interpretation of the nonlinear simulations, and an understanding of physical mechanisms. The theoretical study included the following elements:

- a nonlocal model for the collisionless Simon-Hoh instability was derived;
- MATLAB based spectral code was developed to solve this model numerically;
- the role of density, magnetic and electric field profiles on the eigenmode structure and their frequency and growth rate in typical Hall plasma experiments conditions [22, 23] was investigated.

The experimental efforts in this thesis had two main goals: development of the advanced diagnostic to study the large-scale coherent oscillations in $\mathbf{E} \times \mathbf{B}$ plasma; and to explore methods of control and suppression of coherent plasma structures in these plasma systems by active control of discharge parameters, such as anode potential.

Advanced diagnostic of $\mathbf{E} \times \mathbf{B}$ plasma is required for developing and validation of numerical tools to simulate the physical processes observed experimentally. One of the most important characteristic of the ion flow in the Hall thruster is the ion velocity distribution function (IVDF). It can help to develop an understanding of plasma kinetic processes, and can be directly compared to the results of Particle-in-Cell (PIC) simulations. In this research, the Time-Resolved Laser-Induced Fluorescence diagnostic (TR-LIF) was developed and implemented to study breathing mode and evolution of the IVDF during the discharge current oscillations, and an investigation of the effect of strong oscillations of plasma parameters (density, temperature, potential) on TR-LIF signal was conducted. In these experiments, intrinsic breathing mode oscillations were locked into the externally driven anode voltage modulations. This project included the following stages:

- Time-averaged LIF diagnostic setup and data acquisition system (DAQ) was modified in order to collect the time-resolved signal. This required optics realignment, control of a phase shift between laser pulses and anode modulations, as well as modifications in software.
- TR-LIF signals were obtained in various operation regimes.
- The external modulations of the anode potential were applied at different frequencies

and amplitudes, and IVDFs were collected.

During these experiments two phenomena were found. First, two types of thruster response on the external modulations were identified, depending on the amplitude of the modulation: linear (amplitude <10% of DC anode voltage level) and nonlinear (amplitude >10% of DC anode voltage level). Second, the collapse of the LIF signal in nonlinear regime was observed. In order to explain the collapse of the LIF signal

- emissive probes, an electric circuit and a data acquisition system were made;
- a study of plasma parameters oscillations with the emissive probes was conducted at different external modulations of anode potential.

Active control of plasma oscillations can potentially mitigate the detrimental effects of large-scale modes and affect the performance and lifetime of plasma devices [24]. Therefore, investigation of different thruster responses on various external modulations gave the start to the new project. The aim of this project was to study the effect of the breathing mode amplification on the discharge and the ion currents, and on the thruster performance. In order to verify our experimental findings, the 1D fluid model of breathing oscillations was developed and simulations with BOUT++ framework were performed. The following studies were done:

- The discharge and the ion currents as a function of the external modulation amplitude and frequency were measured.
- The propellant and current utilizations were calculated and the change in the thruster efficiency was estimated.
- The fluid model, which describes breathing oscillations, was developed. This is a time-dependent, 1D model with three species: neutrals, singly charged ions, and electrons.
- Before time-dependent simulations, the stationary solutions were obtained, and analyzed. These stationary solutions were used as initial conditions in BOUT++ simulations.
- The experimental results were compared with model predictions.

As described before, the proposed mechanism for the spoke formation is related to the axial gradients of plasma density and the axial electric field. Breathing mode is responsible for modification of these gradients, potentially affecting the condition for Simon-Hoh instability,

and appearance of the spoke mode. Little work has been done so far to study the interaction between these modes. In our experiments, an active control of the breathing mode with various thruster responses was attempted and the coupling to spoke modes was discovered by the fast imaging diagnostic. These experiments had the following elements:

- The experiments with different modulation amplitudes and frequencies in linear and nonlinear thruster regimes were conducted, and the corresponding signals with a fast frame camera were recorded.
- The image processing algorithm, which is based on techniques from Ref. [25, 26], was developed.
- Recorded signals were analyzed with the developed algorithm realized in MATLAB.

In summary, results of the research projects in this thesis can be represented as follows:

- Linear, nonlocal model for slab and cylindrical geometry for gradient-drift modes (collisionless Simon-Hoh instability) was developed and used to study the global structure of unstable modes in Hall plasma with inhomogeneous profiles of plasma density, electric and magnetic fields. The eigenvalue problem was solved numerically by using spectral methods.
- Time-resolved LIF diagnostic setup was built and implemented for the CHT. Measurements of IVDFs were conducted with various amplitudes of the external modulations. The collapse of the IVDF was observed in the nonlinear (amplitude of the external modulation >10% of the DC anode voltage level) regime.
- The collapse of IVDF was explained with oscillations of the electron temperature. It was shown that the minimum value of the oscillating electron temperature can be below the level needed for ions excitation. At the same time, it can still be sufficient to produce ground-state ions. Therefore, the total ion density is sufficient for the thruster operation, but the density of metastable ions is below the LIF detection limit. This result shows the limitations of the conventional LIF technique for measurements of IVDF, particularly for xenon ions, in plasmas with significant oscillations of plasma parameters (e.g., electron temperature, ion density).
- Experiments with the external modulations revealed two types of the thruster responses: linear and non-linear. In the linear regime the discharge current amplitude grows

proportionally to the modulation amplitude. In the non-linear regime, the discharge current amplitude depends non-linearly on the modulation amplitude.

- Measurements of the discharge and ion currents during modulations showed that the root-mean square value of these quantities increases with the amplitude of modulation, and has resonance nature. Maximum response occurs at the modulation frequency, close to the intrinsic natural breathing mode frequency ~ 13 kHz, when thruster works in linear regime. When thruster operates in non-linear stage, the maximum is shifted towards the lower frequencies, ~ 10 kHz.
- It was demonstrated that the RMS value of the ion current is amplified stronger than the RMS value of the discharge current resulting in an increase of the current utilization (of about 5%) and the propellant utilization efficiencies (of about 40%). The thruster efficiency, defined as a product of the current and propellant utilization coefficients, shows an increase of about 20%.
- The image processing technique was developed and tested, breathing and spoke mode in Hall thruster were identified.
- It was found that the azimuthally rotating spoke mode can be suppressed by the external modulation of the anode potential at frequencies around natural breathing mode and nonlinear thruster response. This result shows that there is an interaction between the azimuthal and axial modes.

1.3 Thesis outline

This thesis is organized as follows. Propulsion basics and introduction to electric propulsion are presented in Chapter 2. This includes: an overview of the general principles of propulsion; basic ideas behind the electric propulsion, its benefits and limitations; a short review of electric propulsion history and future trends; challenges and problems for the development of efficient propulsion devices. Descriptions of Hall thruster and its principle of operation are given. Devices with similar physics, such as Penning discharge and magnetrons, are briefly described. The latter illustrates that the studies of low-temperate plasmas in $\mathbf{E} \times \mathbf{B}$ fields have a wide range of applications outside the space propulsion field. Finally, a description of the most common oscillations in such plasmas is provided.

Chapter 3 is devoted to the description of the experimental facility and diagnostics which were used in this research. General descriptions of Small Hall Thruster Facility (SHTF), LIF setup, and electrical scheme for anode potential modulation are given. An introduction to LIF diagnostic is made. The method of determining the electron temperature from emissive probes is described.

An investigation of a nonlocal model for Simon-Hoh instability is presented in Chapter 4. Several cases were considered and presented to show the difference between predictions of local and nonlocal models. The results of the eigenvalue problem for complex profiles of the magnetic field, electric field, and density relevant to Hall thruster experiment [27] have been studied as well. This chapter is based on a previously published paper [28]. Author's contribution to this work included: writing the code for the eigenvalue problem, analyzing various cases presented in the manuscript, and writing the first draft of the manuscript.

Chapter 5 presents the investigation of the LIF signal collapse. Measurements of plasma parameters are presented and a discussion of possible causes for the collapse are given. The proposed explanation is related to a strong dependence of xenon ion metastable excitation cross-section on the electron temperature oscillations. This poses an important question about limitations of the commonly used LIF technique in systems with strong oscillation of plasma parameters, such as electron temperature and plasma density. This chapter is based on the previously published paper [29]. Author's contribution to this work included: designing the experiment and diagnostics, performing the experiments, analyzing obtained experimental data, and writing the first draft of the manuscript.

Chapter 6 is devoted to the analysis of the stationary profiles obtained from the developed fluid model. The method used to find such profiles is presented and several cases are considered.

Chapter 7 describes the results of the discharge and ion current measurements at various modulations of the anode potential. The experimental results of linear and non-linear types of the thruster response to modulations are presented. The effect of those modulations in terms of the current and propellant utilization is studied. It is shown that the total increase of the thruster efficiency can be up to $\sim 20\%$. The results of the 1D fluid simulations, which show a good agreement with the experimental data, are given. This chapter is based on another

previously published paper [30]. Author's contribution to this work included: designing the experiment, performing the experiments, writing the simulation code and conducting simulations, analyzing obtained experimental data and comparing it with simulations results, and writing the first draft of the paper.

Chapter 8 discusses experiments with the modulated breathing oscillations and their effect on the spoke mode. Image processing from a high-speed camera is described. It is shown that modulation of the breathing mode at the resonance frequency can suppress spoke mode. This chapter is based on the paper submitted to Plasma Physics Reports. Author's contribution to this work included: setting up the fast camera diagnostics, performing experiments, designing the algorithms and codes for data processing, analyzing obtained experimental data, and writing the first draft of the paper.

Chapter 9 provides a summary and discusses some implications and future work.

Chapter 2

Principles of electric propulsion and Hall thrusters

At the current stage of space exploration, there exist a variety of space missions which require more advanced methods of propulsion rather than conventional chemical schemes. Over the years, electric propulsion (EP) has advanced as a main tool for deep space missions, orbit corrections, and station keeping. One of the main advantages is the propellant mass savings that EP can offer. The reduction of the required propellant mass makes a spacecraft smaller and increases the payload and mission lifetime. Another advantage of the EP is a higher specific impulse compared to chemical rockets. This allows a spacecraft to accelerate to higher velocities making deep space missions possible, even though acceleration time is longer due to smaller thrust. This chapter contains background information about propulsion basics, specific features of EP, and principles of the operation of Hall thrusters (HT). Detailed reviews on these topics can be found in Ref. [16, 31, 32].

A definition of plasma and plasma in Hall thrusters is given. A short overview of relevant devices with plasmas in $\mathbf{E} \times \mathbf{B}$ fields is done. Typical plasma parameters and the most important oscillation modes in such plasmas are introduced.

2.1 Principles of propulsion

Rocket propulsion is based on the conservation of momentum; the rocket engine changes the momentum of a spacecraft by changing the momentum of the ejected mass (reaction mass). This reaction mass (or propellant) is accelerated by some kind of engine. Due to

the conservation of momentum, the spacecraft gains a velocity in the opposite direction. There are other exotic types of rocket engines such as solar sails [33] or Bussard ramjet [34]; however, at the current level of technological development, they have not been used in any real mission.

Typically, the propellant is stored on board the spacecraft and then ejected in order to create an acceleration. Therefore, during the rocket engine operation, the spacecraft mass changes. The main equation, which describes the motion of a system with changing mass, can be derived from Newton's second law [35, 36]

$$\mathbf{F}_{ext} + \mathbf{v}_{ex}\frac{dm_p}{dt} = \mathbf{F}_{ext} + \dot{m}_p\mathbf{v}_{ex} = M\frac{d\mathbf{v}}{dt}, \tag{2.1}$$

where $M = m_d + m_p$ is the total mass of the spacecraft including the delivered mass m_d and the propellant mass m_p, $\dot{m}_p$ is the propellant mass flow rate, $\mathbf{v}_{ex}$ is the constant exhaust velocity, and $\mathbf{F}_{ext}$ is external forces (e.g. gravity). By neglecting all external forces, and projecting all vectors on the direction of $\mathbf{v}$, the solution to Eq. 2.1 is

$$\Delta v = v_{ex}\ln\left(\frac{m_d + m_p}{m_d}\right), \tag{2.2}$$

where Δv is the change in velocity of the spacecraft. The latter equation is called the Tsiolkovsky rocket equation [35], or just the rocket equation. From this equation one can see that high final velocity can be achieved by either an increase of v_{ex} or by expulsion of a large amount of propellant. This equation can be modified in terms of mass ratio

$$\frac{m_d}{m_d + m_p} = e^{-\Delta v/v_{ex}}. \tag{2.3}$$

From this formula it is clear that if a payload mass fraction is large, the exhaust velocity v_{ex} should be comparable with the required Δv. Each space mission has its own value of Δv, and it is a fundamental characteristic of the mission. A list of Δv for most common missions can be found in Table 2.1 (data taken from Ref. [37, 38]).

Table 2.1: List of Δv for various space missions (LEO: low-Earth orbit; GEO: geosynchronous orbit; L1: Lagrangian point).

Mission	Δv, m/s
Satellite drag compensation	30
Station keeping	50

Earth to LEO	$9.7 \cdot 10^3$
LEO to GEO	$4.3 \cdot 10^3$
LEO to L1	$3.7 \cdot 10^3$
LEO to Moon	$5.9 \cdot 10^3$
Solar system exploration	$(5 - 15) \cdot 10^3$
Closest stars	10^6

While Eq. 2.2 defines general characteristics of the space mission, there are two main parameters which define spacecraft engine performance: thrust and specific impulse. From Eq. 2.1 one can see that there is a force applied by the engine to the spacecraft due to the exhaust mass. This force T is defined as a thrust and can be written as

$$T = \frac{d}{dt}\Big(m_p v_{ex}\Big) = \dot{m}_p v_{ex}. \tag{2.4}$$

Specific impulse is a measure of thrust efficiency and means the impulse gained by the spacecraft per unit of ejected propellant, or, equivalently, the thrust per unit of the propellant mass. It can be expressed as

$$I_{sp} = \frac{\int_0^{t_p} T(t)dt}{\int_0^{t_p} \dot{m}_p dt} = \frac{T}{\dot{m}_p} = v_{ex}. \tag{2.5}$$

Conceptually, specific impulse is equal to an exhaust velocity (if measured in m/s). However, more often it is defined as v_{ex}/g, where g is the standard gravitational acceleration of the Earth.

In general, thrust of any engine can be characterized by two variables: the exhaust velocity and the propellant mass flow rate. However, specific impulse is solely defined by the exhaust velocity. Therefore, limitations on the specific impulse have a fundamental nature. Low values of the specific impulse lead to an increase of the mass of the propellant, which might not be compatible with overall mission goals.

2.1.1 Energy limits on the specific impulse and thrust

The conventional propulsion system is an energy conversion machine. It converts potential energy of some sort into the kinetic energy of motion. Such systems can be split into several groups. First, based on the way energy is supplied to them: either stored in form of the propellant and then released during the chemical reactions; or supplied from various external

power sources, then energies for an acceleration and a propellant are decoupled. Second, by the manner the propellant is accelerated: by converting the thermal energy into the kinetic energy of the exhaust, or by accelerating the preliminary ionized propellant with the electric field, or a combination of electric and magnetic fields.

Chemical propulsion is when energy is stored in the form of propellant, released during chemical reactions in the form of heat, and then converted into the kinetic energy of the exhaust. Essentially, it is a thermal machine. Energy density stored in such engines is defined by the propellant type and cannot be changed. Therefore, the maximum achievable combustion temperature is limited. One can estimate the lowest achievable exhaust velocity as a thermal velocity of gas molecules in a flame. Typical chemical rocket engines use nozzles to further accelerate the propellant. At the narrowest cross-section of the nozzle the velocity reaches sonic speed, which is proportional to the square root of the temperature. At the expanding part of the nozzle, the speed is further multiplied by a factor of 2 or 3. This multiplication is limited by various factors. Jahn [32] identified the following constraints: the energy density of the chemical propellant; the produced heat load; and heat losses. All these factors restrict the exhaust velocity of a chemical thruster at about 5 km/s [16, 32]. Therefore, achievable specific impulse from this type of thrusters is fundamentally limited.

Nuclear thermal propulsion is an example of another propulsion system where an acceleration of the propellant is achieved by converting thermal energy into the kinetic energy of the exhaust [39]. However, energy in this case is supplied from the external source (nuclear reactor) in form of the heat. Energy density in such systems is not limited by the internal characteristics of the propellant. Therefore, higher thermal velocities are achievable. However, such systems have similar limiting factors as in the case of chemical propulsion: the produced heat load and heat losses. The predicted specific impulse for such systems is 9-10 km/s [40]. The main constraint for these types of engines comes from structural limits of the materials.

Electric propulsion is when the energy source is separated from the propellant, and the propellant acceleration is done by the electric field or a combination of electric and magnetic fields, which requires a preliminary ionization of the propellant. Acceleration can be achieved by the propellant heating by using the electrical power as well. Energy in such systems can

be supplied by nuclear reactors [41], batteries, solar panels, or radioisotope thermoelectric generators [37]. As it was shown in Ref. [38], the thrust per unit of the input power is defined as

$$\frac{T}{P_{elec}} = \frac{2\eta}{I_{sp}}, \tag{2.6}$$

where P_{elec} is the available electric power and η is the thrust efficiency. From this equation, one can see that the thrust is determined by the available power. Moreover, because the exhaust velocity is high, the thrust is always low. Typical values of the exhaust velocity are about 20-30 km/s [16]. Therefore, the main constraint of electric propulsion systems is the available power.

From the above consideration it is clear that characteristics of any rocket engine are defined by the specific impulse and the thrust. These parameters should be matched with the mission specific limitations, especially with the required Δv. For example, cargo delivery in Earth's orbit requires high thrust, so it can compensate for the Earth's gravity and a rocket can vertically take off the ground (see, Eq. 2.1). This can be accomplished only by using chemically powered engines, as high thrust can be achieved only with high mass flows, which is typical for chemical propulsion systems. However, most of the space missions in Earth orbit (station keeping, satellite orbit correction, maneuvering) require a high ratio of useful mass to the total mass of the spacecraft. These requirements can be fulfilled with electric propulsion systems. Deep space missions, such as Solar exploration or beyond, require high values of Δv which can be completed only by electric propulsion systems. Despite low thrust and longer acceleration, the higher final velocity can be achieved.

Nonetheless, while planning space missions one has to take into account the fact that higher specific impulse requires more powerful and larger energy sources. Therefore, increasing the weight of the power supply can prevail over mass savings due to high specific impulse. All of these factors should be taken into account.

2.2 Electric propulsion

Electric propulsion is based on utilizing electrical energy in order to accelerate propellant. Based on the way the propellant is accelerated, electric propulsion devices are divided into three subcategories [32, 42]:

- Electrothermal, when the electrical power is used to heat or ionize gas and acceleration is achieved by conversion of the thermal energy into kinetic energy through the nozzle.
- Electrostatic, when the electrical power is used for propellant ionization, and its follow-up acceleration in an electric field.
- Electromagnetic, when the ionization of the propellant and its acceleration is achieved by the combination of electric and magnetic fields due to the Lorentz $j \times B$ force.

This thesis is focused on the study of electrostatic thrusters, namely Hall thrusters. Up to date there are two types of electrostatic propulsion devices which are commonly used: Ion thrusters and Hall thrusters. In both types of thrusters inert gases like argon, krypton, or xenon, are used as propellants. Ionization occurs due to inelastic collisions with electrons. Ionized gas is accelerated through the electric field only. In ion thrusters the electric field is applied between closely located grids, providing vacuum acceleration of ions. In Hall thrusters the electric field is applied between the cathode and the anode, and the electron current is limited by the externally applied magnetic field. Such configuration of fields causes the closed drift of electrons in the azimuthal direction. That is why such thrusters have another name: thrusters with closed electron drift. A detailed description of Hall thrusters and their principles of operation will be given below.

2.2.1 Brief history of Hall thruster development

The detailed history of electric propulsion can be found in various books [43, 44] and review papers [31, 45, 46]. A review of Hall thruster development can be found in [47]. In this section a brief history is presented.

The first description of thrusters with closed electron drift was presented in 1962 by Janes, Dotson, and Wilson [15]. However, significant progress in the development of such thrusters was achieved in Russia by groups led by A.I. Morozov [14, 48–50] and A. V. Zharinov [51, 52]. The efforts of the first group were focused on thrusters with an extended acceleration zone, or stationary plasma thrusters (SPT). The second group studied anode layer thrusters (TAL), where the acceleration region, compared to SPT, is shorter.

The first space flight of a SPT type thruster occured in 1972 on the Meteor satellite. It operated for more than 170 hours [53]. Since then, such devices have been used on over

240 different missions with 100 percent success [54]. Huge progress in their development was done in the 1970s-80s. In the United States, ion thrusters received more attention, and the development of Hall thrusters was discontinued.

Interest in such systems resumed in the USA and Europe in the 1990s. Since that time, several modifications of SPT and TAL thrusters were used in various missions, such as the National Reconnaissance Office (NRO), Space Technology Experiment Satellite (STEX), European Space Agency (ESA) Small Mission for Advanced Research in Technology (SMART)-1 [16], U.S., Space Systems/Loral [55] and many other projects.

Hall thrusters have several advantages over gridded ion thrusters. First, ions are generated and accelerated in a quasi-neutral plasma, so there is no saturation current limitation (which follows from Child-Langmuir law). This helps to reduce the size of the thruster, compared to gridded ion thrusters. Another advantage is that Hall thruster design does not require one of the most problematic parts - a gridded cathode.

2.2.2 Future trends

Current applications of Hall thrusters mainly include satellite orbit correction or station keeping. There are several projects which propose to use them for deep space missions, such as Solar system exploration and asteroid capturing. However, current trends in space exploration expand the possible application of electric propulsion in general and Hall thrusters in particular. Micro - and nanosatellites (commonly called CubeSats) are an emerging technology, which are rapidly becoming one of the major tools for achieving the goals of various space missions, from space exploration to Earth observation [56, 57]. It is important to note that CubeSats are widely used for educational purposes [58]. Fig. 2.1 shows the total amount of CubSats missions over past two decades (plot is taken from [59]).

This demonstrates an important problem of scaling Hall thrusters to small size, as the typical size of a 1 unit CubeSat is $10 \times 10 \times 10$ cm. This problem has a fundamental nature, as the physics of these types of discharges are not completely understood. Therefore, the emerging need in smaller propulsion devices requires increased efforts in theory, diagnostics, and control methods.

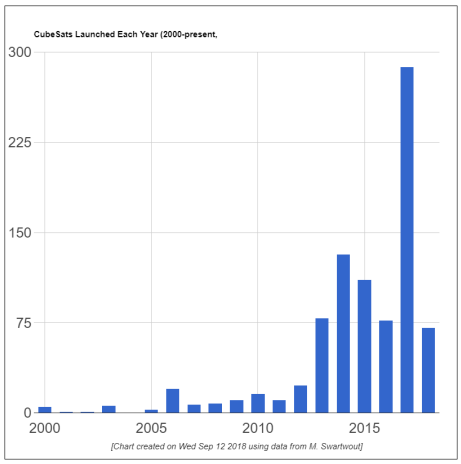

Figure 2.1: Total amount of launched CubeSats, and CubeSats by missions.

When it comes to miniaturization, the electrospray thrusters are considered the most promising candidates, due to their small size, and simple design [60]. However, Hall thrusters have an important advantage in the thrust density, and consequently the volume and mass required for the propulsion system. Low power Hall thrusters regularly achieve thrust densities in the range of 4 N/m^2 to 10 N/m^2, whereas currently available electrospray systems provide 0.15 N/m^2. This higher density implies that a thruster, based on Hall thruster principles, could have a fraction of volume and mass of electrospray thruster with comparable thruster power consumption and performance. The lower mass requirements of a compact Hall thruster allow for a higher Δv. For a 4kg satellite (typical weight of 1U CubeSat) with 100g of propellant on board, modern electrospray propulsion can achieve 267 m/s while a similar low power Hall thruster can achieve 333 m/s. With this configuration, a Hall thruster would provide an extra year of station-keeping over electrospray thrusters, as well as faster cruising time and more orbit options.

However, it is important to emphasize that the scaling to larger powers for Hall thrusters is a high priority task as well. This is required to enable deep space missions with high Δv and heavy payloads [54]. Such missions require up to 100kW thrusters or an array of thrusters with the MW range power unit. One of the most critical problems for such thrusters is a lifetime, which is defined predominantly by the erosion rate. Moreover, thruster characteristics will change over time, requiring a valid physical model in order to predict thruster parameters and adjust mission parameters.

2.3 Principles of operation

Hall thrusters is a common name for a class of EP devices. As it was noted before, there are two main types of Hall thrusters which found practical applications: thrusters with extended acceleration zone (or stationary plasma thrusters); and thrusters with an anode layer. SPTs usually have a channel made out of a dielectric material, which causes secondary electron emission and leads to lower electron temperature. Because of this reason, the channel is relatively long, its length is longer than channel width. Another name for such design is a thruster with extended ionization zone. Contrary to SPT, TAL has a conducting wall, which leads to higher plasma temperature near the anode region, so the ionization process happens in a thin layer near the anode. Because of this, the channel length is shorter compared to the channel width. Stationary plasma thrusters had been developed much wider and had more real-life applications compared to thrusters with an anode layer.

While stationary plasma thrusters and thrusters with anode layer are the two most common schemes, new designs for Hall thrusters have been developed. One of the reasons for this is that conventional schemes become inefficient when scaled to small sizes. One of the attempts to overcome this was the development of a cylindrical Hall thruster (CHT). Because of its magnetic field geometry and discharge chamber without a central coil, it can be easily scaled to smaller sizes [61–63]. Detailed description of the CHT will be given in Chapter 3.

2.3.1 Stationary plasma thruster

First, a description of the operation of conventional SPTs will be given. A Hall thruster is a coaxial discharge plasma system, which has orthogonal electric (**E**) and magnetic (**B**) field. [47]. The general scheme is presented in Fig. 2.2. Two main parts can be distinguished in the Hall thruster: the anode block and the cathode. The cathode is a source of electrons to compensate for the charge of ions outside of the thruster exit plane, which sustains the discharge by closing the electric circuit. A hollow cathode is the most popular scheme. The anode part consists of a magnetic system (electromagnets and magnetic circuit), a discharge chamber, and an anode, which is responsible for maintaining the electric field and functioning as an inlet for neutral propellant. Ionization and particle acceleration occur inside the dis-

charge chamber, which has a coaxial structure. Typical materials for the discharge channel walls are boron nitride (BN) or Borosil (BN-SiO_2) because of their insulation, heat resistance, and secondary electron emission properties. Output plasma flow has a ring structure. A magnetic system is responsible for a radial magnetic field within the discharge chamber volume.

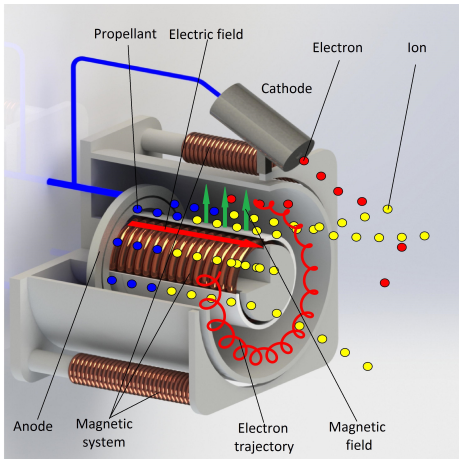

Figure 2.2: Scheme of Hall thruster and electric and magnetic fields.

SPT works as follows. The electric potential is created between the anode and cathode. Electrons from the cathode move inside the discharge chamber by the electric field and are subject to the crossed electric and magnetic fields. The magnetic field is used to modify local electron mobility and to change the shape of an accelerating potential. This field is sufficiently strong to make the electron's Larmor radius much smaller than the chamber characteristic length, thus creating the strong azimuthal $\mathbf{E} \times \mathbf{B}$ flow of electrons. However, ions remain unmagnetized. Therefore, the conditions

$$\rho_e = \frac{v_{th}}{\omega_{ce}} \ll L, \tag{2.7}$$

$$\rho_i = \frac{v_{th}}{\omega_{ci}} \gg L \tag{2.8}$$

are applied. Here, $\rho_{e,i}$ is the Larmor radius of elections and ions, $\omega_{ce,ci}$ are election and ion cyclotron frequencies, v_{th} is the electron or ion thermal velocity, and L is the characteristic size of the system. Collisions force electrons to move to the anode in the axial direction (across the magnetic field). The azimuthal current ($\mathbf{E} \times \mathbf{B}$ drift) can be ten times larger than the axial electron current. This ratio is essentially the Hall parameter, which is defined as a ratio between the electron cyclotron frequency and the electron collisional frequency (all

types of collisions)

$$\Omega_H = \frac{\omega_{ce}}{\nu_e} \gg 1, \tag{2.9}$$

where ν_e is the effective collision frequency. A large value of the Hall parameter [16] ensures long residence time for electrons which leads to an almost full ionization of the propellant flow, creating more electrons, and supporting the discharge. Usually the propellant is a noble gas with low ionization potential, large atomic mass, and a sufficiently large ionization cross-section. The fraction of doubly charged ions is usually small, however not negligible [47]. Ions move out of the acceleration region by gaining energy from the axial electric field. This ion beam is neutralized by a fraction of electrons emitted by the cathode.

2.3.2 Momentum exchange in Hall thruster

The general principle of operation of Hall thrusters is in the ionization of the propellant and its acceleration by the applied electric field. However, it is important to clarify the exact mechanism of momentum transfer from ions to the thruster and the spacecraft.

Even though Hall thrusters are considered as being an electrostatic accelerator, the real momentum transfer mechanism is due to the electromagnetic forces, acting between the accelerating ions and the electromagnetic coils, as can be seen from the following arguments. The ions are accelerated by the electrostatic force generated from the applied electric field. Because ions are unmagnetized, the force on them is

$$\mathbf{F}_i = 2\pi \iint en_i \mathbf{E} r dr dz. \tag{2.10}$$

This force is opposite in sign to the electrostatic part of the force acting on the electrons $\mathbf{F}_e$. However, electrons are confined by the magnetic field, and cannot move in an axial direction. Therefore, electrostatic force on electrons is balanced by the Lorentz force $\sim \mathbf{v}_e \times \mathbf{B}$. This can be written as

$$\mathbf{F}_e = -2\pi \iint en_e \mathbf{E} r dr dz - 2\pi \iint en_e \mathbf{v}_e \times \mathbf{B} r dr dz. \tag{2.11}$$

Because forces on electrons and ions should be equal, the net force acting on ions is

$$\mathbf{F}_i = \mathbf{J}_{Hall} \times \mathbf{B}, \tag{2.12}$$

where the Hall current is defined as $\mathbf{J}_{Hall} = -en_e \mathbf{v}_e$. According to Newton's second law, this force acts on the magnetic system with the opposite sign. Thus, the momentum is transferred

from the ions to the thruster due to the Lorentz force acting on the Hall current. This is the reason why such thrusters are sometimes considered electromagnetic.

2.3.3 Thrust, specific impulse, and thruster efficiency

Thrust and specific impulse are the main characteristics of any rocket engine. Electric propulsion devices are characterized by additional important parameters: thruster efficiency and input power. Let's consider how these parameters can be obtained and what information they can provide. For Hall thrusters the accelerated ions are the main source of thrust, so it can be described as

$$T = \dot{m}_p v_{ex} = \dot{m}_i v_i. \tag{2.13}$$

The ions are accelerated by the electric field, so from the conservation of energy the ion velocity is given by

$$v_i = \sqrt{\frac{2qV_b}{M_i}}, \tag{2.14}$$

where V_b is the net voltage through the acceleration region, q is the charge, and M_i is the ion mass. The mass flow rate can be represented through the ion beam current I_b

$$\dot{m}_i = \frac{I_b M_i}{q}. \tag{2.15}$$

Substituting Eqs. 2.14 and 2.15 into 2.13 we have

$$T = \dot{m}_p v_{ex} = I_b \sqrt{\frac{2M_i}{q} V_b}. \tag{2.16}$$

It is important to note that beam voltage V_b is an average beam voltage due to a spread in beam energies.

This equation requires two corrections. First, due to the beam divergence, and second due to multiply charged ions. The correction factor due to the beam divergence is defined as

$$F_t = \frac{2\pi \int_0^r rJ(r)\cos\theta dr}{I_b}, \tag{2.17}$$

where $J(r)$ is the ion current density as a function of radius.

The correction due to multiply charged ions is given in the form

$$\alpha = \frac{1 + \frac{1}{\sqrt{2}}\frac{I^{++}}{I^{+}}}{1 + \frac{I^{++}}{I^{+}}}, \tag{2.18}$$

where I^+ and I^{++} are currents from singly and doubly charged species respectively. The total correction factor is then the product of these two factors, and is

$$\gamma = \alpha F_t. \tag{2.19}$$

Therefore, Eq. 2.16 becomes

$$T = \gamma I_b \sqrt{\frac{2M_i}{q} V_b}. \tag{2.20}$$

In general, specific impulse is defined by Eq. 2.5. For the case of EP, by using the definition for thrust from Eq. 2.13, the following expression can be obtained

$$I_{sp} = \frac{\dot{m}_i v_i}{\dot{m}_p}. \tag{2.21}$$

The mass utilization efficiency can be introduced here. It is a parameter, which is specific to the electric propulsion and defined by the relation

$$\eta_m = \frac{\dot{m}_i}{\dot{m}_p}. \tag{2.22}$$

Thus, the specific impulse can be presented as

$$I_{sp} = v_i \eta_m, \tag{2.23}$$

and after substituting Eq. 2.14 into 2.23 we have

$$I_{sp} = \eta_m \sqrt{\frac{2q}{m_i} V_b}. \tag{2.24}$$

The total thruster efficiency is defined as the beam power P_b divided by the total input power P_T or, by using the fact that the beam power is defined as the thrust multiplied by the exhaust (or ion) velocity, it can be written as

$$\eta_T = \frac{P_b}{P_T} = \frac{T v_{ex}}{P_T}. \tag{2.25}$$

By using the Eq. 2.5 for the specific impulse, the following expression for the total efficiency can be obtained

$$\eta_T = \frac{P_b}{P_T} = \frac{T^2}{2\dot{m}_p P_T}. \tag{2.26}$$

The total gas flow in Hall thrusters is the sum of flows through the cathode and the anode

$$\dot{m}_p = \dot{m}_a + \dot{m}_c, \tag{2.27}$$

where $\dot{m}_a$ is the anode mass flow, and $\dot{m}_c$ is the cathode mass flow. In order to characterize the ionization efficiency of the thruster, the mass utilization efficiency is introduced

$$\eta_m = \frac{\dot{m}_i}{\dot{m}_a + \dot{m}_c}, \tag{2.28}$$

where $\dot{m}_i$ is the ion mass flow. This coefficient shows what fraction of the propellant is ionized and produces thrust. In laboratory experiments, cathode mass flow is often ignored, and anode efficiency is used

$$\eta_a = \frac{\dot{m}_i}{\dot{m}_a}. \tag{2.29}$$

This is done to separate the effects of cathode and magnetic system losses from plasma generation and acceleration. Another useful coefficient is the current utilization efficiency. It is defined as a ratio of the beam current I_b to the total discharge current I_d

$$\eta_b = \frac{I_b}{I_d}. \tag{2.30}$$

Modern devices have the efficiency in the range 40-60 %. The efficiency of Hall thrusters is defined as power of outgoing stream divided by the input power. There are a lot of factors that impact the efficiency of a Hall thruster, but from a physical point of view, the most important aspect is electron mobility. Electron mobility determines the potential distribution inside the thruster and defines the balance between ion and electron currents.

2.3.4 Anomalous current and thruster performance

The equation for the thruster efficiency 2.26 can be written in terms of the ion electron currents

$$\eta_T = \frac{T^2}{2\dot{m}_p P_{in}} \propto \frac{I_i}{I_i + I_e}.$$

From this equation it is clear that a large electron current reduces the efficiency of the thruster. However, electron mobility should be high enough to maintain the ionization process. The classical collision model predicts the axial electron current to be an order of magnitude smaller than the experimentally observed values. Most models describing profiles of plasma properties inside the channel use "anomalous" transport coefficients [64,65]. These coefficients are measured in experiments and are not universal. Such empirical models cannot satisfy modern requirements for the efficiency and lifetime of Hall thrusters. That is why a lot of research efforts are focused on finding a model that can predict the anomalous electron current.

There are two main ideas to explain the anomalous transport in Hall thrusters. Near wall conductivity was proposed and experimentally detected by Morozov [66, 67]. Anomalous transport is the result of electron collision with the walls. Another mechanism is connected

with fluctuations in plasma. Oscillations in a wide range of frequencies have been reported in plasma discharges for a long time [68–70]. Previous studies of anomalous transport suggest that such fluctuations in plasma can be responsible for it.

In Hall accelerators, azimuthal structures were already observed in very early works [64] where it was also suggested that ionization processes play important role. However, physical mechanisms of this behavior have not been explained. Electron drift in $\mathbf{E} \times \mathbf{B}$ direction is an important source for instabilities for crossed-field plasmas. Instabilities due to plasma parameter inhomogeneity have an azimuthal propagation.

Understanding processes in $\mathbf{E} \times \mathbf{B}$ plasmas can help optimize thruster parameters to create systems for active control and suppression of the instabilities. Moreover, an ability to predict a cross-field transport in magnetized plasmas will have a drastic effect on many applications, for example magnetized plasma fusion [71].

Before a brief introduction to the common types of modes relevant to Hall thrusters, a description of devices, which share similar physics, will be given in the next section.

2.4 Relevant $\mathbf{E} \times \mathbf{B}$ discharges

A description of relevant $\mathbf{E} \times \mathbf{B}$ devices should begin with a device which has been used for studies of Hall plasmas at Princeton Plasma Physics Laboratory (PPPL) in parallel to Hall thrusters. An important part of instability studies is an experimental investigation of plasma fluctuations and validation of theoretical and numerical models. The Hall thruster is not convenient from an experimental point of view, especially when probe measurements are performed. Thus, a more flexible and versatile setup is required. A Penning trap is a classical example of a plasma device with crossed electric and magnetic fields. The magnetic field is applied in an axial direction, and the electric field is in radial direction, so this discharge has an inverse Hall thruster configuration, but it allows much easier access for plasma diagnostics, due to larger size.

The radial electric field is generated by a set of three electrodes: a ring and two endcaps. The magnetic field in combination with the electric field causes charged particles to move in the radial plane with a motion which traces out an epitrochoid. The general scheme of the device and fields inside the Penning discharge are shown in Fig. 2.3.

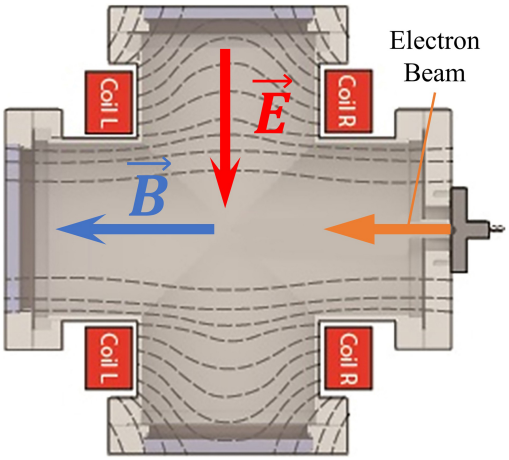

Figure 2.3: Scheme of a Penning trap at PPPL.

Experiments with Penning discharges have demonstrated many instabilities which seem to be similar to those in Hall thrusters. One could expect that there are essential common physics elements between these two systems. The geometry of Penning discharge is similar to the geometry of Hall thrusters especially in latest designs with strong axial magnetic field. The particular experimental design at PPPL has the axial beam of energetic electrons that serves as a cathode and the coaxial outer electrode as an anode. The applied voltage creates the radial electric field and the axial magnetic field is created by the external solenoid, thus creating crossed E and B field configuration. However, Penning discharge is simpler to design and easy to study, which is why it is used in experiments where parameters of different instabilities are measured. It is even more important that this configuration is very similar to the central region of the magnetically shielded Hall thruster. This similarity concerns not only the magnetic field configuration, which is almost axial in the near axis region for magnetically shielded Hall thruster H6MS [72], but also due to the presence of high energy electrons emitted by axially mounted cathode in H6MS. It is worth noting here that the presence of high energy electrons emitted from the cathode may be an important factor in triggering the spokes as it was demonstrated in PPPL experiments with hollow cathode in over-run regimes [73].

Another example of a device widely used in industry, especially for microelectronic productions, is magnetrons [6]. A general scheme of a planar magnetron is shown in Fig. 2.4. Magnetron itself is a diode with a magnetic system. The magnetic field is required to confine electrons, produced by a target bombardment with the working gas. Magnetic system is

developed in a way that electrons are confined close to the target surface. Confinement is achieved by a combination of electric **E** and magnetic **B** fields. The electric field is directed perpendicular to the target surface, and the magnetic field is tangential to the surface. This combination of field forces electrons to flow in a direction parallel to the target.

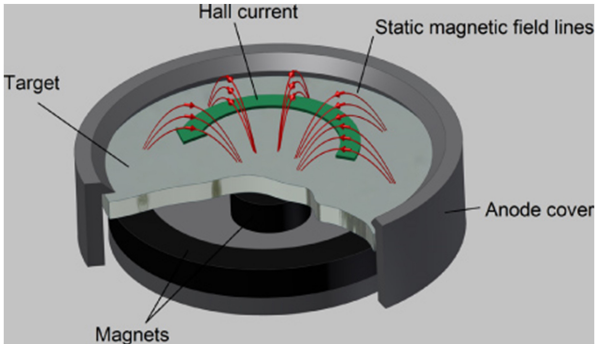

Figure 2.4: Scheme of a planar magnetron (figure is taken from Ref. [1]).

There are other industrial applications for devices with $\mathbf{E} \times \mathbf{B}$ plasmas. Table 2.2 lists the properties of the plasma used in these applications. A common characteristic of plasma in all of these applications is strong electron currents due to the crossed electric and magnetic fields, and strong density, magnetic field and temperature gradients.

Table 2.2: Plasma properties in cross-field plasma devices for advanced applications. It is important to note that $T_e \gg T_i$; however, there is ion acceleration in some cases.

	Atomic scale etcher	Magnetron, Fig. 2.4	Hall thruster	High-current plasma switch, Fig. 2.5
Characteristic size, cm	10^2	10^2	$< 10^2$	10^0
Working gas	Ar	Ne, Ar, Kr, Xe	Kr, Xe	He, Ar
Gas pressure, Torr	10^{-3}	10^{-3}	10^{-4}	10^{-1}
Plasma density, cm^{-3}	10^{11}	$10^9 - 10^{13}$	$10^{10} - 10^{12}$	$10^{12} - 10^{13}$
Magnetic field, Gauss	10^2	$10^2 - 10^3$	10^2	$10^2 - 10^3$
Electric field, V/cm	1	1-10	10^3	$< 10^2$
Electron temp., eV	1-10	10-100	10-100	10-100

An example of the high-current switch is shown in Fig. 2.5. Essentially it is a gas tube device, which is an enabling technology for increased security in power grids. Crossed electric and magnetic fields are utilized in this system. This allows or an increase of operation voltage up to 100 kV.

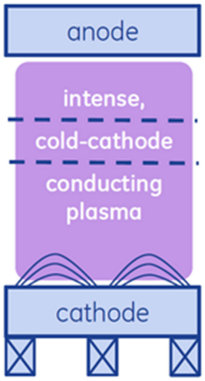

Figure 2.5: High-current plasma switch.

2.5 Plasma and its characteristics in Hall thrusters

In general, plasma can be defined as an ionized gas, where neutrals, electrons and ions of different charge are presented. When the temperature is high, all neutrals become ionized and plasma is called a fully-ionized plasma. Each of these species has its own characteristic temperature, thus, it should be defined for each species independently. For plasma description, an electron temperature T_e and an ion temperature T_i are typically used. For most plasma conditions, the electron temperature is larger than the ion temperature. This is a consequence of the fact that ions (m_i) are much heavier than electrons (m_e) and that in most situations energy is supplied to electrons first. Therefore, plasma is a strongly non-equilibrium system, with electrons and ions at significantly different temperatures.

Quasi-neutrality

An important characteristic which allows to define the collection of charged particles as plasma, is that it is a quasi-neutral system. This means that the electron charge density (en_e, where n_e is the electron number density) on average is equal to the ion charge density ($Z_i e n_i$, where Z_i is the ion charge, and n_i is the ion number density). Due to thermal particles motion, local quasineutrality breaks and an electric field arises, which tries to return charges

back to the equilibrium. Therefore, the distance at which particles can be separated is limited by their thermal (kinetic) energy. One can estimate this characteristic distance from simple assumptions. Let's assume that ions are cold ($T_i \approx 0$), meaning that they almost do not move, compared to electrons. Then, the electric field would appear only due to electron motion. If electrons move to some distance L, it would lead to the electric field $E \sim 4\pi e n_e L$. Because this distance is limited by the electron's thermal energy, it implies $EL \sim T_e$, therefore

$$L \sim \sqrt{\frac{T_e}{4\pi n_e e^2}} \sim \lambda_D. \tag{2.31}$$

This distance is called a Debye length, and denoted as λ_D. Within this distance, quasi-neutrality condition might not be satisfied, whilst at the distances larger than λ_D, quasi-neutrality always holds. Another meaning of the Debye length is the length at which charge is screened. If test charge Q is immersed in plasma, its potential will decay with the distance r as

$$\phi(r) = \frac{Q e^{-r/\lambda_D}}{r}, \tag{2.32}$$

which is faster than it would follow from Coulomb's law

$$\phi(r) = \frac{Q}{r}. \tag{2.33}$$

This additional term e^{-r/λ_D} appears due to finite electron temperature, which partially compensates for the electric field of the test charge.

When an electric field arises in plasma in order to compensate for the charge separation, it returns the electrons to their equilibrium position. However, due to the inertia effect, electrons do not stop at this position, but oscillate around it with certain frequency. This frequency can be defined as follows

$$\omega_{pe} = \sqrt{\frac{4\pi n_e e^2}{m_e}}. \tag{2.34}$$

The ω_{pe} frequency is called the electron plasma frequency. It shows how fast charge separation occurs, and is a characteristic frequency of the fundamental plasma eigenmode - Langmuir oscillations.

Collective behavior

The second fundamental plasma characteristic is that it exhibits the collective behavior. Interaction in neutral gases occurs through binary collisions, therefore only two closely located

particles interact. Contrary to neutral gases, particles in plasma can interact through long-distance Coulomb forces. However, as it was shown before, this interaction can happen only within the Debye length. In three dimensions this forms a sphere, called the Debye sphere. Such interaction is collective, as it involves many particles inside the sphere. This collective behavior results in plasma wave oscillations. Therefore, the plasma dynamics are significantly different from waves in neutral gases.

Collective behavior becomes dominant in plasma when the number of particles within the Debye sphere is sufficiently large. This can be written as a following condition

$$n\lambda_D^3 \gg 1, \tag{2.35}$$

where n is the particles number density. The quantity $n\lambda_D^3$ is called the plasma parameter and it shows the number of particles within the Debye sphere.

Particle motion in electric and magnetic fields

As was mentioned before, the magnetic field in Hall thrusters prevents free electron motion to the anode. However, ions are not affected by magnetic field. The main reason for this is their mass, which is much greater than the electron mass. Particle motion in electric and magnetic fields is determined by the Lorentz force

$$F_L = m\frac{d\mathbf{v}}{dt} = q(\mathbf{E} + \mathbf{v} \times \mathbf{B}). \tag{2.36}$$

Under the influence of this force a particle has circular motion which is characterized by Larmor radius ρ_L. Larmor radius is defined as

$$\rho_L = \frac{v_\perp}{\omega_c}, \tag{2.37}$$

where $\omega_{ce,i} = qB/m_{e,i}$ is cyclotron frequency of electron or ion. Thus, electrons are "magnetized" because electron Larmor radius is smaller than a region where a strong magnetic field exists. This region is characterized by length L.

In crossed electric and magnetic fields, particles are subject to $\mathbf{E} \times \mathbf{B}$ drift. The characteristic velocity of this drift is in a direction perpendicular to magnetic and electric fields, and is equal to

$$\mathbf{V}_0 = \frac{\mathbf{E} \times \mathbf{B}}{B^2}. \tag{2.38}$$

2.5.1 Hall plasmas

Plasma in all $\mathbf{E} \times \mathbf{B}$ devices, described before, have the following common characteristics

- Magnetized electrons $\rho_e < L$, $\omega < \omega_{ce}$.
- Unmagnetized ions $\rho_i \geq L$, $\omega > \omega_{ci}$. However, there are cases when ion magnetization becomes important.
- Electron-neutral and ion-neutral collisions could be important for low-frequency oscillations.

Such plasmas are referred to in this thesis as Hall plasmas.

2.6 Oscillations and plasma dynamics in $\mathbf{E} \times \mathbf{B}$ discharges

A wide range of oscillations have been observed in the experiments with different types of $\mathbf{E} \times \mathbf{B}$ discharges. Characteristic frequencies of observed fluctuations and their amplitudes may differ depending on the operating regimes. However, they can all be grouped into three categories:

- Low frequency (1-100 kHz). There are two main types of oscillations in this range: azimuthal and longitudinal, which often appear as coherent modes, eg. spokes and breathing mode.
- Mid-range oscillations 70-500 kHz. These oscillations are mostly electrostatic waves which can be relatively incoherent.
- High-frequency oscillations - from 0.5 MHz up to 5 MHz. These modes are difficult to measure and their role in the operation of Hall thrusters and their relation to low frequency modes is not understood.

Low frequency

Coherent axial oscillations in the range from 1 to 20 kHz are referred to as "loop" or "breathing" oscillations. The amplitude of these oscillations can be up to 100 % of the total current amplitude. There is a strong dependence on amplitude of these oscillations in the magnetic field, so there is an "optimal" operation regime where these oscillations are almost suppressed. It is often thought that these oscillations are related to the instability of the ionization zone.

Oscillations in an axial direction with a wider frequency band - 20-100 kHz are considered

to be low-frequency too. One of the sources for instabilities is collisions with neutrals, which dominate in weakly ionized plasma. A relevant case of oscillations is in frequency range $\nu_{in} < \omega < \nu_{en}$ [74].

There are low-frequency modes, which propagate in azimuthal direction. The "spoke" mode was observed in many experiments in various types of $\mathbf{E} \times \mathbf{B}$ discharges. This instability occurs in the 5-25 kHz range and can reach significant amplitudes and affect thruster efficiency. There are some conditions when these oscillations can be suppressed. However, there is no satisfactory physical model which would allow to predict the appearance and behavior of this mode. It is assumed to be related to the ionization, however its mechanism can also be similar to the Simon-Hoh instability. These structures may have crucial relations to the nature of anomalous mobility in the thrusters; for example, experimental measurements had shown that significant fraction of the total current (above 50%) occurs within the spoke region [21]. Thus, it is important to understand physical mechanisms of the coherent structures and their relations to the instabilities and fluctuations. Their understanding is a fundamental physics problem which opens the way for active control of fluctuations [75] and regimes with enhanced performance [20].

Another type of azimuthal modes are gradient-induced oscillations, which have frequencies in a band of 20-60 kHz. Their amplitude has a strong dependency on the magnetic field profile. Azimuthal oscillations in this band are mostly electrostatic waves with $k_z \ll k_y$ (here k_y is in azimuthal and k_z is in axial directions). The main sources of instabilities for these oscillations are due to gradients of the magnetic field and density. Sometimes these waves are associated with fast magnetosonic waves.

Intermediate frequency

The frequency of oscillations in this range can be roughly estimated as a V_{0i}/L, where L is the system length and V_{0i} is the ion flow velocity. Their amplitude can be up to 30 % of discharge current and can affect the thruster efficiency. These oscillations are relatively turbulent and are believed to be responsible for anomalous diffusion. The nature of these oscillations is quasiaxial electrostatic waves. Their behavior is well described by the linear theory. Essentially, these oscillations are gradient driven magnetosonic waves with almost

axial propagation. They are caused by inhomogeneity in the ion beam [76].

High frequency

Oscillations in this range become important in the "optimal" regimes of operation when oscillations at lower frequencies become weak. These oscillations have a strong dependency on magnetic field. Their amplitude can be relatively high and can play an important role in thruster efficiency.

Even though it seems that lower frequency oscillations play a more important role in Hall thruster operation, it is believed that higher frequency oscillations, like gradient-driven oscillations, can be responsible for anomalous transport. It is also possible that these oscillations can cause lower frequency oscillations with higher amplitude, like spokes.

2.6.1 Types of waves in partially magnetized plasmas

The above description gives a qualitative picture of oscillations in Hall plasmas. In this section, the description of several characteristic velocities and frequencies is given.

- The first important characteristic velocity is the ion sound speed
$$c_s = \sqrt{\frac{T_e}{m_i}}, \tag{2.39}$$
which corresponds to the ion sound mode $\omega^2 = k^2 c_s^2$, where k is the wavevector.
- Azimuthal (closed drift) $\mathbf{E} \times \mathbf{B}$ flow of electrons in crossed $\mathbf{E} \times \mathbf{B}$ fields has the characteristic velocity
$$\mathbf{V}_0 = \frac{\mathbf{E} \times \mathbf{B}}{B^2} \sim \frac{E_0}{B_0}. \tag{2.40}$$
It corresponds to the frequency $\omega_0 = k_y V_0$, where k_y is the wavevector in azimuthal direction.
- Ion flow across the magnetic field, accelerated by the potential difference V
$$V_i = \sqrt{\frac{2eV}{m_i}}. \tag{2.41}$$
Corresponding frequency is proportional to the system length L, $f = V_i/L$.
- Axial gradients of density and magnetic field are responsible for diamagnetic and magnetic drifts
$$\mathbf{v}_* = \frac{T_e \mathbf{B} \times \nabla \ln n_e}{eB^2} \sim -\frac{T_e}{eB_0 L_N}, \tag{2.42}$$

$$\mathbf{v}_D = \frac{T_e \mathbf{B} \times \nabla \ln B}{eB^2} \sim -2\frac{T_e}{eB_0 L_B}, \tag{2.43}$$

where

$$L_n^{-1} = |\nabla \ln n_0(x)|\,, \tag{2.44}$$

$$L_B^{-1} = |\nabla \ln B_0(x)| \tag{2.45}$$

and L_n is the characteristic length of the density gradient and L_B is the characteristic length of the magnetic field gradient.

These sources are characterized by frequencies $\omega_D = k_y v_D$ and $\omega_* = k_y v_*$.

- Lower-hybrid frequency

$$\omega_{LH}^2 = \Omega_{ci}\Omega_{ce}, \tag{2.46}$$

where Ω_{ci} is the ion cyclotron frequency, and Ω_{ce} is the electron cyclotron frequency.

The basic modes shown above are stable; however, under certain conditions, these waves can be destabilized. Mechanisms for their destabilization will be described more in detail in Chapter 4.

2.7 Summary

In this chapter, the basic principles of propulsion, in general, and electric propulsion, in particular, are presented. It was shown that electric propulsion is more preferable for most space missions, because of the reduction of the required propellant mass and increased payload.

A history of Hall thruster development is reviewed, and future trends are highlighted. One of the biggest challenges for modern electric propulsion systems is the scaling to larger and smaller sizes. On the one hand, development of CubeSats and nanosatellites requires very efficient propulsion systems which can remain efficient even after they are scaled down. On the other hand, deep space missions require thrusters in the 100s kW range and higher, with stable and predictable operation over a long period of time.

The principles of operation of stationary Hall thrusters are given, and the physical mechanism of the momentum transfer from the exhaust to the spacecraft is described. It was

shown how to characterize thrust and the specific impulse for the Hall thruster. Total efficiency of the thruster was derived, as well as anode and beam efficiencies, which are helpful for thruster characterization under laboratory conditions. From the definition of total efficiency, it was shown that the anomalous current has a negative impact on the efficiency, and that the problem of anomalous current has a fundamental nature.

A brief introduction into relevant $\mathbf{E} \times \mathbf{B}$ devices and their parameters has been presented. These devices share similar physics, and resembling oscillations and instabilities were observed experimentally; even though plasma parameters, such as electron temperature, pressure, or electric field, can vary by an order of magnitude. This shows the importance of the research in this field, as it can have an impact in many areas where these devices are used.

A basic description of stable eigenmodes relevant to the plasma conditions in Hall thrusters is presented. These waves can become unstable due to gradients of plasma and due to the external perturbations or fields. An overview of experimentally observed oscillations in Hall thrusters is given. These oscillations are divided into three bands: low frequency, intermediate frequency, and high frequency. Two modes of interest (spoke and breathing) belong to the low frequency band, and are the most prominent ones.

Chapter 3

Experimental Setup and Techniques

In this Chapter, a description of the experimental facilities and diagnostics, used in this thesis, is presented. All experiments were conducted at the Small Hall Thruster Facility at Princeton Plasma Physics Laboratory (PPPL). The main test subject was the 200W cylindrical Hall thruster. A conventional electrical circuit, which is used to control thruster operation, was modified in order to apply external modulation of anode potential to study thruster response on external modulations and to implement Laser-Induced Fluorescence (LIF) diagnostics. LIF was used to obtain time-resolved ion velocity distribution functions (IVDF) in the thruster plume during the breathing mode. Emissive and biased planar probes were used to measure plasma properties (plasma potential, electron temperature, and ion density) during the external modulations. An investigation of the coupling between spoke and breathing modes was done with a fast frame camera and subsequent image processing. The description of the image processing technique will be given in Chapter 8.

3.1 Small Hall Thruster Facility

The Small Hall Thruster Facility (SHTF) includes a vacuum system, a control system, and a cylindrical Hall thruster. The vacuum system consists of a stainless-steel vacuum chamber 1 m in length and 0.8 m in diameter ($\sim$ 1 m^3 volume) and equipped with a blower, a mechanical pump, and Osaka TG3203M turbo-molecular pumping system. This vacuum system achieves the base vacuum pressure of about 10^{-8} Torr without any gas supplied into the chamber. During operation, propellant for the thruster is supplied from the xenon tank. Typical flow rates are 3-4 sccm through the anode and 2 sccm through the cathode. Under

these conditions, the background gas pressure in the vacuum chamber did not exceed $6 \cdot 10^{-5}$ Torr (corrected for xenon). Pressure was measured with an external ion gauge, mounted on top of the vacuum chamber. The thruster was operated from the control rack, which allows for setting and monitoring of the operating parameters. A general view of the vacuum chamber and the control rack is shown in Fig. 3.1a and b respectively.

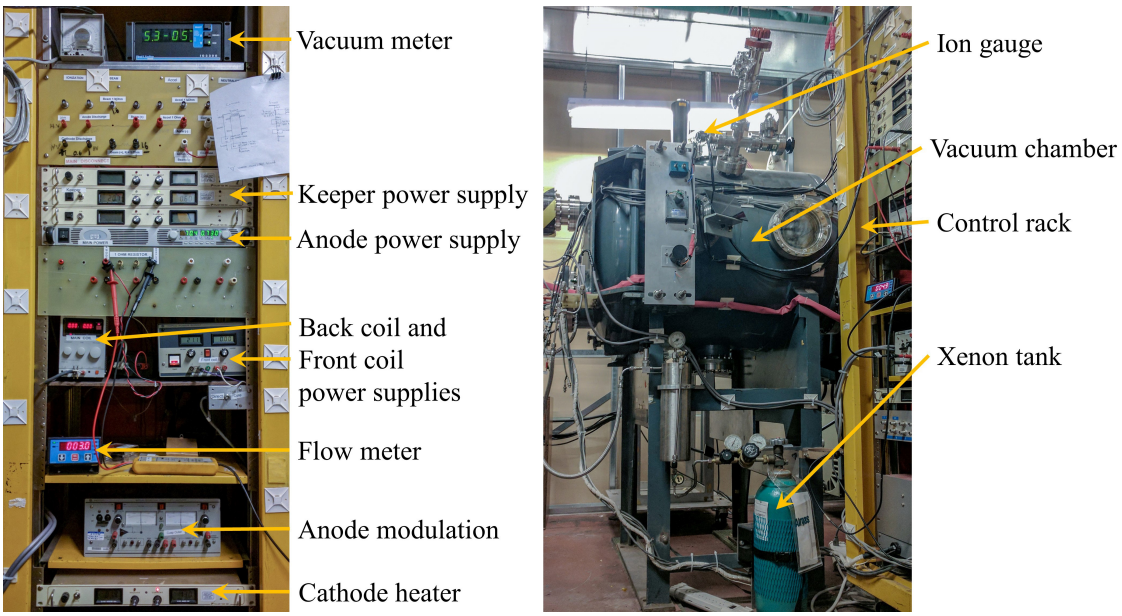

Figure 3.1: a) General view of the Small Hall Thruster Facility (SHTF); b) the control rack of SHTF.

The control rack includes a vacuum meter reading box, cathode keeper power supply, anode power supply, back (main) and front coils power supplies, 2-channel flow controller for anode and cathode flows, Kepco amplifier BOP50-4M for anode modulation, and cathode heater power supply. The main control parameters during the operation are the anode voltage, the gas flow, and the magnetic field configuration. Typically, the thruster works in voltage control mode, meaning that the discharge current adjusts itself. Electric circuitry is shown in Fig. 3.2.

An important modification of this circuitry from the conventional setup is the Kepco amplifier BOP50-4M for anode modulation, which allows to append an amplified function generator signal to the DC anode voltage level. The sine wave signal from the function generator drives the Kepco amplifier BOP50-4M, which has a bandwidth of 23 kHz, an output range of ± 50 V, and a current draw ± 4 A. It is connected in series between the main

power supply (GEN600-1.3) and the anode. Therefore, anode voltage becomes:

$$V_{anode} = V_{DC} + V_{amp}, \tag{3.1}$$

where V_{DC} is the DC anode voltage and V_{amp} is the driving voltage from the amplifier. A similar idea was used in works by Yamamoto et. al. [77, 78].

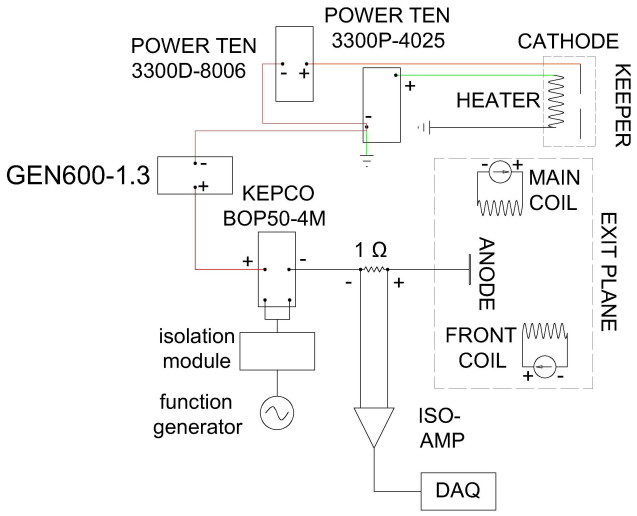

Figure 3.2: Electrical circuitry for operating the CHT thruster. It includes systems for anode voltage modulation and electrical measurement.

This facility allows for installation of various diagnostics. Multiple electric feedthroughs let to install probes for plasma parameters measurements. Viewports allow for the implementation of optical diagnostic.

3.1.1 Cylindrical Hall thruster

The main test subject for all experiments was a 2.6 cm diameter 200W cylindrical Hall thruster. As mentioned before, the miniaturization of Hall thrusters is an important requirement for modern space exploration devices. Attempts to reduce size of SPT were not very successful; thus, the idea of a different scheme appeared. It was proposed to remove the inner part of the SPT, which allows for a reduction of the channel radius. This type of thruster is called a cylindrical Hall thruster (CHT) and was developed by Raitses, et al. at PPPL [61]. A general scheme of the CHT is shown in Fig. 3.3. The thruster consists of three main blocks: magnetic system (back and front coils); the cathode-neutralizer, and the anode. The main difference from SPT is in the organization of the magnetic system and the absence of

the central part in the channel.

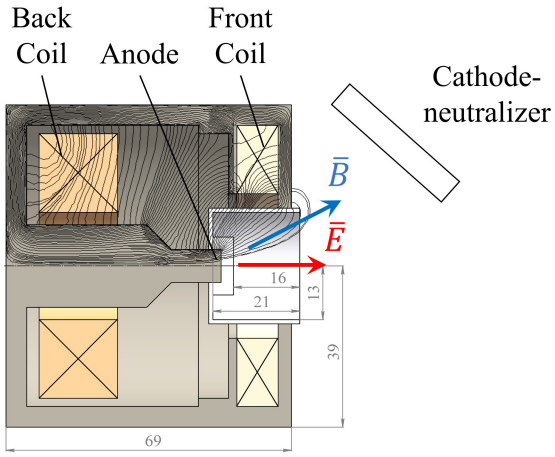

Figure 3.3: Scheme of cylindrical Hall thruster. All sizes are in millimeters. Location of the cathode-neutralizer can be varied. Black lines are magnetic field lines.

This type of thruster has increased ionization efficiency, small surface to volume ratio, which leads to reduction of the erosion, and performance comparable to typical SPT levels [79, 80]. Aside from the absence of the central part, this thruster has a significantly different shape and magnitude of the magnetic field, see Fig. 3.4. This is related to the fact that the magnetic field scales inversely with the thruster size [61]; therefore, for smaller thruster size the magnetic field should increase. Magnetic fields for SPT-100 and SPT-50 in Fig. 3.4 are shown for comparison.

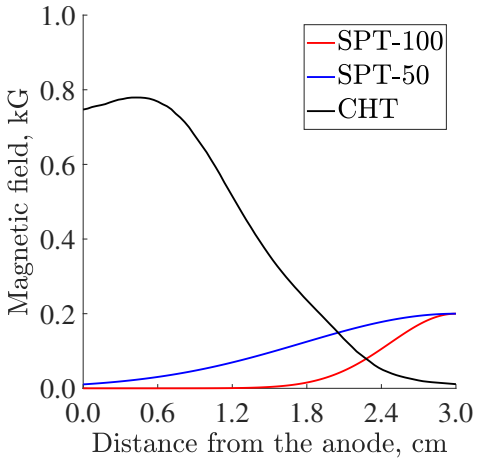

Figure 3.4: Radial magnetic field profiles for CHT and widely used SPT-50 and SPT-100 thrusters.

In all experiments, the thruster was operated with xenon-gas as a propellant. The flow

rates through the anode and the cathode were 3.5 sccm and 2.0 sccm, respectively. The thruster was operated in the direct magnetic field configuration with co-direct currents through the main (back) and the front coils. This magnetic field configuration has been extensively studied in the past and was shown to provide the highest efficiency for this thruster [80]. The coil currents were 2.5 A and 0.5 A, respectively. The magnetic field profiles, produced in this thruster, with this set of coil currents, are described in Ref. [81]. An example of the magnetic field lines and field distribution in the thruster is given in Fig. 3.5.

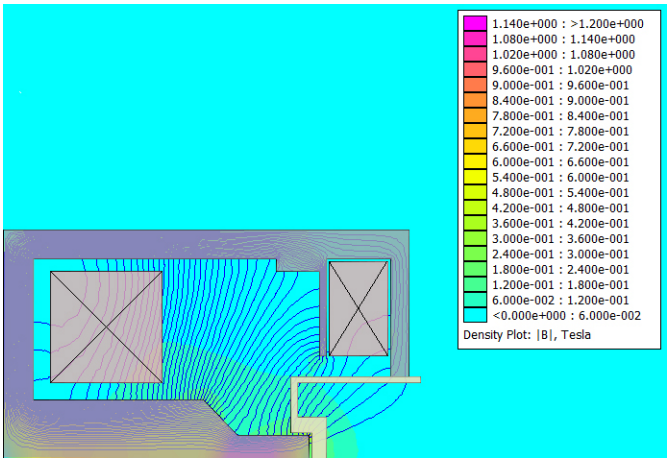

Figure 3.5: Magnetic field distribution in the CHT with the main (back) coil current set at 2.5 A and the front coil current at 0.5A.

Throughout the present experiments, the DC discharge voltage was 220 V, while the root mean square (RMS) value of the discharge current, without applied modulations of the anode potential, was at about 0.8 A.

In previous studies of this thruster, both spoke and breathing modes were observed. In the experiments, described in this thesis, the thruster operated in a regime with a strong intrinsic breathing mode. This breathing mode was externally amplified by modulation of the anode potential. This was done to study the effect of breathing oscillations on the laser-induced fluorescence diagnostic, investigate the effect of the external modulations on thruster efficiency, and examine the coupling between the spoke and breathing modes.

3.2 Laser-Induced Fluorescence diagnostic

Laser-induced fluorescence measurements are very important for characterization of plasma flow, and can provide valuable insights into kinetic processes in plasma. This technique

is applied widely in studies of plasma and fluid dynamic. A time-resolved version of this diagnostic provides the ability to track the evolution of VDF in time. This information enables us to determine the evolution of electric field structures, and to evaluate the thruster performance. In general, this diagnostic can be defined as follows. Laser-induced fluorescence (LIF) is an optical measurement technique that allows for measurements of the velocity distribution functions (VDF) of atoms and ions along the laser beam direction by detecting the Doppler shift. This section is focused on a description of basic principles of LIF diagnostic and its realization for plasma measurements in CHT.

In general, the LIF process consists of two steps. First, particles (atoms or ions) are excited by the absorption of photons to a higher energy state. Before the excitation, those particles are at some energy state (this can be a metastable or ground state), called a probed state. A probed state is chosen to be well populated, which is determined by plasma parameters (mainly temperature and density). Excitation from the particular state requires the light source to be operating at a specific frequency, called the resonance frequency (or wavelength). The transition between two energy states is called the LIF scheme. In the second step, due to spontaneous emission, collisions, or stimulated emission, the excited ions or atoms emit photons and transition to some lower state occurs. Depending on the final energy state, there are two types of emission. When particles return to the same energy state as before the excitation, it is called a resonant emission. If particles decay to a different energy level, such emission is called nonresonant. For most LIF diagnostics transitions non-resonant emission is used, so the emitted wavelength can be easily separated from the strong laser light. The strength of the emitted light is proportional to the particle density and the laser intensity. The emitted light is then collected by the collection optics and analyzed by various methods. However, plasma emits light in a broad range of wavelengths, creating strong background light and the LIF signal is hidden by the background emission. Typically, the collected light is filtered by a monochromator or a band-pass filter; however, even a filtered signal is still dominated by the background, and signal recovery methods are required. In this work, the lock-in amplifier was used. It allows even periodic signals with very small amplitudes to be extracted from the noisy background. In order to use the lock-in, the laser light is chopped at some frequency so the LIF signal becomes periodic. Thus, the collected light has two

components: one from the periodic LIF signal, and another from the spontaneous plasma emission. A description of lock-in amplifier basics will be given in Section 3.3.1.

In the present work, xenon ions (Xe II) at the metastable level $5d^2[4]_{7/2}$ were probed. It was assumed that their dynamics is the same as the dynamics of the whole ion population. These ions were excited by the laser to $6p^2[3]^{5/2}$ (centered at 834.724 nm; air) level. The de-excitation state is $6s^2[2]_{3/2}$, leading to a fluorescence signal at 541.915 nm. The partial energy-level diagram is shown in Figure 3.6.

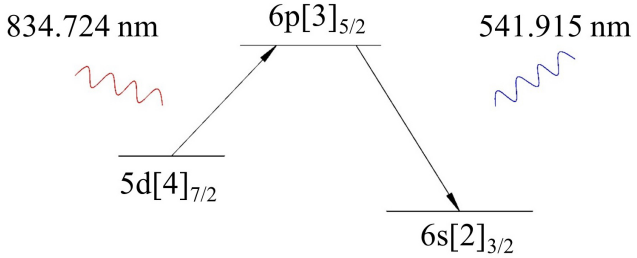

Figure 3.6: LIF scheme used for Xe II study.

A detailed description of the probed transition, line broadening mechanisms, a a time-averaged version of the LIF setup, and discussion about results of time-averaged measurements, can be found in Ref. [2].

3.2.1 Broadening mechanisms

Even though energy states are related to an average energy, their spectra typically consist of several lines located close to each other. There are a number of physical mechanisms which are responsible for the broadening of the lineshape. In general, the resulting shape is subject to broadening mechanisms related to the hyperfine structure of the line, isotopic splitting, Zeeman splitting, and lifetime broadening. Therefore, the measured LIF profile $f_{LIF}(\omega_L)$ is a convolution of the Doppler line shape, effects of broadening mechanisms, and the laser intensity

$$f_{LIF}(\omega_L) \propto f(\omega_L) \otimes \phi_L(\omega_L) \otimes \phi_b(\omega_L), \tag{3.2}$$

where $f(\omega_L)$ is the amplitude of the Doppler lineshape, $\phi_L(\omega_L)$ is the laser intensity profile (which is typically negligible), and $\phi_b(\omega_L)$ is the Doppler free lineshape, which includes all broadening mechanisms. This is illustrated in Fig. 3.7, where convolution process is marked as $\otimes$ symbol

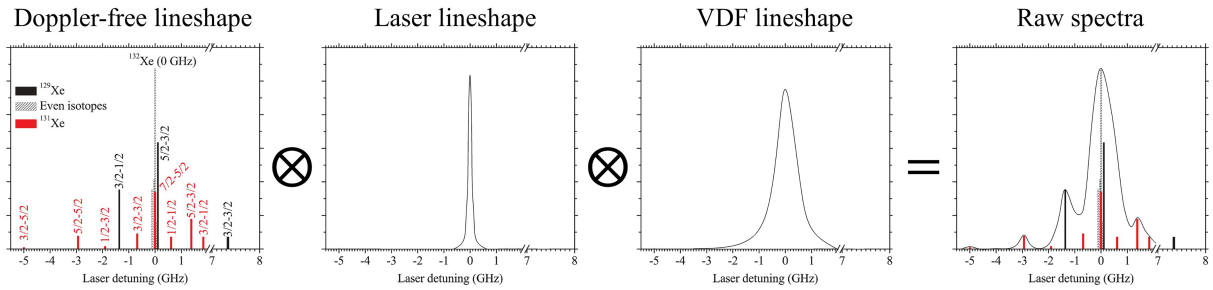

Figure 3.7: Graphical example of convolution for a xenon atom transition. Schematic of hyperfine structures is taken from [2].

The convolution is defined mathematically as

$$C(x) = \int_{-\infty}^{\infty} f(t-\tau)g(\tau)d\tau, \tag{3.3}$$

where f and g are convoluted functions. Thus, the VDF can be recovered from the LIF profile by the deconvolution process. Let's consider broadening mechanisms more in detail.

3.2.2 Doppler broadening

The first broadening mechanism is called Doppler broadening. It is related to the fact that probed species have both thermal and direct velocities. If a particle is at rest, and then is excited by the laser, the spectrum of the emitted light will contain only one line, related to the de-excitation transition. However, if the particle moves, the wavelength of the emitted light will be shifted due to the Doppler effect. Moreover, the excitation wavelength will depend on the particle velocity as well.

The general idea behind the measurements of VDF is based on measurements of the transition resonant frequency shift due to the motion of particles. Let's consider the laser with a frequency ω_L and a wavevector $\mathbf{k}$ (all in the laboratory frame). For the particle traveling with some non-relativistic velocity $\mathbf{v}$, the shift in the laser frequency $\Delta\omega$ in the particle frame is

$$\frac{\Delta\omega}{\omega_L} = -\frac{\mathbf{v}\cdot\mathbf{k}}{c}, \tag{3.4}$$

where c is the speed of light. One can find a relation for the required laser frequency ω_{Trans}, at which the transition occurs, as a function of the particle velocity $\mathbf{v}$

$$\omega_{Trans} = \omega_L + \Delta\omega = \omega_L\left(1 - \frac{v_k}{c}\right), \tag{3.5}$$

where v_k is the projection of the particle velocity $\mathbf{v}$ on the laser wavevector $\mathbf{k}$. Therefore, there

is a one-to-one relation between the laser frequency and particle velocities, which participate in a fluorescence event.

Therefore, the LIF diagnostic is based on the scanning of laser frequencies near the selected transition, and measuring the fluorescence response. Each laser frequency corresponds to a population of particles with a particular velocity. The velocity distribution can be represented as a function of the laser frequency

$$f(v_k) \sim F\left(\frac{\omega_{Trans}}{1-\frac{v_k}{c}}\right). \tag{3.6}$$

It is important to mention that the VDF, represented by the Eq. 3.6 is measured only along the laser beam direction, and provides information only about one-dimensional velocity distribution function. It is possible to measure VDFs by the set of orthogonal lasers in 3D; however, there will be no information about how these velocity components are correlated to each other. Nonetheless, in the case of electric propulsion it is less important, as there is a strong flow of ions in one direction.

3.2.3 Hyperfine structure and isotope splitting broadening

Broadening due to the hyperfine structure of energy levels and isotope splitting is another mechanism which leads to a significant disturbance of the LIF lineshape. The structure of the hyperfine energy levels is defined by the total angular momentum **F**, which is a result of a coupling between the total electron angular moment **J** and the orbital angular momentum **I**, $\mathbf{F} = \mathbf{J} + \mathbf{I}$. Xenon atoms have 9 isotopes, for 7 of which the orbital momentum is zero, because they have an even number of neutrons. Therefore, only two isotopes contribute to the hyperfine structures. The shift in energy levels due to the hyperfine structure can be found in the following equations [82]

$$E_{HFS} = A\frac{C}{2} + BD, \tag{3.7a}$$

$$C = F(F+1) - I(I+1) - J(J+1), \tag{3.7b}$$

$$D = \frac{(3C/4)(C+1) - I(I+1)J(J+1)}{2I(2I-1)J(2J-1)}. \tag{3.7c}$$

Here A is the magnetic dipole moment constant, B is the electric quadrapole moment constant, C and D are functions of quantum numbers of the states, I is the total orbital angular quantum number, J is the total electron angular momentum quantum number, and F is the

total angular momentum quantum number. The F number can take values in the range

$$|I - J| \leq F \leq |I + J|. \tag{3.8}$$

For Xe II transition, which was used in this work, there are nineteen split components. There is no data about isotope shifts, only about the nuclear splitting constants of the upper state. However, previous work with this transition [83] shows that the deconvolution is not necessary for proper extraction of the ion VDF. Moreover, the most probable velocities can be easily recovered from the location of the LIF signal peak, which is not affected by this broadening mechanism. Nonetheless, when a precises shape of VDF is important, this effect should be taken into account.

3.2.4 Lifetime broadening

This broadening mechanism can be understood from the Heisenberg uncertainty principle. Similar to position and momentum, which cannot be observed with arbitrary accuracy, energy and time cannot be known with absolute certainty. This can be written as

$$\Delta E \Delta t \geq \hbar. \tag{3.9}$$

The uncertainty in the photon energy $\Delta\omega$ depends on the lifetime of the upper energy level τ_p. The lineshape is then modified into the Lorentzian function [84]

$$\phi(\omega) = \frac{\Delta\omega}{(\omega - \omega_0)^2 + (\Delta\omega/2)^2}, \tag{3.10}$$

$$\Delta\omega = \frac{1}{2\pi\tau_p}. \tag{3.11}$$

For the Xe II metastable level $5d^2[4]_{7/2}$ the lifetime is about 7-9 ns, and the resulting broadening is one or two orders of magnitude smaller than the effect of the Doppler broadening; therefore, it can be neglected.

3.2.5 Effects of electric and magnetic fields

Two other mechanisms, which are responsible for the spectral line splitting are the Stark and Zeeman effects. The Stark effect is the effect of splitting due to strong electric fields. If the field is strong enough, it can cause additional angular momentum between the nucleus and the electron cloud. However, the electric field in Hall thrusters is not high enough to cause this to happen, and resulting VDF is not affected. Usually, the Stark effect is ignored in all

studies (to the author's knowledge).

The Zeeman effect, which causes line splitting due to the effect of the magnetic field, is more pronounced and can significantly affect the LIF shape. Simulations of the Zeeman effect for values of the magnetic field, which can be found in Hall thrusters, are shown in Fig. 3.8.

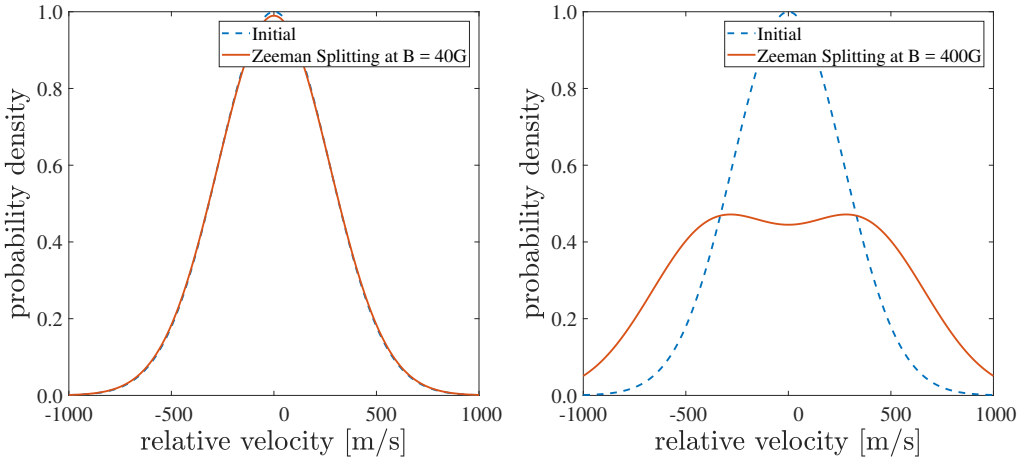

Figure 3.8: Effect of Zeeman splitting on the VDF shape at 40 G (left) and at 400 G (right). There is an evident splitting in the case of high magnetic field (400 G).

From these figures one can see that the Zeeman effect indeed plays an important role when measurements are done at regions with high magnetic field. However, in this work the collection point was located outside of the thruster channel, where field strength was small (less than 10 Gauss), see Fig. 3.5. Therefore, an impact of this splitting mechanism on the shape of a measured VDF was neglected.

3.2.6 Saturation broadening

The effect of saturation occurs when the input laser intensity is high enough and the emission intensity becomes independent of it. This effect causes the spectral line to be broader. In order to avoid this, effect the laser power calibration was done. Results are shown in Fig. 3.9.

From this figure one can see that the intensity response was linear in the whole range of laser powers; thus, measurements were done in an unsaturated regime.

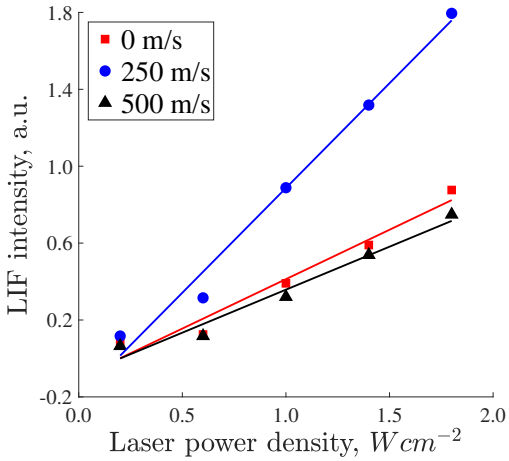

Figure 3.9: LIF intensity as a function of the laser power for three groups of ions with different velocities.

3.3 Optical and measurement setup

A schematic of the optical setup for measurements of IVDFs is shown in Fig. 3.10. The TLB-6917 Vortex^{TM} II laser head produces pump laser beam A with a wavelength of 834 nm and a cross section of about 2 mm. The output power is $\sim$ 60 mW. The beam wavelength can be adjusted, within a range of hundredths of nm, using LabVIEW-based software. The beam splitter (BS1) reflected a part of the laser beam into the Bristol WM621 wavemeter/power meter. The wavemeter continuously measured the wavelength during the experiment. The beam power was monitored during all experiments, and it was very stable. The beam then entered an Acousto-Optic Modulator (AOM), where it was modulated. Modulation pulses were driven by the same function generator, which was used for anode potential driving, but from a different channel. This allowed for control of the phase shift between these two signals. The frequency of the laser modulation was different, because it was necessary to distinguish between the laser-induced fluorescence signal and the bulk plasma emission, which intensity oscillates at the frequency of the modulated breathing mode. AOM provided two beams: a 0th and a 1st order. Only the 1st order beam is modulated, and the 0th order beam was blocked by the iris. The second beam splitter (BS2) reflected a part of the beam into a fast photodiode (PD). The signal from the PD is sent into the lock-in amplifier SRS830 DSP. Then, the beam is sent through the collimating lenses (L1 & L2), and reflected by two mirrors (M1 & M2) before being sent into the chamber though the viewport. Since the viewport was

below the thruster axis, the beam had to be redirected inside the chamber. This was done via turning prisms (M3 & M4), such that the beam coincided with the thruster axis.

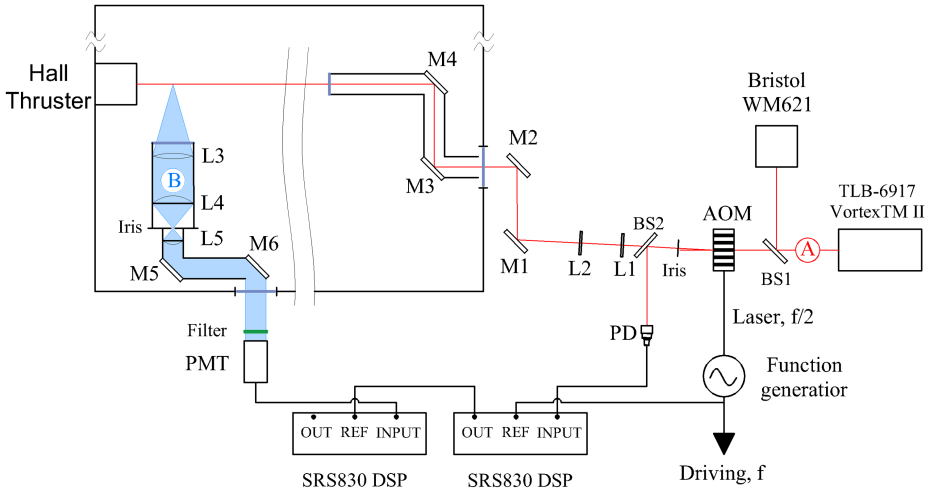

Figure 3.10: Optical setup for the LIF experiment. M1-6 – mirrors; BS1,2 – beam splitters; PD – photodiode; PMT – photomultiplier tube; AOM – acousto-optic modulator; L1,2 – collimating lenses; L3-5 – collection lenses; A – pump laser beam; B – LIF signal beam; f – anode potential driving frequency.

On the collection branch of the system, lens L3 collected light from the point on the thruster axis. This point was located 12 mm away from the thruster exit plane. At the collection point the laser beam had the power of approximately 8 mW, which yielded a good signal-to-noise ratio and no saturation of the transition. A combination of plano-convex lenses (L3, L4), and iris sent the collected light into a collimation lens L5. Light was then passed into a photomultiplier tube (PMT) by two mirrors (M5 & M6). The desired wavelength was extracted from the collected light by a 540 nm filter with a 10 nm bandwidth. An exact description of the anode modulation and laser modulation is given in section 5.4.

3.3.1 Lock-in Amplifier basics

Lock-in amplifiers are used to extract very small periodic signals from noisy backgrounds. To make this possible, lock-in requires a reference signal. It can be obtained from an external or internal source. For experiments in this thesis, the laser modulation frequency was used as a reference. The reference signal was obtained as follows. The signal from the photodiode was fed into the first lock-in amplifier, which generated a reference sine wave with the frequency

and phase shift equal to the laser modulation signal. Then this signal was fed to the second lock-in amplifier, where it was compared to the signal from the PMT, and the LIF signal was extracted.

The principle of operation of a lock-in amplifier is that the sinusoidal functions are orthogonal. If a sinusoidal function with frequency ω_1 is multiplied to another sinusoidal function ω_2, different from ω_1, and then the product is averaged over many periods, the result will be zero. However, if ω_1 and ω_2 are equal, the resulting average is equal to one-half of the product of their amplitudes. Therefore, the lock-in amplifier takes the input signal and multiplies it to the reference signal. After this, the obtained product is averaged over time, and all components, which are not at the reference signal frequency, or not close in phase, are attenuated to zero. In general, the output of lock-in is:

$$V_{out} = 1/2 V_{sig} V_{ref} \cos(\theta_{sig} - \theta_{ref}), \tag{3.12}$$

where V_{sig} and V_{ref} are amplitudes of the input and the reference signals. θ_{sig} and θ_{ref} are phases of the input and the reference signals. To get rid of phase dependency, signal is multiplied by the reference signal, which is shifted by 90^o, and its output will be

$$V_{out} = 1/2 V_{sig} V_{ref} \sin(\theta_{sig} - \theta_{ref}). \tag{3.13}$$

Now there are two signals, which are called in-phase and quadrature signals, respectively:

$$X = V_{sig} \cos\theta, \tag{3.14}$$

$$Y = V_{sig} \sin\theta. \tag{3.15}$$

Lock-in tries to keep the difference between phases as close to zero as possible, so θ is zero. In this case X represents the signal, and Y is zero. Signal magnitude is

$$R = \sqrt{X^2 + Y^2}. \tag{3.16}$$

Phase difference is

$$\theta = \tan^{-1} \frac{Y}{X}. \tag{3.17}$$

This method allows for an extraction of a periodic signal from very noisy initial signal. Lock-in amplifiers were used for both, time-averaged and time-resolved measurements.

3.3.2 Data acquisition system and software

The data acquisition (DAQ) system consist of a National Instruments NI-6255 board and a BNC-2090A connector block. This board was used to collect signals from photodiode, lock-in amplifiers, Langmuir and planar probes, the discharge current, and function generator signals. It was used to control laser frequency as well. In order to collect data and control the experiment, LabVIEW based software was developed. It is based on the state machine structure, and provided the control over experiment parameters. The front panel of the software is presented on Fig. 3.11.

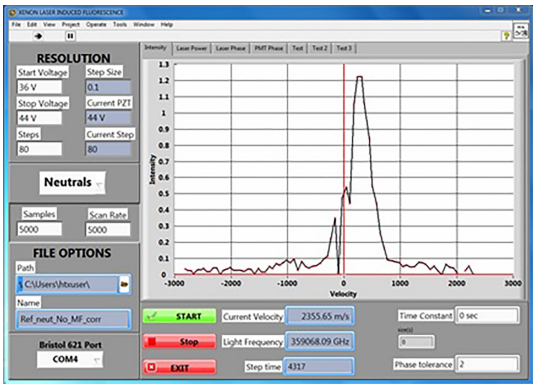

Figure 3.11: Software main window.

3.4 Probe diagnostic basics

Emissive probes have been used for measurements of the plasma potential ϕ_{pl} and the electron temperature T_e in a wide variety of plasma devices. The floating point technique was used in order to deduce plasma potential in this work. Direct measurements of plasma potential, in cases for plasma flows and for the changing in time potential, can be obtained by this method. Biased planar probe was used to measure ion density n_i. This was done by measurements of the ion saturation current from the probe.

The main goal of probe measurements was to investigate the variations of plasma parameters during the natural breathing mode and when it was amplified with the external modulations. This helped to identify the reason of IVDFs collapse, which was observed in some experiments. A more detailed description will be given in Chapter 5.

In this section, methods to derive the desired plasma parameters from the probe mea-

surements are given.

3.4.1 Emissive probe diagnostic

If a non-emitting floating probe is immersed in plasma, there is a flux of ions and flux electrons on its surface. These two fluxes result in the sheath formation at the probe surface. As a result, the probe potential adjusts itself in such a way, that there is no net current. This is called floating potential V_F. If the probe is at some potential V with respect to the plasma, electron or ion currents will be induced by the probe. The value of these currents depends on the value of the probe potential and on the ratio a/λ_D, where a is the probe radius.

The basic physical picture of the emissive probe is shown in Fig. 3.12. In the case of a cold (floating) probe, the sheath is formed at the probe surface due to electron flux Γ_e. The electric potential at the probe surface causes the ion flux Γ_i. The profile of the electric potential is shown as a blue line in Fig. 3.12. In the case of the emitting probe surface, there is an extra electron flux Γ_{em} from the surface, which modifies the potential distribution in the sheath region (red line).

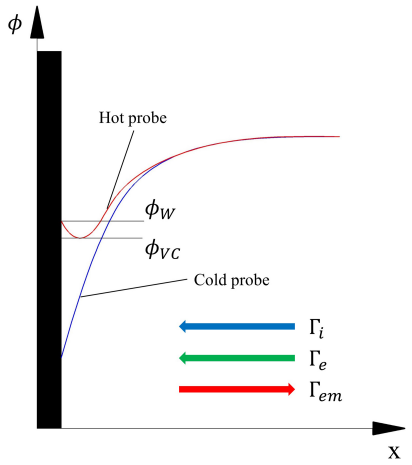

Figure 3.12: Emissive probe physics (fluid description from Ref. [3]): ϕ_{VC} is the virtual cathode potential, ϕ_W is the wall potential, Γ_i is the ion flux to the probe surface, Γ_e is the electron flux to the probe surface, Γ_{em} is the electron flux from the probe surface. Blue line represents the potential distribution in the case of a cold probe. Red line is the potential distribution for a hot probe.

When the probe radius is much larger than the Debye length $a \gg \lambda_D$, ions should be

accelerated to the Bohm velocity before they can enter the sheath [12, 85]. This is called a thin (planar) sheath limit. For xenon plasma, the floating potential of the cold probe is related to the plasma potential as [86]

$$\phi_f^{cold} = \phi_{pl} - 5.77T_e. \tag{3.18}$$

In the opposite case of the thick sheath ($\lambda_D \gg a$) the floating potential can be found as

$$\phi_f^{cold} = \phi_{pl} - 5.24T_e. \tag{3.19}$$

Therefore, these two formulas give the lowest and the highest limits for the value of the floating potential for various ratios between λ_D and a. It is important to note that these approximations work only for plasmas where the electron temperature has a Maxwell distribution. This is not always the case in Hall thrusters, however, there is no simple formula for such situations.

If the probe is heated, the electron emission from the surface appears, and the potential difference between the probe and the plasma reduces. Due to the effect of the space charge, there is a saturation of the sheath around the hot probe. Therefore, the floating potential of the hot probe ϕ_f^{em} is lower than the plasma potential ϕ_{pl} by a value around the electron temperature T_e [3, 87]

$$\phi_f^{em} = \phi_{pl} - 1.5T_e. \tag{3.20}$$

By using Eqs 3.20 and 3.18, the electron temperature in the case of the thin sheath can be deduced as

$$T_e^{exp} = \frac{\phi_f^{em} - \phi_f^{cold}}{4.27}. \tag{3.21}$$

This is the value of the electron temperature, which can be obtained in the experiments. However, the real value of the electron temperature should be determined from the appropriate formula. Therefore, the maximum possible uncertainty in the temperature measurements should be determined. Let's use formula 3.19 for the cold probe and represent the hot emissive probe potential as

$$\phi_f^{em} = \phi_{pl} - \alpha T_e, \tag{3.22}$$

where α is the positive coefficient (because the floating potential of the emissive probe is less than the plasma potential), which can change its value from zero to 1.5 (see Eq. 3.20). Thus,

the following estimation can be obtained

$$T_e = \frac{4.27 T_e^{exp}}{5.24 - \alpha}. \tag{3.23}$$

This gives a rough estimation of uncertainty for the electron temperature as

$$\Delta T_e = 0.17 T_e^{exp}. \tag{3.24}$$

By using these results, the plasma potential and the electron temperature were determined in various thruster operation regimes, an evolution of these characteristics in time was obtained as well.

The experimental procedure for the emissive probe diagnostic can be described as follows. The emissive probe was heated by a DC power supply with the power of about 20 W. The heating current and voltage were controlled with the multimeter. Measurements of the probe floating potential with and without heating were conducted relative to the ground with the DAQ system described above. The DAQ software was modified accordingly.

The probe was located approximately 12 mm from the thruster exit, and 10 mm from the channel axis. Measurements were conducted in a steady-state thruster operation regime, as well as with the applied anode modulation (a more detailed description of thruster operation regimes will be given in Section 7). After the thruster started, the cold probe floating potential ϕ_f^c was measured. Then, the heating of the probe began. Heating was done in steps, until the saturation of the floating potential was reached. If measurements were done with applied modulations of the anode potential, the saturation was reached first and then the modulations were applied.

3.4.2 Planar probe diagnostic

Measurements of the ion density are based on measurements of the ion saturation current with the planar probe. The probe saturation current can be estimated as

$$I_i(V) = \frac{2 e N_i A_p}{\pi} \sqrt{\frac{e T_e}{2 M_i}}, \tag{3.25}$$

where T_e is the electron temperature, A_p is the probe area, M_i is the ion mass. In the experiments, the probe was biased to -40 V. Therefore, by measurements of the probe current one can estimate the ion density. It is important to note that this diagnostic is a subject of large uncertainties.

3.5 Summary

A description of the experimental facility was given in this chapter. The SHTF allows for conducting experiments with the 200 W cylindrical Hall thruster and control of its operation regimes by applying external modulations to the anode potential. An electric schematic of the control circuit is given. Plasma parameters were measured with optical (LIF) and probe diagnostics.

A time-resolved laser induced fluorescence diagnostic was implemented for measurements of the IVDF in the thruster plume during the natural and induced breathing oscillations. Principles of LIF were described; the optical setup and measurement scheme were presented. LIF signal was extracted by means of the lock-in amplifier. The general idea behind the operation of this device is given.

Plasma parameters, such as plasma potential, electron temperature, and the ion density, were measured by means of emissive probes and the biased planar probes. A description of the probe measurement procedures were given.

The above diagnostics were used in experiments related to studies of the time-resolved LIF. As it will be shown in Chapter 5, the collapse of the VDF was observed at high amplitudes of external modulations. A probe diagnostic helped to reveal the oscillations of the electron temperature, which led to a depopulation of the probed transition. Therefore, the density of probed ions was not enough for LIF detection.

Probe diagnostics were used in experiments with external modulations of the breathing mode. The phase reduction between the plasma density and the electric field was shown, which led to increased thruster efficiency. Similar behavior was observed in simulations, described in Chapter 7.

Chapter 4

Waves and instabilities in partially magnetized Hall plasma discharges

4.1 Preface

In this chapter, an introduction to the main types of eigenmodes in partially magnetized plasmas is given. Various instabilities mechanisms are discussed, and the main features of gradient-drift and lower-hybrid instabilities are described. In the second part of this chapter, a detailed analysis of nonlocal effects on gradient-drift instabilities is presented. We consider the nonlocal model for Simon-Hoh and lower-hybrid instabilities, which takes into account electron inertia as well as the global effects of plasma parameters profiles, such as the electric, magnetic fields and plasma density. Contrary to local models, nonlocal analysis predicts multiple unstable modes, which exist in the regions, where local instability criteria is not satisfied. This is especially pronounced for the long wavelength modes which provide a larger contribution to anomalous transport. The second part of this chapter is based on a paper, published in Physics of Plasmas [28].

4.2 Eigenmodes and instabilities of partially magnetized plasmas

As was mentioned in Chapter 2, there are several types of waves that exist in magnetized plasmas. In this section, a more detailed description of relevant plasma eigenmodes is given. Several assumptions were made for a description of Hall plasmas. First, ions are considered to be cold, unmagnetized and collisionless. Nonetheless, several types of waves, for which collisions and ion magnetization are important, are presented. The electric field is an elec-

trostatic field and the electron temperature is constant. In such conditions, the following continuity and momentum equations for ions an electrons can be written

$$\frac{\partial n_i}{\partial t} + \nabla \cdot (n_i \mathbf{v_i}) = 0, \tag{4.1a}$$

$$m_i n_i \frac{\partial \mathbf{v_i}}{\partial t} + m_i n_i (\mathbf{v_i} \cdot \nabla)\mathbf{v_i} = e n_i E, \tag{4.1b}$$

$$\frac{\partial n_e}{\partial t} + \nabla \cdot (n_e \mathbf{v_e}) = 0, \tag{4.1c}$$

$$m_e n_e \frac{\partial \mathbf{v_e}}{\partial t} + m_e n_e \mathbf{v_e} \cdot \nabla \mathbf{v_e} = -e n_e (\mathbf{E} + \mathbf{v_e} \times \mathbf{B}) - \nabla p_e, \tag{4.1d}$$

where n_i, n_e are ion and electron densities, $\mathbf{v}_i$, $\mathbf{v_e}$ are ion and electron velocities, $p_e = k_B n_e T_e$ is the electron pressure term, $\mathbf{E} = -\nabla\phi$ is the electric field, and $\mathbf{B}$ is the magnetic field. The electric potential ϕ can be found from the Poisson equation

$$\nabla^2 \phi = \frac{e}{\epsilon_0}(n_e - n_i). \tag{4.2}$$

All plasma parameters (density n, velocity v, potential ϕ, etc.) can be expanded around the equilibrium in a form

$$x = x^0 + \tilde{x}, \tag{4.3}$$

where x^0 is the equilibrium value, and $\tilde{x}$ is the perturbed value. When all terms in Eq. 4.1 are replaced with expansion and a linear approximation ($x_0 \gg \tilde{x}$) is used, the following system of equations is obtained

$$\frac{\partial \tilde{n}_i}{\partial t} + n_i^0 \nabla \cdot \tilde{\mathbf{v}}_i + \tilde{\mathbf{v}}_i \cdot \nabla n_i^0 = 0, \tag{4.4a}$$

$$\frac{\partial \tilde{\mathbf{v}}_i}{\partial t} + \mathbf{v}_i^0 \cdot \nabla \tilde{\mathbf{v}}_i = -\frac{e}{m_i} \nabla \tilde{\phi}, \tag{4.4b}$$

$$\frac{\partial \tilde{n}_e}{\partial t} + n_e^0 \nabla \cdot \tilde{\mathbf{v}}_e + \tilde{\mathbf{v}}_e \cdot \nabla n_e^0 = 0, \tag{4.4c}$$

$$\frac{\partial \tilde{v}_e}{\partial t} + \mathbf{v}_e^0 \cdot \nabla \tilde{\mathbf{v}}_e = \frac{e}{m_e} \nabla \tilde{\phi} - \frac{e}{m_e} \tilde{\mathbf{v}}_e \times \mathbf{B} - k_B T_e \frac{\nabla \tilde{p}_e}{m_e n_e^0}. \tag{4.4d}$$

Here, it is assumed that the equilibrium electric field E^0, ion v_i^0 and electron velocities v_e^0 are equal to zero.

The system of linear equations (4.4) can be solved with the Fourier method. The perturbed quantities can be represented in form

$$\tilde{x} \sim e^{i(\mathbf{k}\cdot\mathbf{x} - \omega t)}. \tag{4.5}$$

Thus, the time derivative of the perturbed quantity is

$$\frac{\partial \tilde{x}}{\partial t} = -i\omega \tilde{x} e^{i(\mathbf{k}\cdot\mathbf{x} - \omega t)} \tag{4.6}$$

and the space derivative is

$$\nabla \tilde{x} = i\mathbf{k}\tilde{x}e^{i(\mathbf{k}\cdot\mathbf{x}-\omega t)}. \tag{4.7}$$

The full system of equations 4.4 describes several relevant eigenmodes in particular for Hall plasmas. It is instructive to consider these modes separately to simplify the exposition.

4.2.1 Plasma waves

Let's consider a plasma where ions are cold and do not move forming positively charged background, while electrons can freely oscillate around an equilibrium position. Such plasma can be described with continuity and momentum equations for electrons. In the linearized form they are

$$-i\omega\tilde{n}_e + ikn_e^0\tilde{v}_e = 0, \tag{4.8a}$$

$$-i\omega m_e n_e^0\tilde{v}_e = -iken_e^0\tilde{\phi}. \tag{4.8b}$$

The electrostatic potential satisfies the Poisson equation, which in linearized form is

$$-k^2\tilde{\phi} = \frac{e}{\epsilon_0}\tilde{n}_e, \tag{4.9}$$

here $\tilde{n}_i = 0$, as ions do not move. Solutions of the equations (4.8 - 4.9) yields

$$\omega^2 = \omega_{pe}^2 = \frac{e^2 n_0}{\epsilon_0 m_e}, \tag{4.10}$$

which is known as electron plasma frequency. This is typically the highest frequency in plasmas, and the ion motion can be neglected at such timescales.

4.2.2 Ion sound waves

Ion acoustic waves are similar to compressible sound in neutral gases. In plasmas, the restoring force on ions is provided by the electric field and inertia is due to finite ion mass. Electrons maintain quasi-neutrality by regulating the local electric field. In fully magnetized plasma ($\rho_{e,i} \ll L$, Larmor radius is less than a system length), ion sound waves propagate only in the direction of the magnetic field. In partially magnetized plasmas, where ions are not magnetized, ion sound waves can propagate in an arbitrary direction as long as there is a finite component of the wavevector along the magnetic field, i.e. the standard ion sound waves do not exist for strictly perpendicular propagation.

Let's consider unmagnetized ions with a finite temperature. The linearized equation of

motion is

$$-i\omega m_i n_i^0 \tilde{v}_i = -iken_i^0\tilde{\phi} - ikk_B T_i \tilde{n}_i. \tag{4.11}$$

Continuity equation for ions has a form

$$i\omega\tilde{n}_i = ikn_i^0\tilde{v}_i. \tag{4.12}$$

The momentum equation with included pressure term for unmagnetized electrons is

$$0 = -iken_e^0\tilde{\phi} - ikk_B T_e \tilde{n}_e. \tag{4.13}$$

In this equation the electron inertia is neglected (left-hand side is zero), as the electron mass is much smaller compared to the ion mass. It is assumed that they respond instantaneously, resulting in the Boltzmann response

$$\frac{\tilde{n}_e}{n_e^0} = \frac{e\tilde{\phi}}{k_B T_e}. \tag{4.14}$$

Now, by imposing the quasi-neutrality $n_i = n_e$ and using Eqs 4.11 - 4.13, the following dispersion relation can be obtained

$$\omega^2 = k^2\Big(\frac{k_B T_i + k_B T_e}{m_i}\Big). \tag{4.15}$$

It is important to note that the wave is damped if the ion temperature is comparable to the electron temperature. For this Eq. 4.15 to be valid, the electron temperature T_e should be much larger than the ion temperature T_i, so that $c_s \gg v_{Ti}$ (ion thermal velocity), which ensures the absence of the ion Landau damping. This condition is always satisfied for Hall thrusters. Therefore, the dispersion relation can be written as

$$\omega^2 = k^2 c_s^2, \tag{4.16}$$

where $c_s^2 = k_B T_e/m_i$ is the ion sound velocity.

The result can be generalized if one considers deviating from quasi-neutrality. The linearized Poisson's equation is

$$k^2\tilde{\phi} = \frac{e}{\epsilon_0}(\tilde{n}_i - \tilde{n}_e). \tag{4.17}$$

The ion density can be found from Eq. 4.12, while electron density is determined by (4.14). By substituting densities from these equations into Eq. 4.17, using quasi-neutrality $n_e^0 = n_i^0 = n^0$, and Eqs 4.11, 4.12 one has the following result

$$\omega^2 = \frac{k^2 c_s^2}{1 + k^2\lambda_D^2}. \tag{4.18}$$

This equation is the same as Eq. 4.16, except for the $1 + k^2\lambda_D^2$ term. The long wavelength ion sound wave is the limit of $k^2\lambda_D^2 \ll 1$. In the short wavelength limit $k^2\lambda_D^2 \gg 1$, the ion

plasma frequency is obtained.

4.2.3 Hybrid modes

For the waves considered above, the magnetic field **B** was assumed to be zero. In this section, modes, which are caused by the effect of the magnetic field on electron and ion motion, will be considered.

First, we consider the effect of the magnetic field on ion sound waves in plasma. It is done in the limit $\omega < k_z v_{T_e}$ (electron thermal velocity). Because wavevector is chosen to be almost perpendicular to the magnetic field line the Boltzmann relation (4.14) can be used for electrons. The linearized continuity and momentum equations for ions are

$$-i\omega\tilde{n}_i + ikn_i^0\tilde{v}_{ix} = 0, \tag{4.19a}$$

$$-i\omega\tilde{v}_{ix} = ik\frac{e}{m_i}\tilde{\phi} - \frac{e}{m_i}\tilde{v}_{iy}B, \tag{4.19b}$$

$$-i\omega\tilde{v}_{iy} = \frac{e}{m_i}\tilde{v}_{ix}B. \tag{4.19c}$$

The following dispersion relation is derived

$$\omega^2 = \Omega_{ci}^2 + k^2 c_s^2, \tag{4.20}$$

which describes the electrostatic ion cyclotron waves. This wave is different from the ion sound waves due to the effect of the magnetic field.

Now let's consider waves in a direction exactly perpendicular to the applied magnetic field ($\mathbf{k} \perp \mathbf{B}$) and along the electric field ($\mathbf{E} \parallel \mathbf{k}$), including the electron inertia. The Boltzmann approximation does not work, therefore the linearized continuity and momentum equations should be solved

$$-i\omega\tilde{n}_e + ikn_e^0\tilde{v}_{ex} = 0, \tag{4.21a}$$

$$-i\omega\tilde{v}_{ex} = ik\frac{e}{m_e}\tilde{\phi} - \frac{e}{m_e}\tilde{v}_{ey}B, \tag{4.21b}$$

$$-i\omega\tilde{v}_{ey} = \frac{e}{m_e}\tilde{v}_{ex}B. \tag{4.21c}$$

By using the Poisson equation (4.2) and solving Eqs 4.19 with 4.21 the following dispersion relation can be obtained

$$1 - \frac{\omega_{pe}^2}{\omega^2 - \Omega_{ce}^2} - \frac{\omega_{pi}^2}{\omega^2 - \Omega_{ci}^2} = 0. \tag{4.22}$$

If use the limit $\omega_{pi}^2 \ll \omega^2$, then the above equation can be re-written as

$$\omega^2 = \omega_{pe}^2 + \Omega_{ce}^2 = \omega_{uh}^2. \tag{4.23}$$

The frequency ω_{uh} is known as the upper hybrid frequency. This is a frequency of electrons in the electrostatic field across the magnetic field.

In the limit of $\omega^2 \ll \Omega_{ce}^2$ and $\Omega_{ci}^2 \ll \Omega_{ce}^2$ the following dispersion relation can be derived from Eq. 4.22

$$\omega^2 = \frac{\omega_{pi}^2 \Omega_{ce}^2}{\Omega_{ce}^2 + \omega_{pe}^2} = \omega_{LH}^2, \tag{4.24}$$

which is a lower hybrid wave, and it is correct only when the frequencies are below both electron and ion plasma frequencies.

4.2.4 Drift waves in fully magnetized plasmas and gradient-drift mode in partially magnetized plasma

Drift waves are maintained by plasma density gradient and are common in plasmas with magnetized electrons and ions. Let's consider the motion of ions in crossed electric and magnetic fields. Here, we assume that the magnetic field is in z direction, the electric field and gradients are in x direction, and the particles' motion is in y direction. Ions are subject to the $\mathbf{E} \times \mathbf{B}$ drift, with velocity

$$\mathbf{V}_0 = \frac{\mathbf{E} \times \mathbf{B}}{B^2}. \tag{4.25}$$

The perturbed velocity can be re-written as

$$\tilde{\mathbf{V}}_0 = -i \frac{k_y \tilde{\phi}}{B} \hat{x}. \tag{4.26}$$

The continuity equation for ions in linearized form is

$$-i\omega \tilde{n}_i - \tilde{\mathbf{V}}_0 \cdot \nabla n_i^0 = 0, \tag{4.27}$$

which yields the following equation for plasma density perturbations

$$\tilde{n}_i = -\frac{1}{\omega} \frac{k_y \nabla_x n_i^0}{B} \tilde{\phi}. \tag{4.28}$$

The electron density perturbations can be obtained from the Boltzmann relation (4.14); by imposing the quasineutrality and using the definition (2.44), the following dispersion relation is obtained

$$\omega = \omega_*, \tag{4.29}$$

which is the dispersion relation for drift waves in fully magnetized plasmas.

Standard drift waves, which require magnetized ions, do not exist in conditions inherent to Hall plasmas where ions are essentially unmagnetized. Hall plasmas, however, support

the so called "anti-drift" mode. This mode exists when $k_z = 0$, and the dominant electron motion is in a direction perpendicular to the magnetic field so electron velocity $\mathbf{v}_e = \mathbf{V}_0$. Similar to the derivation for ions (drift velocity is the same for both species) and by using Eqs 4.11, 4.12 for the case of cold ions $T_i = 0$ the following equation can be derived

$$\omega = \frac{k_\perp^2 c_s^2}{\omega_*} = -k^2 L_n \Omega_{ci}/k_y, \tag{4.30}$$

where $k_\perp^2 = k_x^2 + k_y^2$ is the wavevector in the direction perpendicular to the magnetic field. This equation represents a dispersion relation for the anti-drift mode [88]. From the latter equation one can see that this mode does not depend on the electron temperature, contrary to the ion-sound mode and the drift wave in the fully magnetized plasma.

4.2.5 Instabilities in partially magnetized plasmas

As will be presented below, partially magnetized plasmas exhibit a number of instabilities. In general, their mechanisms can be referred to as negative energy modes instabilities. Normally, perturbations from the equilibrium are assumed to have a positive energy. Implicitly, this means that the equilibrium is presumed to be a thermodynamic state with the lowest possible energy so that any perturbations would have a larger, therefore positive energy. As a simple example, one can consider the kinetic energy of plasma/fluid perturbed from the state $v_0 = 0$

$$E = \int \rho dx \tilde{v}^2 dt/2 > 0, \tag{4.31}$$

where $\tilde{v}$ is the perturbation velocity.

However, confined plasmas are often in states far from thermodynamic equilibrium, and may include equilibrium flows with $v = v_0$, e.g. diamagnetic fluxes. In systems with equilibrium flows, the perturbations are possible in such a way that their energy is lower than the initial equilibrium energy

$$E = \int \rho dx v^2 dt/2 < E_0 \int \rho dx v_0^2 dt/2, \tag{4.32}$$

where v_0 is the flow velocity and $v = \tilde{v} + v_0$ is the perturbation velocity.

A simple example is a perturbation, which has a lower velocity than the flow velocity v_0. These are the negative energy waves [74, 89], which are common in physics of fluids and plasmas. The amplitude of the negative energy mode increases if energy is removed from the system. This may occur due to dissipation processes in the system (e.g. collisions), or due to coupling between negative and positive energy modes. In the latter case energy is

transferred from the negative energy mode to the positive energy mode. Thus, amplitudes of both modes increase. Most instabilities in partially magnetized plasmas with $\mathbf{E} \times \mathbf{B}$ flows can be classified as dissipative or reactive instabilities of negative energy modes.

Ion sound waves can be destabilized by dissipation mechanisms in systems when $\mathbf{E} \times \mathbf{B}$ flow is present and electron-neutral collisions are included. In this case the electron continuity equation is

$$-i\omega\tilde{n}_e + ik_y V_0 \tilde{n}_e + n_e^0 \nabla_z v_{ez} = 0 \tag{4.33}$$

and the momentum equation is

$$ik_z e n_e^0 \tilde{\phi} - ik_z k_B T_e \tilde{n}_e - m_e n_e^0 \nu_e v_{ez} = 0, \tag{4.34}$$

where ν_e is the electron collision frequency and $\omega_0 = k_y V_0$ is the $\mathbf{E} \times \mathbf{B}$ drift frequency. By using equations 4.12 and 4.11 for the perturbed ion density, one can find the following dispersion relation for the ion-sound instability destabilized by collisions

$$\omega^2 = k^2 c_s^2 - i \frac{c_s^2}{v_{Te}^2} \nu_e (\omega - \omega_0). \tag{4.35}$$

The instability occurs for $\omega < \omega_0$ when $\omega = \omega_r + i\gamma$ and $\gamma > 0$ (here γ is the growth rate). Electron collisions remove energy from the system, and phase shift between the current and potential supports the instability.

Reactive instabilities in partially-magnetized plasmas occur due to gradients of density, electron temperature and magnetic field. These gradients are responsible for gradient drift instabilities. Mentioned above anti-drift mode can be destabilized in the systems with electron $\mathbf{E} \times \mathbf{B}$ drift. The continuity equation for electrons in this case leads to

$$-i\omega\tilde{n}_e + \tilde{V}_0 \nabla n_e^0 + ik_y V_0 \tilde{n}_e = 0. \tag{4.36}$$

Therefore, the equation 4.30 becomes

$$\frac{\omega_*}{\omega - \omega_0} = \frac{k_\perp^2 c_s^2}{\omega^2}, \tag{4.37}$$

which is a dispersion relation for collisionless Simon-Hoh instability [17,18,90]. The condition for this instability is $\omega < \omega_0$ and $\omega_*/\omega_0 > 0$.

The magnetic field gradient modifies the above equation into the following [91]

$$\frac{\omega_* - \omega_D}{\omega - \omega_0 - \omega_D} = \frac{k_\perp^2 c_s^2}{\omega^2}, \tag{4.38}$$

where ω_D is defined in Chapter 2, is the drift due to magnetic field gradient.

Lower hybrid modes become more important in situations when electron inertia plays a

bigger role. They can be destabilized by gradients, shear flows, and collisions. For example, here is a dispersion relation for a case of the low hybrid modes with magnetic gradients and electron inertia [92]

$$k^2\lambda_D^2 - \frac{k^2 c_s^2}{\omega^2} + k^2\rho_e^2 + \frac{\omega_* - \omega_D}{\omega - \omega_0 - \omega_D} = 0. \tag{4.39}$$

More details on instability mechanisms relevant to Hall plasmas can be found in [92, 93]. In the following section, a more advanced treatment for Simoh-Hoh instability will be given. Instead of local approximations, used in this section, the nonlocal model will be used. It includes the effects of plasma parameter profiles.

4.3 Structure of nonlocal gradient-drift instabilities in E× B discharges

This section is based on a publication: I. Romadanov, A. Smolyakov, Y. Raitses, I. Kaganovich, T. Tian, and S. Ryzhkov, Structure of nonlocal gradient-drift instabilities in Hall $\mathbf{E}\times\mathbf{B}$ discharges, *Physics of Plasmas* 23, 122111 (2016), reproduced here verbatim.

4.3.1 Abstract

Gradient-drift (collisionless Simon-Hoh) instability is a robust instability often considered to be important for Hall plasma discharges supported by the electron current due to the $\mathbf{E}\times\mathbf{B}$ drift. Most of the previous studies of this mode were based on the local approximation. Here we consider the nonlocal model which takes into account the electron inertia as well as the effects of the entire profiles of plasma parameters such as the electric, magnetic fields and plasma density. Contrary to local models, nonlocal analysis predicts multiple unstable modes, which exist in the regions, where local instability criteria is not satisfied. This is especially pronounced for the long wavelength modes which provide larger contribution to the anomalous transport.

4.3.2 Introduction

Plasmas with crossed electric $\mathbf{E}$ and magnetic $\mathbf{B}$ fields are often used as ion sources in various applications. For moderate values of the magnetic field, the discharge is maintained by the electron $\mathbf{E}\times\mathbf{B}$ drift, while allowing the extraction, separation and acceleration of un-

magnetized ions. Such regimes, generally referred here as Hall plasmas, are widely employed in material processing (magnetrons [6, 94, 95]) and electric propulsion (Hall thrusters [7, 8]) devices. The electron current across the magnetic field in such systems often exceeds the collisional value by orders of magnitude. Presumably, this anomalously large electron current is a result of plasma instabilities which are present in these devices for a wide range of plasma parameters and operational regimes. Despite long history of Hall plasmas applications, the understanding of the nature and mechanisms of plasma instabilities and plasma turbulence is still lacking.

Among different types of unstable modes, relevant to $\mathbf{E} \times \mathbf{B}$ Hall plasmas, gradient-drift modes have long been considered as a possible source of fluctuations [50, 96, 97]. These modes are closely related to the so called anti-drift mode [88] that exists in Hall plasmas with density gradient

$$\omega = \frac{k_\perp^2 c_s^2}{\omega_*}, \tag{4.40}$$

where $c_s^2 = T_e/m_i$ is the ion-sound velocity and

$$\omega_* = k_y v_* = -\frac{k_y T_e}{eB_0 L_n}$$

is the electron diamagnetic drift frequency due to density gradient; L_n is the characteristic length scale of the density gradient, $L_n^{-1} = \nabla \ln n_0(x)$; $k_\perp^2 = k_y^2 + k_x^2$ is the wave vector perpendicular to the magnetic field, $\mathbf{B}_0 = B_0 \widehat{\mathbf{z}}$. Note that the standard drift waves do not exist in Hall plasmas with unmagnetized ions. The frequency of the anti-drift mode (4.40) in fact does not depend on the electron temperature and the dispersion relation can also be written in the form $\omega = -\omega_{ci} k_\perp^2 L_n / k_y$, where $\omega_{ci} = eB_0/m_i$ is the ion cyclotron frequency. The condition $\omega > k_z v_{Te}$, where k_z is along the magnetic field lines, is required so that the mode is propagating almost perpendicular to the magnetic field. When the latter condition is not satisfied, the mode converts into the ion sound mode, $\omega^2 = k^2 c_s^2$, which may propagate at a finite angle with respect to the magnetic field [98].

When the stationary electron current due to the $\mathbf{E} \times \mathbf{B}$ drift is present, the anti-drift mode becomes unstable due to coupling with the ballistic mode $\omega = k_y V_0$ [17, 18]. Resulting gradient drift instability is described by the dispersion equation

$$-\frac{\omega_{ci} k_\perp^2 L_n}{k_y} = \frac{\omega^2}{\omega - \omega_0}, \tag{4.41}$$

where $\omega_0 = \mathbf{k}\cdot\mathbf{V}_0$ is the azimuthal (closed drift) flow of electrons in crossed $\mathbf{E}\times\mathbf{B}$ fields and $\mathbf{E}_0 = E_0\widehat{\mathbf{x}}$. This is the reactive instability of negative energy perturbations with a phase velocity below the stationary $V_0 = \mathbf{E}\times\mathbf{B}/B^2$ velocity. This mode is referred here as the collisionless Simon-Hoh instability [17, 18, 99]. The condition $\mathbf{E}\cdot\nabla n > 0$ is required for the instability [90].

The gradient-drift instability was identified in early Hall thruster experiments [50, 51] as related to violent large scale structures (spokes). It was shown [96] that properly profiled magnetic field improves the stability of the Hall thruster. The modified condition for the instability was derived in the form $\mathbf{E}\cdot\nabla\left(n/B\right) > 0$.

The gradient drift instability in plasmas with inhomogeneous magnetic field was revisited in Ref. [91,100] where the full compressibility was included resulting in the modified dispersion relation

$$\frac{\omega_* - \omega_D}{\omega - \omega_0 - \omega_D} = \frac{k_\perp^2 c_s^2}{\omega^2}, \tag{4.42}$$

where

$$\omega_D = k_y v_D = -\frac{2k_y T_e}{eB_0 L_n}$$

is the magnetic drift velocity due to the axial gradient of the magnetic field; $L_B^{-1} = \nabla \ln B_0(x)$ is characteristic length of such a gradient. One consequence of this modification was that the magnetic field gradient enters in the combination $\nabla\left(n/B^2\right)$ rather than $\nabla\left(n/B\right)$ in original work [96]. In a finite temperature plasma, there also exists an additional contribution due to magnetic field gradient because of the compressibility of the electron diamagnetic velocity [97] (the term with ω_D in the denominator on the left hand side). It was also shown in Ref. [91] that finite temperature fluctuations are also important in situations with strong magnetic field gradient (complete dispersion relation for this case is given in Ref. [100]).

The collisionless Simon-Hoh instability has been considered among the most important sources of plasma fluctuations, in particular, as a cause of large scale structures or spokes [19–21, 101]. Much of the previous work on gradient-drift instabilities [102–104], see also other works cited in Ref. [102], was done within the local approximation neglecting the effects of the density and electric field profiles. The authors in Ref. [72] have considered nonlocal solution to compare the eigenmode structure and eigenmode frequency with the data from Hall thruster experiments [72]. However, the theoretical model used in Ref. [72]

(following to Refs. [105, 106]) does not apply to the collisionless Simon-Hoh instability in which ions are not magnetized. The global analysis has been employed in Refs. [102, 107] for linear stability studies of Hall thruster for rather general fluid model that included effects of ionization, collisions and heat flow. This model involved several different unstable modes and destabilization mechanisms; therefore, it is somewhat difficult to directly compare results of the local and nonlocal analysis.

The standard collisionless Simon-Hoh instability is considered to be a low frequency mode with the eigenfrequency well below the $\mathbf{E} \times \mathbf{B}$ frequency [100]. However, it was shown recently [92] that depending on the value of the k_x wave vector (along the electric field direction) the mode frequency becomes comparable to the $\mathbf{E} \times \mathbf{B}$ frequency, $\omega_0 = \mathbf{k} \cdot \mathbf{V}_0$, and thus, for the short-wavelengths, may become comparable with the lower hybrid frequency $\omega_{LH} = (\omega_{ce}\omega_{ci})^{1/2}$ which require the account of electron inertia.

The goal of this work is to develop a nonlocal model for the collisionless Simon-Hoh instability and related higher frequency lower-hybrid modes and investigate the role of density and electric field profiles on the eigenmode structure, real part of the frequency, and growth rate in conditions typical for Hall plasma experiments. In case of the general profiles of the electric field and plasma density, the non-local stability problem is reduced to the eigenvalue problem which is solved here by the spectral method with Chebyshev polynomials [108]. The results from the spectral code have been verified by a finite-difference differentiation matrix, and shooting method. Both, spectral and finite-difference methods, show good convergence and precision for low mode numbers. However, higher modes require significant increase in number of polynomials or number of steps for finite difference method to achieve the accurate solution.

For our simulations we used parameters relevant to two Hall plasma devices: Penning discharge and Hall thruster. Typical plasma parameters and profiles for such devices were taken from the experiments at Princeton Plasma Physics Laboratory [22, 23, 109, 110].

Penning discharge is a device with cylindrical geometry, in which applied magnetic field is along the $z-$ axis, and the electric field is in radial direction. Plasma is created by the electron beam injected along the $z-$ axis, from either filament cathode or plasma cathode such as a hollow cathode or RF plasma cathode. Magnetic field is created by Helmholtz

coils. The experiments with the Penning discharges demonstrate range of instabilities and structures (spokes) similar to the Hall thruster [23, 110] and provide easier access for plasma diagnostics. Typical experimental parameters are: electric field $E = -50\ V/m$, magnetic field $B = 50\ G$, $v_0 = 1 \cdot 10^4\ m/s$, $L_n = -0.1... - 0.04\ m$, system length $L = 0.1\ m$, $\omega_{ci} = 3.7 \cdot 10^3\ s^{-1}$, $\omega_{LH} = (\omega_{ce}\omega_{ci})^{1/2} = 1.8 \cdot 10^6\ s^{-1}$. For calculations in Sections 4.4.1, 4.4.2, the parameters of Penning discharge were considered in slab geometry, with the magnetic field along the $z-$ axis, and electric potential and density gradient along the $x-$ axis.

Hall thruster is another device of interest in which the gradient-drift instabilities play an important role. Typical device has coaxial or cylindrical, for the Cylindrical Hall Thruster (CHT) [22, 81], geometry. The discharge in the Hall thruster is created in the channel between the anode, which can be used as a gas distributor, and the cathode-neutralizer. A gas propellant, typically argon or xenon, is supplied to the channel through anode and then is ionized by high energy electrons from the cathode and as well electrons heated in the discharge. Magnetic field is sufficiently strong to make the electron Larmor radius much smaller than the chamber characteristic length thus creating the strong azimuthal $\mathbf{E} \times \mathbf{B}$ current of electrons. Collisions allow the electrons move to the anode in the axial direction, across the magnetic field and in the direction of the stationary electric field. The azimuthal current due to the $\mathbf{E} \times \mathbf{B}$ drift can be tens of times larger than the axial electron current. The axial field accelerates the ions towards the channel exhaust, where they are neutralized by electrons from the cathode neutralizer. The thrust is a reaction force to this electrostatic acceleration, applied to the magnetic circuit. Even though azimuthal current is responsible for the ion thrust, axial current is important as well, because it completes the electric circuit.

The axial electron current in Hall thruster is typically an order of magnitude larger than the collisional value. This anomalous current is created by fluctuations driven by the electric field and gradients of the magnetic field, plasma density, and electron temperature which are strongly inhomogeneous along the thruster axis. For the Hall thruster configuration the electric field, magnetic field and density gradients are in the $x-$ (axial) direction, the $y-$ direction is periodic (azimuthal) direction. Typical magnetic field, electric field, and density profiles will be presented in Section 4.4.3.

4.3.3 Basic equations

Here we formulate the eigenmode problem for the slab geometry with uniform axial magnetic field $\mathbf{B_0} = B_0\widehat{\mathbf{z}}$, and inhomogeneous plasma density $n_0 = n_0(x)$ and equilibrium potential $\phi_0 = \phi_0(x)$. We consider the nonlocal modes in the form $\widetilde{\Phi} = \widetilde{\phi}(x)\exp(-i\omega t + ik_y y)$. The y direction is assumed to be periodic, a finite length interval is considered in the radial direction x. This geometry is an approximation for the cylindrical geometry of the Penning discharge with axial magnetic field as in Ref. [22], in which case y is an azimuthal direction and x is radial.

The linearized ion momentum equation has the form

$$-i\omega m_i \mathbf{v_i} = -e\nabla\widetilde{\phi}. \tag{4.43}$$

Here we assume cold ions and neglect the effect of the magnetic field on ion motion. The linear continuity equation for ions is

$$-i\omega n_i + \nabla\cdot(n_i\mathbf{v}_i) = 0. \tag{4.44}$$

After substitution of $\mathbf{v}_i$ into the ion continuity equation one finds

$$-i\omega n_i - \frac{ie}{m_i\omega}(n_0\nabla^2\phi + \nabla n_0\cdot\nabla\phi) = 0. \tag{4.45}$$

In neglect of the electron inertia, electron motion along the magnetic field, and electron temperature, the electron velocity is a sum of the $\mathbf{E}\times\mathbf{B}$ drifts due to the stationary electric field $\mathbf{E}_0 = -\nabla\phi_0$, and the perturbed potential $\widetilde{\phi}$, with velocity $\widetilde{\mathbf{v}}_E = \nabla\widetilde{\phi}\times\mathbf{B}$. The resulting density perturbation is

$$\widetilde{n}_e = -i\frac{\widetilde{\mathbf{v}}_E\cdot\nabla n_0}{(\omega-\omega_0)}. \tag{4.46}$$

Using the quasineutrality one gets the eigenvalue equation in slab geometry

$$\frac{\partial^2\phi}{\partial x^2} - k_y^2\phi + \frac{n_0'}{n_0}\frac{\partial\phi}{\partial x} - \frac{\omega^2}{(\omega-\omega_0)}\frac{k_y}{\omega_{ci}}\frac{\nabla n_0}{n_0}\phi = 0, \tag{4.47}$$

where ω is an eigenvalue problem for prescribed boundary conditions on ϕ. In general case, ω and ϕ are complex. This eigenvalue problem is solved with following boundary conditions: $\tilde{\phi}(a) = \tilde{\phi}(-a) = 0$, or $\tilde{\phi}(a) = \tilde{\phi}(0) = 0$, depending on the geometry type.

It is convenient to use the transformation

$$\phi(x) = \frac{1}{(n_0(x))^{1/2}}\psi(x). \tag{4.48}$$

Then the equation (4.47) is reduced to the form

$$\frac{\partial^2\psi}{\partial x^2} - k_y^2\psi + \left[-\frac{\omega^2}{(\omega-\omega_0)}\frac{k_y}{\omega_{ci}}\frac{n_0^{'}}{n_0} + \frac{1}{4}\frac{n_0^{'2}}{n_0^2} - \frac{1}{2}\frac{n_0^{''}}{n_0}\right]\psi = 0, \tag{4.49}$$

For the constant gradient profile

$$n_0(x) = n_0 \exp\left(\frac{x}{L_n}\right) \tag{4.50}$$

one has the following equation

$$\frac{\partial^2\psi}{\partial x^2} - k_y^2\psi + \left[-\frac{\omega^2}{(\omega-\omega_0)}\frac{k_y}{L_n\omega_{ci}} - \frac{1}{4L_n^2}\right]\psi = 0, \tag{4.51}$$

For constant L_n and ω_0, from (4.51) one gets the following local dispersion relation:

$$\left(k_\perp^2 + \frac{1}{4L_n^2}\right)\frac{c_s^2}{\omega^2} = \frac{\omega_*}{\omega-\omega_0} \tag{4.52}$$

This equation, basically, is a modified Eq. (4.41). From this equation, one can see that density gradient increases the effective value of $k_\perp$ modifying the spectrum of unstable modes. This is illustrated in Fig. 4.1 (a) for $L_n = -0.1\ m$, and $L_n = -0.04\ m$ in Fig. 4.1 (b). Profile of the ω_0 is uniform and system size $L = 0.1\ m$. Bold lines are growth rate calculated from the local Eq. (4.52) with effect of L_n. Thin dashed lines is growth rate from Eq. (4.41). Density gradient effect leads to a slight increase of growth rates at low k_x values. Square marks are the discrete unstable growth rates obtained from numerical solution of Eq. (4.47) for the the system size $L = 0.1\ m$.

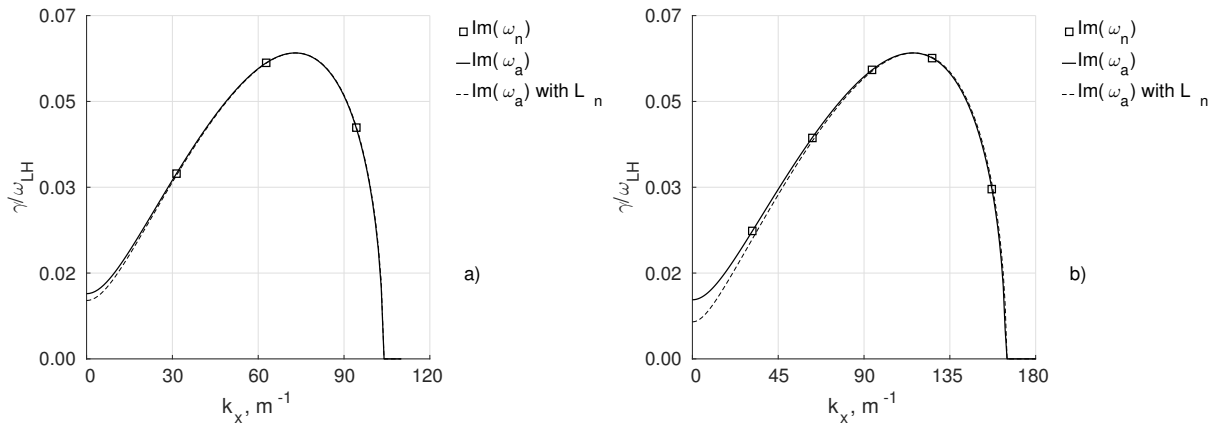

Figure 4.1: The growth rate as a function of k_x, and $k_y = 10\ m^{-1}$; (a) for $L_n = -0.1$ m, and (b) for $L_n = -0.04\ m$. Bold lines – growth rates from Eq. (4.52); thin dashed lines – growth rates from Eq. (4.41); squares – growth rates from Eq. (4.47).

It is important to stress that k_x values are not arbitrary and are defined by the size of the system. Another thing to note is that stronger density gradients (smaller absolute values

of L_n) significantly increase a number of unstable modes and range of unstable values of k_x; however the maximal value of the growth rate is not changed.

Dependency of growth rate on k_y wavenumber with and without the effect of L_n is shown on Fig. 4.2. Results were obtained for $L_n = -0.04\ m$. Consideration of L_n term leads to the constant shift of growth rate. Therefore, for moderate gradient values, this effect does not lead to significant change of the maximum growth rate. One can see from Figs 4.1, 4.2 that for the considered plasma parameters, the effect of $n_0^{'}/n_0(\partial\phi/\partial x)$ term is not essential.

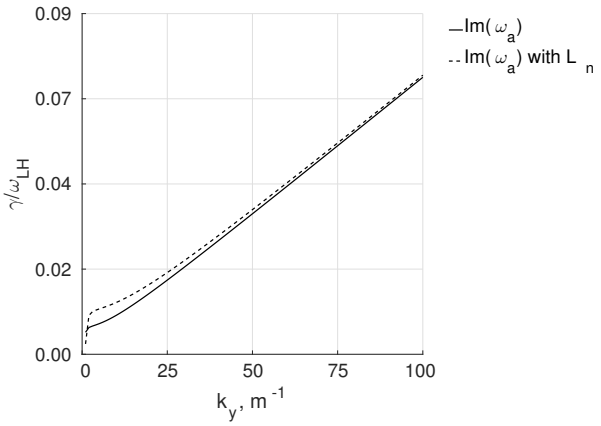

Figure 4.2: The growth rate as a function of k_y, for $k_x = 31\ m^{-1}$ and $L_n = -0.04\ m$. Bold line – growth rates from Eq. (4.41); thin dashed line – growth rates from Eq. (4.52).

However, Eq. (4.47) does not take into account effect of electron inertia. Important result presented in Fig. 4.1 is that the maximum of the eigenfrequency is close to the ω_0 frequency. In fact, one can show [92] that for continuous k_x, the eigenmode with the maximum growth rate is $\omega = \omega_0 + i\omega_0$. Therefore, it may become comparable with the lower-hybrid frequency and electron inertia has to be included. The respective equation can be written as in Ref. [92] (similar equation was also given in [111, 112])

$$\frac{\partial^2\phi}{\partial x^2} - k_y^2\phi - F(\omega)\frac{1}{(\omega-\omega_0)}\frac{k_y}{\omega_{ci}}\frac{\nabla n_0}{n_0}\phi = 0, \tag{4.53}$$

where

$$F(\omega) = \frac{\omega^2}{1-\omega^2/\omega_{LH}^2}$$

The full spectra of unstable solutions for two values of k_y with and without the effect of electron inertia are shown on Fig. 4.3. These spectra was obtained by solving Eq. (4.47) and

Eq. (4.53) for constant ω_0 profile and $L_n = -0.04\ m$. For low values of k_y (empty circles and squares), unstable frequencies are much lower than ω_{LH}, so inertia effect does not play a big role; however, for the case of high k_y values (solid circles and squares) electron inertia leads to the significant decrease of unstable frequency and growth rate values.

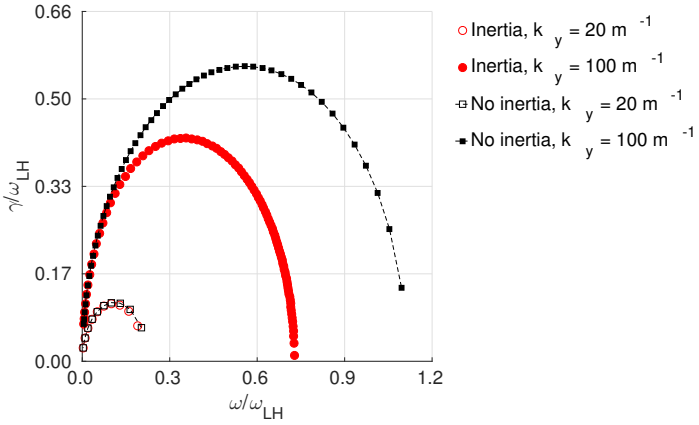

Figure 4.3: The full spectrum of unstable solutions with (circles) and without (squares) electron inertia effect for $L_n = -0.04\ m$: empty markers – $k_y = 20\ m^{-1}$; filled markers – $k_y = 100\ m^{-1}$.

Another critical effect of the electron inertia is the stabilization of the instability at large values of the k_y. These results are shown in Fig. 4.4 (a) and (b). The results for fixed value of the k_x, are shown in Fig. 4.4 (a); $k_x = 31\ m^{-1}$ value is chosen as a minimal possible for this system. As was shown above, the value of the k_x at which the growth rate is maximal, changes as a function of k_y. The dependence of the maximum growth rate on the k_y is shown in Fig. 4.4 (b). The value of k_x is different at each k_y value.

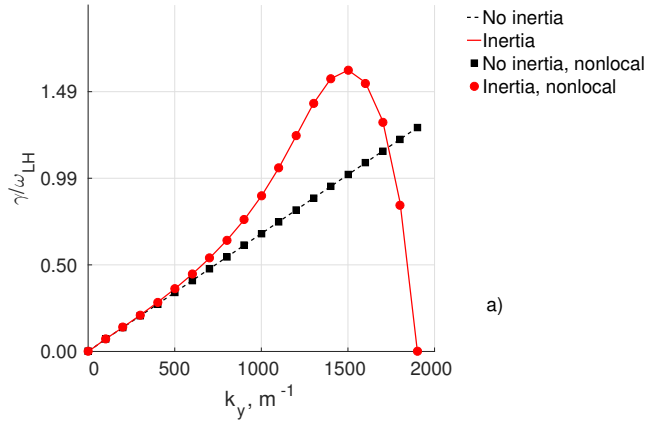

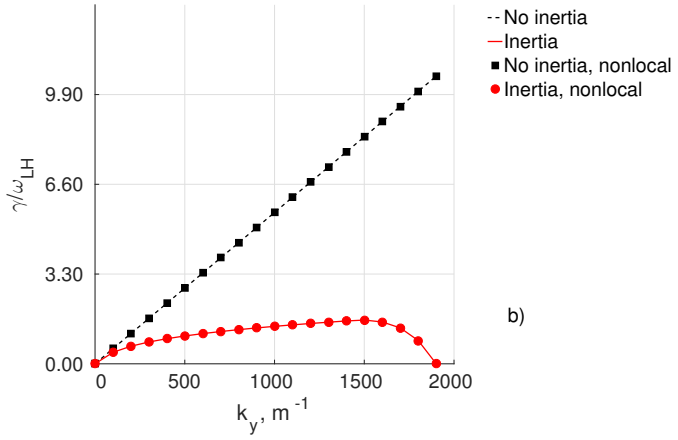

Figure 4.4: The growth rate as a function of k_y at $L_n = -0.04\ m$. Dashed line – growth rate without electron inertia effect; solid line – growth rate with electron inertia effect; squares and circles – growth rates from nonlocal model without and with electron inertia effect, respectively. (a) for fixed $k_x = 31\ m^{-1}$; (b) maximal growth rate at each k_y value, k_x changes with k_y.

Dependency on k_x obtained from equations (4.47) and (4.53) is presented in Fig. 4.4 for two different k_y and L_n values. As before, stronger density gradients leads to increase of a number of unstable modes. For low k_y values inertia does not bring significant effect, but for higher k_y values inertia increase the range of unstable modes and causes the appearance of unstable modes with much higher k_x values.

Therefore, electron inertia causes qualitative change in behavior of unstable solution with growth of k_y, bringing the cutoff of the instability at high k_x values. Changes in dependency on k_x are more quantitative, and appears mostly at high k_y values.

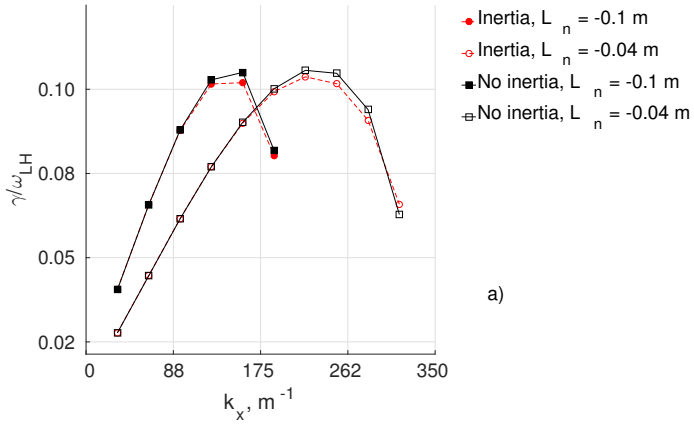

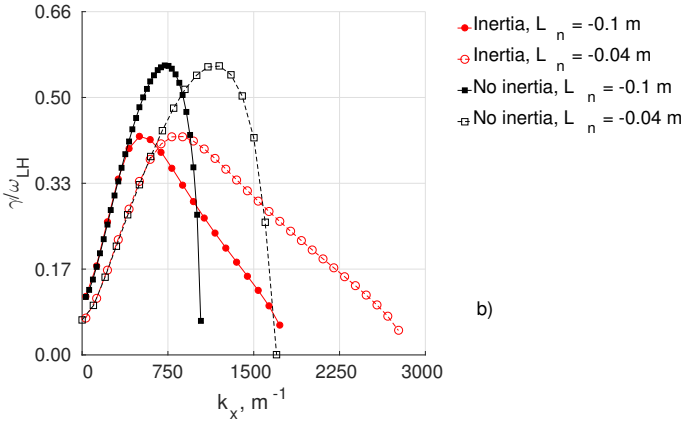

Figure 4.4: The growth rate as a function of k_x for $k_y = 20\ m^{-1}$ (a), and $k_y = 100\ m^{-1}$ (b). Circles – results with the inertia; squares - results without the inertia. Filled markers – results for $L_n = -0.1\ m$; empty markers – results for $L_n = -0.04\ m$.

4.4 Nonlocal eigenmodes for some model profiles

Here we analyze the properties of the eigenmodes for different model profiles of $\mathbf{E} \times \mathbf{B}$ velocity. These simple profiles illustrate some characteristic features of the eigenmodes which also persist in more realistic cases.

4.4.1 Step-like profile of the $\mathbf{E} \times \mathbf{B}$ velocity

Eigenvalue problem (4.47) with a step-like profile of the $\mathbf{E} \times \mathbf{B}$ drift frequency ω_0, is in Fig. 4.5. Solution inside of each region can be obtained in form of the harmonic functions, $\phi \sim A_i \cos(\lambda_i x) + B_i \sin(\lambda_i x)$ and the dispersion relations is easily obtained from matching conditions. A formal dispersion relation is not very illuminating. Here we just emphasize the main features of such solutions and compare the nonlocal modes with the predictions of the local theory.

First, we consider a case with the low k_y wavenumber values. As was noted above, the k_x range of the unstable modes, is decreasing for lower values of k_y. Since the allowed wavenumber k_x is discrete, the number of unstable eigenmodes decreases with decreasing k_y. Effect of density gradient L_n on nonlocal unstable eigenmodes is similar to the effect of k_y; thus density gradient is fixed and taken $L_n = -0.04\ m$ for one wavenumber $k_y = 20\ m^{-1}$. A characteristic feature of the ω_0 profile, shown in Fig. 4.5, is that the local theory predicts

the instability only in the region $-5 < x < 0$, while the region $0 < x < 5$ should be stable. The nonlocal solutions may exist in the locally stable region.

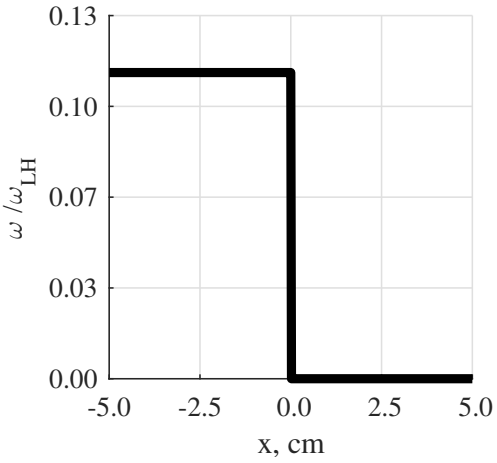

Figure 4.5: Profile of ω_0.

Full spectra of unstable solutions is shown in Fig. 4.6(a). Three characteristic modes are chosen to show the shape of eigenfunctions in Fig. 4.6(b): point (1) with the lowest value of the real part of the frequency $\omega = (0.01 + 0.04i) \cdot \omega_{LH}\ s^{-1}$; point (2) with the largest growth rate $\omega = (0.11+0.1i)\cdot\omega_{LH}\ s^{-1}$; and point (3) with smallest growth rate $\omega = (0.14+0.01i)\cdot\omega_{LH}\ s^{-1}$. All solutions have the nonlocal structure across the whole domain $-5 < x < 5$ including the region $0 > x > 5$ which is locally stable.

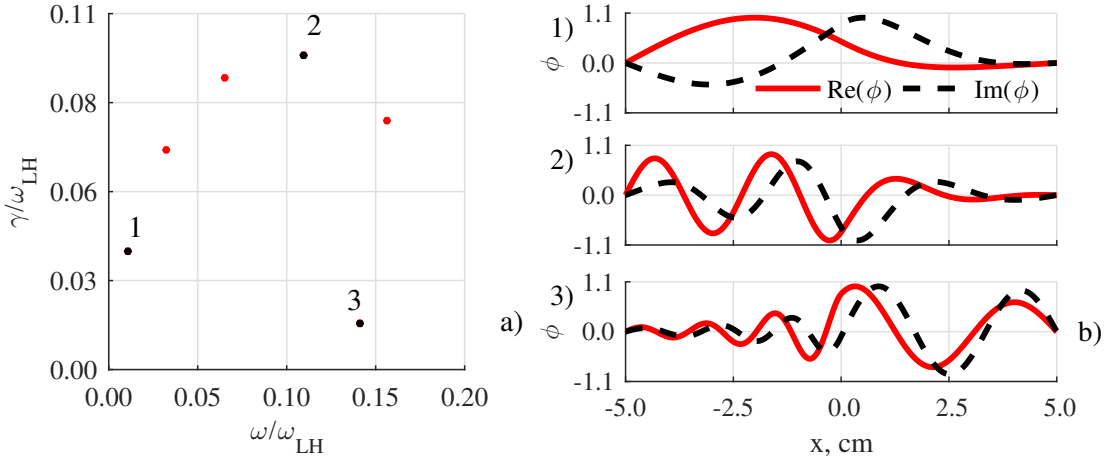

Figure 4.6: Results for step-like profile of the ω_0 with $k_y = 20\ m^{-1}$ and $L_n = -0.04\ m$. (a) The full spectra of unstable eigenvalues. (b) The eigenfunctions are for eigenvalues (from top to bottom): $1 - \omega = (0.01 + 0.04i) \cdot \omega_{LH}\ s^{-1}$, $2 - \omega = (0.11 + 0.1i) \cdot \omega_{LH}\ s^{-1}$, $3 - \omega = (0.14 + 0.01i) \cdot \omega_{LH}\ s^{-1}$.

The tendency toward the local theory increases for larger k_y, as is expected. Full spectrum of eigenvalues in phase space for step-like profile of ω_0 with $k_y = 100m^{-1}$ is shown on Fig. 4.7 (a). Some characteristic eigenfunctions are shown on Fig. 4.7 (b); one can see that there are solutions extending in the locally stable region.

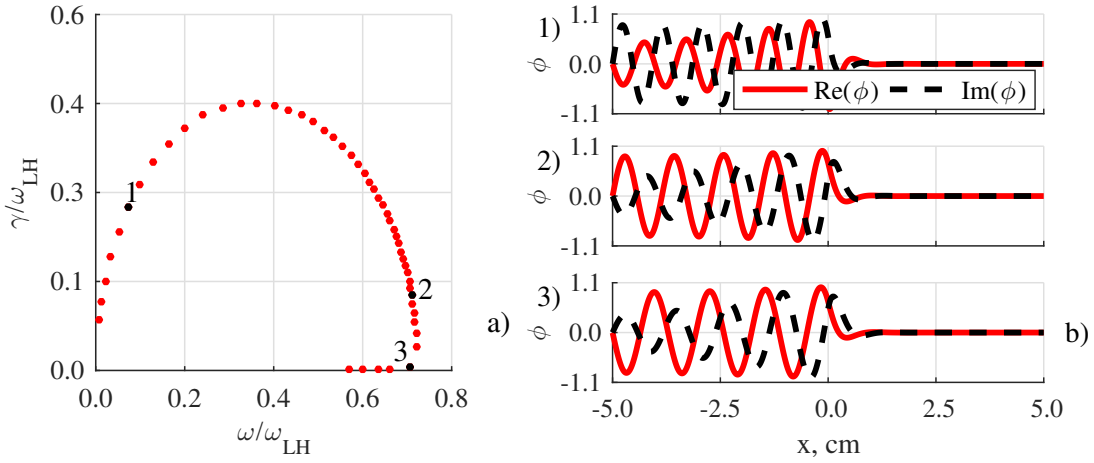

Figure 4.7: (a) Full spectrum of the eigenvalues for $k_y = 100\ m^{-1}$. (b) The eigenfunctions are for eigenvalues (from top to bottom): $1 - \omega = (0.07 + 0.25i) \cdot \omega_{LH}\ s^{-1}$, $2 - \omega = (0.71 + 0.12i) \cdot \omega_{LH}\ s^{-1}$, $3 - \omega = (0.71 + 0.004i) \cdot \omega_{LH}\ s^{-1}$.

General tendency is that the solutions with the lower growth rates are more deeply extended into the locally stable region.

4.4.2 Linear profile of the E × B velocity

Here we investigate the eigenmode problem for the parabolic potential profile $\phi = \alpha x^2$ corresponding to the case of a constant shear of the $\mathbf{E} \times \mathbf{B}$ velocity and exponential density profile $n = n_0 \exp(-x/a)$ which makes the density gradient length scale constant, $L_n^{-1} = n_0^{-1}\partial n_0/\partial x = const$. Such profiles may occur in Penning discharge configurations where ions are confined radially by the inward radial electric field [110].

We assume that $\omega_0 = k_y v_0 x/L$, where L is the width of the region in the radial direction x. Several unstable eigenfunctions for $k_y = 20\ m^{-1}$ and $L = 20\ cm$ are shown in Fig. 4.8. Full spectrum of the unstable solutions is presented in Fig. 4.8 (a).

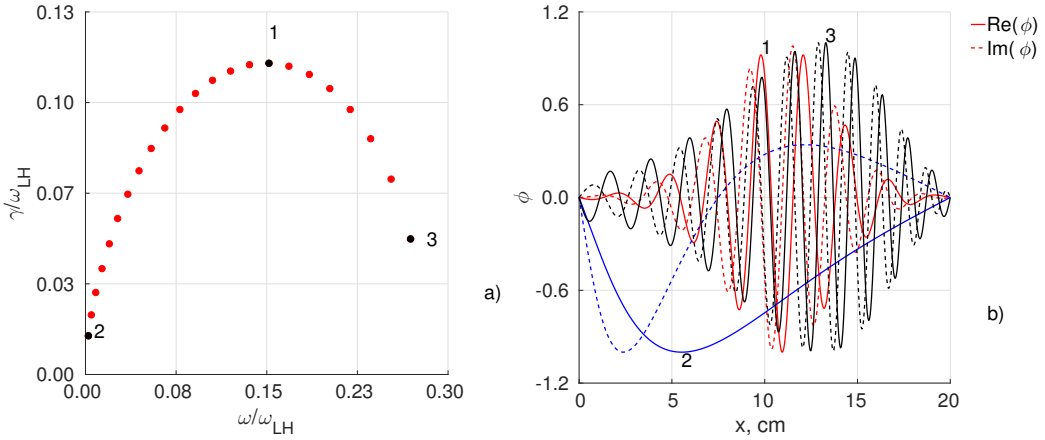

Figure 4.8: (a) Full spectrum of the unstable eigenvalues; (b) Unstable eigenfunctions for the constant $\mathbf{E} \times \mathbf{B}$ shear profile; wavenumber $k_y = 20\ m^{-1}$. The eigenfunction with the largest growth rate, $\omega = (0.15 + 0.11) \cdot \omega_{LH}\ s^{-1} - 1$ (red); the ground state unstable eigenfunction with $\omega = (0.002 + 0.014i) \cdot \omega_{LH}\ s^{-1} - 2$ (blue); the eigenfunction with largest real frequency $\omega = (0.27 + 0.05i) \cdot \omega_{LH}\ s^{-1} - 3$ (black).

For the $\mathbf{E} \times \mathbf{B}$ velocity with a constant shear there exists a discrete spectrum of multiple unstable modes. Similar to the local theory results, the ground state is not the most unstable solution. The eigenmode with the largest growth rate for $k_y = 20\ m^{-1}$ is shown in Fig. 4.8 (b) with respect to the profile of the $\mathbf{E} \times \mathbf{B}$ frequency, $\omega_0(x)$. Lines with circles and squares represent growth rate obtained from local theory for $k_x = 0$ and $k_x = 63\ m^{-1}$ respectively. As it is seen, with the increase of k_x value, unstable region shifts to the right.

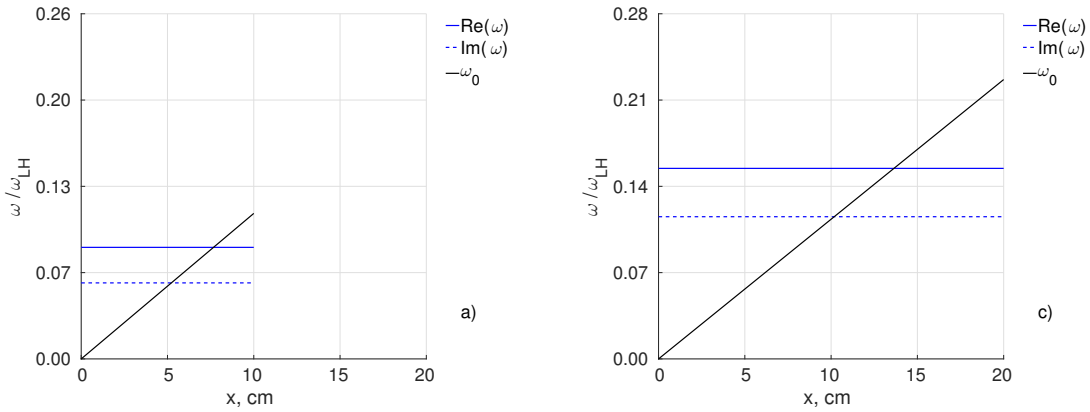

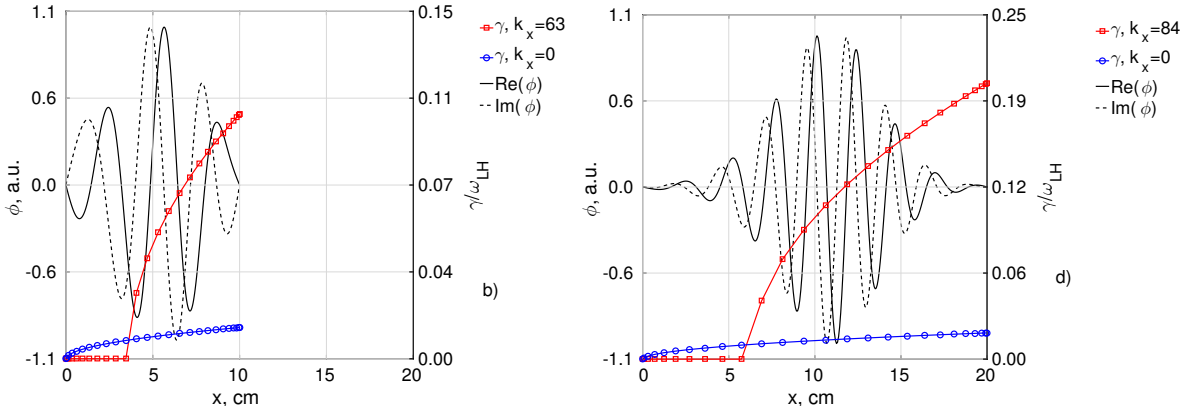

Figure 4.8: Left side: the eigenfunction with the largest growth rate $\omega = (0.09 + 0.6i) \cdot \omega_{LH}\ s^{-1}$ (b), with respect to the profile of the $\mathbf{E} \times \mathbf{B}$ frequency (a), $k_y = 20\ m^{-1}$ and $L = 10\ cm$. The growth rates from the local theory for the same parameters and $k_x = 0$ – squares (red), $k_x = 63\ m^{-1}$ – circles (blue). Right side: the eigenfunction with the largest growth rate $\omega = (0.07 + 0.06i) \cdot \omega_{LH}\ s^{-1}$ (d) in the extended domain: $L = 20$ cm, for $k_y = 20\ m^{-1}$, with respect to the $\mathbf{E} \times \mathbf{B}$ frequency profile (c). The growth rates from the local theory for the same parameters and $k_x = 0$ – squares (red), $k_x = 84\ m^{-1}$ – circles (blue).

The eigenfunctions with the largest growth rate are approximately localized close to the resonance point $Re(\omega) \simeq \omega_0$; however, there is an asymmetrical shift due to the finite growth rate. Similar to the local theory, the growth rate increases with the effective value of the radial wave number k_x. This is illustrated by the eigenfunction for the same value of $k_y = 20$ m^{-1} as in Fig. 4.8 (b) but for the extended domain with the length $L = 20\ cm$, see Fig. 4.8 (d). In the extended domain, the most unstable eigenfunction has larger growth rate, higher effective k_x and the localization region shifts to the right (toward higher local ω_0), compare Figs. 4.8 (b) and 4.8 (d). Again, there is very little resemblance between the results of the local theory and the nonlocal solution. The local growth rates for comparison are shown in Fig. 4.8 (b, d) for two different values of the radial wave number k_x. The local theory predicts that the mode with $k_x = 0$ is unstable in the wide region. For the $k_x = 84$ m^{-1}, the instability exists locally only in the region for $x > 6$ cm. In fact, the nonlocal solution has the effective k_x which is higher than $k_x = 84\ m^{-1}$ and for which the local theory predicts no instability in the whole domain $0 < x < 20\ cm$.

The growth rate increases almost linearly with the wavenumber k_y, and the localization

region becomes narrower around the resonance point $Re(\omega) \simeq \omega_0$. The most unstable eigenfunction for $k_y = 100\ m^{-1}$ and system length $L = 10\ cm$ is shown in Fig. 4.9 (b) with respect to the profile of the $\omega_0(x)$.

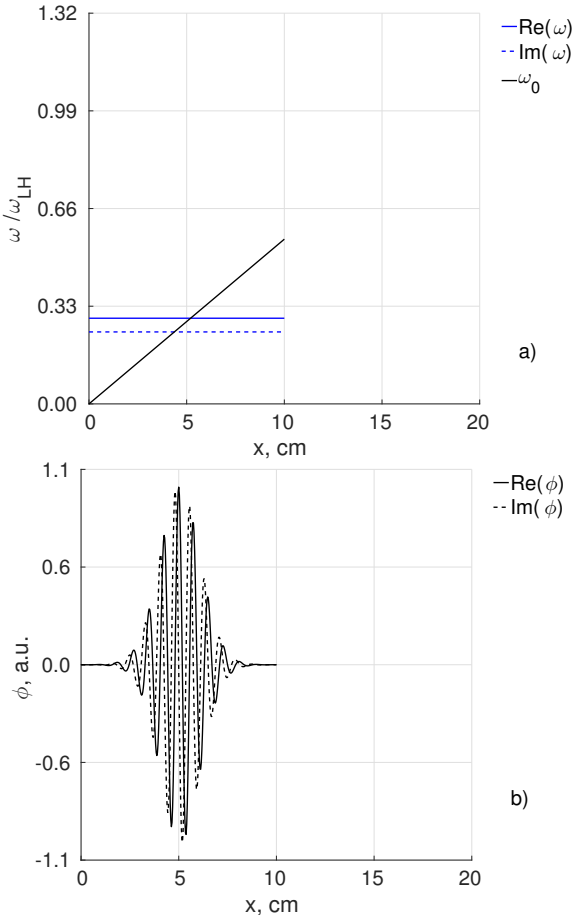

Figure 4.9: The eigenfunction with largest growth rate $\omega = (0.29 + 0.24i) \cdot \omega_{LH}\ s^{-1}$, $k_y = 100\ m^{-1}$, $L = 10\ cm$.

Several unstable eigenfunctions in the extended domain $L = 20\ cm$ with the same value of $k_y = 100\ m^{-1}$ are shown in Fig. 4.10. One can see that these modes are relatively local in the sense that they are weakly dependent on the boundary conditions at $x = 0$ and $x = L$. The eigenfunction with $\omega = (0.29 + 0.24i) \cdot \omega_{LH}\ s^{-1}$ and localized at $x \simeq 5\ cm$, shown in Fig. 4.9, corresponds to almost the same frequency $Re(\omega)$ and localized at the same $x \simeq 5\ cm$ as mode (2) which is shown in Fig. 4.10 (b). However, localization of mode (1) is far from resonant point for this eigenmode, see line (1) in Fig. 4.10. This is due to the effect of the electron inertia.

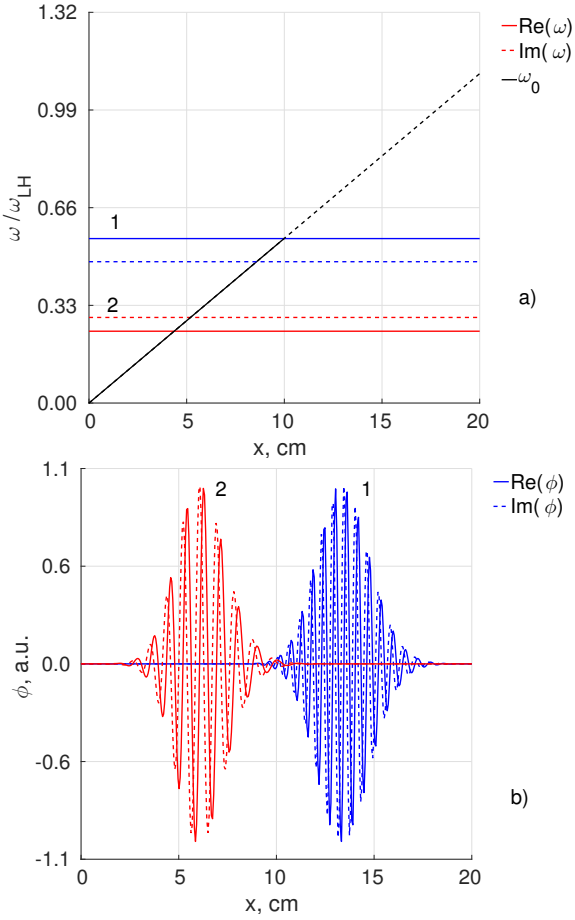

Figure 4.10: Several eigenfunctions are shown for the extended domain $L = 20\ cm$, $k_y = 100\ m^{-1}$. The eigenfunction with the largest growth rate for the extended domain, $\omega = (0.56+0.48i)\cdot\omega_{LH}\ s^{-1} - 1$ (blue); $\omega = (0.24+0.29i)\cdot\omega_{LH}\ s^{-1} - 2$ (red). The eigenfunction with the eigenvalue $\omega = (0.24 + 0.29i)\cdot\omega_{LH}\ s^{-1} - 2$ (red), has approximately the same frequency and localization as mode on with Fig. 4.9, for $L = 10\ cm$.

Therefore, another property of nonlocal modes can be understood from the example with the linear profile of ω_0. For unstable eigenmodes with absolute values of frequencies and growth rates well below of the ω_{LH}, the localization region is approximately determined by the point of the resonance $Re(\omega) = \omega_0$. For higher frequencies this is not true, in general.

4.4.3 Nonlocal eigenmodes in plasmas with temperature, density and magnetic field profiles.

Inhomogeneous magnetic field plays an important role in operation of Hall thrusters [7, 8] and magnetrons [6, 94, 95]. Modification of the instability criteria due to the magnetic field

was noted in Refs. [7,8]. An additional effect of the magnetic field gradient occurs due to the finite temperature [91,97]. The appropriate eigenvalue equation [113] is

$$\frac{\partial^2\phi}{\partial x^2} - k_y^2\phi + \frac{1}{1-\omega^2/\omega_{LH}^2}\frac{\omega^2(\omega_* - \omega_D)}{(\omega - \omega_0 - \omega_D)}\frac{1}{c_s^2}\phi = 0, \tag{4.54}$$

For simulations, we use typical parameters from experiments in a Hall thruster [27]. The density n_0, electron temperature T_e, electric field E, and magnetic field B profiles along the thruster axis ($x-$ direction) are shown in Fig. 4.11.

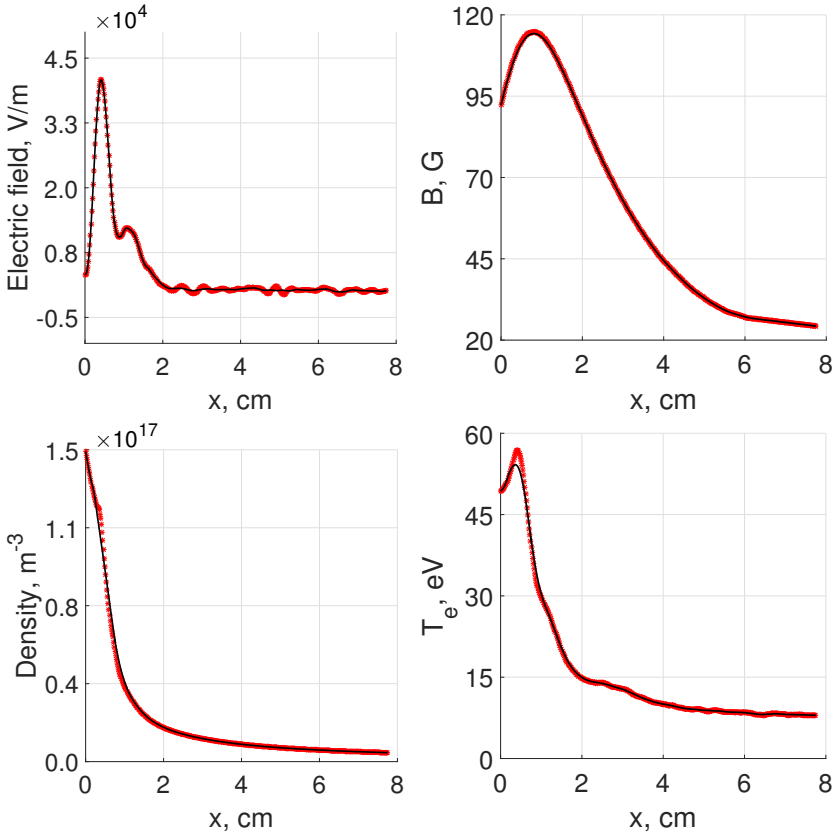

Figure 4.11: Initial profiles of electric, magnetic fields, electron density, and electron temperature for Hall thruster experiment.

The profiles of the drift frequencies ω_0, ω_*, ω_D, and ω_{LH} are shown in Fig. 4.12. Calculation were done for parameters from Fig. 4.11 and $k_y = 8.1\ m^{-1}$. For the complex profiles of plasma parameter, the nonlocal solution in general require high number of polynomials in the spectral method. To verify the solutions obtained with spectral and shooting methods, and confirm the convergence, we have also used the integral relations that follow from Eq. 4.54

$$\int \left(|\phi|'^2 + k_y^2 |\phi|^2 \right) dx = \int Re \left(\frac{1}{1 - \omega^2/\omega_{LH}^2} \frac{\omega^2(\omega_* - \omega_D)}{(\omega - \omega_0 - \omega_D)} \right) \frac{1}{c_s^2} |\phi|^2 dx, \tag{4.55}$$

and

$$0 = \int Im \left(\frac{1}{1 - \omega^2/\omega_{LH}^2} \frac{\omega^2(\omega_* - \omega_D)}{(\omega - \omega_0 - \omega_D)} \right) \frac{1}{c_s^2} |\phi|^2 dx. \tag{4.56}$$

The ratio of left hand side and right hand side integrals was tracked with the increase of the number of polynomials. Desired accuracy was 10^{-5}.

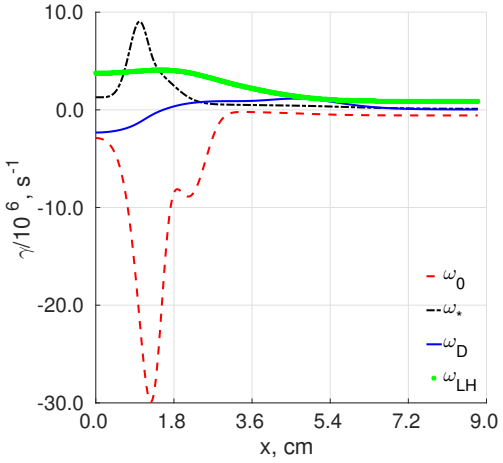

Figure 4.12: Characteristic frequencies profiles and unstable solutions for $k_y = 8.1$ m^{-1}.

Similar to general trend, for a given k_y, there exist multiple eigenmodes with different growth rates and different localization regions. However, full spectra of unstable solutions looks very different from spectra for simple profiles. Example of such spectra for $k_y = 8.1$ m^{-1} is presented in Fig. 4.12. Three distinct groups of unstable solutions can be identified.

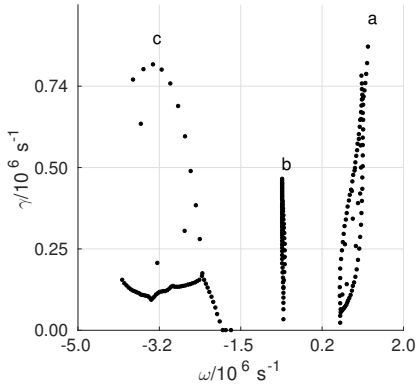

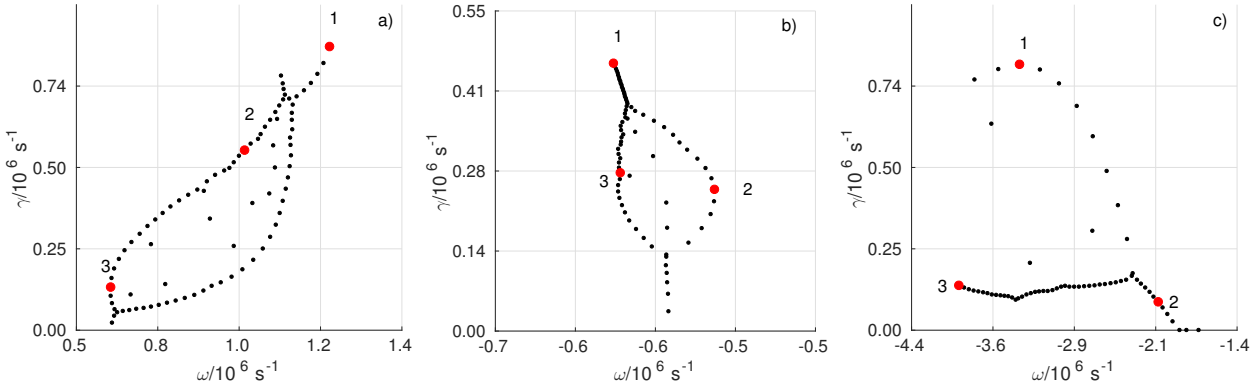

Figure 4.12: Full spectra of unstable solutions for Hall thruster profiles at $k_y = 8.1$ m^{-1}. Three groups of unstable solutions are marked as (a), (b), (c). Eigenvalues for numbered dots are presented in Table 4.1.

An important difference is the sign of the real part of the frequency. There exist unstable modes with positive and negative frequencies. Note that the negative sign of the real part of the frequency correspond to the rotation in the $\mathbf{E} \times \mathbf{B}$ direction. Corresponding eigenvalues and eigenfunctions for the numbered point in each group are given in Table 4.1 and Fig. 4.13, respectively.

Table 4.1: Eigenvalues for Fig. 4.12

Fig. 4.12 (a)	1	$\omega = (1.2 + 0.9) \cdot 10^6\ s^{-1}$
	2	$\omega = (1.0 + 0.6) \cdot 10^6\ s^{-1}$
	3	$\omega = (0.6 + 0.1) \cdot 10^6\ s^{-1}$
Fig. 4.12 (b)	1	$\omega = (-0.6 + 0.5) \cdot 10^6\ s^{-1}$
	2	$\omega = (-0.5 + 0.2) \cdot 10^6\ s^{-1}$
	3	$\omega = (-0.6 + 0.3) \cdot 10^6\ s^{-1}$
Fig. 4.12 (c)	1	$\omega = (-3.4 + 0.8) \cdot 10^6\ s^{-1}$
	2	$\omega = (-2.1 + 0.9) \cdot 10^6\ s^{-1}$
	3	$\omega = (-4.0 + 0.1) \cdot 10^6\ s^{-1}$

Unstable eigenfunctions for marked points are shown in Fig. 4.13. Eigenfunctions, corresponding to different groups, have different localization. Contrary to the case of simple profiles, narrowly localized modes appear even for low k_y value. Modes in group (c) have

almost exactly the same localization, thus local theory should work very well in this region. However, modes in group (a) are located in the region, where the local theory does not predict any instability (see in Fig. 4.17).

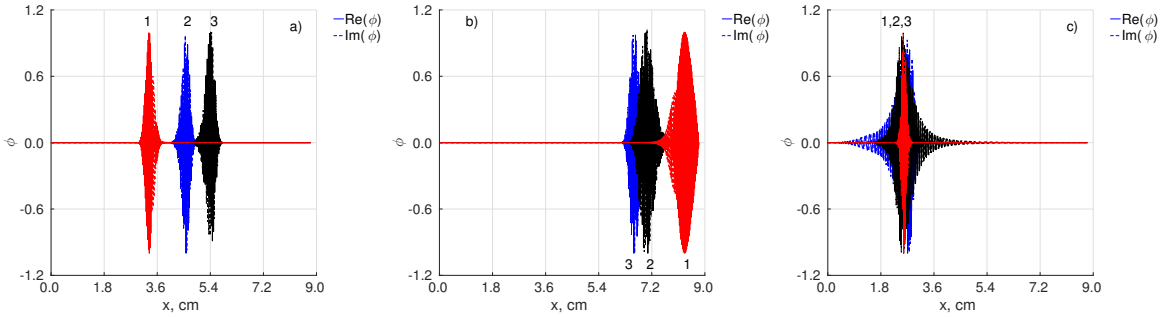

Figure 4.13: Unstable eigenfunctions from each group of unstable solutions.

For higher value of k_y full spectra of unstable solutions is modified, there appeared fourth group of unstable solutions, see Fig. 4.14. Group (d) appeared in between of groups (a) and (b) from Fig. 4.12.

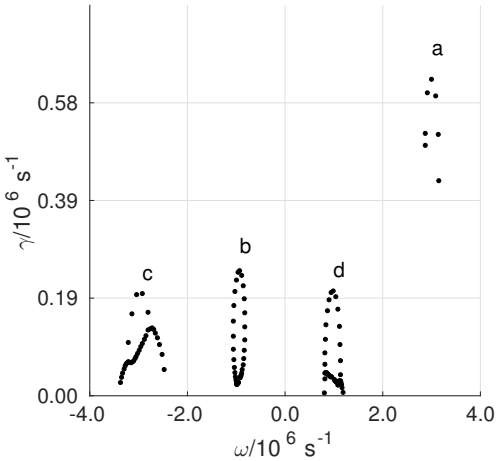

Figure 4.14: Full spectra of unstable solutions for Hall thruster profiles at $k_y = 81$ m^{-1}. Four distinct groups of the unstable solutions can be identified.

Detailed view of each group is presented in Fig. 4.15. Corresponding eigenvalues and eigenfunctions for the numbered point in each group are given in Table 4.2 and Fig. 4.16, respectively.

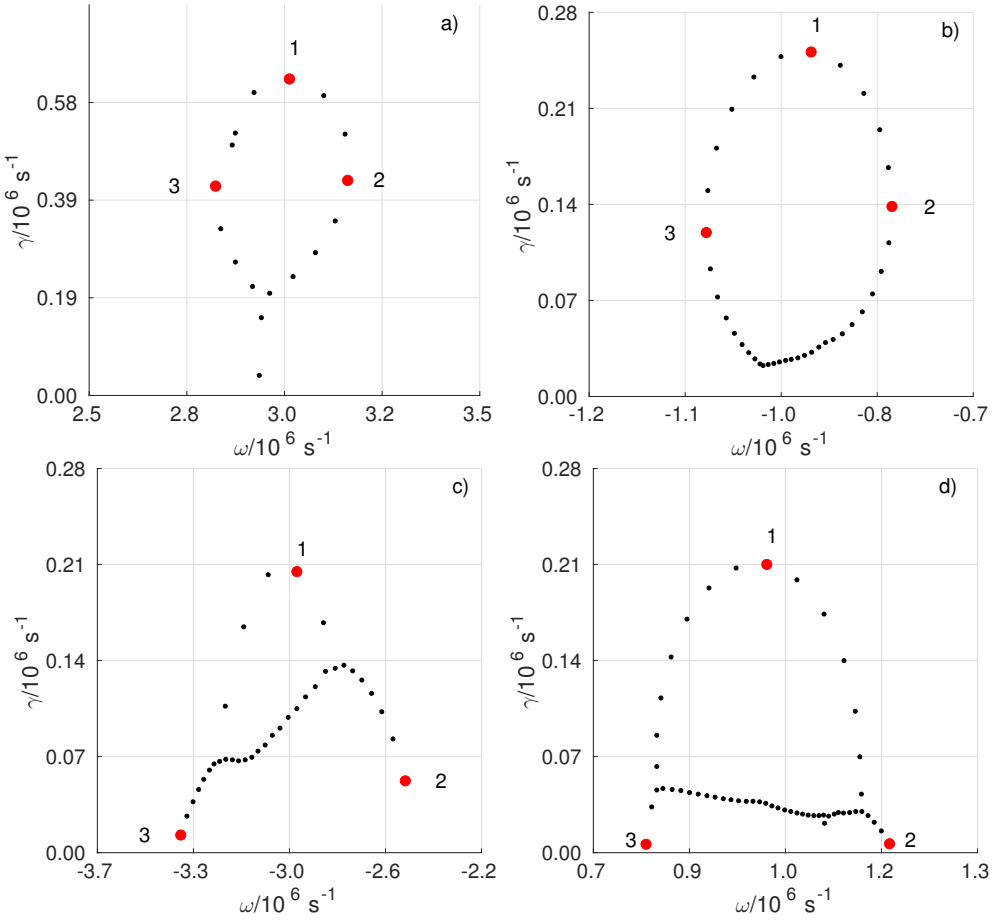

Figure 4.15: Each group of unstable solution from Fig. 4.14. Eigenvalues for numbered dots are presented in Table 4.2.

Table 4.2: Eigenvalues for Fig. 4.15

Fig. 4.16 (a)	1	$\omega = (3.0 + 0.6) \cdot 10^6\ s^{-1}$
	2	$\omega = (3.1 + 0.4) \cdot 10^6\ s^{-1}$
	3	$\omega = (2.8 + 0.4) \cdot 10^6\ s^{-1}$
Fig. 4.16 (b)	1	$\omega = (-0.9 + 0.23) \cdot 10^6\ s^{-1}$
	2	$\omega = (-0.8 + 0.13) \cdot 10^6\ s^{-1}$
	3	$\omega = (-1.0 + 0.1) \cdot 10^6\ s^{-1}$
Fig. 4.16 (c)	1	$\omega = (-2.9 + 0.14) \cdot 10^6\ s^{-1}$
	2	$\omega = (-2.4 + 0.03) \cdot 10^6\ s^{-1}$
	3	$\omega = (-3.4 + 0.02) \cdot 10^6\ s^{-1}$

	1	$\omega = (1.2 + 0.01) \cdot 10^6\ s^{-1}$
Fig. 4.16 (d)	2	$\omega = (1.0 + 0.17) \cdot 10^6\ s^{-1}$
	3	$\omega = (0.8 + 0.02) \cdot 10^6\ s^{-1}$

Unstable eigenfunctions are presented in Fig. 4.16. Modes for groups (a) and (b) become local, as it is expected for higher k_y values. However, unexpected result is that the modes in groups (c) and (d) become highly nonlocal.

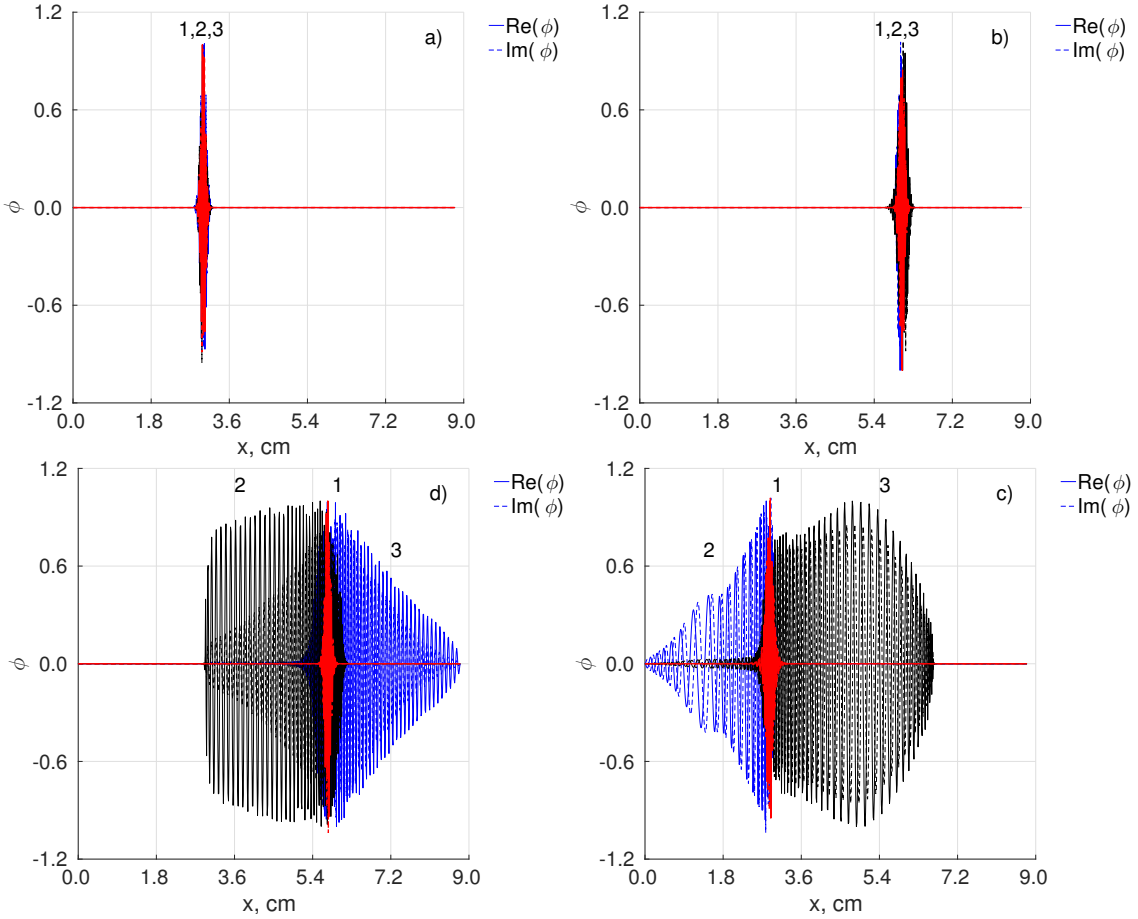

Figure 4.16: Unstable eigenfunctions from each group of unstable solutions.

Absolute values of frequencies are comparable in these two groups, but growth rates are lower in the region farther from the anode (group (d)). Moreover, the real and imaginary parts of the most unstable eigenvalue almost do not change with the $k_y$wavenumber. Growth rate of the unstable mode mostly depend on mode localization. Real part of frequencies for fastest modes are comparable with low-hybrid frequency $\omega_{LH} = 3.4 \cdot 10^6\ s^{-1}$.

The nonlocal modes (with the least number of nodes) have the lower growth rates com-

pared to the localized (with the higher effective higher k_x) modes. The nonlocal unstable modes, presented in Figs 4.13, 4.16 are present in the regions where local modes are stable (shown in Fig. 4.17). It is important to note that the fast instabilities are absent in the acceleration region where the electric field is large.

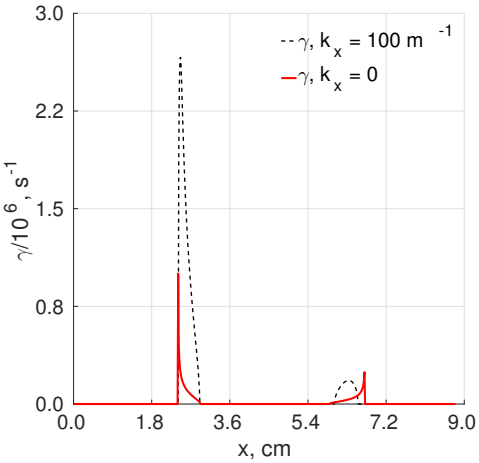

Figure 4.17: The growth rate from local model are shown as a function of distance along the thruster axis for $k_y = 8.1\ m^{-1}$, and $k_x = 0\ m^{-1}$, $k_x = 100\ m^{-1}$.

The integral forms, Eqs. 4.55 and 4.56, were used to track the convergence. Example of the convergence for one group is shown in Fig. 4.18. Each marker and color represent different number of polynomials. Green markers are solutions for low polynomials number. With the increase of the number of polynomials, eigenvalues reach asymptotically the limit values which are shown as solid black circles.

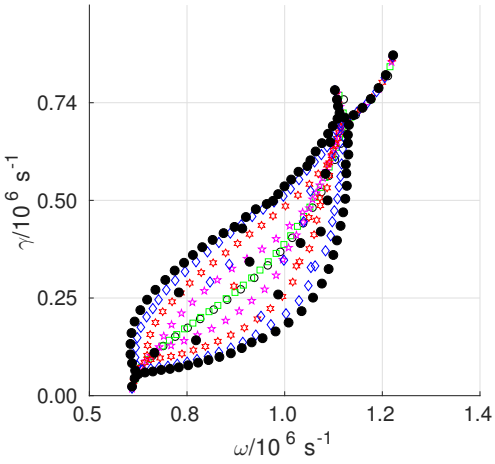

Figure 4.18: Convergence of group (b) in Fig. 4.12 with the increase of the number of polynomials. Filled black circles – the stage when convergence is reached.

4.4.4 Conclusion

Linear, nonlocal model for gradient-drift modes including the collisionless Simon-Hoh and lower-hybrid instabilities was developed and used to study the nonlocal structure of unstable mode in Hall plasma with inhomogeneous profiles of plasma density, temperature, electric and magnetic fields. The eigenvalue problem was solved numerically by using spectral and shooting methods and verified by the integral relations.

Our model includes the collisionless Simon-Hoh destabilization mechanism [90] $\mathbf{E} \cdot \nabla n > 0$ and electron inertia that couples this mode to the lower-hybrid mode. A number of factors were not included in the model, such as collisional [114, 115], ionization [102] effects and additional terms that explicitly include the shear flow effects [92, 115]. In general, neglect of these effects may limit the applicability of our model to some practical Hall devices. Our emphasis, however, was on the higher frequency modes with frequencies much higher than some typical low frequency (kHz range) oscillations, such as breathing mode due to ionization process. We have considered the eigenmode structure in the axial direction of the Hall thruster, and radial direction for the Penning discharge. One of the important results of our analysis is demonstration of the existence of multiple modes with the eigenmode frequencies comparable to the electron drift frequency [116].

There are significant differences between predictions of the local and nonlocal models, as it has been noted earlier [102,107]. The nonlocal model for the step-like ω_0 profiles shows that for the low wavenumbers k_y nonlocal solutions can propagate into the region of the domain where local instability criteria is not satisfied. For higher k_y modes, the results of nonlocal model become similar to the local model that is unstable mode is highly localized. However, there are still unstable modes that extend into the region of stability and grow there even for high k_y values.

Simulations for the $\mathbf{E} \times \mathbf{B}$ flow with a constant shear and constant density gradient show that there exist multiple unstable eigenmodes with different growth rates and different localization regions. Mode localization becomes more evident with increase of k_y. Moreover, such modes are almost independent on boundary conditions at $x = 0$ and $x = L$.

We have also studied the eigenmode structure for complex profiles of the magnetic field,

electric field, and electron temperature relevant to Hall thruster experiments [27]. In general, the results demonstrate characteristic features similar to outlined above. There exist multiple eigenmodes with different growth rates and different localization regions. The most unstable modes tend to localize in the region with higher gradients; however, modes with lower growth rates are present in the whole domain. There are significant differences between the predictions of the local and nonlocal models. This discrepancy is especially important for the modes with low $k_y\,(m)$ and low effective k_x (longer wavelength).

Often, the modes with largest growth rate are thought to dominate the dynamics on the longer time scales. However, in case of complex profiles, different eigenmodes may be localized in different spatial regions, even in regions which are locally stable. For example, in case of Hall thruster profiles there are modes which reside at the middle of the domain, where local model predicts no instability. Some modes propagate from locally unstable regions to locally stable. The anomalous current in these condition is due to the electron convection in the direction of the equilibrium electric field, $\sim \left\langle \widetilde{n}\widetilde{V}_x \right\rangle$ [117]. Then one can estimate the diffusion transport using a mixing length formula, $D_a \simeq \gamma/k_y^2$, where γ is the mode growth rate, k_y is the azimuthal wave number. Hence, significance of multiple modes is especially important for low k_y modes which have the nonlocal character and whose stability criteria could be very different from predictions of the local theory and which provide larger contribution to the anomalous transport ($D_a \simeq \gamma/k_y^2$). These features of nonlocal solutions will be important for nonlinear transport calculations. In view of different stability criteria for multiple modes, especially for low k_y values, the predictions of the local theory may be misleading.

Acknowledgements

Authors thank Ivan Halzov and Winston Frias for help with numerical methods and model formulation. This work was supported in part by NSERC of Canada, US Air Force Office for Scientic Research $FA9550-15-1-0226$. S.R. was partially supported by the Russian Ministry of Science and Education (Minobrnauka), Project No $13.79.2014/K$.

4.5 Summary

In this chapter waves and instabilities, characteristic for Hall plasmas were considered. An overview of negative energy mode instabilities due to the electron $\mathbf{E} \times \mathbf{B}$ drift was presented. Dissipative modes, like ion-sound instability, can be driven by electron-neutral collisions. Gradients of a magnetic field and plasma density serve as additional sources of reactive modes. It is expected that such instabilities play an important role in spoke formation [21, 118].

Nonlocal model for Simon-Hoh instability was presented in the second part of this Chapter. It was shown, that consideration of effects from axial profiles of plasma parameters (electric field, magnetic field, and density) can significantly modify the criteria for instability so that the unstable regions can be different from those predicted by the local theory. This is more pronounced for long wavelength modes, which are considered to be more important for the anomalous current.

The global effects of plasma profiles can be even more important for the interactions between axial and azimuthal modes. As it will be shown in Chapter 8, the azimuthal spoke mode can be suppressed by control of the axial breathing mode. The breathing mode changes the axial profiles of plasma parameters, therefore changing the conditions for the azimuthal Simon-Hoh type modes that are thought to be important for spoke modes.

Chapter 5

On limitations of laser-induced fluorescence diagnostics for xenon ion velocity distribution function measurements in Hall thrusters

5.1 Preface

A Laser-induced fluorescence diagnostic is widely used for studies of plasma, especially in Hall thruster community. This diagnostic allows to obtain spatial and temporal evolution of plasma parameters, and velocity distribution functions for ions or neutrals. This section discusses important limitation of the laser-induced fluorescence technique, which are crucial for investigation of plasmas in Hall thrusters, as they are affected by strong oscillations of plasma temperature and density. These two effect can corrupt data interpretation.

This Chapter is based on a publication: I. Romadanov, Y. Raitses, A. Diallo, K. Hara, and A. Smolyakov, On limitations of laser-induced fluorescence diagnostics for xenon ion velocity distribution function measurements in Hall thrusters, *Physics of Plasmas* 25, 033501 (2018), reproduced here verbatim.

5.2 Abstract

Hall thruster operation is characterized by strong breathing oscillations of the discharge current, plasma density, temperature, and the electric field. Probe and laser-induced fluorescence (LIF) diagnostics were used to measure temporal variations of plasma parameters and the xenon ion velocity distribution function (IVDF) in the near-field plasma plume in regimes with moderate ($< 18\%$) external modulations of applied DC discharge voltage at the frequency of the breathing mode. It was shown that the LIF signal collapses while the ion

density at the same location is finite. The proposed explanation for this surprising result is based on a strong dependence of the excitation cross-section of metastables on the electron temperature. For large amplitudes of oscillations, the electron temperature at the minimum enters the region of very low cross section (for the excitation of the xenon ions); thus, significantly reducing production of the metastable ions. Because the residence time of ions in the channel is generally shorter than the time scale of breathing oscillations, the density of the excited ions outside the thruster is low and they cannot be detected. In the range of temperature of oscillations, the ionization cross section of xenon atoms remains sufficiently large to sustain the discharge. This finding suggests that commonly used LIF diagnostic of xenon IVDF can be a subject to large uncertainties in the regimes with significant oscillations of the electron temperature, or other plasma parameters.

5.3 Introduction

For many low temperature plasma applications with accelerated ions, such as ion sources, plasma thrusters, sputtering magnetrons, material processing devices, the ion velocity distribution function (IVDF) is a key parameter characterizing ion dynamics. For measurements of IVDF, laser-induced fluorescence (LIF) based on the detection of the fluorescence signal from the de-excitation of the metastable state of ions became a standard non-invasive diagnostic technique. Difficulties with interpretation of LIF measurements arise when IVDF oscillates due to unstable behavior of the plasma. In this paper, we demonstrate the limitations of LIF for measurements of IVDF in Hall thrusters. This limitation is due to strong low frequency temperature oscillations that are commonly observed in these plasma devices.

The Hall thruster is a plasma propulsion device in which ions are accelerated by crossed electric and magnetic field applied in a quasineutral plasma with magnetized electrons and non-magnetized ions [7]. The operation of a typical Hall thruster is characterized by two most powerful modes of low frequency oscillations ($\sim$ 10-30 kHz); namely: longitudinally propagating breathing oscillations [119–121] and azimuthal propagating spoke oscillations [64, 103]. Although both these modes are not well understood, it is commonly accepted that the breathing mode is due to ionization instability, while the azimuthal mode is due to a coupling between electrostatic and ionization instabilities. In both modes, plasma properties,

including electron temperature, plasma density and space potential are changing both in time and space. It is believed that these modes are responsible for the anomalous current, which cannot be predicted by a classical collisional mechanism [122]. In the present work, we are focused on the breathing mode, but the main conclusions are applicable to azimuthal oscillations as well.

The breathing mode is usually observed as discharge current oscillations [123]. Depending on the thruster input parameters, including magnetic field, discharge voltage and gas flow rate, the breathing mode may become strong with the amplitude of current oscillations reaching almost 100% of a time-averaged value of the discharge current. The correlation between the amplitude of current oscillations and thruster performance is not so clear, but it is known that high performance regimes are not free of breathing oscillations [76, 124].

Breathing can be synchronized via application of the external modulations of the anode [125–127] or the cathode-keeper voltage [128]. This technique has been used in Time-Resolved Laser-Induced Fluorescence (TR-LIF) diagnostics for studies of breathing [129, 130] oscillations. In contrast, spoke [131, 132] oscillations can be studied without such modulations.

In these previous studies, the modulation amplitude was limited to a few percent of the discharge voltage. In present paper, our goal was to study the effect of strong breathing oscillations on LIF measurements of IVDF by applying the 5-20% modulations (of the discharge voltage).

5.4 Experiment and diagnostic description

The experiments were conducted in the small Hall thruster facility at the Princeton Plasma Physics Laboratory. This facility consists of a 0.5 m^3 vacuum chamber equipped with a turbo-molecular pump and a mechanical pump. A 200 W cylindrical Hall thruster (CHT) with the channel diameter and length of 2.6 cm and 2 cm, respectively, was operated at the applied DC discharge voltage of 220V, using xenon gas. The xenon flows through the anode and the hollow cathode-neutralizer were 3.5 sccm and 2 sccm, respectively. Under such conditions, the background pressure in the chamber did not exceed 70 μTorr. The details of the vacuum facility and CHT are described elsewhere [81, 126]. For the modulation of the discharge voltage, the thruster discharge circuitry has a driving power source (a 200 W

bi-polar Kepco amplifier driven by a functional generator) connected in series with the main 600 W thruster power supply [133].

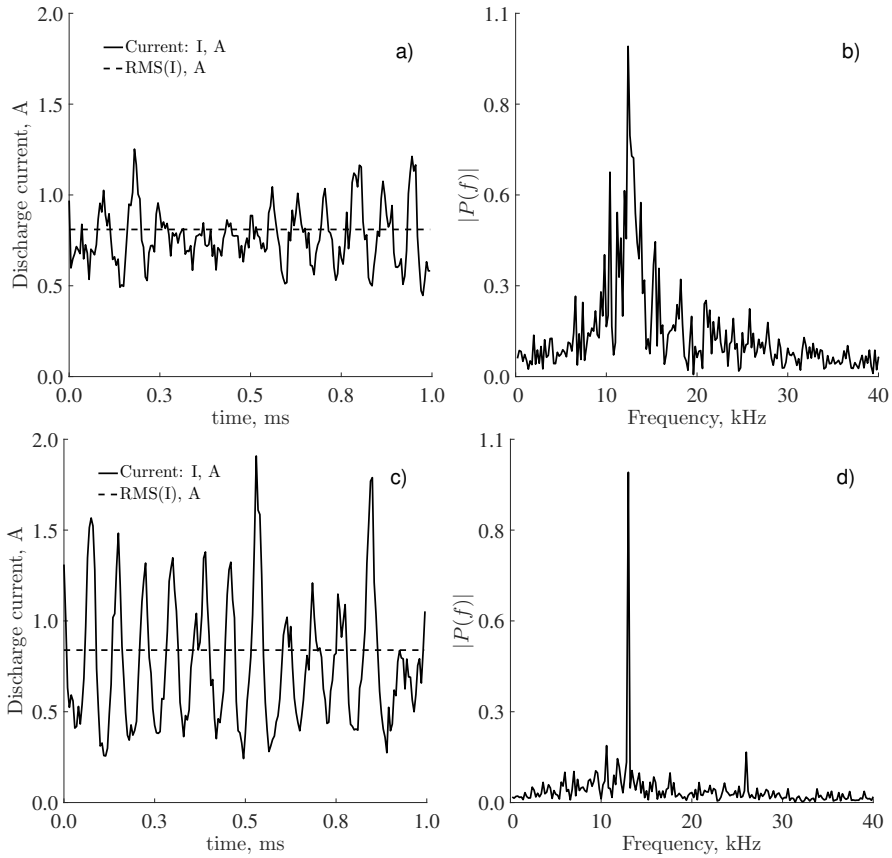

Figure 5.1: Effect of the external drive on the discharge current: (a) discharge current trace without applied driving of the anode voltage, $I_{rms} = 0.81$ A; (b) the corresponding FFT of the discharge current trace, $f_{max} = 12.9$ kHz; (c) discharge current trace with the anode voltage driving at 32 V peak-to-peak amplitude, $I_{rms} = 0.84$ A; and (d) the corresponding FFT of the discharge current trace, $f_{max} = 13.0$ kHz.

For measurements of breathing oscillations, the thruster discharge circuitry includes a low-impedance shunt resistor connected in series between the thruster anode and the modulating power supply. Current oscillations were recorded on oscilloscope and using DAQ board controlled by LabVIEW software simultaneously with the LIF measurements. Under the above thruster operating conditions, the frequency of breathing oscillations without modulation was 13 kHz (Figs. 5.1(a) and 5.1(b)). The modulated voltage was applied with the respect to this DC voltage and with the same frequency as the natural breathing mode (Figs. 5.1(c) and 5.1(d)).

All plasma measurements were conducted in the near-field plasma plume, 1.3 cm from the thruster exit. The following diagnostics were used: LIF for the measurement of IVDF, floating, emissive, and biased probes for the measurement of oscillations of the plasma potential and density, respectively. The LIF diagnostic setup used in these experiments is described elsewhere. The setup is built around a TLB-6917 Vortex^{TM} II laser head. In the described experiments, it probes xenon ions at the metastable level $5d[4]_{7/2}$, which is commonly used for similar thruster studies. For LIF measurements, these ions are excited by the laser to the $6p[3]_{5/2}$ (centered at 834.724 nm; air) level. The de-excitation state is $6s[2]_{3/2}$, leading to a fluorescent signal at 541.915 nm. A majority of existing studies of xenon LIF uses the assumption that dynamics of these metastable ions represents well the dynamics of the whole ion population. However, since this LIF transition scheme is not connected to the ground state of xenon ions, it is more reliable to say that the LIF measures the profile of IVDF.

In order to correlate LIF measurements with the discharge current oscillations, the laser beam can be modulated using an acoustic opto-modulator (AOM). Therefore, emission from the plasma contains two periodic components: one from the discharge current oscillations and another from the fluorescence light. The ion velocity is deduced from the Doppler shift of the signal detected by a PMT with an optical setup that includes a narrow bandpass filter of 2 nm width. In the present work, we measured the axial component of ion velocity, i.e., the laser beam of nm diameter was directed along the axis. The PMT collected light normal to the thruster axis with the focus on the thruster axis. A characteristic size of the collection volume is about 0.5 mm. The signal from the PMT is sent into a lock-in amplifier, which enables the extraction of the LIF component based on homodyne detection technique [2,134].

The plasma density was deduced from measurements of the ion saturation current using a 0.05 cm diameter planar probe biased -40 V with respect to the floating potential. For the emissive probe, a 0.2 cm filament made from a 0.01 cm diameter thoriated tungsten wire was operated in the regimes with a strong electron emission (hot probe) and no-emission (cold probe), respectively. Assuming Maxwellian electron energy distribution function, the plasma potential and the electron temperature were estimated from the measured floating potentials of hot and cold probes using a standard procedure described in Ref. [135,136]. The deduced electron temperature was also used to estimate the ion Bohm velocity and then, the

ion density from the measured ion saturation current collected by the planar probe.

The following procedure of LIF measurements was applied. The excitation of the LIF signal was only applied at certain phases during the discharge modulation. For example, Figure 5.2 shows the discharge current oscillation and laser pulses for two situations when the laser pulse was locked to the maximum and the minimum of the discharge current. This was achieved using a lock-in amplifier which kept a selected phase shift between the AOM-modulated laser beam of the LIF and the modulated thruster discharge voltage. The exposure of the laser beam to the near-field plasma plume was pulsed using the AOM. The pulse duration was ~ 15 μs shorter than the oscillations period ($\sim 75\mu$s). This is in order to minimize changes of the plasma parameters during a short time when LIF measurement is taken. It was found that this pulse duration was sufficient to achieve an acceptable signal-to-noise (not less than 3). Moreover, the frequency of LIF pulses was smaller than the frequency of the current oscillations (Fig. 5.2). This is in order for the lock-in amplifier to distinguish between two periodical components of the signal: one from the background light, and one from the induced fluorescence. Finally, this measurement procedure was repeated over a large number of the current oscillation cycles with these different phase shifts to assure the measurement accuracy.

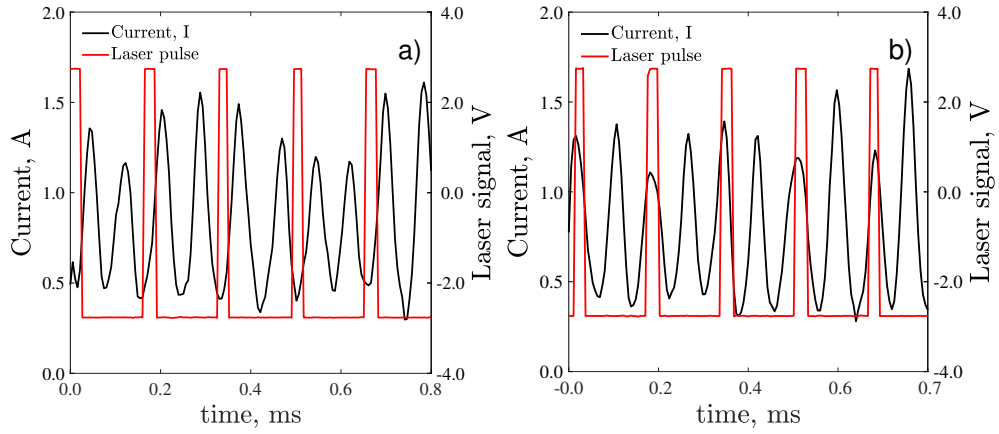

Figure 5.2: Laser pulse locked (a) at the minimum and (b) at the maximum (b) of the discharge current oscillations.

Note that the discharge current path between the anode and the cathode in the near-field plasma plume is unknown. Therefore, there may be a time lag between the oscillations of the discharge current measured in the electric circuitry and the LIF measurements of ion velocities measured in the plume. A rough estimate of the time of flight of ions from the

anode to the location of the LIF measurements: $\tau = L/V_i$, where $L \approx 3$ cm is the ion path from the anode to the location of LIF measurements and $V_i \sim 10^6$ cm/s is the average ion velocity along the path, gives the time lag of 3 μs that is much smaller than the duration of the LIF pulse (15 μs).

5.5 Results and discussion

The results of time-resolving LIF measurements for three different modulating amplitudes are shown in Fig. 5.3. Each figure shows the IVDF profiles measured during the discharge current oscillations and averaged for the maximum and minimum values of the current. For low and moderate amplitudes, 8 V_{pp} and 16 V_{pp} [Figs. 5.3(a) and 5.3(b)], the IVDF centers (or the most probable ion velocities) follow the modulated voltage. For the maximum peak voltage, the most probable velocity is higher than that of the minimum voltage. This result is generally similar to the results reported in Ref. [126]. There are also changes in the peak values of the most probable ion velocity corresponding to the maximum and minimum currents measured at these modulating voltages. However, these changes are insignificant as compared to the results of the large modulating voltage of 32 V_{pp} [Fig. 5.3(c)]. In this regime, the IVDF profile is detected only at the maximum discharge current [see Fig. 5.3(c)], while the LIF signal collapses at the minimum current.

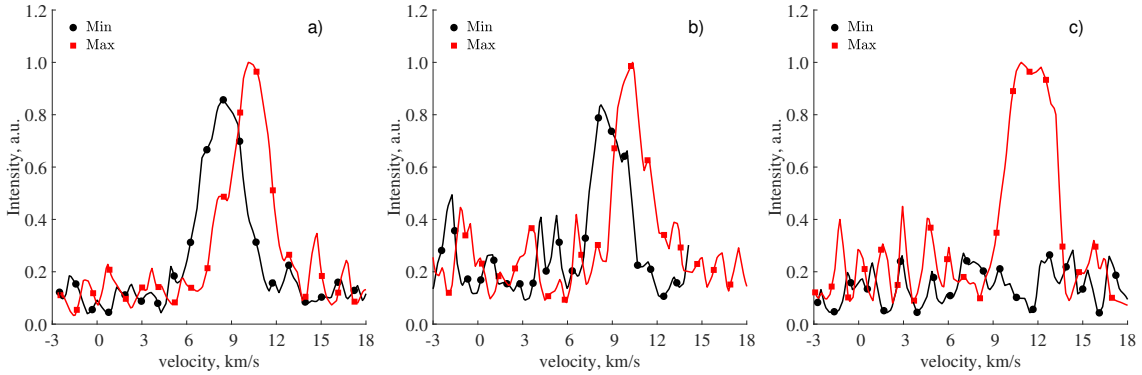

Figure 5.3: Ion velocity distribution functions at the minimum (black circles) and the maximum (red squares) of the discharge at: (a) 8 V_{pp}; (b) 16 V_{pp}; and (c) 32 V_{pp}. Intensities are normalized to the maximum intensity of the LIF signal at the highest point of the discharge oscillations.

This surprising result is in strong contradiction with the probe measurements of the ion

density in the plume (Fig. 5.4). Ions are present during the whole cycle of the discharge current oscillations and their density remain well above the LIF detection limit.

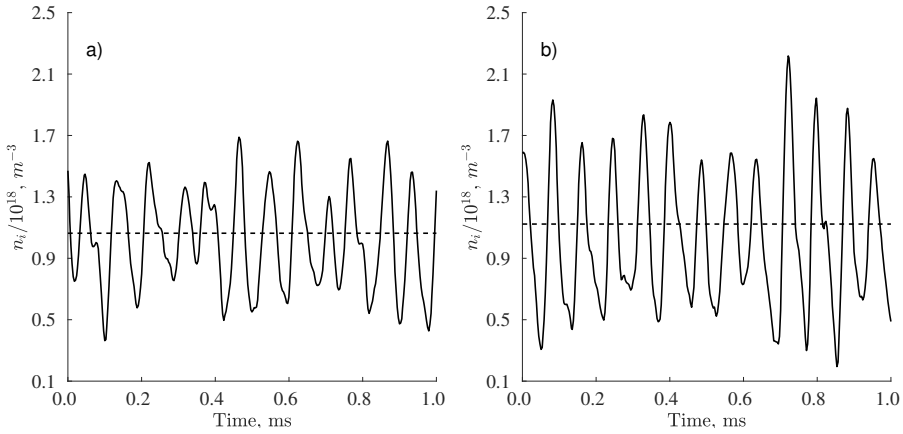

Figure 5.4: Plasma density measurements at (a) 16 V_{pp} and (b) 32 V_{pp} driving voltage amplitude. Dashed line is the RMS value of the density.

One could consider the collapse of the IVDF at the minimum current as a result of a strong outward shift of the ion acceleration region to the near-field plasma plume [137]. However, Fig. 5.5 shows that changes in the accelerating voltage drop are insufficient to explain the collapse of IVDF. Here, the accelerating voltage was estimated as $V_{accel} = V_d \pm V_{pp}/2 - V_{pl}$, where V_d is the discharge voltage and V_{pl} is the plasma potential measured by the emissive probe. Even if changes in the position of the acceleration region would lead to the redistribution between different components of ion velocities, they would not lead to the collapse of IVDF measured in the axial direction. This is because, if the radial component would increase, there would be a distribution closer to zero velocity in axial IVDF which is not observed in experiments.

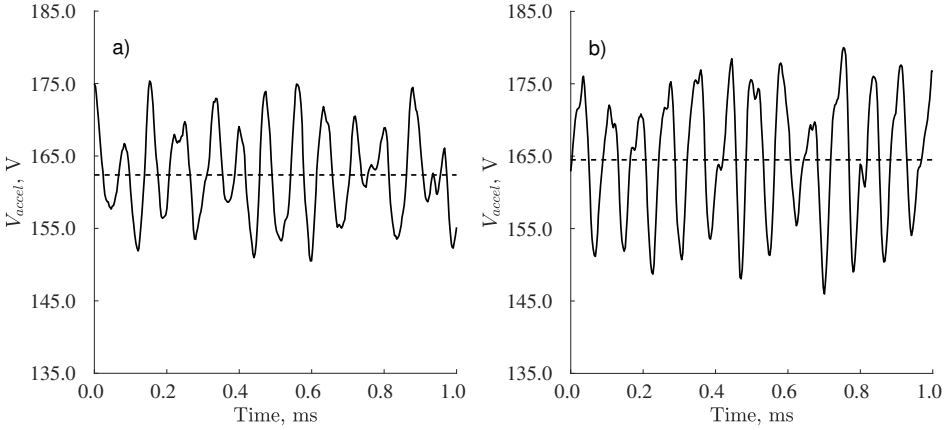

Figure 5.5: Acceleration potential measurements at (a) 16 V_{pp} and (b) 32 V_{pp} driving voltage amplitude. Dashed line is the RMS value of the density.

The current oscillations appear to have a strong effect on the electron temperature, but less effect on the ion density and the accelerating voltage. Figure 5.6 shows a strong increase in the oscillation amplitude of the electron temperature, along with a decrease in the RMS and minimum values. The RMS value dropped from 9.2 eV to 8.3 eV, and the minimum value dropped from 7.4 to 6.3 eV. This decrease is larger than the experimental uncertainty, which is of the order of 1.0 eV.

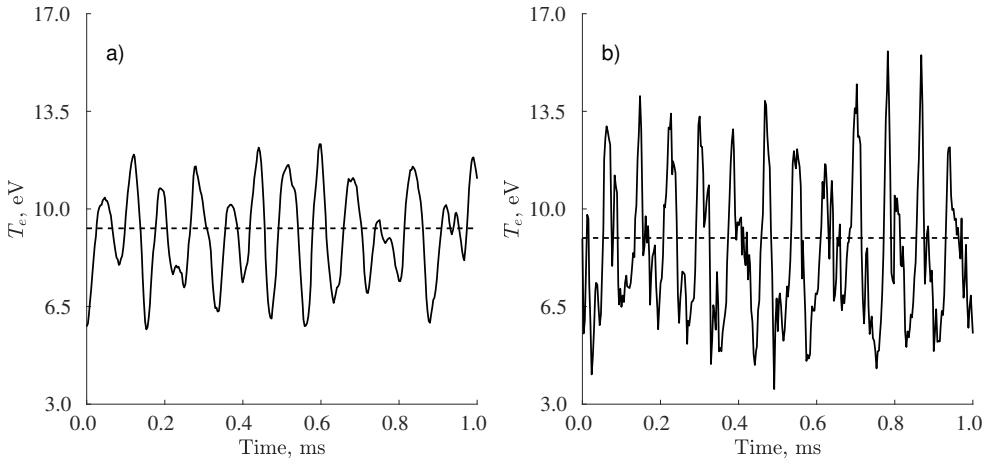

Figure 5.6: Electron temperature measurements at (a) 16 V_{pp} and (b) 32 V_{pp} driving voltage amplitude. Dashed line is the RMS value of the density.

Increase of the amplitude of the electron temperature oscillations from $\sim$ 5 eV to $\sim$ 9 eV (Figs. 5.6(a) and 5.6(b), respectively) provides a clue to the most likely mechanism of the signal loss in the strongly nonlinear driving regime. Our hypothesis is that for large amplitudes of discharge current oscillations, the electron temperature enters the regime of very low excitation cross-sections of xenon ions. Figure 5.7 compares the cross-sections for excitation of xenon ions [138] and ionization of xenon atoms [139]. There is an assumption, that excited metastables mainly are produced from election-neutral collisions, rather than electron-ion collisions, because for typical thruster conditions the density of ions is smaller than the density of atoms (at least an order of the magnitude) and because the cross-section of excitation collisions of ions is much smaller than that of the atoms [140]. In the present experiments, we did not have access to probes to measure the electron temperature inside the thruster channel. However, for the range of the electron temperatures between 20 and 30 eV, which is typical for Hall thrusters, the excitation cross-section shows a sharp drop, while

the ionization cross-section remains significant. Therefore, temperature oscillations in this range would cause a significant drop in the population of density of metastable ions, leading to the loss of the LIF signal, but not the density of ions.

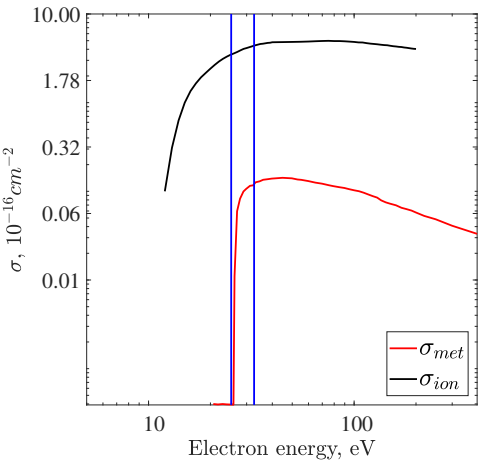

Figure 5.7: Ionization (black) and metastable excitation (red) cross-sections for Xe ions.

Since the residence time of ions ($\sim \mu$s) is much shorter than the time scale of discharge current oscillations (10's of μs), the ions born during the low electron temperature phase corresponding to the small ion excitation cross-sections can escape from the channel without being excited by electrons. These ions are measured by the biased probe, but not detected by the LIF.

5.6 Conclusion

The effects of plasma parameter oscillations on LIF diagnostics in the cylindrical Hall thruster were performed in regimes with the breathing mode. These measurements included LIF detection of the xenon ion VDF and measurement of the electron temperature and ion density in the near field plasma plume of the thruster. We have demonstrated that for a Hall thruster operating with large amplitude discharge current oscillations (100% of the steady-state discharge current) corresponding to a typical strong breathing mode, the collapse of the LIF signal occurs. Our probe measurements show the ion density oscillations can affect the LIF signal, however, the oscillating total ion density remains sufficiently large to sustain the discharge, and well above the LIF detection limit. Thus, oscillations of the ion density alone

cannot explain the observed collapse of the IVDF corresponding to the minimum amplitude of the discharge current oscillations. The proposed explanation of the loss of the LIF signal is that the minimum value of oscillating electron temperature can cross the range corresponding to the sharp reduction of the cross-section for the excitation of ions, while the temperature can still be sufficient to produce ground-state ions. In this situation, the density of metastable ions is too low for such LIF diagnostic to work, even though the total ion density is large in the plasma flow of the thruster and the near-field plasma plume. In this paper, this result has been obtained for the thruster operating with xenon gas, but a similar situation may occur in the thruster operating with other gases. The observed collapse of the LIF signal poses a question about the limitations of the conventional LIF technique for measurements of IVDF in plasma thrusters and other plasma applications where oscillations of the electron temperature can be significant (e.g., sputtering magnetrons, $\mathbf{E} \times \mathbf{B}$ Penning discharges). It is worth noting that the production of metastable ions may also be affected by strong nonlinear oscillations of the plasma density and the electric field [141], which could lead to the modification of the electron distribution function, in particular, the high energy tail. The role in and the relative contribution of the oscillations of the electron distribution function to the production of metastable ions require further experimental and theoretical studies.

Acknowledgements

This work was supported by AFOSR. We acknowledge Scott Keller, Yuan Shi, and Vladislav Vekselman for fruitful discussions, and Alex Merzhevskiy for his technical support.

Chapter 6

Steady-state profiles and oscillations of the axial flows in Hall thrusters

The research, presented in this chapter, was motivated by needs to model breathing modes in Hall thrusters. Generally, it is widely agreed that breathing modes involve the complex nonlinear dynamics of the ionization, ion acceleration, electron mobility, and diffusion. The interaction of these processes determines the steady state profiles as well as spatial and temporal variations of the plasma density, ion velocity, neutral density, and total current.

Fluid models for breathing simulations usually include the ion and electron density conservation (including ionization), ion momentum balance, and the electron flow in drift-diffusion approximation. Dynamics of the electron energy and dependence of the ionization on the electron energy was also considered in a number of works [142–144].

Fluid simulations of the quasi-neutral breathing modes require the imposition of the boundary conditions. Usually, boundary conditions for the ion flow at the anode, and for the electron temperature on the cathode are used. The exact form of such boundary conditions is not obvious a priory and is not clear, either from our previous research or the literature. Both, zero value and the Bohm velocity, were used as boundary condition for the ion velocity at the anode sheath boundary. However, as it was noted earlier [145], there are stationary profiles for the Hall thruster in different anode sheath regimes, suggesting that different boundary conditions may exist at the anode sheath.

Before considering the stability, we have proceeded to the analysis of the conditions and nature of the steady-state profiles in the simplest case of a constant temperature; the approx-

imation, which was often considered previously [146,147]. One-dimensional axial plasma flow in a Hall thruster with ionization, a fixed velocity of neutral injection, and without wall losses, was analyzed. It was shown that in this situation regularization of the sonic point transition can be done analytically, resulting in relatively simple constraints for operational parameters and existence of steady-state solutions. The presence of the regularized sonic point makes steady-state plasma profiles rather stiff; therefore, the range of boundary conditions, where the solutions exist, may be limited. The operational space of the system parameters (total current, neutral flux, and plasma density) was investigated and was shown to have a quite complex structure.

It was conjectured further that oscillations may occur for two different reasons: the steady-state profiles with a given set of boundary conditions are not stable, leading to oscillations; or the boundary conditions, imposed on the system, are incompatible with the existence of globally steady solutions and the system oscillates, trying to re-adjust itself to "wrong" boundary conditions. We have performed time-dependent simulations with the obtained steady-state profiles as initial conditions. Steady-state regimes with and without oscillations were found and oscillation regimes of different nature (strongly coherent vs. multimode) were identified, depending on the operational parameters of the discharge.

6.1 Basic model for one dimensional axial flow

Breathing mode in Hall thrusters is one of the most prominent and violent modes, which can be observed as oscillations of the discharge current with an amplitude up to 100 % of the DC current level and which may lead to the discharge termination. The breathing mode has attracted a lot of attention in the past, and a number of numerical models were developed and tested. Among early works trying to explain the its oscillation mechanism was a 0D model by J. M. Fife and M. Martinez-Sanchez [120], which is based on classical Lotka-Volterra equations where plasma plays the role of predators and neutral particles play the role of preys. However, this model is too simplistic and does not include many important processes. Subsequently, 1D models have been used and studied extensively due to their relative simplicity and more realistic assumptions.

Such models have been used to study both stationary plasma flow [142,147–149] as well

as low-frequency axial oscillations. There are several types of time-dependent models: hybrid (where ions treated with a kinetic approach, and electrons are treated with fluid equations) [140, 150] and fluid for both species [8, 144, 151]. Some comparison between a fluid and kinetic simulations is presented in Ref. [151]. It is important to notice that the predator-prey oscillations are always damped in 1D case, as it was shown by K. Hara [121].

In this Chapter, the main focus is on the semi-analytic analysis of the steady-state plasma flow at given values of the discharge current I_D and the neutral flux J_a. The properties of obtained solutions were investigated in J_a and I_D operational space. Time-dependent simulations were conducted, and the stability of the obtained profiles was considered. Stationary profiles were considered also in a number of previous studies [147–149], where the role of a singular point was discussed. However, the constraints imposed by the regularity condition were not analyzed in general form.

The general one-dimensional scheme for the time evolution of plasma parameters along the axial direction x, used in our model and simulations, is presented in Fig. 6.1.

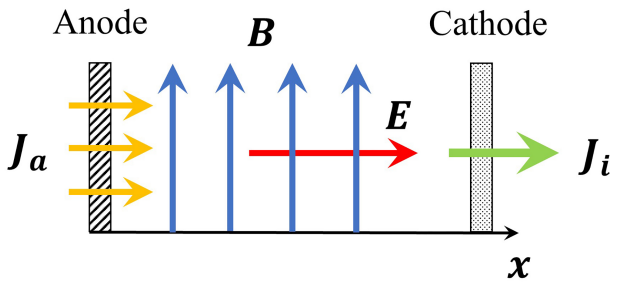

Figure 6.1: Scheme of the Hall thruster. Here B is the magnetic field, E is the electric field, J_a is the mass flux through the anode, J_i is the ion current flux.

The model includes continuity equations for the plasma density $n(x,t)$ and the neutral density $N(x,t)$, the ion momentum $v_i(x,t)$ equation, and the electric field E (obtained from the Ohm's law)

$$\frac{\partial N}{\partial t} + v_a \frac{\partial N}{\partial x} = -\beta N n, \tag{6.1a}$$

$$\frac{\partial n}{\partial t} + \frac{\partial}{\partial x}\left(n v_i\right) = \beta N n, \tag{6.1b}$$

$$\frac{\partial v_i}{\partial t} + v_i \frac{\partial v_i}{\partial x} = \frac{e}{m_i} E + \beta N \left(v_a - v_i\right), \tag{6.1c}$$

$$E = \frac{J_T}{en\mu_e} - \frac{v_i}{\mu_e} - \frac{1}{en}\frac{\partial T_e n}{\partial x}, \tag{6.1d}$$

where β is the ionization rate, μ_e is the electron mobility perpendicular to the magnetic field, v_a is the neutral flow velocity, T_e is the electron temperature. These equations imply quasi-neutrality $n_i = n_e = n$. The diffusion term $\frac{1}{en}\frac{\partial T_e n}{\partial x}$ in Ohm's law is important to describe the plasma flow in the anode region and results in the sonic point singularity.

The electron mobility μ_e is given by the classical expression for collisional transport in the transverse magnetic field:

$$\mu_e = \frac{e}{m_e \nu_m} \frac{1}{1 + \omega_{ce}^2/\nu_m^2}, \tag{6.2}$$

where $\omega_{ce} = eB/m_e$ is the electron cyclotron frequency and ν_m is the total electron momentum exchange collision frequency. In general, ν_m is

$$\nu_m = \nu_{en} + \nu_{walls} + \nu_B, \tag{6.3}$$

where ν_B is the anomalous cross-field transport due to field fluctuations and ν_{walls} is the collision frequency with walls. However, in this work, classical value of the electron mobility was used.

The plasma parameters typical for the cylindrical Hall thruster, were used for simulations. Electron temperature T_e was taken constant along the channel, what implies that the ionization rate coefficient β is constant as well. All parameters are summarized in the Table 6.1.

Table 6.1: Typical plasma parameters in CHT

Parameter	Value
Gas	Xe
Channel length, L	3.0 cm
Channel radius, R	1.2 cm
Channel area, S	4.5 cm^2
Mass flow, $\dot{m}$	0.34 mg/s
Electron temperature, T_e	20 eV
Ion sound, c_s	3833 m/s
Neutral velocity, v_{a0}	156 m/s ($T = 400$ K)
Electron-neutral collisions, ν_{en}	10^6 s^{-1}

Electron mobility, μ_e	2.6639 m^2/Vs

The full time-dependent model, given by equations (6.1), should be solved numerically as an initial value problem with certain set of boundary and initial conditions.

Our initial experience with this system was that the solutions can be very sensitive to the choice of boundary conditions and it is not always possible to solve it for an arbitrary choice of initial/boundary conditions. Therefore, we have proceeded to studies of the stationary solutions first and then investigated the stability of the obtained solutions.

6.2 The steady-state flow solutions and regularization of the sonic point transition

Stationary solutions can be obtained from the system (6.1) by setting all time derivatives to zero. Therefore, the system of stationary equations is written as follows

$$v_a \frac{\partial N}{\partial x} = -\beta N n, \tag{6.4a}$$

$$\frac{\partial}{\partial x}(n_i v_i) = \beta N n_i, \tag{6.4b}$$

$$v_i \frac{\partial v_i}{\partial x} = -\frac{e}{m_i}\frac{d\phi}{dx} + \beta N (v_a - v_i), \tag{6.4c}$$

$$\frac{d\phi}{dx} = -\frac{J_d}{e n_i \mu_e} + \frac{v_i}{\mu_e} + \frac{1}{e n_i}\frac{\partial T_e n_i}{\partial x}, \tag{6.4d}$$

where the discharge current flux is $J_d = n_i v_i - n_e v_e$, and the neutral density N can be deduced from the equation $N = \dfrac{\dot{m}}{M_i v_a A} - \dfrac{n_i v_i}{v_a}$. The mass flux is defined from the latter equation as $Ja = \dfrac{\dot{m}}{M_i A}$. The above system of equations can be re-written as

$$n_i v_i' + v_i n_i' = -\beta N n_i + \nu_w n_i, \tag{6.5a}$$

$$v_i v_i' \frac{e}{m_i}\frac{d\phi}{dx} - \beta N (v_a - v_i) = 0, \tag{6.5b}$$

$$\phi' + \frac{J_d}{e n_i \mu_e} - \frac{v_i}{\mu_e} - \frac{T_e}{e n_i} n_i' = 0, \tag{6.5c}$$

where $\phi' = \partial\phi/\partial x$, $v_i' = \partial v/\partial x$, $n_i' = \partial n/\partial x$. From this a set of three ordinary differential equations for v_i', n_i', and ϕ' can be derived

$$v_i' = -\frac{1}{c_s^2 - v_i^2}\left(v_i \frac{J_d - n_i v_i}{\mu_e n_i} - \frac{J_a - n_i v_i}{v_a}\beta(c_s^2 + v_i^2 + v_a v_i)\right), \tag{6.6a}$$

$$n_i' = \frac{1}{c_s^2 - v_i^2}\left(\frac{J_d - n_i v_i}{\mu_e} + \frac{J_a - n_i v_i}{v_a}\beta n_i (v_a - 2v_i)\right), \tag{6.6b}$$

$$\phi' = \frac{1}{c_s^2 - v_i^2}\left(v_i^2\frac{J_d - n_i v_i}{\mu_e n_i} + \frac{J_a - n_i v_i}{v_a}\beta c_s^2 (v_a - 2v_i)\right), \tag{6.6c}$$

where $c_s^2 = T_e/m_i$. As one can see, this system contains two parameters, which define the operational space: J_d and J_a. If they are given, one can integrate these equations numerically with a proper set of boundary conditions for ion density n_i and ion velocity v_i at the anode sheath. However, it is clear that there is a discontinuity at $v_i = \pm c_s$, and the special treatment at the sonic point is required.

The flow acceleration from the subsonic to supersonic regimes (via the sonic point) in Hall thrusters is similar to the gas acceleration in the Laval nozzle. This transition must be smooth and no discontinuities in plasma parameters are expected at this point for regular solution [146]. The smooth transition requires the RHS of the equations (6.6) to be zero at the sonic point. As it will be shown below, this condition makes the solution from the anode to the cathode stiff and restricts the possible choice of boundary conditions.

In this work, we assumed that the sheath is formed at the anode. This requires the Bohm criterion to be satisfied, meaning that ions should be accelerated to the sound velocity toward the anode [12] so there is a negative ion flow in the system near the anode. Thus, we expect the ion velocity profile to increase from the $-c_s$ to c_s at the sonic point and then to a supersonic velocity at the thruster exit. The ion density n_i is expected to have a maximum between the anode and c_s point at ion velocity $v_i = 0$. Ion density will gradually decrease in the supersonic region. The potential ϕ is expected to drop in both directions from the sonic point: to the anode, to ensure the sheath formation, and to the cathode, to accelerate ions. As it was discussed previously, in general, various regimes of anode sheath possible. Therefore, in addition to the Bohm condition $-c_s$, we also allow for values $v_i > -c_s$ at the anode sheath boundary.

The ion velocity at the sonic point is known ($v_i = c_s$), value for the potential can be set to 0 (the only constraint on potential is the potential difference between the anode and the cathode), and there is a condition for RHS of Eqs 6.6 to be zero. By using this information, values of n_i and derivatives for density, potential and ion velocity can be determined at the

sonic point by the expansion. After this, profiles can be reconstructed by simple integration from the sonic point in both directions: to the anode and to the cathode. The only remaining free parameter is the potential difference, which has to be selected to be consistent with the discharge length.

Let's describe this procedure in more detail. Equations from the system (6.6) can be represent in a form of $(F_1, F_2, F_3)/D$, where F_1, F_2, F_3 are corresponding numerators, and denominator $D = c_s^2 - v_i^2$, which is 0 at the sonic point. For smooth transition all functions $F_1 = F_2 = F_3$ should be equal to 0 at this point as well. From the condition $F_i = 0$, and by substituting $v_i = c_s$ an equation for the ion density at the sonic point ($n_i = n_s$), as a function of J_d and J_a is obtained. It is important to note that all three functions F_1, F_2, and F_3 reduce to a single equation at a sonic point

$$\beta\mu_e c_s(v_a - 2c_s)n_s^2 + (c_s v_a + \beta\mu_e J_a(2c_s - v_a))n_s - J_d v_a = 0. \tag{6.7}$$

This is a quadratic equation, which gives two values of n_s for given values of J_a and J_d. The detailed investigation of the roots of this equation will be given below. At the sonic point, the equations (6.6) have 0/0 singularity which can be resolved by applying the L'Hospital's rule

$$\lim_{v_i \to c_s} \frac{F}{D} = \frac{dF/dx}{dD/dx}. \tag{6.8}$$

After taking the derivatives from F_1, F_2, and F_3 and substituting $v_i = c_s$ and $n_i = n_s$ one can obtain the following equations for v_i' and n_i'

$$v_i'^2 - \frac{v_a n_s(J_d - 2c_s n_s) + \beta\mu_e n_s^2(2c_s n_s - J_a)(2c_s - v_a)}{2\mu_e v_a c_s n_s^2} v_i' - \frac{\beta\mu_e c_s^2 n_s^2(2c_s - v_a) - J_d c_s v_a}{2\mu_e v_a c_s n_s^2} n_i' = 0, \tag{6.9a}$$

$$n_i' = \frac{v_a n_s(1 + \beta\mu_e n_s) + 2\beta\mu_e n_s(J_a - 2c_s n_s)}{(c_s v_a + \beta\mu_e(J_a - 2c_s n_s)(v_a - 2c_s) + 2c_s\mu_e v_a v_i')} v_i'. \tag{6.9b}$$

The value of ϕ' can be obtained from the Eq. 6.6c after n_i and v_i are known. The equation for v_i' is a quadratic equation as well, so two roots of v_i', n_i' and ϕ' are possible for each value of n_s.

It is interesting to note, that if the same approach is used for $-c_s$ point, values of n_s become negative, therefore the negative sonic point cannot be made regular.

The described procedure allows for the calculation of all variables, which are necessary for the integration. However, the real solutions for n_s, v_i', n_i' and ϕ', exist only in a certain range of the values of J_a and J_d, which can be easily found from the quadratic equation.

6.3 Operational space diagram and steady state solution

In this section examples of n_s, v_i', n_i', and ϕ' diagrams, calculated for parameters from the Table 6.1, are given. For each value of n_s, the v_i', n', ϕ' derivatives are calculated, and stationary solutions were obtained by the integration from the sonic point in both directions: to the anode and to the cathode. Integration was done by using a 4th order Runge-Kutta method in two directions from 0 to $-L$ and from 0 to L, where 0 is the location of the sonic point. When integration was done in a negative direction, it was stopped after the ion velocity reached $-c_s$ value, so the solution is obtained over the interval X larger than the thruster length L. By selecting the interval of the given length L, various possible solutions with different values of the potential difference across can be defined. Selecting both the length L and the potential difference will define a unique solution.

Different types of the solution of Eq. 6.7 are presented in Fig. 6.2a as a function of I_d, at a fixed value of J_a. For values of the total current smaller than some maximum value, equation 6.7 has two roots: high density and low density branches. However, not all solutions are possible. For some values, the corresponding values of the velocity, density and potential gradients become complex. It can be seen in figures 6.2(b-d) obtained from Eqs 6.9a. These regions are shown by dashed-green line in Fig. 6.2 (and in zoomed-in and rescaled figure 6.5). Three different points "A", "B" and "C" in n_s diagram were chosen to illustrate different types of solutions; they are shown in Figs. 6.2(b-d) with subscripts.

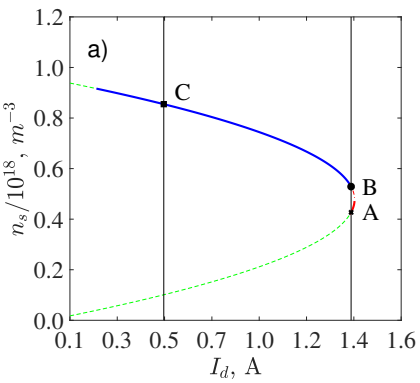

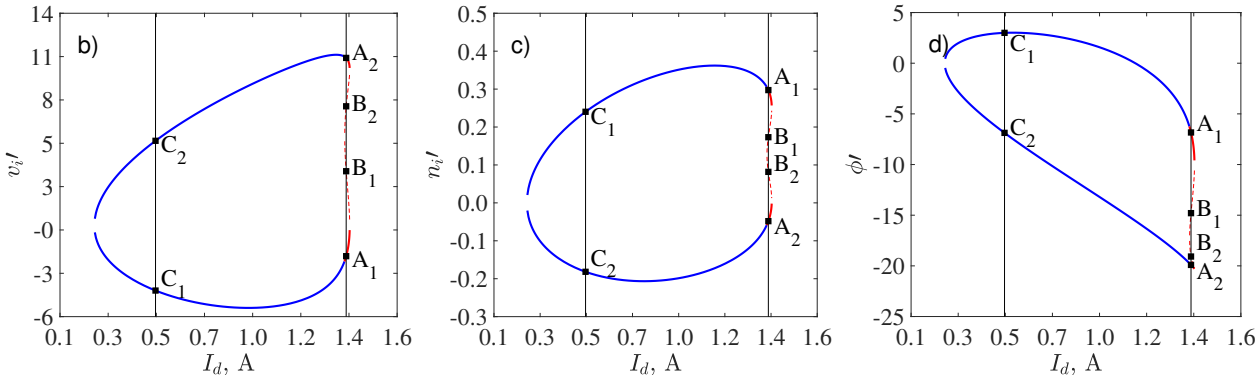

Figure 6.2: Diagrams of a) n_s; b) v_i'; c) n_i'; d) and ϕ' as functions of the discharge current I_d at fixed value of J_a. Three n_s roots "A", "B" and "C" were chosen to illustrate different solutions.

The high density "n_s" root "C", corresponding to low current I_d, generate two different real roots for v_i', n', and ϕ' - "C_1" and "C_2". The profiles of the ion velocity, density and potential for these roots are shown in Fig. 6.3. As one can see, the velocity for the "C_2" root is decelerating and is of no interest for ion thrusters. The v_i profile for "C_1" root shows supersonic ion acceleration with possible $-c_s$ value at the anode sheath boundary.

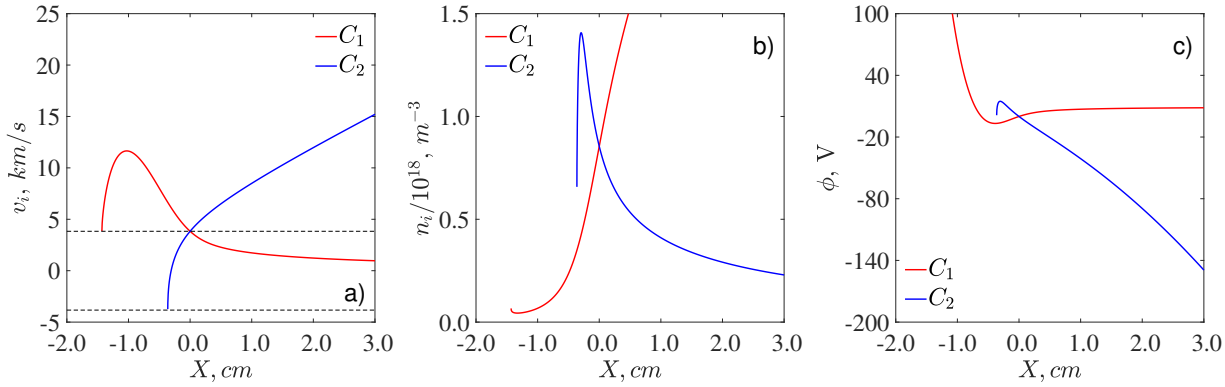

Figure 6.3: Profiles of a) v_i (dashed lines – $\pm c_s$); b) n_i; c) and ϕ for root "C".

The situation with for "A" and "B" roots, for the discharge current values close to the maximum, is more complex, as shown in Fig. 6.4 (see also rescaled Figs. 6.5 and 6.6). There are four different solutions in this case. Two solutions, corresponding to the root "B" are not compatible with the anode sheath, as the velocity does not go to $-c_s$. For the root "A", there are two solutions, one of them corresponds to the supersonic ion acceleration, similar to one of the "C" root.

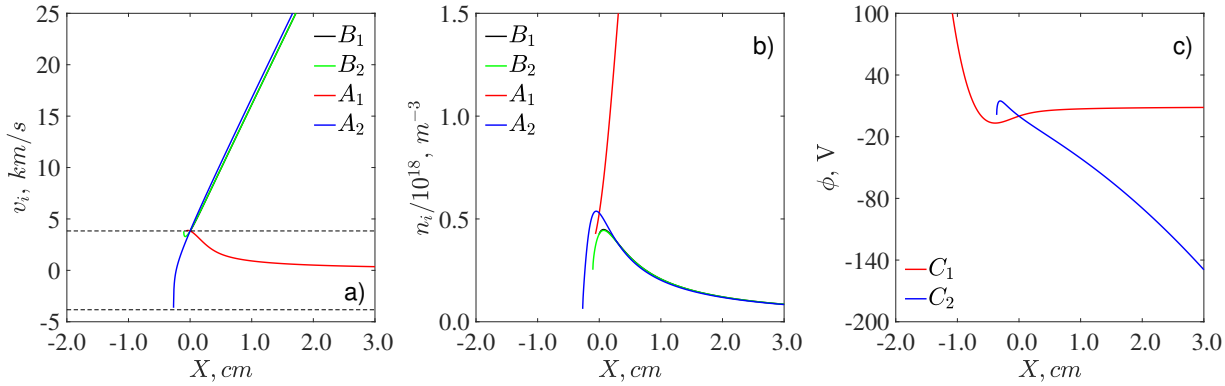

Figure 6.4: Profiles of a) v_i (dashed lines – $\pm c_s$); b) n_i; c) and ϕ for roots "A" and "B".

Therefore, for each value of the discharge current I_d at a fixed value of the mass flow J_a, there is only one set of n_s, v_i', n', and ϕ' which provides a solution with expected ion acceleration.

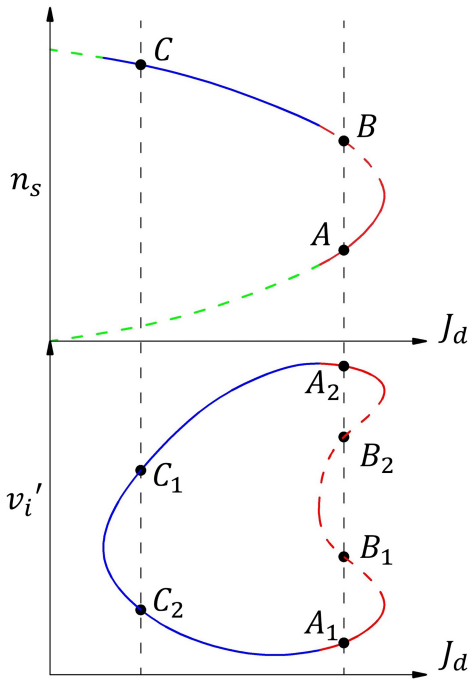

Figure 6.5: Diagrams for n_s (top) and v_i' (bottom) as functions of the discharge flux J_d at a fixed value of J_a, not to scale: Dashed-green – no real solutions. Solid blue – two roots, one of which is the expected solution corresponding to the ion acceleration. Red (dashed and solid) – the regions with four solutions, only A_2 root corresponds to the accelerating solutions.

From previous description it is clear that for the given value of the mass flux J_a there exist a range of the discharge fluxes J_d, where it is possible to find a solution with accelerating ions; for some range of J_a and J_d values, there are no solutions. Part of the diagram marked with red color corresponds to the n_s range where there are four roots of v_i'. Two roots "$B_{1,2}$", corresponding to the point "B", have the non-monotonic velocity profiles with two c_s points, which is not possible in case of a pre-sheath region near the anode with the negative ion flow. For the point "A", there are two monotonic solutions, of which "A_2" produces a profile with supersonic acceleration and which can be matched to the anode sheath.

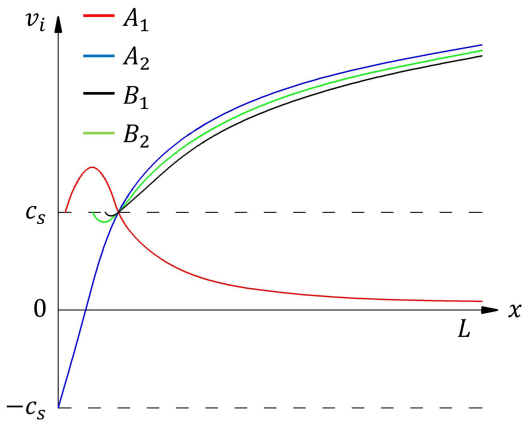

Figure 6.6: Velocity profiles for roots "A" and "B"; not to scale.

6.4 Potential difference across the discharge and boundary conditions

As it was stated before, for each set of J_a and J_d there is only one combination of n_s, n_i', v_i', and ϕ' which gives a physically sound solution. Integration of Eqs. 6.4 from the sonic point with proper values of n_i, v_i, ϕ and their derivatives results in density, ion velocity, and potential profiles from which a unique solution can be obtained by applying a constraint on the fixed voltage drop across the given thruster length L.

In general, different values of the ion velocity (different from Bohm condition, $v_i = -c_s$) at the left boundary can be used. Then, the potential differences can be determined as a function of the position of the left boundary. Fig. 6.7 shows the potential difference $\Delta\phi$ across the length L as a function of the position of the left boundary for roots "A_2" and "C_2". Boundary conditions for ion velocity at the left boundary can be in a range $v_i > -c_s$.

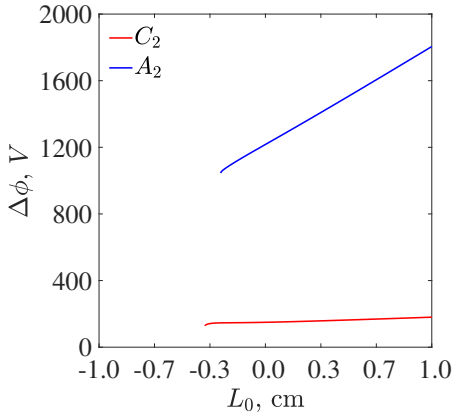

Figure 6.7: Potential difference $\Delta\phi$ at length L, as a function of initial position L_0 for roots "A_2", "C_2" as calculated from profiles in Figs 6.3 and 6.4.

Examples of the profiles with Bohm condition $v_i = -c_s$ at the left boundary are shown in Fig. 6.8. The ion velocity, density, and potential difference are shown as a function of the discharge length.

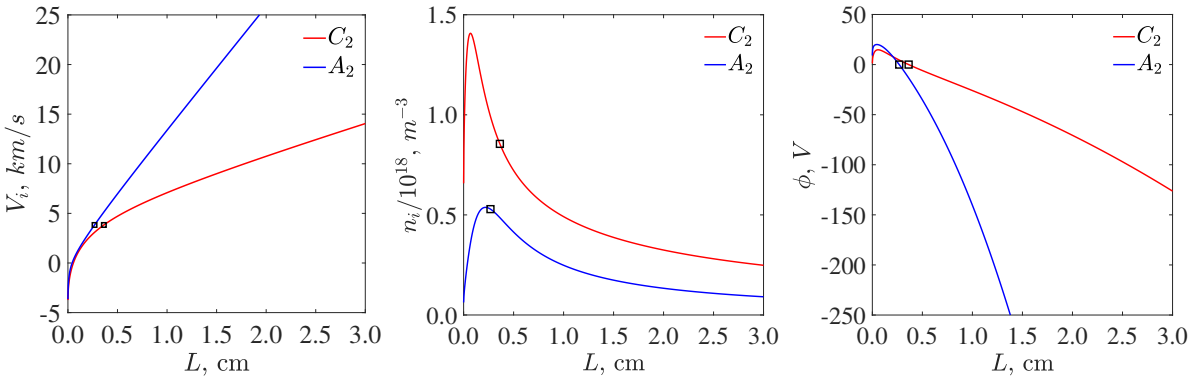

Figure 6.8: Profiles of (from the left to the right) v_i, n_i, ϕ for roots "A_2", "C_2". Squares represent position of the sonic point for each case.

Boundary conditions for two selected profiles with $v_i = -c_s$ are summarized in Table 6.2. These profiles will be used as the initial conditions for the time-dependent simulations. Note that the values of v_i shown in Table 6.2 are slightly different from the exact value of the c_s as we had to stop integration before reaching the exact value, because of the singular nature of the velocity profile at the left boundary.

Table 6.2: Boundary conditions (BC) on the anode sheath from profiles in Fig. 6.8

Profile	v_i, m/s	$N_n \cdot 10^{19}$, m^{-3}	$n_i \cdot 10^{18}$, m^{-3}	$\Delta\phi$, V	μ_e	I_d
C_2	-3828	3.769	0.691	-113.5	2.66	0.50

A_2	-3807	2.211	0.009	-1063.7	2.66	1.39

The procedure, described in this section, summarizes the method of obtaining the stationary profiles of plasma parameters and an appropriate set of boundary conditions at the anode sheath, which can be used for time-dependent simulations. Examples of such simulations are presented in the next section.

6.5 Time-dependent simulations for different regimes

In this section, we study the stability of obtained stationary profiles in time-dependent simulations. Only profiles with Bohm boundary condition at the left boundary, $v_i = -c_s$, are considered. Time-dependent simulations were performed where the obtained stationary profiles (with corresponding boundary conditions) were used as an initial state. The time history of the discharge current and characteristic frequency were followed.

The main results of these simulations are outlined in the diagram Fig.6.9. Roots, corresponding to different values of J_d, resulted in profiles with different behavior. Detailed description is given below.

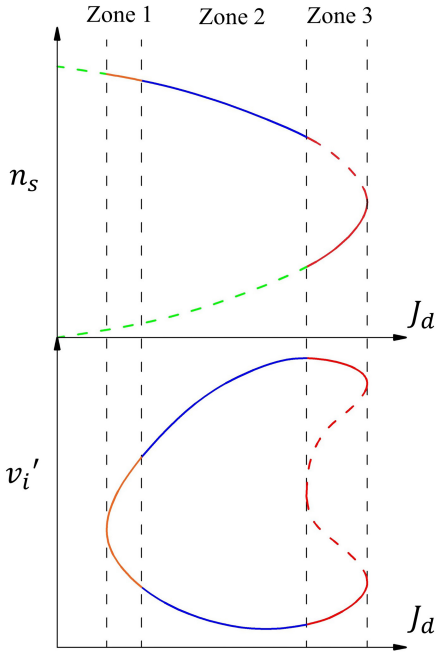

Figure 6.9: Stability diagram of stationary solutions in the n_s/v_i', J_d space at a fixed value of J_a. In Zone 1 (orange solid), there are no oscillations. In Zone 2 (blue solid), there exist strongly coherent oscillations. In Zone 3 (red solid and dashed), the multimode oscillations are present.

It was found that for lower values of the discharge current (Zone 1) the stationary profiles remain stable and there are no current oscillations in this region. The discharge current oscillations appear for values of J_d from Zone 2. It is important to note that the nature of oscillations, as well as their amplitude and frequency, changes as the value of J_d increases. At the beginning of the Zone 2, for lower values of J_d, the oscillations have small amplitude and frequency (see Fig. 6.10a, b) and have well pronounced single frequency (see Fig. 6.10a, d). When we move closer to the end of Zone 2, oscillations amplitude and frequency grow. In Zone 3, there is a transition to multimode oscillations (see Fig. 6.10b, e) with further increase of amplitude and frequency. At the end of Zone 3 oscillations amplitude reaches its maximum, however, oscillations become strongly non-linear with an abrupt drop of the frequency.

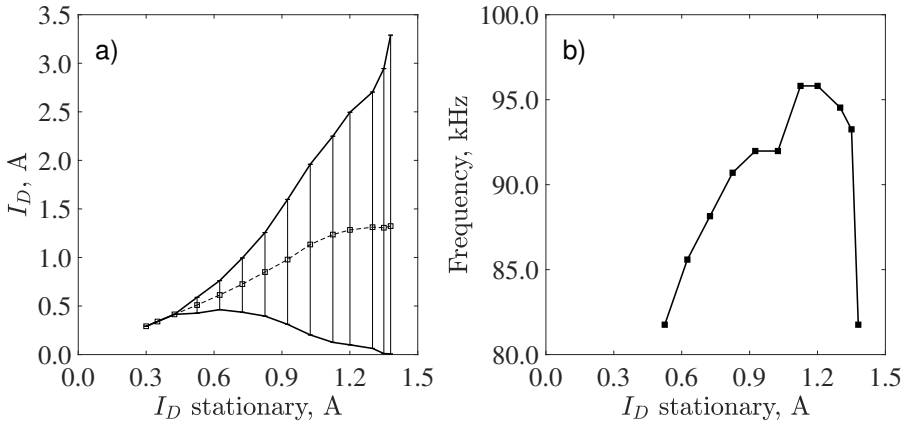

Figure 6.10: a) Maximums and minimum of the oscillation amplitude (solid lines) as a function of the discharge current set for stationary solutions. Red line is for comparison, between linear and nonlinear regions. b) Oscillation frequency as a function of the discharge current set for stationary solutions.

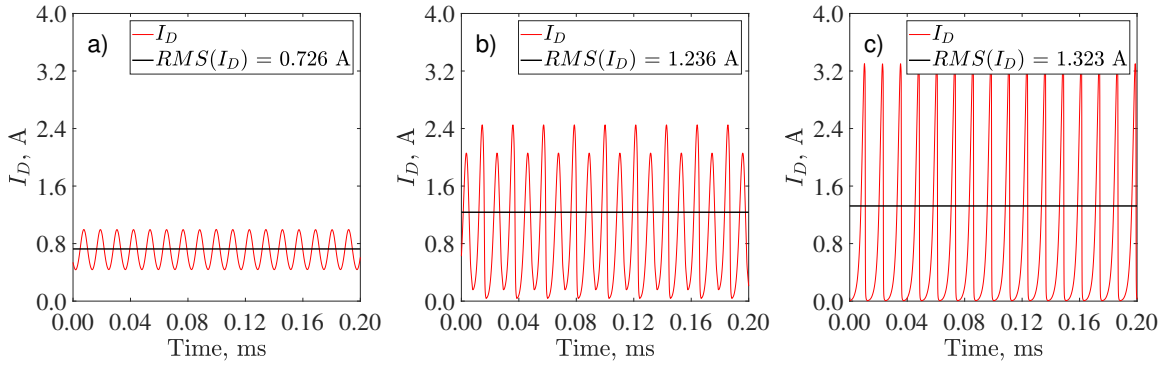

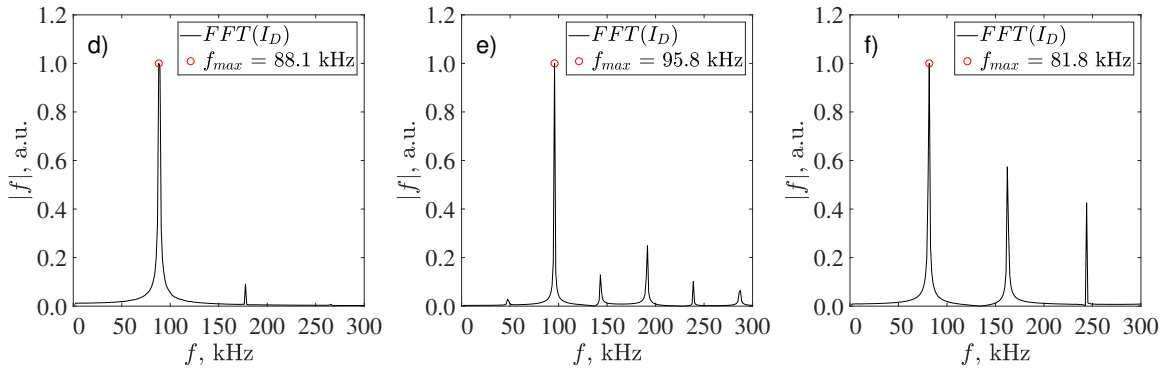

Figure 6.10: Discharge current traces (a-c) and Corresponding spectra (d-f) for different values of I_D.

6.6 Summary

In this Chapter, the procedure to obtain stationary solutions for plasma flow in Hall thrusters was discussed. This requires finding values of plasma density n_s and values of derivatives v_i', n', and ϕ' at the sonic point. It was shown that dependency of these values on operational space parameters J_d, J_a has complex structure and different types of stationary profiles can be obtained. For the given values of the mass flow and the discharge current, there exists only one set of n_s, v_i', n', and ϕ' which produces the physically reasonable solution.

Integration from the sonic point to the anode and to the cathode results in generic plasma parameters curves. Plasma parameters profiles can be obtained from these curves by fixing a given value of the potential difference $\Delta\phi$. This procedure will be used in Chapter 7 in order to get initial profiles and boundary conditions for time-dependent simulations with externally driven potential.

Stability analysis with time-dependent simulations was done for profiles corresponding to different values of the discharge current I_D. When the discharge current grows, the nature of oscillations changes. The states with no oscillations change to the state with single mode (coherent) oscillations, and then to states with multimode oscillations, and finally, when the discharge current is at about its maximum value, the oscillations become non-sinusoidal. This behavior is similar to the one observed in other work [121] and in our experiments.

For further work on this problem, it would be informative to investigate the system response on boundary conditions incompatible with stationary solutions. Parametric investigation of profiles stability on J_a, μ_e, etc. would also provide valuable insights.

Chapter 7

Hall thruster operation with externally driven breathing mode oscillations

7.1 Preface

This chapter is dedicated to investigation of effect of external modulations of the anode potential on the thruster efficiency. External modulations were implemented on the same way as in previous Chapter 5 and discussed there in Section 5.4. It was found that the total increase of propellant and current utilizations can be as high as 20%. This results were supported by the fluid simulations, conducted in BOUT++ framework.

This Chapter is based on a publication: I. Romadanov, Y. Raitses, and A. Smolyakov, Hall thruster operation with externally driven breathing mode oscillations, *Plasma Sources Sci. Technol.* 27, 094006 (2018), reproduced here verbatim.

7.2 Abstract

The discharge and plasma plume characteristics of the cylindrical Hall thruster were studied in regimes with external modulations of the applied voltage. It is found that the amplitude and the root-mean-square (RMS) value of the discharge and ion currents increase with the amplitude of the external modulation exhibiting two different regimes. For smaller amplitudes of the modulation voltage, the oscillations amplitude and RMS value of the discharge and ion currents follow the amplitude of modulations approximately linearly. For larger voltage modulations, the amplitude and the RSM value of the discharge and ion currents grow faster and nonlinearly. In the non-linear regime, the discharge and the ion currents demonstrate pronounced dependence on the frequency of the external modulations. Moreover, the RMS

value of the ion current is amplified stronger than the RMS value of the discharge current resulting in an increase of the current utilization (of about 5%) and the propellant utilization efficiencies (of about 40%). The thruster efficiency, defined as a product of the current and propellant utilization coefficients, shows an increase of the about 20%. We also present the results of theoretical modelling of a plasma response to driven oscillations in a simplified 1D model of resistive-ionization mode in quasineutral plasma. This modelling demonstrates the nonlinear property of the fundamental breathing mode similar to the experimental results.

7.3 Introduction

Hall thrusters are satellite propulsion devices, which accelerate the plasma in applied crossed electric and magnetic fields. The description of the design, and operation characteristics can be found elsewhere (see, for example Refs. [7, 16, 47]). A typical Hall thruster is powered by a DC power supply operating in voltage regulated mode. Since the voltage is kept constant, the thruster exhaust velocity, V_{ex}, or specific impulse $I_{sp} = V_{ex}/g$, where g is the gravity is assumed to be constant as well. Despite DC input power, Hall thruster operation is often a subject to low-frequency oscillations [152] of the discharge current or so-called breathing oscillations, which have characteristic frequency about 10-20 kHz [140,153]. These oscillations can be very powerful with almost 100% of the steady-state values of discharge current and are usually non-stationary and semi-coherent in time. Such strong oscillations may result in unstable thruster operation and cause degradation of the thruster performance, and the reduction of the thruster lifetime [65, 137, 154, 155]. The physical mechanism responsible for breathing oscillations is usually attributed to some sort of ionization instability [121,144,156].

Since the introduction of the Hall thruster concept in late 60's of the last century, many studies and developments were focused on understanding and mitigation of breathing oscillations. In the present work, we explore an approach to control breathing oscillations by modulating the applied voltage. In our recent studies, we already demonstrated this approach with application to time-resolved laser-induced fluorescence diagnostic [133]. The applied voltage was externally modulated by adding a sinusoidal voltage component to the anode potential. These studies revealed a non-linear response of the ion velocity distribution function (IVDF) to the voltage modulations. In this work, we study the effect of voltage

modulations, including their amplitude and frequency, on the discharge and the ion currents, and its implications on the thruster performance. Because of the increase in the discharge current and faster growth of the ion current, compared to the discharge current, increase in the thruster efficiency, in terms of the propellant utilization and current utilization, was expected.

7.4 Experimental setup

For studies of breathing oscillations, we use the cylindrical Hall thruster (CHT). Similar to conventional annular design Hall thrusters (so-called stationary plasma thruster or SPT), the CHT accelerates the ions by $\mathbf{E} \times \mathbf{B}$ fields [61]. The main difference from SPT thrusters is that CHT has a cylindrical channel with diverged magnetic fields. In present research a 200 W CHT with 2.6 cm channel diameter was used 7.1) [81].

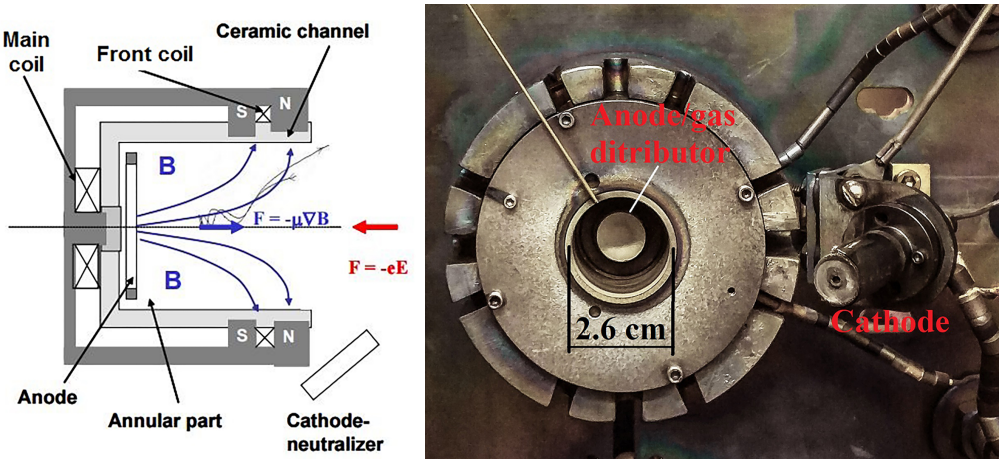

Figure 7.1: Schematic of CHT (left) and image of 2.6-cm CHT (right).

This CHT has two electromagnet coils – back coil and front coil [157] which are used to produce and control the magnetic field distribution in the CHT channel. The description of this thruster design and operation can be found in Refs. [80, 81, 157, 158]. The thruster was powered by a DC power supply and operated at the discharge (anode) voltage of 220V. This voltage was chosen because the natural breathing mode exists at this operation condition. Xenon gas was used as a propellant with 3.5 sccm flow rate through the anode and 2 sccm though the cathode-neutralizer. In the described experiments, currents in both electromagnetic coils were co-directed to form the so-called direct magnetic configuration with

diverging magnetic field [80]. Experiments were conducted in the small Hall thruster facility at PPPL [158] equipped with a turbo-molecular pumping system. During the thruster operation, the background pressure did not exceed 70 μtorr.

To study the breathing oscillations and their control, the electrical circuit of the thruster discharge was modified compared to previous experiment [79], so the modulations can be added to the applied DC discharge voltage (see Fig. 7.2). In particular, amplitudes and frequencies of the modulation voltage were controlled with a function generator. Its signal was amplified and then added to the DC level of the anode potential by Kepco BOP50-4M amplifier, which was connected in series with the thruster power supply. The amplitude of the modulation V_{mod} was varied from 8 to 50 Volts peak-to-peak. The upper limit was determined by the thruster stable operation. The modulation frequency was varied from 6 to 18 kHz.

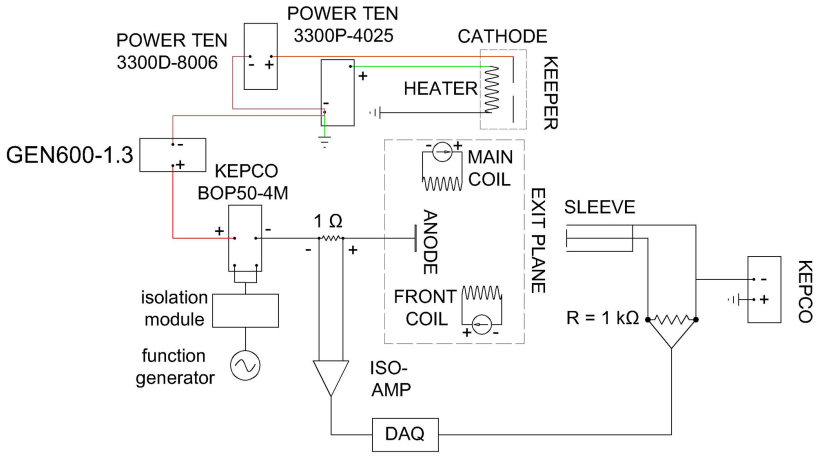

Figure 7.2: Electric schematic for the driving circuit and the planar probe measurements.

Two main parameters were measured during these experiments: the discharge current (I_d) and the ion (or beam) current (I_b). The discharge current was measured using a low impedance current shunt placed in the thruster electrical circuit between the thruster and the modulation amplifier [159]. Measurements of the ion current were done with a negatively biased (to -40 V) movable flat electrostatic graphite probe with a guarding sleeve [160]. Probe was located on the rotating arm and distance from the CHT exit plane to the collecting surface of the probe was 14 cm. The total ion flux was determined by integrating over the measured

angular ion flux distribution [157, 161]. Detailed description of the procedure is given in Appendix A. Schematics of the planar probe measurements and general experiment scheme are shown in Figure 7.3. In addition, in a separate set of experiments, the IVDF was measured using laser induced florescence diagnostic. Moreover, the plasma properties at the channel exit of the CHT, including plasma potential, plasma density and the electron temperature were measured too. Results of these probe and IVDF measurements are described in Ref [29].

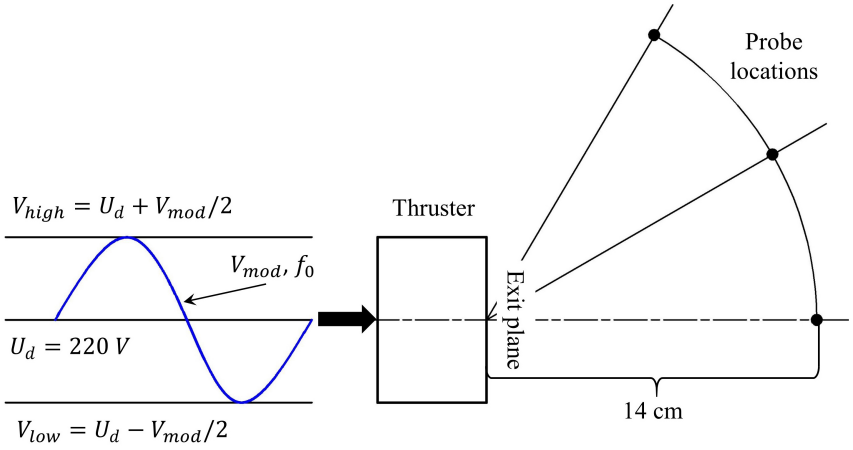

Figure 7.3: Schematics of the anode potential modulation and the planar probe measurements, where V_{DC} is the anode applied voltage, V_{mod} is the modulation voltage with the frequency f_0.

As is described in the Appendix B, we have investigated the circuitry response to modulations without the thruster to ensure that the observed phenomena do not come from the power supply.

7.5 Experimental Results and Discussions

The linear and non-linear responses of the thruster to the anode potential modulation were described in Ref. [133]. The linear response was identified as a regime when the amplitude of the discharge current grows linearly with the increase in the modulation voltage amplitude, while the RMS value remains approximately constant. The non-linear response was defined as the thruster regime when modulation of the discharge voltage results in stronger (faster) increase of the RMS of the discharge current. In this regime, there is a nonlinear rise in the RMS value and oscillation amplitudes (Fig. 7.4).

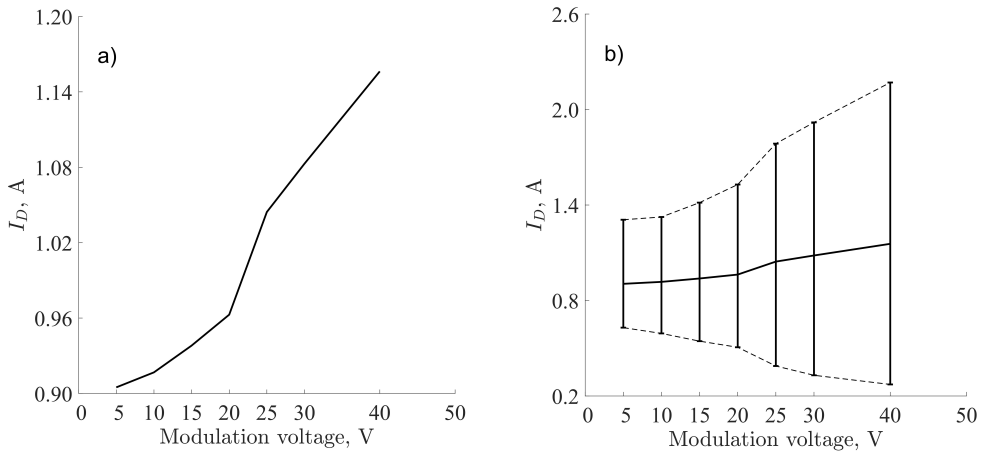

Figure 7.4: a) RMS value of the discharge current as a function of the external modulation voltage. b) Amplitudes of the discharge current oscillations as a function of the external modulation voltage. Dashed lines represent maximums and minimums of the oscillations amplitude.

7.5.1 Effect of the modulation amplitude and frequency on the discharge current and ion current oscillations

Without the applied modulation, the discharge current exhibits intrinsic breathing oscillations at a frequency about 13 kHz. With the applied modulations, the amplitude of the current oscillations depends on the modulation amplitude. This dependence has a resonant-kind behavior reaching maximum amplitude at a certain modulation frequency. We define the resonant modulation frequency as the frequency at which RMS value of the current oscillations and their amplitude reached maximum. In the described experiments, this frequency was determined by monitoring the discharge current oscillation amplitude while modulation frequency was varied (Fig. 7.5). When the modulation amplitude was below 10 % of the DC discharge voltage level, the resonance was at frequency near the frequency of natural breathing oscillations $\sim$ 12-13 kHz. This can be seen in Fig. 7.5a, at the modulation amplitude of $V_{mod} = 16$ V the RMS value and corresponding amplitude (shown with vertical bars) of the discharge current reach their maximum at $\sim$ 13 kHz of the modulation frequency. At higher values of the modulation amplitude, the resonance frequency shifts towards the lower frequencies $\sim$ 10 kHz. In Fig. 7.5b, when $V_{mod} = 40$ V, the maximum of the RMS value and the oscillation amplitude is at $\sim$ 10 kHz.

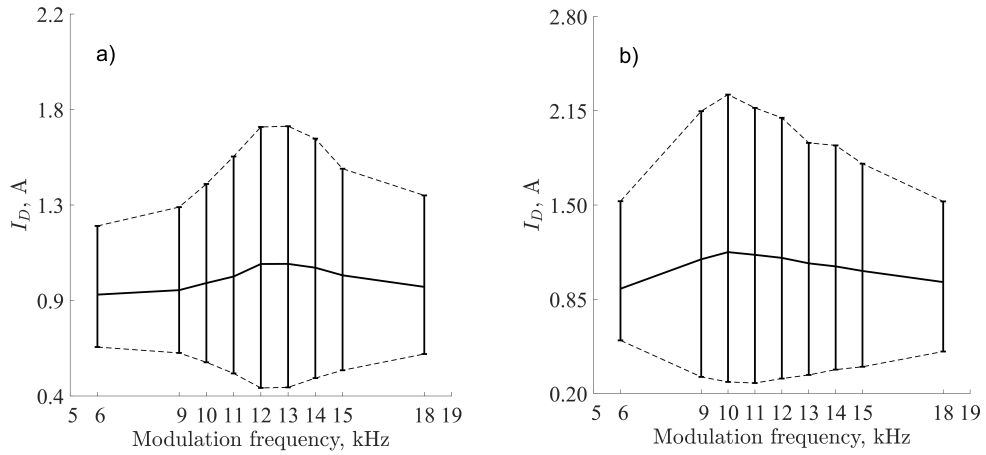

Figure 7.5: RMS values of the discharge current as a function of the external modulation frequency at a) $V_{mod} = 16$ V; b) at $V_{mod} = 40$ V. Dashed lines represent maximums and minimums of oscillation amplitude.

Therefore, the increase of the modulation amplitude leads not only to the nonlinear increase of the RMS value of the discharge current but affects the resonance frequency as well. To investigate this behavior, the anode potential of the thruster was modulated with frequencies in the range from 6 to 18 kHz, and amplitudes in the range from 5 to 50 V peak-to-peak. The discharge and the ion currents were monitored; results are shown in Figure 6. At $V_{mod} = 50$ V and modulation frequencies below 13 kHz, thruster operated very unstable and it was impossible to collect data.

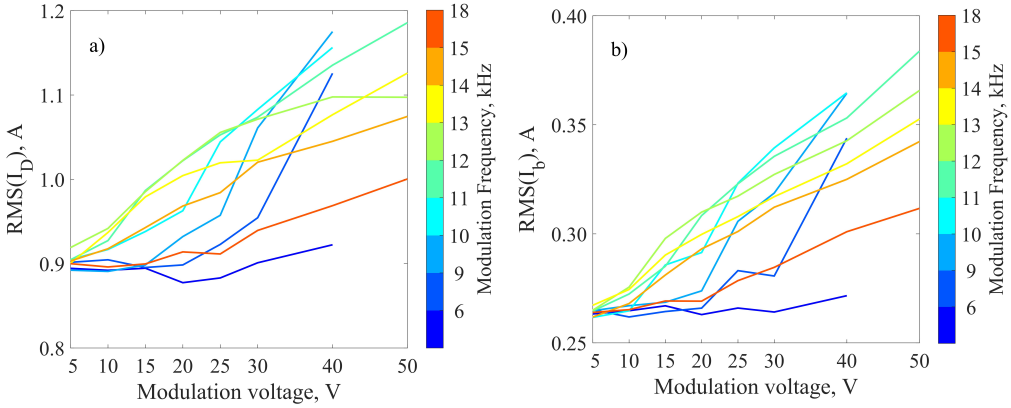

Figure 7.6: RMS value of the discharge current (a) and the ion current (b) as a function of the amplitude of the external modulation and at different modulation frequencies. Different colors on the color bar represent different modulation frequencies.

As it shown in Fig 7.6, there is a growth of the RMS values of the discharge current and the ion current with the increase of the modulation amplitude. At low amplitudes, RMS values are not affected by frequency change. However, with the increase of the modulation amplitude, there is a clear resonant behavior with a maximal response at a frequency which shifts towards lower values for higher modulation amplitude.

7.5.2 Effect of the modulation on the thruster efficiency

The thruster efficiency is the ratio of the thruster kinetic power to the input electric power. It can be characterized in terms of the current utilization, the propellant utilization, and the voltage utilization [16, 61]. The total thruster efficiency is defined as

$$\eta_T = \frac{T^2}{2\dot{m}_p P_{in}} = \gamma \eta_b \eta_v \eta_m \eta_0, \tag{7.1}$$

where T is the thrust, $\dot{m}_p$ is the total propellant mass flow, γ is the beam divergence, η_b is the current utilization, η_v is the beam voltage utilization, η_m is the propellant utilization, and η_0 is the electrical utilization efficiency. In this work we investigate only effects from the current utilization and the propellant utilization.

The current utilization is defined as

$$\eta_b = \frac{I_b}{I_a}, \tag{7.2}$$

where I_b is ion beam current, I_d is the total discharge current. It shows what part of the discharge current goes to the ion current, and it is limited by the axial electron current, because $I_d = I_e + I_i$.

The propellant utilization is defined as

$$\eta_b = \frac{\dot{m}_i}{\dot{m}_a} = \frac{I_i}{I_a}, \tag{7.3}$$

where $\dot{m}_p$ is the ion mass flow, $\dot{m}_a$ is the anode flow rate, and $I_i = e\dot{m}_i/M_i$ and $I_m = e\dot{m}_a/M_i$, here e is the charge and M_i is the xenon atom mass. We did not account for the cathode flow rate. This coefficient reflects the efficiency of the ion production, affected by the losses in the channel. Results for the current utilization are shown in Fig. 7.7. In the linear regime, when the modulation amplitude is small, the current utilization remains approximately constant at all frequencies. In the non-linear regime when modulation amplitude increases, the current efficiency slightly increases, but there is not clear dependency on the modulation frequency.

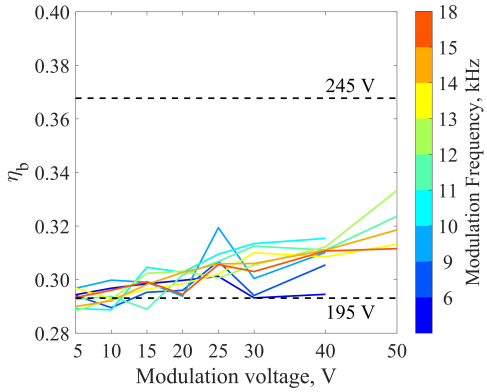

Figure 7.7: The current utilization as a function of the amplitude of the external modulation and at different modulation frequencies. Different colors on color bar represent different modulation frequencies. Dashed lines show current utilization at 195 and 245 V discharge voltage without any modulation.

Fig. 7.8 shows that the propellant utilization increases significantly with the increases of the modulation amplitude. This increase reaches its maximum at the resonant frequency, which depends on the amplitude as well.

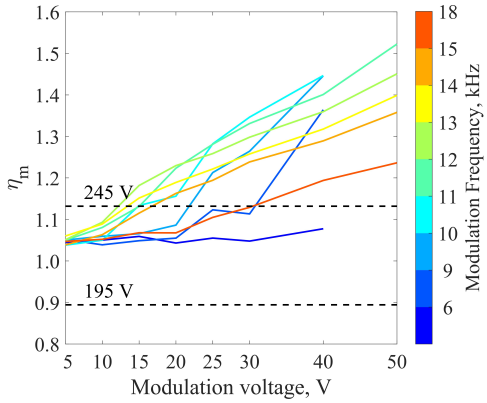

Figure 7.8: The propellant utilization as a function of the amplitude of the external modulation and at different modulation frequencies. Different colors on color bar represent different modulation frequencies. Dashed lines show current utilization at 195 and 245 V discharge voltage without any modulation.

Propellant and current utilization efficiencies were deduced from measured results for the discharge voltages of 195 V and 245 V DC without the external modulation for the comparison. These values correspond to maximum and minimum levels of the discharge voltage during the modulation around 220 V with 50 V amplitude. As it is shown in Figs.

7.7 and 7.8, there is a strong evidence of the increased ionization during the modulation. The propellant utilization growth is significant even in comparison with the 245 V level.

Finally, the total contribution to the thruster efficiency was estimated as a product of the propellant the current utilization efficiencies. Results are shown in Fig. 7.9. It can be seen, that when modulation is at resonant frequency and amplitude is large, efficiency can be increased up to 20%. However, in comparison with the 245 V DC discharge without the external modulation, increase is only about 10%.

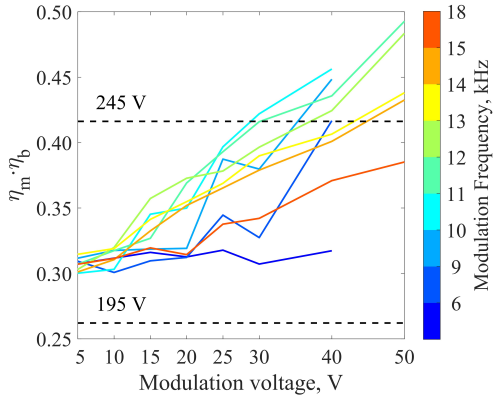

Figure 7.9: Product of the propellant utilization and the current utilization as a function the amplitude of the external modulation and at different modulation frequencies. Different colors on color bar represent different modulation frequencies. Dashed lines show current utilization at 195 and 245 V discharge voltage without any modulation.

It is important to notice, that beam divergence is almost unaffected by the external modulations. Results of measurements of ion beam divergence are presented in Appendix A, Fig. A.1. As one can see, divergence is almost the same in case of linear regime (Fig. A.1a) and in case of nonlinear regime (Fig A.1b). Therefore, beam divergence coefficient γ remains approximately the same.

7.6 Theoretical modelling of externally driven ionization breathing mode

In this section, we consider a simple time dependent 1D model of ion acceleration across the magnetic field in a quasineutral plasma. This is the simplest model used to describe

the stationary flows of ions [145, 147–149] as well as breathing modes oscillations in Hall thrusters. It is a time dependent, 1D with model with three species: neutrals, singly charged ions, and electrons. Neutrals are injected with constant velocity $v_a = const$ at the left side of the simulation region and described by continuity equation

$$\frac{\partial n_a}{\partial t} + v_a \frac{\partial n_a}{\partial x} = -\beta n_a n_i, \tag{7.4}$$

The neutral flow is depleted due to ionization with a constant ionization rate β. Respectively, the ion and electron continuity equations have the source due to ionization on the right-hand side

$$\frac{\partial n_i}{\partial t} + \frac{\partial n_i v_i}{\partial x} = \beta n_a n_i, \tag{7.5}$$

$$\frac{\partial n_e}{\partial t} + \frac{\partial n_e v_e}{\partial x} = \beta n_a n_e, \tag{7.6}$$

Ionization adds the drag to the ion acceleration (given by the last term) in the ion momentum balance

$$\frac{\partial v_i}{\partial t} + v_i \frac{\partial v_i}{\partial x} = \frac{e}{m_i} E + \beta n_a (v_a - v_i), \tag{7.7}$$

here β is the ionization rate, v_a is the neutral flow velocity, and v_i is the ion flow velocity. The electrons are modeled in the drift-diffusion approximation

$$0 = e n_e \mu_e E - e\mu_e \frac{\partial T_e n_e}{\partial x} - m_e n_e v_e, \tag{7.8}$$

where μ_e is the electron mobility perpendicular magnetic field, v_e is the electron flow velocity, T_e is the electron temperature. The diffusion (due to pressure gradient) is especially important near the anode, or in the so-called diffusion region, resulting in the inversion of the electric field in this region and leading to a backflow of ions to the anode. Our model is quasineutral, so there is no sheath effect included. By using the quasineutrality $n_i = n_e = n$ condition Eq. 7.5 7.6 become

$$\frac{\partial}{\partial x}(n_e v_e + n_i v_i) = 0.$$

Then the Ohm's law can be written as

$$E = \frac{J_d}{e n \mu_e} - \frac{v_i}{\mu_e} - \frac{1}{en} \frac{\partial T_e n}{\partial x}, \tag{7.9}$$

where $J_d = e(n_i v_i - n_e v_e)$ is the total current density which is uniform in space but can oscillate in time. The electric field in the system is constrained by the potential drop U_d

between anode and cathode

$$\int_0^L E dx = U_d$$

where L is the channel length (neglecting the sheath voltage). The external voltage U_d will be modulated in time. The electron mobility μ_e is given by the classical expression for collisional transport in the transverse magnetic field is:

$$\mu_e = \frac{e}{m_e \nu_m} \frac{1}{1 + \omega_{ce}^2/\nu_m^2},$$

where $\omega_{ce} = eB/m_e$ is the electron cyclotron frequency, and ν_m is the total electron momentum exchange collision frequency. Note that in thruster conditions the value of μ_e is likely to be anomalous so the electron transport model should be viewed as a simple parametrization of anomalous mobility and diffusion rather than exact equation based on the classical transport coefficients.

This model neglects a number of effects, e.g. sheath wall losses and wall recombination effects due to 2D geometry. Several other simplifications are invoked such as constant electron temperature (and, therefore, the ionization coefficient), electron mobility (and Hall parameter), and neutral velocities.

As such, our model does not reproduce exact experimental conditions. Neither the anomalous conductivity is well known for these conditions. Therefore, here we do not attempt to match the outcome of our theoretical model with experimental data. Our goal is to demonstrate that the basic model of ionization modes in $\mathbf{E} \times \mathbf{B}$ discharge as given above (and as was used in Refs [147, 148]) is capable of capturing the nonlinear phenomena which occurs during the external modulations of the applied voltage.

The ion acceleration within the framework of equations 7.4, 7.5, 7.7, 7.8, 7.9 exhibits a removable singularity at the sonic point where the ion velocity is equal to the ion sound velocity [147, 149]. The conditions that the sonic point becomes regular impose strong constraints on the stationary solutions as has been recently discussed in Ref. [162].

The full system of nonlinear equations (4-8) was solved in BOUT++ framework [163–165] as an initial value problem. Upwind terms in these equations were treated with third order central WENO scheme. This scheme allows to simulate flows from subsonic to supersonic and deals with shock wave discontinuities.

7.6.1 Simulation parameters

Simulations were conducted with parameters close to ones measured during the CHT operation. List of typical values is shown in Table 7.1.

Table 7.1: Simulation parameters

Parameter	Value
Gas	Xenon
Channel length, L	3.0 cm
Channel radius, r	1.2 cm
Channel area, A	4.5 cm^2
Mass flow, $\dot{m}$	0.34 mg/s
Discharge current, I_d	0.8 A
Discharge voltage, U_d	230.8 V
Electron temperature, T_e	20 eV
Ion sound, c_s	3833 m/s
Neutral velocity, v_a	200 m/s ($T_a \approx 650$ K)
Collision frequency, ν_m	10^6 s^{-1}
Electron mobility, μ_e	0.1 m^2/Vs

It is important to notice, that the initial value simulations in this model require boundary conditions (B.C.) at the anode [29]. These B.C. were defined from stationary solutions of the above system of equations obtained by different method [26, 27].

7.6.2 Intrinsic breathing mode oscillations

First, the natural (intrinsic) breathing oscillations were obtained for the given set of parameters and in neglect of the external modulations. Initial value simulations were started with arbitrary profiles for n_i, n_a, and v_i, and B.C. defined from stationary solutions. The system shows intrinsic breathing mode oscillations as shown in Fig. 7.10. Root mean square (RMS) value of the discharge current I_d is equal to the value obtained from the stationary solution.

There are current oscillations with the frequency $f_0 = 79.1$ kHz, and amplitude about 0.4 A peak-to-peak. It is important to note that the self-consistent dynamics of the electric field, ion and electron response, together with ionization is important for the occurrence of oscillations [141]. No oscillations can be obtained with continuous analog of the predator-prey model; i.e. exclusively within the coupled ion-neutral dynamics [120] alone and neglecting the electrons and total current coupling. Also note that since our model assumes the constant electron temperature, the feedback coupling mechanism for the oscillations discussed in Ref. [121, 166] is not involved.

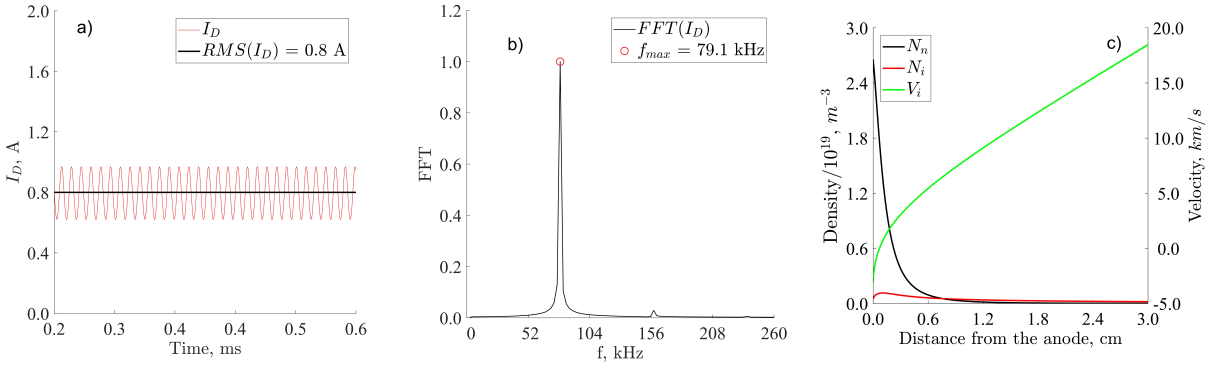

Figure 7.10: a) The discharge current I_d trace. b) Fast Fourier transform of I_d. c) Averaged in time profiles of n_i (red), n_a (black), and v_i (green).

The intrinsic oscillations in our model have the frequency different from the one observed in experiments. It was shown previously that the oscillation frequency is very sensitive to the value of the mobility [141]. Inhomogeneous magnetic field (inhomogeneous mobility) also affects the frequency of oscillations. The constant value of Hall parameter $\beta = 0.11$ was used in our simulations. Since the value of the anomalous mobility was not well known in our experiments, we did not attempt to match the frequency to experimental value by varying the anomalous mobility and other plasma parameters. However, nature of those oscillations is the same as for oscillations in Ref. [8, 144, 151].

7.6.3 Effect of the discharge voltage modulations

The discharge voltage was modulated by applying a sin wave at a frequency equal to the intrinsic breathing oscillations frequency $f_0 = 79.1$ kHz. Modulation amplitudes V_mod were chosen to be in the range 5%, 12.5%, 25%, and 50% of the applied potential U_d. The resulting

RMS values of the discharge and ion currents, and their oscillation amplitudes as a function of the modulation amplitude are shown in Fig. 7.11.

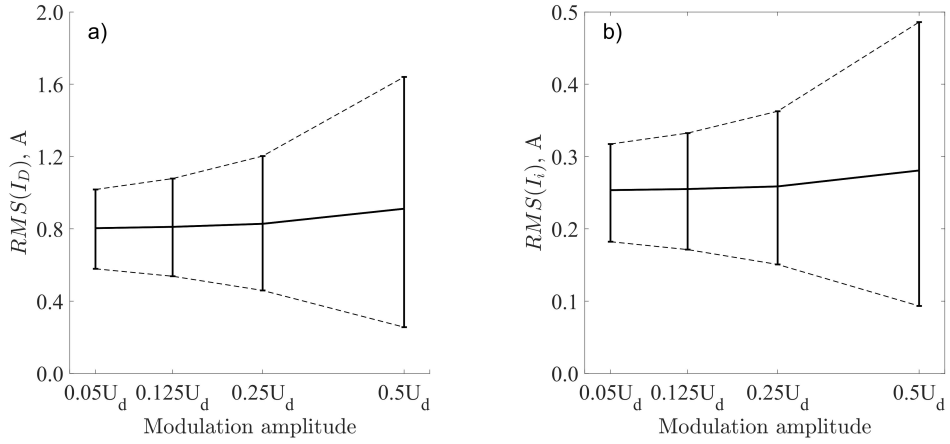

Figure 7.11: The RMS values of a) the discharge current I_d; b) the ion current I_i, and corresponding oscillation amplitudes as a function of modulation voltage.

Similar to the experiments, we observe a nonlinear increase of the discharge current RMS value and oscillation amplitude with the modulation amplitude (see Fig. 7.4 and 7.5). Same behavior is observed for the ion current.

We have studied the behavior of the ion velocity v_i and ion density n_i at the channel exit. Examples of such time traces for $V_{mod} = 0.05U_d$ – linear regime and $V_{mod} = 0.5U_d$ – nonlinear regime are shown in Fig. 7.12a, b respectively.

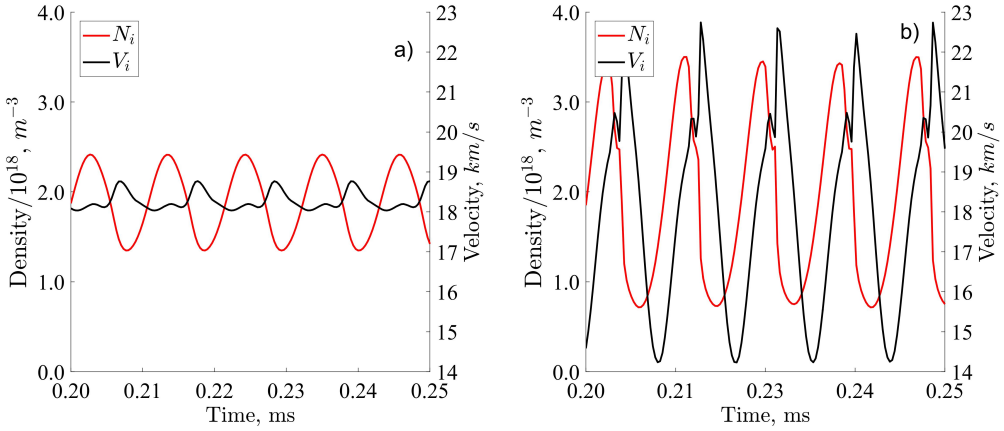

Figure 7.12: Ion density and ion velocity at the exit plane at a) $V_{mod} = 0.05U_d$, and b) $V_{mod} = 0.5U_d$ modulation amplitude in the simulation.

There is a noticeable difference between the linear and nonlinear regimes. First, one observes an increase in the amplitude of oscillation for larger modulation amplitude. One can also see that in nonlinear regime the modulated v_i acquires the higher nonlinear harmonics (second and higher). The contribution of the quadratic terms (e.g. $\sin^2$) to the mean values is in part responsible for the RMS enhancement. Secondly, there is a strong reduction of the phase difference between density and ion velocity oscillations with increase of modulation as shown in Fig. 7.13, so that the enhanced correlation result in the increase of the mean value.

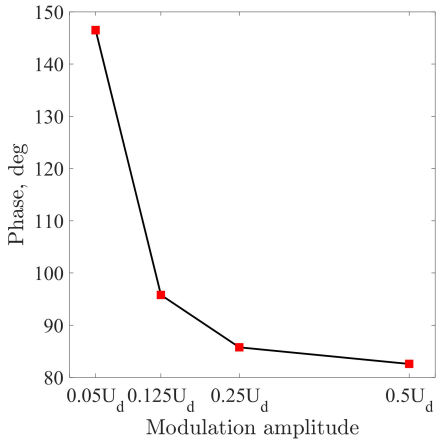

Figure 7.13: Phase difference between ion velocity and ion density as a function of modulation amplitude.

This reduction of phase differences was confirmed by measurements of plasma parameters in linear and nonlinear regimes. Results for these measurements were taken from our previous paper, see Ref. [29]. Measurements were done for two modulation amplitudes: 16 V_{pp} and 32 V_{pp}. The procedure for probe data treatment can be found, for example, in Ref. [109]. Phase differences between the ion density, the acceleration potential, the modulation voltage and the discharge current signal were obtained. Phasor plot is a simple way to show phases between different signal. Phasor is a vector, with length equal to the amplitude of the signal and directed at angle, which represents a phase shift.

Each signal has its amplitude and phase shift with respect to some base signal. The modulation voltage signal was chosen as a base signal. Phase difference between signals was determined by applying Hilbert transform to each signal, and then calculating corresponding angle between transformations. The more detailed description can be found in Ref. [167].

After these procedure phases ϕ were obtained for each signal. Time lag due to different probe position was included as well. Amplitude of signals is not important in this analysis, so amplitude of each signal was set to unity. Two phasor plots, for linear and nonlinear regimes are show in Figure 7.14a and b respectively. The modulation voltage signal (red) was chosen to be the reference once, and it has 0 phase shift. The discharge current (orange) and the ion density (green) oscillations are almost in phase for both linear and nonlinear regimes. The acceleration potential (yellow) was measured during the experiment, and the electric field was obtain by shifting it by $\pi/2$. As one can see, there is a reduction in phase between the electric field and the ion density.

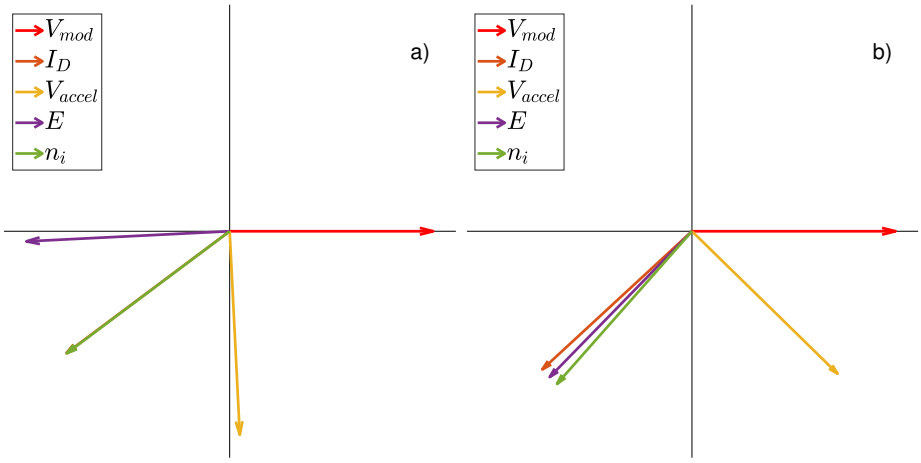

Figure 7.14: Phasor plots for linear (a) and nonlinear (b) regimes from the experiment. Modulation voltage was chosen as a reference, and has 0deg phase shift. In the nonlinear regime (b) the electric field E phase almost coincides with the ion density n_i and the discharge current I_D, contrary to the linear regime when there is a finite phase difference (of the order of ∼40deg) between the electric field and ion density. Note that the discharge current is almost in phase with ion density, both in a) and b).

Similar behavior for the electric field is observed for our simulations. The ion density and the electric field trace for linear and nonlinear regimes are shown in Fig. 7.15a and b respectively. Phase shift reduced significantly for the nonlinear regime.

Therefore, the observed increase of the ion current is related to the increase of the amplitude of oscillations as well as to the reduction of phase shift between density and electric field (or ion velocity) oscillations.

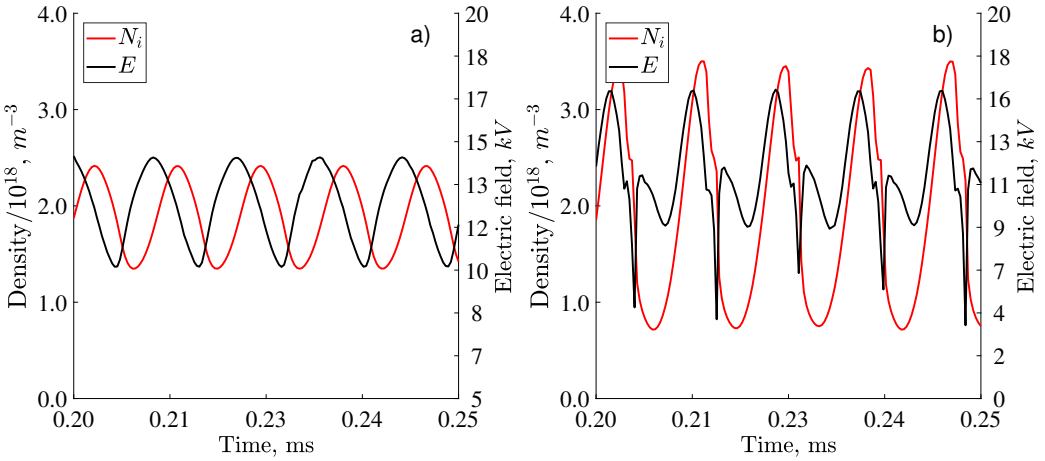

Figure 7.15: Ion density and the electric field at the exit plane at a) $V_{mod} = 0.05U_d$, and b) $V_{mod} = 0.5U_d$ modulation amplitude in the simulation.

7.7 Conclusion

In this paper, we report on the studies of the thruster response to the externally applied modulations of the DC discharge voltage. Application of external modulations in the frequency range of breathing oscillations (6-18 kHz) results in increased amplitudes of the discharge and ion currents oscillations [133]. Two distinct, linear and non-linear, response regimes were observed. The RMS values of the ion and the discharge currents increased as a result of the externally driven modulations. Effect of the modulation on the thruster efficiency was investigated in terms of the current and propellant utilization coefficients. The total contribution to the thruster efficiency defined as a product of the above two coefficients, shows the increase up to 20%, compared to regimes without the external drive. Similar results trend was shown in recent work by Wei et.al. [168]; however, in their work amplification of the breathing mode was due to changes in thruster operating parameters. Results of the experiments and our simulations with 1D model suggest that the observed behavior is due to decrease of phase shift between ion velocity and ion density oscillations, increase in the amplitudes for both quantities, as well as the contribution of the average of the nonlinear (quadratic) terms. Combination of these effects leads to the rapid increase of the mean ion current in nonlinear regime. One has note that the total thruster efficiency is also affected by other factors (electrical utilization efficiency, discharge voltage utilization), so that the total efficiency will be lower than the current and propellant utilization. In summary, the

experiments with the external modulations of applied voltage reveal the nonlinear regime of the response of the breathing mode oscillations. In this regime, controlled amplification of the breathing mode results in the improvement of the thruster performance in terms of the current and propellant utilization. These main features, observed experimentally, have been qualitatively reproduced in a simple theoretical model.

Acknowledgements

This work was supported by AFOSR. We acknowledge Yuan Shi, Scott Keller, Ahmed Diallo, Ken Hara, and Igor Kaganovich for fruitful discussions, and Alex Merzhevskiy for his technical support.

Chapter 8

Control of coherent structures via external drive of the breathing mode

8.1 Preface

This Chapter is devoted to studies of the interaction between the spoke mode and the externally controlled breathing mode. As it was said before, there is an assumption that the azimuthal large-scale instabilities are coupled with the gradients in the axial direction. The breathing mode is responsible for changes in plasma parameters profiles, therefore by controlling it, one can change corresponding gradients. In this research, both modes were identified by using a fast-frame camera and developed image-processing technique. It was shown that changes in breathing mode can suppress the spoke. Therefore, this research provide an important evidence of the coupling between two mode.

This Chapter is based on a publication: I. Romadanov, Y. Raitses, and A. Smolyakov, Control of coherent structures via external drive of the breathing mode, *Plasma Physics Reports*, under review (2018), reproduced here verbatim.

8.2 Abstract

The Hall thruster exhibits two types of large scale coherent structures: axially propagating breathing mode ($m = 0$) and azimuthal, with low m, typically $m = 1$, spoke mode. In our previous work it was demonstrated that axial breathing mode can be controlled via the external modulations of the anode potential. Two regimes of the thruster response, linear and nonlinear, have been revealed depending on the modulation amplitude. In this work, using the high-speed camera images and developed image-processing technique, we have investigated

the response of the azimuthal mode to the external modulations. We have found that in linear regime, at low modulation voltages, axial and azimuthal structures coexist. At larger amplitudes, in the nonlinear regime, the azimuthal mode is suppressed, and only axial driven mode remains.

8.3 Introduction

Hall thruster is an electric propulsion device, in which the thrust is generated by the axial acceleration of ions in a quasineutral plasma [14, 169]. This is achieved in the configuration with the magnetic field transverse to the applied electric field. The magnetic field is chosen sufficiently strong to keep electrons magnetized, thus preventing them streaming to the anode, while ions remain only weakly affected by the magnetic field and can be accelerated by the electric field. Initial designs were prone to various instabilities, including azimuthal modes. A special profiling of the magnetic field suggested by Morozov [50] stabilized the most violent modes and allowed the development of the Hall thruster concept (so-called Stationary Plasma Thruster or SPT) into practical space flights applications in Russia under the general guidance of A. I. Morozov [170–172]. Two types of large-scale modes, axial breathing mode and azimuthal spoke, typically $m = 1$ (here m is the azimuthal mode number), are still fairly prominent in most of the thrusters. Their physics mechanisms are not fully understood and their effects on thruster performance, in particularly, the role of the breathing mode, is under discussion [30]. It is also believed that large scale azimuthal structures conduct most of the anomalous current [21, 173]. Prominent role of the large-scale structures in thruster behaviour and performance has long been the motivation for the development of the methods for control of the breathing modes [29, 49, 127, 174, 175] and spokes [75]. Control of plasma behaviour is an important topic, with a lot of practical applications [176–178]. Typical control methods are based on a feedback principle or on an active control by applying external forces or varying plasma parameters at certain frequencies [179]. Here, we briefly describe ways to control large scale oscillations in Hall thrusters.

The breathing mode [8, 120] is normally associated with oscillations of the ionization front propagating in the axial direction with $m = 0$ and affecting the whole plasma volume. This mode can be crucial for the thruster operation and may lead to the termination of

the discharge. In previous work we have demonstrated the control of this mode [29, 127] by applying the external AC modulations (V_{mod}) to the DC anode potential (U_d, which was set to 220 V in our experiments). It was found that thruster has two types of response on those modulations [30]. In the linear regime, when amplitude of the applied AC component was below 10% (of the DC level) the root-mean-square (RMS) values of the ion and discharge currents and their oscillation amplitudes grow linearly with the increase of the modulation amplitude. One can see that the error bars for these points mostly overlap (Fig. 8.1a); therefore, changes in RMS values are negligible. In the non-linear regime, the RMS of the discharge and ion currents and their oscillation amplitudes grow faster (non-linearly) than the applied AC component. The amplitude of the discharge current oscillations becomes much larger, than in the linear regime (Fig. 8.1b).

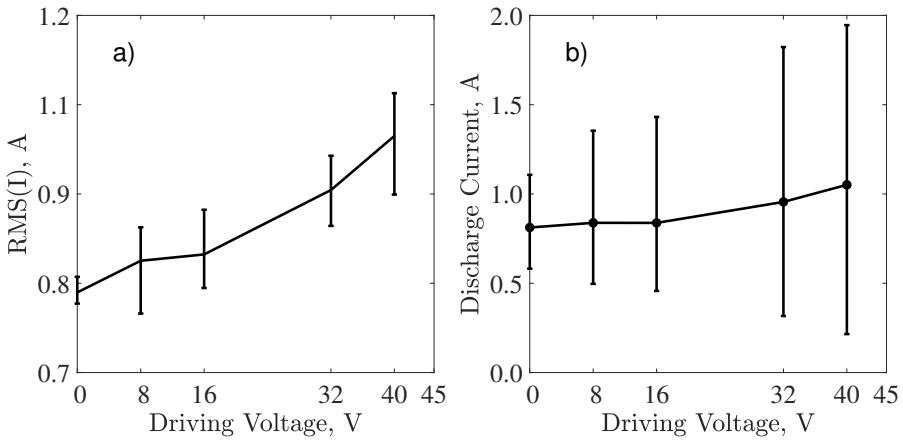

Figure 8.1: a) RMS values of the discharge current as a function of driving voltage. The error bars represent the standard deviation of the discharge current measurements (for 10 points). b) RMS values of the discharge current and corresponding amplitudes.

It was demonstrated that in the nonlinear regime, the breathing mode, controlled by the external modulations, leads to the increase of the current and propellant utilization [30]. It was shown that this effect has a resonant nature, as the RMS and the oscillation amplitudes reach the maximum at a certain frequency, which depends on the amplitude of the AC component.

Strong $\mathbf{E} \times \mathbf{B}$ flow of electrons and other plasma inhomogeneities provide energy source for various other instabilities in Hall thrusters. In particular, they form azimuthal large-scale structures, namely spoke [141] propagating in the azimuthal direction with $m = 1$ or

higher [96,180]. The spoke can cause the increase of the cross-field transport in a wide variety of devices with $\mathbf{E} \times \mathbf{B}$ fields, including Hall thrusters [181], Penning discharges [182], and magnetrons [6,95]. For the Hall thruster, the current conducting spoke is of special interest, because the anomalous transport affects thruster efficiency [21].

While theoretical mechanism for the spoke formation is still not clear, there have been some attempts to control its appearance. The spoke can be suppressed by adjusting operational thruster parameters: magnetic field profile [21,173], increasing the cathode electron emission current [25]. Active control method was demonstrated in works of: Nevrovskii, by inducing oscillations on inserted in plasma electrode [183]; Griswold et al. [75,173] and Yuan Shi at. al. [184] based on the feedback control of the voltage by use the segmented anode. It was implemented in the cylindrical Hall Thruster (CHT). Experiments in Ref. 8 demonstrated that spoke suppression leads to the reduction of the total discharge current.

In this paper, we study the effect of the external AC modulations on the azimuthal and axial modes. External modulations were applied at different amplitudes and frequencies, so thruster was operated in both linear or non-linear regimes. It was earlier established that large scale density and potential fluctuations are well correlated with plasma emission [21]. Therefore, the large-scale plasma structure, such as spoke and breathing modes, can be detected by the emission observation. In our experiments, the changes in plasma emission intensity inside the thruster channel were observed by the fast imaging camera. Both types of modes, the breathing and rotating spoke, contribute to changes of the emission intensity. Since the camera located in front of the thruster, the collected signal is the light intensity integrated along the axial direction. Therefore, it is not possible to determine the axial spoke location, however the difference between the $m = 0$ (from breathing modes) and $m = 1$ (from the spoke) structures can be identified from image analysis.

8.4 Experiment and data acquisition system

Research was performed at Small Hall Thruster Facility (SHTF) at the Princeton Plasma Physics Laboratory (PPPL) [61,81]. The vacuum vessel is about 1 m^3 volume and equipped with turbopump, so the background pressure did not exceed 70 μTorr during the operation. Experiments were done with the CHT with 2.6 cm channel diameter and a 2.3 cm channel

length [79, 157]. CHT is the device with crossed electric and magnetic fields that create and accelerate a plasma jet. Thruster was operated at $U_d = 220$ V DC level of the applied potential between the anode and the cathode, with typical levels of the discharge current $I_d \sim 0.6 - 0.8$ A. Xenon gas was used as a propellant, with the flow rates 3.5 sccm and 2 sccm through the anode and the cathode-neutralizer respectively. Magnetic field was created by means of two electromagnetic coils which operated in so-called "direct" magnetic configuration with diverging magnetic field [80]. Details of the design and operation have been described elsewhere [158].

Under the above conditions and configuration, CHT exhibits intrinsic breathing oscillations at ~ 13 kHz and amplitude of the discharge current oscillations at about 0.1 A. Control of these oscillations was realized with the electric circuitry described in Ref. [30]. In brief, the sinusoidal AC component was added to the DC anode potential. Circuitry allowed to control amplitude of the modulation and frequency. The amplitude of modulation V_{mod} was varied from 1 to 30 V peak-to-peak. The frequency of modulation f_{mod} was varied between 10 and 15 kHz.

Light emission from the plasma during the thruster operation was captured with a Phantom Camera V7.3 in the visible spectrum. The camera frame rate was set at 87 000 frames per second with 128x128 pixel resolution. Camera was located outside the vacuum chamber, looking in through a view port that was ~ 1 m away from the channel exit and along the center plane of the thruster. Due to the location of the view port, the camera was shifted off the thruster centerline by, approximately 15deg. A rotating spoke is observed as a region with increased light intensity, which propagates in azimuthal direction corresponding to $\mathbf{E} \times \mathbf{B}$ direction. A sequence of frames from the camera is shown in Figure 8.2.

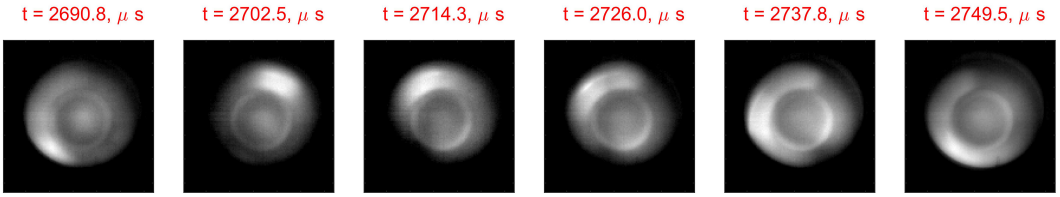

Figure 8.2: A sequence of frames showing the light emission from the plasma in the CHT. Spoke is a region of increased light intensity propagating in the $\mathbf{E} \times \mathbf{B}$ direction (counter clockwise) in part masked by the presence of the m=0 breathing mode with oscillations of the brightness across the whole channel.

It is important to notice, that discharge parameters were different from the ones used in previous studies of CHT [21, 75, 127, 173], which resulted in the reduction of spoke frequency from 15-30 kHz range to 5-8 kHz range in our experiments. A more detailed description of experimental parameters will be given below.

8.5 Image processing

Axial mode can be identified relatively easy from the Fourier analysis of global intensity variation over time; however, azimuthal mode is harder to detect. In previous studies, the special image processing technique in combination with Fourier analysis [25, 185] or the cross-spectral-density (CSD) techniques [26] were used for the detection of azimuthal coherent structures. Signal from plasma is contaminated by noise due to light emission from the walls and other parts of the thruster channel. The overlapping of semi-coherent axial and azimuthal modes, which exist simultaneously, results in spurious harmonics. As a result, identification of the coherent structures exclusively by the Fourier analysis or CSD is a difficult task. Additional complications come due to semi-coherent nature of the azimuthal mode, which has some finite frequency spread (or frequency changes in time), contrary to the breathing modes which exhibits high coherency at a single rather well-defined frequency.

In our work, we implemented a combination of Fourier analysis and cross-spectral-density (CSD) techniques for azimuthal mode detection. Fourier analysis allows to identify the range of frequencies of interest, which are used in CSD analysis. CSD technique allows to map spatial various of the intensity onto the frame at different frequencies f_i. Output of this technique is the information about phase shifts in the emission oscillations between different regions of the image, as well as information about coherence of these oscillations.

Spectrum of azimuthal and axial modes is defined initially from Fourier analysis. For $m = 0$ axial mode the spectrum is obtained by taking a Fourier transform from global light intensity time series. The global light intensity is defined as a summation of all light intensities in one frame, effectively resulting in averaging over azimuthal direction. Finding spectrum of $m = 1$ mode requires some pre-processing of initial frames. Frames were cleaned from background light intensity, the oscillations due axial $m = 0$ mode, and other noise. This part is similar to the technique which was used by McDonald [25, 185] and is described in

the Appendix A. Outcome of this stage is frames where $m = 0$ mode was subtracted, then the frequency and finite m azimuthal mode spectrum is obtained. Spectrum for azimuthal mode gives the range of frequencies of interest, where axial and azimuthal structures can exist. Axial mode is the strongest one, and its frequency can be easily identified from the spectrum. The accurate identification of main frequency of the azimuthal modes is not always possible, due to some noise, and possibly due to some finite frequency spread in the azimuthal modes (non-stationary). The CSD technique is applied to further delineate the coherent structure of the azimuthal modes by calculating the CSD at each frequency of the interest.

The CSD at each frequency f_i is calculated as follows. The reference signal x_i and signals from each pixel y_i were divided into n_d non-overlapping blocks with length T_d. For each block the Fourier transforms X_i and Y_i for reference pixel and pixel of interest are calculated respectively. The following definition for CSD is used

$$\hat{G}_{xy}(f_i) = \frac{2}{n_d T_d} \sum_{i=1}^{n_d} X_i^*(f_i) Y_i(f_i),$$

where $n_d = 10$ and $T_d = 512$ where taken. Phase difference between two signals can be defined from the phase angle of complex $\hat{G}_{xy}(f_i)$ value. The coherence then is defined as follows

$$C_{xy} = \frac{|\hat{G}_{xy}|^2}{\hat{G}_{xx}\hat{G}_{yy}},$$

where $\hat{G}_{xx}$ and $\hat{G}_{yy}$ are auto spectral densities of x_i and y_i signals. In our analysis the mean cross-coherence parameter is used defined as follows

$$C_m = \frac{\sum_{x,y} C_{xy}}{M \times N},$$

where M and N are frame size in pixels.

Specifically, the CSD algorithm is implemented as follow. First, the random pixel is selected on the frame, and its intensity variation over time is extracted. Then, by calculation the cross-spectral-density, as described above, differences in phases and coherence between the intensity signal of the reference pixel and other pixels signals were obtained. After all those steps, one has 2D maps of relative coherences and phase differences between the reference pixel and all other pixels for each frequency. In the next step, the coherence maps were averaged for each frequency; therefore, coherence as a function of frequency is obtained. Modes, which have highest averaged coherence are selected. Phase maps are essentially is an

image where value of each pixel represents the phase difference between signal from this pixel and the reference signal. Each pixel position is the same is in real image. This technique was adopted from Ref. [26], were detailed description is given.

The CSD diagnostic is illustrated in Fig 8.3 with the synthetic signal, which contained spoke mode at 7.0 kHz frequency, and 12.0 kHz breathing mode. Spoke mode was simulated as a circle with Gaussian distribution of the intensity. The spoke radius was chosen to 1/3 of the channel radius. Intensity of the breathing mode changes as a sine wave. Additional Gaussian noise was added on the top of this video. This signal was analyzed with developed algorithm, and results are presented in Figs 8.3 and 8.4.

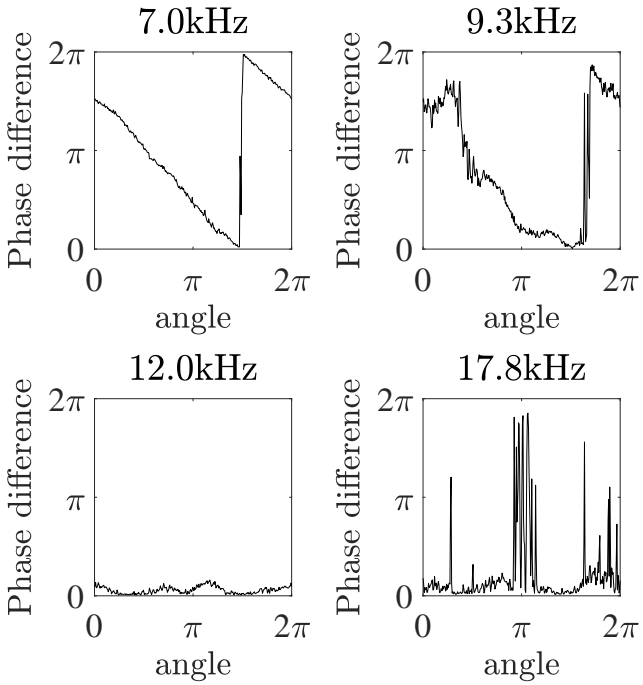

Figure 8.3: Phase difference with respect to reference pixel as a function of azimuthal position (angle). Figure for 7.0 kHz shows the dependency for a spoke mode. Figure for 12.0 kHz shows the dependency for a breathing mode. Figures for 9.3 and 17.8 kHz are chosen to show the difference between the frequencies related to coherent structure and arbitrary frequencies.

Figure 8.3 shows phase difference dependency on azimuthal position (angle) for selected frequencies. For azimuthal mode, at 7.0 kHz frequency, phase difference should depend linearly on azimuthal position, changing 0 to 2π with respect to the reference pixel. If plot

it in cylindrical coordinates, this would look like a helix, which behavior is independent on radius. For axial mode, at 12 kHz, light intensity should change in phase independently on azimuthal position, meaning that the phase difference should be either 0 or 2π. This can be seen in Fig 8.3 for 12.0 kHz mode. Frequencies 9.3 kHz and 17.8 kHz were chosen to illustrate the difference between the frequencies related to coherent structure and arbitrary frequencies. Phase difference dependency on azimuthal position for them has an intermediate behavior between spoke and breathing modes.

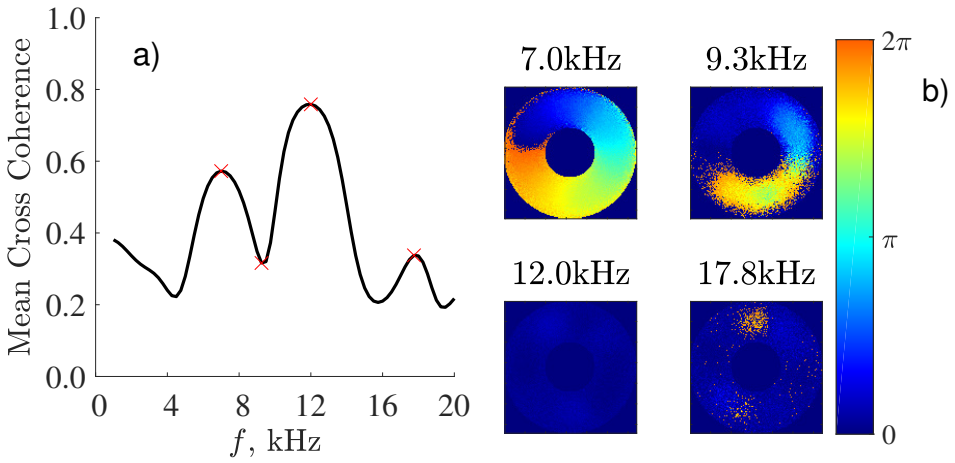

Figure 8.4: a) Mean cross coherence as a function of frequency. Frequencies, for which the phase maps were plotted, are marked with red crosses; b) phase maps for selected frequencies, different colors represent different values of the phase shift, according to the color bar.

To illustrate how the mean cross coherence depends on selected frequency, it was calculated for the range of frequencies between 1 and 20 kHz. Figure 8.4 shows mean cross coherence C_m as a function of frequency and phase maps for frequencies from Fig 8.3. Mean cross coherence C_m is shown in Fig 8.4a. There are two prominent peaks, related to the spoke and breathing modes, marked with red crosses. For the spoke mode on 2D map, we expect to see projection of helices with different radius. Color on such maps represents corresponding value of the phase shift. Therefore, a smooth azimuthal transition from 0 to 2π with respect to the reference pixel will obtained. This is shown in Fig 8.4b for 7.0 kHz frequency. For breathing mode, all pixels change their intensity in phase, there phase difference should be either 0 or 2π, as shown in Fig 8.3 for 12.0 kHz frequency, where all phases are close to

0. It is important to notice, that the method has an error; therefore, color on phase maps are not completely uniform, as it should be for global modes. Other frequencies show the behavior, which is a combination of spoke and breathing mode patterns, because this method is sensitive for higher harmonics of each signal, as well as their linear combinations.

Thus, peaks on coherence plots and shape of the phase map for these peaks are our main criteria to identify coherent structures in real signal.

8.6 Identification of breathing and spoke structures in CHT

First, we applied our analysis to the case without external modulations, so intrinsic breathing and spoke modes could be identified. Fourier spectrum for both modes is shown in Figure 8.5. One can see that the global intensity (averaged over all finite m) oscillations show distinct frequency peak due to the presence of intrinsic axial oscillations at frequency around 13 kHz, as shown in Fig 8.4a. On the contrary, finite m modes have several peaks distributed around 8 kHz, see Fig 8.4b. We select several most prominent peaks (with amplitude > 0.6 of maximum) and determine coherence for these peaks with CSD algorithm.

Results of the CSD mapping are shown in Figure 8.6. Figure 8.6a represents an averaged coherence for each selected frequency from Fig 8.5b. As one can see, not all frequencies from Fourier analysis have high coherence. Now, only frequencies with high coherence (greater than 0.65) were selected. They are marked with red crosses in Fig. 8.6a.

For these frequencies the phase maps were plotted, as shown in Fig. 8.6b. There are three peaks which shows high coherence at 5.6, 6.1 and 8.6 kHz. Phase maps for all of them indicate the existence of azimuthal coherent structures. Phase difference changes linearly in azimuthal direction from 0 to 2π with respect to the reference pixel. These modes move in azimuthal direction and corresponds to $m = 1$ mode (see Fig 8.6b, 7.0 kHz for the reference). This mode is non-stationary, as its frequency changes over time; therefore, the range of frequencies is observed. At frequency about 13.8 kHz, there is a global $m = 0$ mode, which cause all pixels to change their intensity in phase (either 0 or 2π phase difference). Therefore, both $m = 0$ and $m = 1$ modes co-exist at these operation parameters.

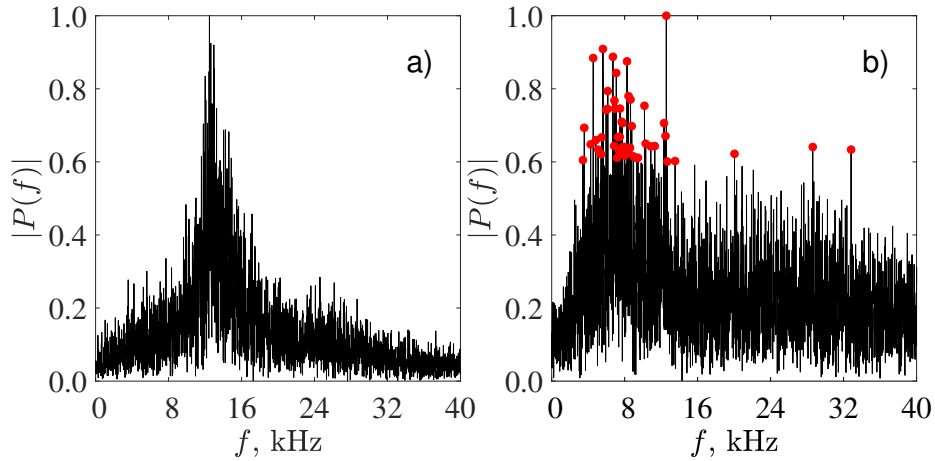

Figure 8.5: a) Spectrum for global intensity for $m = 0$ and b) spectrum for azimuthal modes m. Each plot is normalized to the highest amplitude. No modulation is applied. Red circles mark peaks with the most prominent frequencies (with amplitude > 0.6 of maximum).

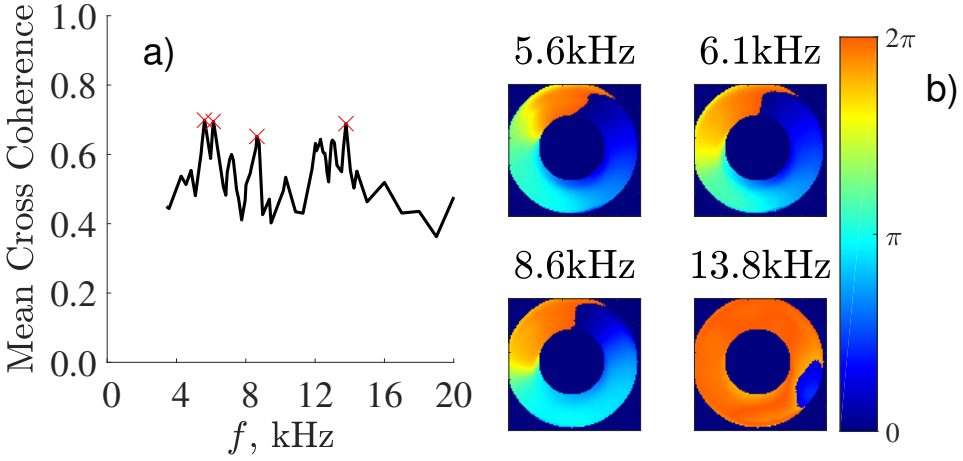

Figure 8.6: a) Averaged coherence value for the range of frequencies of interest from Fig 8.5b. Red crosses show frequencies with large averaged coherence. b) Phase maps for the most coherent frequencies (marked with red crosses on the left panel). The colors representing different phase shift values as shown on the color bar.

After the natural breathing and spoke modes were identified, the external modulation was applied. We started from linear regime with 5 V amplitude and frequencies at 10 and 15 kHz. Spectrum for $m = 0$ and higher m modes at 10 kHz modulations are shown in Fig. 8.7a, b respectively. Spectrum for $m = 0$ shows that there is an intrinsic axial mode at about 13 kHz and a sharp peak at 10 kHz due to modulation (see Fig. 8.7a). Spectrum for azimuthal

modes (see Fig. 8.7b) has again multiple peaks in the range of frequencies 6 to 8 kHz, similar to the case without external modulations. The range of frequencies was selected with peaks higher that 0.6 of the maximum, and the coherence was determined for each frequency.

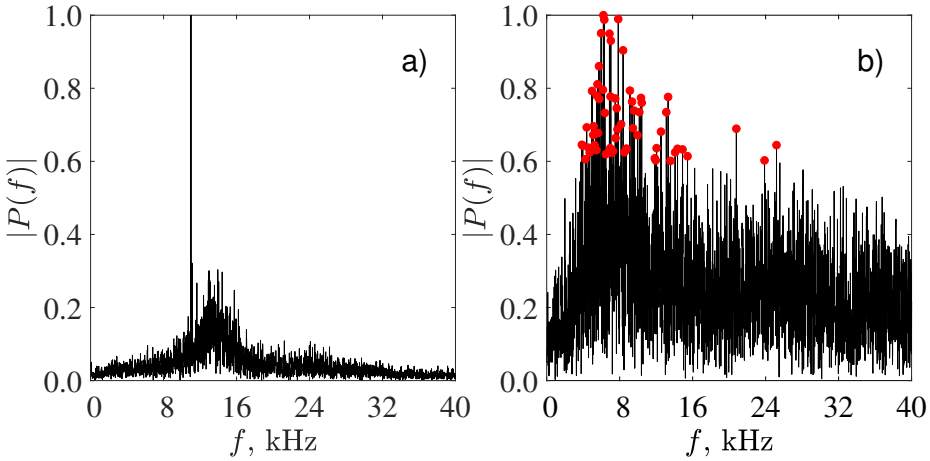

Figure 8.7: a) Spectrum for global intensity for $m = 0$ and b) spectrum for azimuthal modes m at 5V, 10 kHz modulation. Each plot is normalized to the highest amplitude. Red circles mark peaks with the most prominent frequencies (with amplitude > 0.6 of maximum).

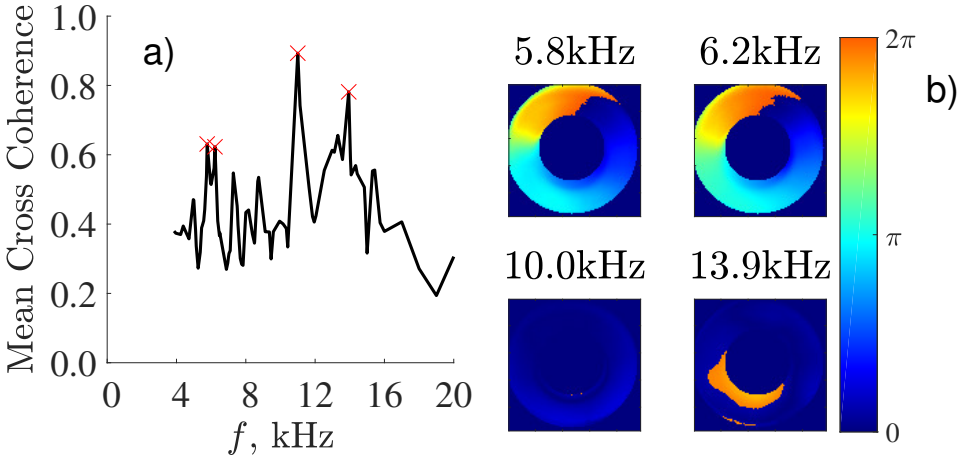

Figure 8.8: a) Averaged coherence value for the range of frequencies of interest from Fig. 8.7b. Red crosses show frequencies where averaged coherence reaches its maximum. b) Phase maps for most coherent frequencies (marked with red crosses on the left panel). The colors representing different phase shift values as shown on the color bar.

Coherence for each selected frequency is shown in Fig. 8.8a. There are two strong peaks related to intrinsic axial mode (∼13.9 kHz) and modulation frequency (10 kHz). For

azimuthal modes, there are two peaks at 5.8 and 6.2 kHz. Phase maps at these frequencies confirm that this is the azimuthally propagating $m = 1$ mode, as there is a smooth transition from 0 to 2π, see Fig. 8.4b for the reference. Spoke mode is still non-stationary, however range of frequencies is narrower in this case and this range overlaps with the natural $m = 1$ mode frequency range. The intrinsic breathing mode is unchanged and exist at the same frequency ~ 13.9 kHz.

Spectra at 5V, 15 kHz modulation case are presented in Fig. 8.9a, b. Spectrum for the $m = 0$ mode is almost the same as in previous case, except for the modulation peak is at 15 kHz. Spectrum for the azimuthal modes shows multiple peaks located in the same region of 6-8 kHz. Frequencies with peaks higher than 0.6 are selected for the CSD analysis.

Analysis of coherence and phase shifts is shown in Fig. 8.10. There is a strong peak related to external modulations at 15 kHz, and several smaller peaks at frequencies of natural breathing. Phase maps shows that pixels intensity changes at these frequencies in phase. Phase maps for two peaks at 5.8 and 7.5 kHz shows that phase changes smoothly from 0 to 2π for both frequencies (see Fig. 8.8b for the reference); therefore, there is a non-stationary spoke mode with $m = 1$, which frequency changes in time.

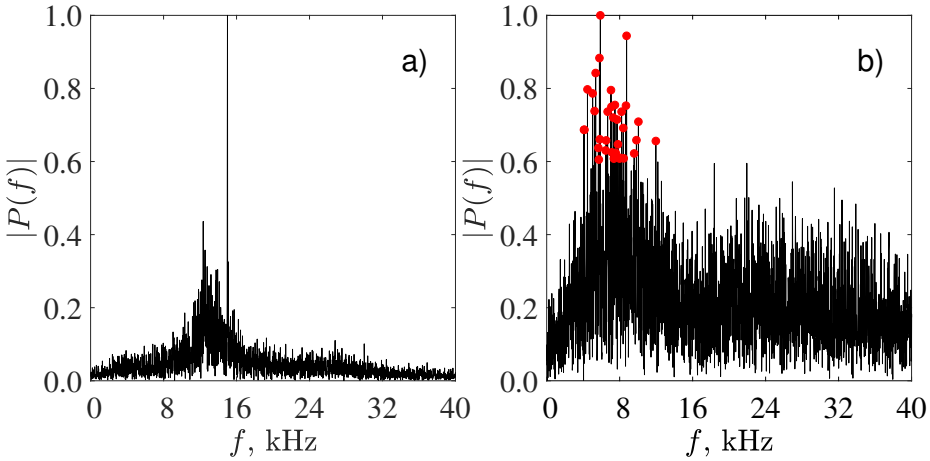

Figure 8.9: a) Spectrum for global intensity for $m = 0$ and b) spectrum for azimuthal modes m at 5V, 15 kHz modulation. Each plot is normalized to the highest amplitude. Red circles mark peaks with the most prominent frequencies (with amplitude > 0.6 of maximum).

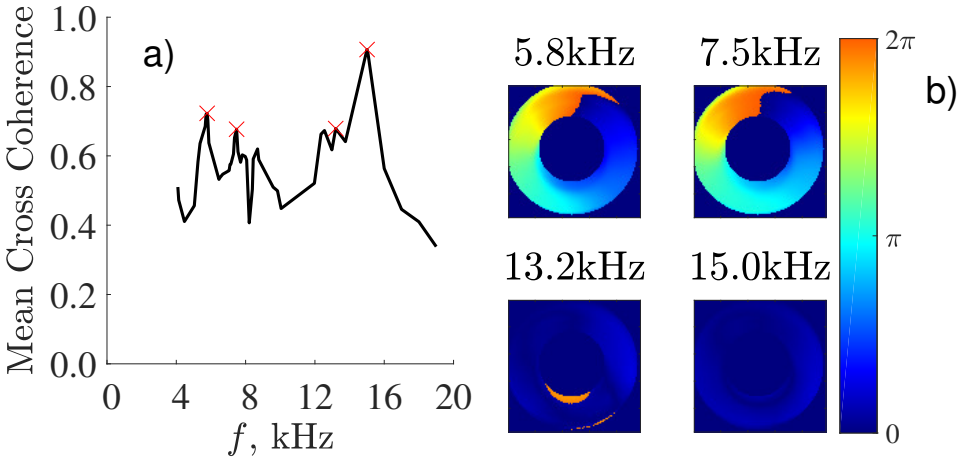

Figure 8.10: a) Averaged coherence value for the range of frequencies of interest from Fig. 8.9b. Red crosses show frequencies where averaged coherence reaches its maximum. b) Phase maps for most coherent frequencies (marked with red crosses on the left panel). The colors representing different phase shift values as shown on the color bar.

In general, as illustrated in Figs. 8.8 and 8.10, external modulations at frequencies of the intrinsic breathing mode in linear regime has no effect on the axial or azimuthal modes. In all cases, the breathing, spoke and external modulation frequencies are clearly present in the linear regime.

The next set of experiments was conducted in non-linear regime, with the amplitude of the external modulations of 30 V. First, the 15 kHz frequency, which is higher than the natural axial mode frequency, was used. Fourier spectra for $m = 0$ and finite m modes are shown in Figure 8.11. There is a strong peak at 15 kHz for $m = 0$ mode, and some small peaks, related to the intrinsic breathing oscillations at ∼13 kHz. For azimuthal m spectrum, there is a significant difference in the spectrum structure. There are peaks in a range of 6 to 8 kHz, however spectrum is are much nosier compare to linear regime or natural oscillations, and it is difficult to identify any prominent frequencies. For CSD analysis all peaks with amplitude higher than 0.6 were selected.

Results of the CSD analysis are shown in Figure 8.12. There are peaks on coherence plot which correspond to natural axial mode at ∼12-13 kHz and modulation at 15 kHz. However, there are no prominent peaks in the region where azimuthal peaks existed. Phase maps show the existence of the intrinsic breathing mode at ∼12 kHz, as well as the effect of oscillations

at 15 kHz. Several frequencies were chosen between 5 to 8 kHz, to show that there is no spoke mode in this case. It becomes clear if compare these phase plots with plot for 7.0 kHz in Fig 8.4b. There is no smooth transition from 0 to 2π in azimuthal direction.

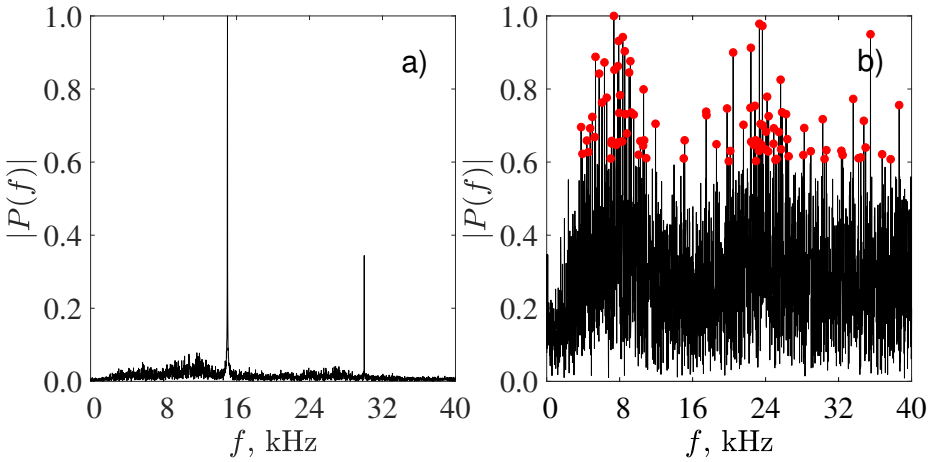

Figure 8.11: a) Spectrum for global intensity for $m = 0$ and b) spectrum for azimuthal modes m at 30V, 15 kHz modulation. Each plot is normalized to the highest amplitude. Red circles mark peaks with the most prominent frequencies (with amplitude > 0.6 of maximum).

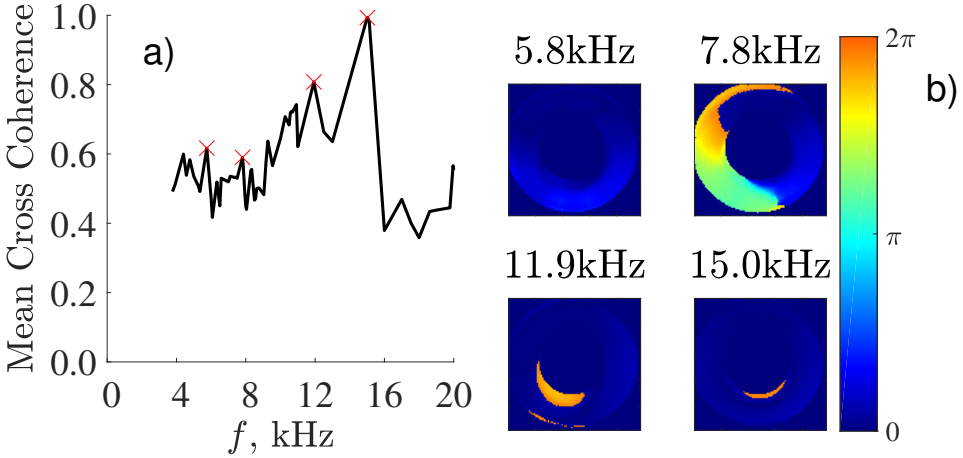

Figure 8.12: a) Averaged coherence value for the range of frequencies of interest from Fig 8.11b. Red crosses shows frequencies related to the external modulation (15 kHz) and intrinsic breathing mode (12 kHz), and two frequencies in the range of natural spoke mode frequency (6-8 kHz). b) Phase maps for selected frequencies, marked with red crosses. The colors representing different phase shift values as shown on the color bar.

Finally, the modulations with 30 V amplitude and 10.0 kHz frequency were applied to the thruster. There are strong peaks related to modulation at 10.0 kHz and nonlinear harmonics on $m = 0$ mode spectrum (see, Fig. 8.13a). However, there are no other visible peaks related to intrinsic breathing oscillations. Spectrum for azimuthal modes, shown in Fig. 8.13b, shows very noisy spectrum for finite m mode, without any identifiable range of frequencies. As in previous case, peaks with amplitudes higher than 0.6 were selected and the CSD technique was applied.

The coherence plot and phase maps for the case of 30V, 10.0 kHz modulations are shown in Figure 8.14. There is a strong peak at modulation frequency on the coherence plot. No other coherent frequencies are identifiable from this plot. In order to plot phase maps, we chose several frequencies in the range of intrinsic spoke mode. Resulting phase maps are presented in Fig. 8.14b. As one can see, there are no azimuthal structures in this case; compare these phase maps to Fig. 8.5b.

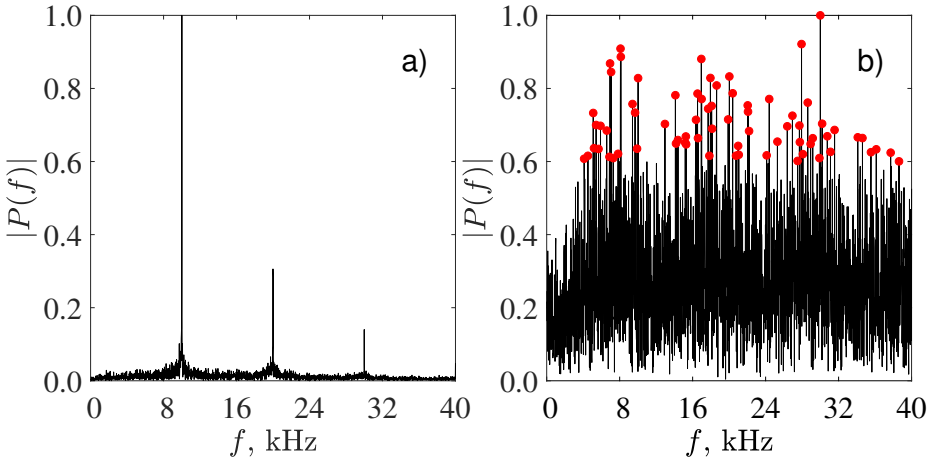

Figure 8.13: a) Spectrum for global intensity for m=0 and b) spectrum for azimuthal modes m at 30V, 10 kHz modulation Each plot is normalized to the highest amplitude. Red circles mark peaks selected for the CSD analysis (with amplitude > 0.6 of maximum).

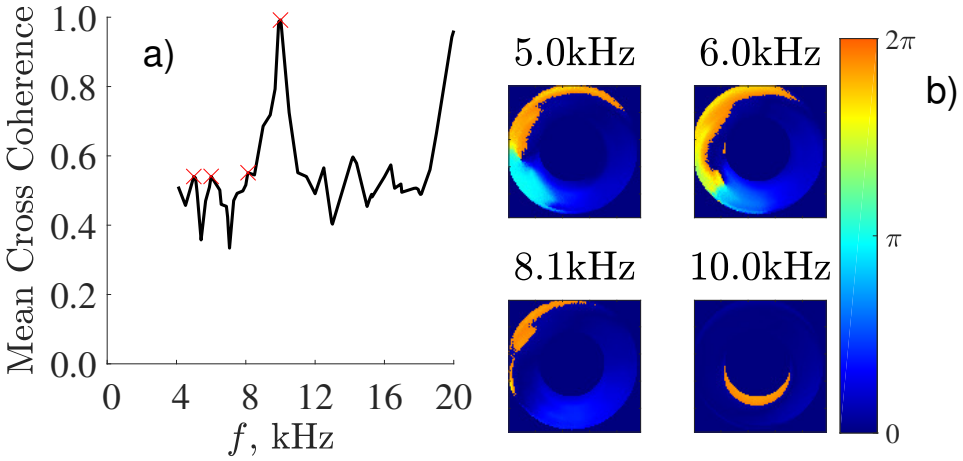

Figure 8.14: a) Averaged coherence value for the range of frequencies of interest from Fig 10b. Red crosses shows frequencies related to the external modulation (10 kHz), and three frequencies in the range of natural spoke mode frequency (6-8 kHz). b) Phase maps for most selected frequencies, marked with red crosses. The colors representing different phase shift values as shown on the color bar.

8.7 Conclusion

In this work, we have demonstrated that the azimuthally rotating spoke mode can be suppressed by the external modulation of the anode potential at frequencies around natural breathing mode. Such behaviour was captured by the combination of image processing techniques from Ref. [25, 185] and Ref. [26], which allowed us to identify coherent axial and azimuthal structures in the cylindrical Hall thruster during normal operation and with externally applied modulations of anode potential.

For normal operation we identify coherent structures (breathing mode) in axial direction at $\sim$ 13.9 kHz, which frequency remains relatively stationary in time. Analysis of the azimuthally propagating structure (spoke mode) revealed that its frequency varied in 5.8-8.5 kHz range, that shows that the spoke mode is non-stationary, as its frequency changes over time.

External modulations were applied in the linear (5V) and nonlinear (30V) thruster response regimes. Modulation frequency was varied in each regime. In the linear regime, no effect on the intrinsic breathing and spoke modes was detected. Both modes have approximately the same frequencies as without modulations. In the nonlinear regime, azimuthal

structures disappear at any modulation frequency in the range 10-15 kHz.

Note that the driving of breathing oscillations in the non-linear regime can suppress all low frequency intrinsic modes including breathing and spoke. In particular, it was also shown that in the non-linear regime (± 30V) at a lower modulation frequency (10.0 kHz) than the intrinsic breathing mode (13.9 kHz), disappears and no other coherent mode frequency (except the 10.0 kHz modulation) is observed. These results show that there is an interaction between the azimuthal and axial modes. There exist several mechanisms which might be responsible for such interaction. The azimuthal modes, such as spoke, are sensitive and can be driven by the axial gradients of plasma density and axial electric field (e.g. via the Simon-Hoh instability mechanism). Such axial gradients occur in the axial mode such as breathing mode. The effectiveness of the coupling (interaction) will depend on the relative frequency spread between the modes. Additional coupling mechanism may also come from the interaction of ionization fronts [25]. Our experiments provide an important evidence that the spoke may be suppressed by proper modulations of the axial parameters.

Acknowledgements

This work was supported by DOE. We acknowledge Yuan Shi, Scott Keller, Ahmed Diallo, and Igor Kaganovich for fruitful discussions, and Alex Merzhevskiy for his technical support.

Chapter 9

Conclusions and future work

Plasmas with low degrees of ionization in crossed electric and magnetic fields, magnetized electrons, and unmagnetized ions have been used in various industrial applications (space propulsion, ion sources, material processing, etc.) for a long time. Numerous experiments showed that such plasmas are subject to strong turbulent oscillations due to various instability mechanisms. This thesis was focused on studies of Hall thrusters, devices used for space propulsion, and two main types of strong large-scale oscillations: axial breathing mode and azimuthally rotating mode or spoke.

The range of research topics in this thesis covered theoretical, modeling, and experimental studies; development and implementation of diagnostic; experimental investigations of methods for active control; and modeling of the real experimental situations. All of these topics have a common goal of uncovering new knowledge about large-scale oscillations, their mechanisms, difficulties of their diagnostic, and finding ways to control them.

The theoretical analysis in the thesis was centered around the nonlocal model for Simon-Hoh and lower-hybrid instabilities, which are considered to be important elements for the formation of the rotating spoke. An azimuthally propagating spoke is a low-frequency mode intrinsic to all $\mathbf{E} \times \mathbf{B}$ devices and is responsible for a large portion of the anomalous current in the system [21]. As described in Chapter 4, predictions of the nonlocal model can be significantly different from the results of local models, especially for long wavelength modes. Global modes can extend into regions where local instability criteria are not satisfied. This is important for studies of anomalous transport, which is more pronounced for low k modes. Nonlocal model for complex profiles of plasma parameters showed that stability regions are different for low and high-frequency modes. Eigenmodes with higher frequency are unstable in spatially narrow regions, while low-frequency eigenmodes can be presented in a whole

domain.

A developed Time-Resolved Laser-Induced Fluorescence diagnostic and its application for studies of the breathing mode were presented in Chapter 5. The LIF diagnostic is widely used in the Hall thruster community for the detection of ion and neutral atoms dynamics [2, 83, 125, 129, 132]. The time-resolved version of this diagnostic allows for monitoring of changes in ion velocity distribution function in time, and corresponding changes in the electric field structure. The results of this diagnostic can be directly compared to kinetic plasma simulations, and play an important role in numerical models verification. The experimental analysis, reported in this thesis critically considered the connection between the evolution of the IVDF and plasma properties, like plasma density and electron temperature. Measurements of plasma parameters were done with Langmuir and emissive probes, and it was shown that oscillations in the electron temperature, by virtue of the presence of large-scale oscillations (here it was the breathing mode), can introduce additional modifications to the shape of IVDF due to a depopulation of the probed meta-stable level, or even cause the collapse of the LIF signal. Therefore, this finding has identified an important limitation of the LIF diagnostic.

Our studies of the breathing mode included the investigation of the effect of active control (implemented by external modulations of the anode potential) on the mode characteristics and thruster efficiency. There are several examples of implementation of systems of active control in Hall thrusters, however not many theoretical modeling of such systems was done [77, 78, 174, 183, 184]. Initially, the system of active control was used as a part of the time-resolved LIF diagnostic in order to make breathing oscillation coherent in time. Further studies have revealed different types of thruster response, depending on an amplitude of these modulations. For small amplitudes ($<$10% of the discharge voltage) the RMS value of the discharge current grows almost linearly with the amplitude. However, for large modulation amplitudes ($>$10% of the discharge voltage), the RMS value of the discharge current grows nonlinearly. These results inspired the further studies of the ion current response on modulations. Measurements of the ion current with the rotating planar probe indicated that the ion current responds similarly to the discharge current. However, the ion current increases faster compared to the discharge current, which leads to a corresponding increase of the propellant

and beam utilizations of the thruster. These results are presented in Chapter 7.

The new regime of the thruster response discovered in our studies motivated our numerical modeling of the breathing mode in Hall thrusters. A one-dimensional time-dependent model with included ionization, constant neutral flux from the anode, constant electron temperature, and without wall losses, was considered.

These studies involved two complementary approaches. First, steady-state profiles of the axial plasma flow in the thruster were obtained. This was a prerequisite for time-dependent simulations, where the proper initial conditions and a set of boundary conditions are required. The special point, where the sonic transition occurs, is present in this model due to the diffusion effect. This results in a discontinuity in the equations, which can be treated analytically. Such treatment allowed for a numerical integration of equations in order to obtain stationary profiles. A step-by-step algorithm for this process was developed. The parametric investigation (as a function of the total current, neutral flux, and the plasma density) of solutions uncovered their complicated structure. Different types of steady-state profiles, when used as initial values in time-dependent simulations, result in different oscillation regimes: single mode or multimode. More details about these results are in Chapter 6.

Secondly, time-dependent simulations with externally modulated potential were conducted. The parameters chosen for simulations were close to CHT conditions, and the stationary profiles were obtained with the method described in Chapter 6. Behavior similar to that observed experimentally was captured with these simulations. The model had two types of response, depending on the applied modulation amplitude. Detailed studies of oscillating plasma profiles suggested that the increase in the ion current values is related to the reduction of the phase shift between oscillations of the ion density and the electric field. The results of these simulations are presented in Chapter 7.

As it was mentioned before, the profiles of plasma parameters can significantly affect the type of unstable modes and regions of stability. Axial profiles in Hall thrusters are modified in the presence of the breathing mode, see results in Chapters 6 and 7. Therefore, the spoke mode can be impacted by the breathing mode through this mechanism. This connection was investigated in experiments with a fast-frame camera diagnostic. Experiments were conducted in the regime when both oscillations were presented. A recorded signal of the

light emission from the plasma was analyzed with the developed algorithm; breathing, spoke modes and their frequencies were identified. It was shown that the spoke mode can be suppressed when the thruster is in the regime of nonlinear response. Thus, the interaction between modes was confirmed. The results of this research are presented in Chapter 8

The author has several suggestions for possible future research directions.

The nonlocal model can be extended by the inclusion of other effects, studied with local models: effect of the magnetic field gradient, collisions, ionization. Effects of the shear flows should be considered as well, as local models cannot predict instabilities related to them.

Studies of stationary profiles revealed that thrust behavior and stability strongly depend on the initial profiles and a set of boundary conditions. This investigation should be extended by the inclusion of the effects of the electron temperature profiles and wall-losses effects. Further simulations with "wrong" boundary conditions should be conducted. This might provide insights into the control of plasma oscillations by controlling boundary conditions.

The effect of the increased thruster performance requires further exploration in order to determine the optimal regimes for such increase, and its feasibility for use with real thrusters. This regime could be used as some kind of throttling regime, causing thrust to increase by the imposed modulations. Another possibility is propellant saving. The breathing mode could be amplified by a reduction of the mass flow. Corresponding thrust reduction could be compensated by the discovered effect. Detailed measurements of plasma parameters with probes and an advanced optical diagnostic, which does not depend on plasma parameters oscillations (two-photon LIF), could help to understand the physical mechanisms of this process better.

The coupling between spoke and breathing mode should be further investigated theoretically and experimentally. Image diagnostic should be supplemented with the probe diagnostic. Theoretical work showed that there might be a case where one mechanism is responsible for both modes [141]; therefore, the observed behavior can be a good benchmark for future models and simulations.

References

[1] J. Winter, A. Hecimovic, T. de los Arcos, M. Böke, and V. S. von der Gathen, "Instabilities in high-power impulse magnetron plasmas: from stochasticity to periodicity," *Journal of Physics D: Applied Physics*, vol. 46, no. 8, p. 084007, 2013.

[2] P. Svarnas, I. Romadanov, A. Diallo, and Y. Raitses, "Laser-induced fluorescence of Xe I and Xe II in ambipolar plasma flow," *IEEE Transactions on Plasma Science*, pp. 1–12, 2018.

[3] G. D. Hobbs and J. A. Wesson, "Heat flow through a Langmuir sheath in the presence of electron emission," *Plasma Physics*, vol. 9, no. 1, p. 85, 1967.

[4] E. H. Lock, D. Y. Petrovykh, P. Mack, T. Carney, R. G. White, S. G. Walton, and R. F. Fernsler, "Surface composition, chemistry, and structure of polystyrene modified by electron-beam-generated plasma," *Langmuir*, vol. 26, no. 11, pp. 8857–8868, 2010. PMID: 20369866.

[5] J. T. Gudmundsson, N. Brenning, D. Lundin, and U. Helmersson, "High power impulse magnetron sputtering discharge," *Journal of Vacuum Science & Technology A*, vol. 30, no. 3, p. 030801, 2012.

[6] S. N. Abolmasov, "Physics and engineering of crossed-field discharge devices," *Plasma Sources Science and Technology*, vol. 21, no. 3, p. 035006, 2012.

[7] A. I. Morozov, "The conceptual development of stationary plasma thrusters," *Plasma Physics Reports*, vol. 29, no. 3, pp. 235–250, 2001.

[8] A. I. Morozov and V. V. Savelyev, "Fundamentals of stationary plasma thruster theory," in *Reviews of Plasma Physics* (B. B. Kadomtsev and V. D. Shafranov, eds.), pp. 203–391, Boston, MA: Springer US, 2000.

[9] F. R. Chang-Díaz, "Plasma propulsion for interplanetary flight," *Thin Solid Films*, vol. 506-507, pp. 449 – 453, 2006. The Joint Meeting of 7th APCPST (Asia Pacific Conference on Plasma Science and Technology) and 17th SPSM (Symposium on Plasma Science for Materials).

[10] T. Lafleur, "Helicon plasma thruster discharge model," *Physics of Plasmas*, vol. 21, no. 4, p. 043507, 2014.

[11] M. N. Rosenbluth and A. N. Kaufman, "Plasma diffusion in a magnetic field," *Phys. Rev.*, vol. 109, pp. 1–5, Jan 1958.

[12] D. Bohm, *The characteristics of electrical discharges in magnetic fields*. McGraw-Hill, 1949.

[13] L. Spitzer, "Particle diffusion across a magnetic field," *The Physics of Fluids*, vol. 3, no. 4, pp. 659–661, 1960.

[14] A. I. Morozov, A. Y. Kislov, and I. P. Zubkov, "Strong-current plasma accelerator with closed electron drift," *Soviet Journal of Experimental and Theoretical Physics Letters*, vol. 7, p. 172, Mar. 1968.

[15] G. Janes, J. Dotson, and T. Wilson, "Electrostatic acceleration of neutral plasmas–momentum transfer through magnetic fields," *Technical Report*, 9 1962.

[16] D. M. Goebel and I. Katz, *Fundamentals of Electric Propulsion*. John Wiley and Sons, Inc., 2008.

[17] A. Simon, "Instability of a partially ionized plasma in crossed electric and magnetic fields," *Physics of Fluids*, vol. 6, no. 3, pp. 382–388, 1963.

[18] F. C. Hoh, "Instability of Penning-type discharges," *Physics of Fluids*, vol. 6, no. 8, pp. 1184–1191, 1963.

[19] J. P. Boeuf and B. Chaudhury, "Rotating instability in low-temperature magnetized plasmas," *Physical Review Letters*, vol. 111, no. 15, 2013.

[20] M. Sekerak, B. Longmier, A. D. Gallimore, D. L. Brown, R. Hofer, and J. E. Polk, "Azimuthal spoke propagation in Hall effect thruster," in *33rd International Electric Propulsion Conference, Washington D.C., USA*, pp. IEPC–2013–143, 2013.

[21] C. L. Ellison, Y. Raitses, and N. J. Fisch, "Cross-field electron transport induced by a rotating spoke in a cylindrical Hall thruster," *Physics of Plasmas*, vol. 19, no. 1, 2012.

[22] Y. Raitses, P. Baele, and V. Donnelly, "A parametric study of DC-RF Penning-type plasma discharge," in *APS Meeting Abstracts*, 2011.

[23] Y. Raitses, J. B. Parker, E. Davis, and N. J. Fisch, "Background gas pressure effects in the cylindrical Hall thruster," *2010-6775, 46TH AIAA/ASME/SAE/ASEE Joint Propulsion Conference & Exhibit*, pp. 995–1006, 2010.

[24] Y. Raitses, D. Staack, and N. J. Fisch, "Controlling the plasma potential distribution in segmented-electrode Hall thruster," *IEEE Transactions on Plasma Science*, vol. 36, pp. 1202–1203, Aug 2008.

[25] M. S. McDonald, *Electron transport in Hall thrusters*. PhD thesis, Michigan University, 2012.

[26] A. D. Light, S. C. Thakur, C. Brandt, Y. Sechrest, G. R. Tynan, and T. Munsat, "Direct extraction of coherent mode properties from imaging measurements in a linear plasma column," *Physics of Plasmas*, vol. 20, no. 8, p. 082120, 2013.

[27] Y. Raitses, D. Staack, M. Keidar, and N. J. Fisch, "Electron-wall interaction in Hall thruster," *Physics of Plasmas*, vol. 12, no. 5, 2005.

[28] I. Romadanov, A. Smolyakov, Y. Raitses, I. Kaganovich, T. Tian, and S. Ryzhkov, "Structure of nonlocal gradient-drift instabilities in Hall $\mathbf{E} \times \mathbf{B}$ discharges," *Physics of Plasmas*, vol. 23, no. 12, p. 122111, 2016.

[29] I. Romadanov, Y. Raitses, A. Diallo, K. Hara, I. D. Kaganovich, and A. Smolyakov, "On limitations of laser-induced fluorescence diagnostics for xenon ion velocity distribution function measurements in Hall thrusters," *Physics of Plasmas*, vol. 25, no. 3, p. 033501, 2018.

[30] I. Romadanov, Y. Raitses, and A. Smolyakov, "Hall thruster operation with externally driven breathing mode oscillations," *Plasma Sources Science and Technology*, vol. 27, no. 9, p. 094006, 2018.

[31] E. Y. Choueiri, "A critical history of electric propulsion: The first 50 years (1906-1956)," *Journal of Propulsion and Power*, vol. 20, no. 2, pp. 193–203, 2004.

[32] R. G. Jahn, *Physics of electric propulsion*. Courier Corporation, 2006.

[33] R. M. Georgevic, "The solar radiation pressure force and torques model.," *Journal of the Astronautical Sciences*, vol. 20, pp. 257–274, 1973.

[34] R. W. Bussard, "Galactic matter and interstellar flight," *Astronautica Acta*, vol. 6, no. 4, pp. 179–194, 1960.

[35] K. E. Tsiolkovsky, "The exploration of cosmic space by means of reaction devices," *The Science Review (in Russian)*, vol. 5, 1903.

[36] W. Moore, *A Treatise on the Motion of Rockets; to which is Added, An Essay on Naval Gunnery, in Theory and Practice: Designed for the Use of the Army and Navy, and All Places of Military, Naval and Scientific Insrtruction*. G. and S. Robinson, 1813.

[37] R. H. Frisbee, "Limits of interstellar flight technology," *Frontiers of Propulsion Science*, vol. 227, pp. 31–126, 2009.

[38] S. Mazouffre, "Electric propulsion for satellites and spacecraft: established technologies and novel approaches," *Plasma Sources Science and Technology*, vol. 25, no. 3, p. 033002, 2016.

[39] S. K. Borowski, D. R. McCurdy, and T. W. Packard, "Nuclear thermal rocket (NTR) propulsion: A proven game-changing technology for future human exploration missions," in *Association Aeronautique et Astronautique de France, Washington, DC; United States*, pp. E–18199, 2012.

[40] W. Robbins, "An historical perspective of the NERVA nuclear rocket engine technology program," in *Conference on Advanced SEI Technologies*, p. 3451, 1991.

[41] M. Gibson, *Development of NASA's small fission power system for science and human exploration.* NASA technical memorandum, National Aeronautics and Space Administration, Glenn Research Center, 2015.

[42] J. W. Dankanich, "Low-thrust propulsion technologies, mission design, and application," in *Aerospace Technologies Advancements* (T. T. Arif, ed.), ch. 12, Rijeka: IntechOpen, 2010.

[43] R. G. Jahn and E. Y. Choueiri, "Electric propulsion," in *Encyclopedia of Physical Science and Technology (Third Edition)* (R. A. Meyers, ed.), pp. 125 – 141, New York: Academic Press, third edition ed., 2003.

[44] O. Gorshkov, V. Muravlev, and A. Shagayda, "Hall and ion electric propulsion for spacecraft," *Mashinostroenie (in Russian)*, vol. 12, 2008.

[45] T. Melkumov, *On fundamentally new sources of energy for rockets in the early works of the pioneers of astronautics*, vol. 1, pp. 186–194. NASA, 1977.

[46] V. Kim, G. Popov, B. Arkhipov, V. Murashko, O. Gorshkov, A. Koroteyev, V. Garkusha, A. Semenkin, and S. Tverdokhlebov, "Electric propulsion activity in Russia," *IEPC Paper*, vol. 5, p. 2001, 2001.

[47] V. V. Zhurin, H. R. Kaufman, and R. S. Robinson, "Physics of closed drift thrusters," *Plasma Sources Science and Technology*, vol. 8, 1999.

[48] P. Kovrov, A. Morozov, L. Tokarev, and G. Y. Shchepkin, "Magnetic field distribution in a coaxial plasma injector," in *Soviet Physics Doklady*, vol. 12, p. 155, 1967.

[49] A. Morozov, V. Nevrovskii, and V. Smirnov, "Effect of a feedback system on the plasma flux in an accelerator with closed electron drift," *Sov. Phys.-Tech. Phys. (Engl. Transl.)*, vol. 18, pp. 344–347, 9 1973.

[50] A. I. Morozov, Y. V. Esipchuk, and e. a. A. M. Kapulkin and, "Axially nonsymmetrical oscillations and anomalous conductivity in plasma accelerators with closed drift of electrons," *Sov. Phys. Tech. Phys.*, vol. 17, p. 482, 1972.

[51] Y. S. Popov and A. V. Zharinov, "Plasma acceleration by a closed-circuit Hall current," *Sov. Phys.–Tech. Phys*, vol. 12, pp. 208 – 211, 1967.

[52] S. Grishin, V. Erofeev, A. Zharinov, V. Naumkin, and I. Safronov, "Characteristics of a two-stage ion accelerator with an anode layer," *Journal of Applied Mechanics and Technical Physics*, vol. 19, no. 2, pp. 166–173, 1978.

[53] L. A. Artsimovich, I. M. Andronov, and Y. V. Esipchuk, "Development of the stationary plasma thruster (SPT) and its test at "Meteor" satellite," *Kosmicheskiye issledovaniya (in Russian)*, vol. 12, no. 3, pp. 451–468, 1974.

[54] M. Meyer, L. Johnson, B. Palaszewski, D. Goebel, H. White, and D. Coote, "NASA: In-space propulsion systems roadmap," 2012.

[55] A. D. Gallimore, "Near-and far-field characterization of stationary plasma thruster plumes," *Journal of Spacecraft and Rockets*, vol. 38, no. 3, pp. 441–453, 2001.

[56] K. F. Long, *Deep space propulsion: a roadmap to interstellar flight*. Springer Science & Business Media, 2011.

[57] I. Levchenko, S. Xu, G. Teel, D. Mariotti, M. Walker, and M. Keidar, "Recent progress and perspectives of space electric propulsion systems based on smart nanomaterials," *Nature communications*, vol. 9, no. 1, p. 879, 2018.

[58] "NASA Cubesat Launch Initiative." https://www.nasa.gov/content/about-cubesat-launch-initiative.

[59] M. Swartwout, "Cubesat database." https://sites.google.com/a/slu.edu/swartwout/home/cubesat-database.

[60] A. R. Tummala and A. Dutta, "An overview of cube-satellite propulsion technologies and trends," *Aerospace*, vol. 4, no. 4, p. 58, 2017.

[61] Y. Raitses and N. J. Fisch, "Parametric investigations of a nonconventional Hall thruster," *Physics of Plasmas*, vol. 8, no. 5, pp. 2579–2586, 2001.

[62] A. Smirnov, "Experimental and theoretical studies of cylindrical Hall thrusters," in *APS Meeting Abstracts*, Oct. 2006.

[63] K. Polzin, E. Sooby, A. Kimberlin, Y. Raitses, E. Merino, and N. Fisch, "Performance of a permanent-magnet cylindrical Hall-effect thruster," in *45th AIAA/ASME/SAE/ASEE Joint Propulsion Conference & Exhibit*, p. 4812, 2009.

[64] G. S. Janes and R. S. Lowder, "Anomalous electron diffusion and ion acceleration in a low-density plasma," *Physics of Fluids*, vol. 9, no. 6, p. 1115, 1966.

[65] N. B. Meezan and M. A. Cappelli, "Kinetic study of wall collisions in a coaxial Hall discharge," *Phys. Rev. E*, vol. 66, p. 036401, Sep 2002.

[66] A. Morozov, "Wall conductivity effect in a well magnetized plasma(anomalous plasma conductivity attributed to presence of insulating walls with electric/ magnetic fields parallel/perpendicular respectively to walls)," *PMTF-Zhurnal Prikladnoi Mekhaniki I Tekhnicheskoi Fiziki*, pp. 19–22, 1968.

[67] A. Bugrova, A. Morozov, and V. Kharchevnikov, "Experimental study on near wall conductivity," *Fiz. Plazmy*, vol. 16, p. 849, 1992.

[68] E. P. Velikhov, V. S. Golubev, and A. M. Dykhne, "Physical phenomena in a low-temperature nonequilibrium plasma and in MHD generators with nonequilibrium conductivity," *Atomic Energy Review*, vol. 14, no. 2, pp. 325–385, 1976.

[69] J. L. Kerrebrock, "Nonequilibrium ionization due to electron heating . 1. Theory," *AIAA Journal*, vol. 2, no. 6, pp. 1072–1080, 1964.

[70] B. B. Kadomtsev and A. V. Nedospasov, "Instability of the positive column in a magnetic field and the 'anomalous' diffusion effect," *Journal of Nuclear Energy. Part C, Plasma Physics, Accelerators, Thermonuclear Research*, vol. 1, no. 4, p. 230, 1960.

[71] B. A. Carreras, "Progress in anomalous transport research in toroidal magnetic confinement devices," *IEEE Transactions on Plasma Science*, vol. 25, pp. 1281–1321, Dec 1997.

[72] B. A. Jorns and R. R. Hofer, "Plasma oscillations in a 6-kW magnetically shielded Hall thruster," *Physics of Plasmas*, vol. 21, no. 5, 2014.

[73] Y. Raitses, A. Smirnov, and N. J. Fisch, "Effects of enhanced cathode electron emission on Hall thruster operation," *Physics of Plasmas*, vol. 16, no. 5, 2009.

[74] A. B. Mikhailovskii, *Theory of plasma instabilities*. Consultants Bureau, 1974.

[75] M. E. Griswold, C. L. Ellison, Y. Raitses, and N. J. Fisch, "Feedback control of an azimuthal oscillation in the $\mathbf{E} \times \mathbf{B}$ discharge of Hall thrusters," *Physics of Plasmas*, vol. 19, no. 5, 2012.

[76] E. Y. Choueiri, "Plasma oscillations in Hall thrusters," *Physics of Plasmas*, vol. 8, no. 4, pp. 1411–1426, 2001.

[77] N. Yamamoto, H. Takegahara, J. Aoyagi, K. Kuriki, T. Tamida, and H. Osuga, "Development of a novel power processing unit for Hall thrusters," *IEEE Transactions on Plasma Science*, vol. 43, pp. 158–164, Jan 2015.

[78] N. Yamamoto, T. Ito, H. Takegahara, H. Watanabe, T. Tamida, and H. Osuga, "Thrust performance in Hall thruster with pulsating operation," *Transactions of the Japan society for aeronautical and space sciences, aerospace technology Japan*, vol. 14, no. ists30, pp. Pb173–Pb176, 2016.

[79] Y. Raitses, A. Smirnov, and N. J. Fisch, "Enhanced performance of cylindrical Hall thrusters," *Applied Physics Letters*, vol. 90, no. 22, p. 221502, 2007.

[80] A. Smirnov, Y. Raitses, and N. J. Fisch, "Experimental and theoretical studies of cylindrical Hall thrusters," *Physics of Plasmas*, vol. 14, no. 5, p. 057106, 2007.

[81] A. Smirnov, Y. Raitses, and N. J. Fisch, "Parametric investigation of miniaturized cylindrical and annular Hall thrusters," *Journal of Applied Physics*, vol. 92, no. 10, pp. 5673–5679, 2002.

[82] S. Svanberg, "Atomic structure," in *Atomic and Molecular Spectroscopy*, pp. 5–30, Springer, 2001.

[83] D. Gawron, S. Mazouffre, N. Sadeghi, and A. Héron, "Influence of magnetic field and discharge voltage on the acceleration layer features in a Hall effect thruster," *Plasma Sources Science and Technology*, vol. 17, no. 2, p. 025001, 2008.

[84] H.-J. Kunze, *Introduction to plasma spectroscopy*, vol. 56. Springer Science & Business Media, 2009.

[85] J. E. Allen, R. L. F. Boyd, and P. Reynolds, "The collection of positive ions by a probe immersed in a plasma," *Proceedings of the Physical Society. Section B*, vol. 70, no. 3, p. 297, 1957.

[86] Y. Raitses, D. Staack, A. Smirnov, and N. J. Fisch, "Space charge saturated sheath regime and electron temperature saturation in Hall thrusters," *Physics of Plasmas*, vol. 12, no. 7, p. 073507, 2005.

[87] L. A. Schwager, "Effects of secondary and thermionic electron emission on the collector and source sheaths of a finite ion temperature plasma using kinetic theory and numerical simulation," *Physics of Fluids B: Plasma Physics*, vol. 5, no. 2, pp. 631–645, 1993.

[88] A. Fridman, "On the phenomena of the critical magnetic field and anomalous diffusion in weakly ionized plasma," in *Soviet Physics Doklady*, vol. 9, p. 75, 1964.

[89] C. N. Lashmore-Davies, "Negative energy waves," *Journal of Plasma Physics*, vol. 71, no. 2, p. 101–109, 2005.

[90] Y. Sakawa, C. Joshi, P. K. Kaw, F. F. Chen, and V. K. Jain, "Excitation of the modified Simon–Hoh instability in an electron beam produced plasma," *Physics of Fluids B: Plasma Physics*, vol. 5, no. 6, pp. 1681–1694, 1993.

[91] W. Frias, A. Smolyakov, I. Kaganovich, and Y. Raitses, "Long wavelength gradient drift instability in Hall plasma devices. II. Applications," *Physics of Plasmas*, vol. 20, no. 5, 2013.

[92] A. I. Smolyakov, O. Chapurin, W. Frias, O. Koshkarov, I. Romadanov, T. Tang, M. Umansky, Y. Raitses, I. D. Kaganovich, and V. P. Lakhin, "Fluid theory and simulations of instabilities, turbulent transport and coherent structures in partially-magnetized plasmas of $\mathbf{E} \times \mathbf{B}$ discharges," *Plasma Physics and Controlled Fusion*, vol. 59, no. 1, p. 014041, 2017.

[93] I. Romadanov, A. Smolyakov, W. Frias, O. Chapurin, and O. Koshkarov, "Generalized lower-hybrid mode with, density gradient, equilibrium $\mathbf{E} \times \mathbf{B}$ drift, collisions and finite electron Larmor radius: Numerical studies with MATLAB solver," *ArXiv e-prints*, Oct. 2016.

[94] P. Kelly and R. Arnell, "Magnetron sputtering: a review of recent developments and applications," *Vacuum*, vol. 56, no. 3, pp. 159 – 172, 2000.

[95] T. Ito, C. V. Young, and M. A. Cappelli, "Self-organization in planar magnetron microdischarge plasmas," *Applied Physics Letters*, vol. 106, no. 25, 2015.

[96] Y. B. Esipchuk, A. I. Morozov, G. N. Tilinin, and A. V. Trofimov, "Plasma oscillations in closed-drift accelerators with an extended acceleration zone," *Sov. Phys. Tech. Phys.*, vol. 18, p. 928, 1974.

[97] A. Kapulkin and M. M. Guelman, "Low-frequency instability in near-anode region of Hall thruster," *IEEE Transactions on Plasma Science*, vol. 36, pp. 2082–2087, Oct 2008.

[98] A. I. Smolyakov, W. Frias, I. D. Kaganovich, and Y. Raitses, "Sheath-induced instabilities in plasmas with drift," *Phys. Rev. Lett.*, vol. 111, p. 115002, Sep 2013.

[99] Y. Q. Tao, R. W. Conn, L. Schmitz, and G. Tynan, "Collisionless Simon–Hoh instability in a strongly double–sheared electric field," *Physics of Plasma*, vol. 1, no. 10, pp. 3193–3198, 1994.

[100] W. Frias, A. Smolyakov, I. D. Kaganovich, and Y. Raitses, "Wall current closure effects on plasma and sheath fluctuations in Hall thrusters," *Physics of Plasmas*, vol. 21, no. 6, 2014.

[101] A. Kapulkin and M. Guelman, "Lower-hybrid instability in Hall thruster," in *Proceedings of the 29th International Electric Propulsion Conference*, 2005.

[102] D. Escobar and E. Ahedo, "Global stability analysis of azimuthal oscillations in Hall thrusters," *IEEE Transactions on Plasma Science*, vol. 43, pp. 149–157, Jan 2015.

[103] Y. V. Esipchuk and G. N. Tilinin, "Drift instability in a Hall-current plasma accelerator," *Sov. Phys. Tech. Phys.*, vol. 21, no. 4, pp. 417–423, 1976.

[104] A. Kapulkin and M. Guelman, "Low frequency instability and enhanced transfer of electrons in near-anode region of Hall thruster," in *Proceedings of the 30th International Electric Propulsion Conference*, 2007.

[105] R. F. Ellis, E. Marden-MarsHall, and R. Majeski, "Collisional drift instability of a weakly ionized argon plasma," *Plasma Physics*, vol. 22, no. 2, p. 113, 1980.

[106] F. F. Chen, "Nonlocal drift modes in cylindrical geometry," *Physics of Fluids*, vol. 10, no. 8, pp. 1647–1651, 1967.

[107] D. Escobar and E. Ahedo, "Low frequency azimuthal stability of the ionization region of the Hall thruster discharge. II. global analysis," *Physics of Plasmas*, vol. 22, no. 10, p. 102114, 2015.

[108] L. N. Trefethen, *Spectral Methods in MATLAB.* Philadelphia: SIAM, 1nd ed., 2000.

[109] A. Smirnov, Y. Raitses, and N. J. Fisch, "Plasma measurements in a 100 W cylindrical Hall thruster," *Journal of Applied Physics*, vol. 95, no. 5, pp. 2283–2292, 2004.

[110] Y. Raitses, I. Kaganovich, and A. Smolyakov, "Effects of the Gas Pressure on Low Frequency Oscillations in ExB Discharges," in *Joint Conference of 30th ISTS, 34th IEPC and 6th NSAT*, 2015.

[111] A. M. DuBois, E. Thomas, W. E. Amatucci, and G. Ganguli, "Density gradient effects on transverse shear driven lower hybrid waves," *Physics of Plasmas*, vol. 21, no. 6, p. 062117, 2014.

[112] G. Ganguli, Y. C. Lee, and P. J. Palmadesso, "Kinetic theory for electrostatic waves due to transverse velocity shears," *The Physics of Fluids*, vol. 31, no. 4, pp. 823–838, 1988.

[113] W. Frias, A. I. Smolyakov, I. D. Kaganovich, and Y. Raitses, "Long wavelength gradient drift instability in Hall plasma devices. I. Fluid theory," *Physics of Plasmas*, vol. 19, no. 7, p. 072112, 2012.

[114] A. A. Litvak and N. J. Fisch, "Resistive instabilities in Hall current plasma discharge," *Physics of Plasmas*, vol. 8, no. 2, pp. 648–651, 2001.

[115] A. A. Litvak and N. J. Fisch, "Rayleigh instability in Hall thrusters," *Physics of Plasmas*, vol. 11, no. 4, pp. 1379–1383, 2004.

[116] A. Lazurenko, V. Krasnoselskikh, and A. Bouchoule, "Experimental insights into high-frequency instabilities and related anomalous electron transport in Hall thrusters," *IEEE Transactions on Plasma Science*, vol. 36, pp. 1977–1988, Oct 2008.

[117] R. Spektor, "Quasi-linear analysis of anomalous electron mobility inside a Hall thruster," in *Proceedings of the 30th International Electric Propulsion Conference*, 2007.

[118] K. Matyash, R. Schneider, and O. Kalentev, "3D PIC simulation of the rotating spoke in a Hall thruster," in *2014 IEEE 41st International Conference on Plasma Sciences (ICOPS) held with 2014 IEEE International Conference on High-Power Particle Beams (BEAMS)*, pp. 1–1, May 2014.

[119] S. Barral and E. Ahedo, "On the origin of low frequency oscillations in Hall thrusters," *AIP Conference Proceedings*, vol. 993, no. 1, pp. 439–442, 2008.

[120] J. Fife, M. Martinez-Sanchez, J. Szabo, J. Fife, M. Martinez-Sanchez, and J. Szabo, "A numerical study of low-frequency discharge oscillations in Hall thrusters," in *33rd Joint Propulsion Conference and Exhibit*, p. 3052, 1997.

[121] K. Hara, M. J. Sekerak, I. D. Boyd, and A. D. Gallimore, "Mode transition of a Hall thruster discharge plasma," *Journal of Applied Physics*, vol. 115, no. 20, p. 203304, 2014.

[122] M. Keidar and I. I. Beilis, "Electron transport phenomena in plasma devices with $\mathbf{E} \times \mathbf{B}$," *IEEE Transactions on Plasma Science*, vol. 34, pp. 804–814, June 2006.

[123] G. J. M. Hagelaar, J. Bareilles, L. Garrigues, and J.-P. Boeuf, "Role of anomalous electron transport in a stationary plasma thruster simulation," *Journal of Applied Physics*, vol. 93, no. 1, pp. 67–75, 2003.

[124] V. Zhurin, J. Kahn, H. Kaufman, K. Kozubsky, and M. Day, "Dynamic characteristics of closed drift thrusters," in *23rd International Electric Propulsion Conference*, 1993.

[125] C. J. Durot, A. D. Gallimore, and T. B. Smith, "Validation and evaluation of a novel time-resolved laser-induced fluorescence technique," *Review of Scientific Instruments*, vol. 85, no. 1, p. 013508, 2014.

[126] A. Diallo, S. Keller, Y. Shi, Y. Raitses, and S. Mazouffre, "Time-resolved ion velocity distribution in a cylindrical Hall thruster: Heterodyne-based experiment and modeling," *Review of Scientific Instruments*, vol. 86, no. 3, p. 033506, 2015.

[127] S. Keller, Y. Raitses, and A. Diallo, "Driving low frequency breathing oscillations in a Hall thruster," in *50th AIAA/ASME/SAE/ASEE Joint Propulsion Conference*, p. 3509, 2014.

[128] J. Vaudolon, L. Balika, and S. Mazouffre, "Photon counting technique applied to time-resolved laser-induced fluorescence measurements on a stabilized discharge," *Review of Scientific Instruments*, vol. 84, no. 7, p. 073512, 2013.

[129] A. Lucca Fabris, C. V. Young, and M. A. Cappelli, "Time-resolved laser-induced fluorescence measurement of ion and neutral dynamics in a Hall thruster during ionization oscillations," *Journal of Applied Physics*, vol. 118, no. 23, p. 233301, 2015.

[130] R. B. Lobbia, *A time-resolved investigation of the Hall thruster breathing mode*. PhD thesis, University of Michigan, 2010.

[131] C. Rebont, N. Claire, T. Pierre, and F. Doveil, "Ion velocity distribution function investigated inside an unstable magnetized plasma exhibiting a rotating nonlinear structure," *Phys. Rev. Lett.*, vol. 106, p. 225006, Jun 2011.

[132] G. Bachet, F. Skiff, M. Dindelegan, F. Doveil, and R. A. Stern, "Laser-induced fluorescence observation of self-organized ion structures induced by electrostatic perturbations," *Phys. Rev. Lett.*, vol. 80, pp. 3260–3263, Apr 1998.

[133] I. Romadanov, Y. Raitses, A. Diallo, I. Kaganovich, K. Hara, and A. Smolyakov, "Time-resolved measurements of modulated breathing oscillations in cylindrical Hall thruster," in *35th International Electric Propulsion Conference*, pp. IEPC–2017–267, 2017.

[134] W. Demtröder, *Laser spectroscopy: basic concepts and instrumentation*. Springer Science & Business Media, 2013.

[135] L. Dorf, Y. Raitses, and N. J. Fisch, "Effect of magnetic field profile on the anode fall in a Hall-effect thruster discharge," *Physics of Plasmas*, vol. 13, no. 5, p. 057104, 2006.

[136] V. A. Godyak, "Measuring EEDF in gas discharge plasmas," in *Plasma-Surface Interactions and Processing of Materials*, pp. 95–134, Springer, 1990.

[137] J. Bareilles, G. J. M. Hagelaar, L. Garrigues, C. Boniface, J. P. Boeuf, and N. Gascon, "Critical assessment of a two-dimensional hybrid Hall thruster model: Comparisons with experiments," *Physics of Plasmas*, vol. 11, no. 6, pp. 3035–3046, 2004.

[138] A. I. Strinic, G. N. Malovic, Z. L. Petrovic, and N. Sadeghi, "Electron excitation coefficients and cross sections for excited levels of argon and xenon ions," *Plasma Sources Science and Technology*, vol. 13, no. 2, p. 333, 2004.

[139] D. Mathur and C. Badrinathan, "Ionization of xenon by electrons: Partial cross sections for single, double, and triple ionization," *Phys. Rev. A*, vol. 35, pp. 1033–1042, Feb 1987.

[140] J. P. Boeuf and L. Garrigues, "Low frequency oscillations in a stationary plasma thruster," *Journal of Applied Physics*, vol. 84, no. 7, pp. 3541–3554, 1998.

[141] O. Koshkarov, A. I. Smolyakov, I. V. Romadanov, O. Chapurin, M. V. Umansky, Y. Raitses, and I. D. Kaganovich, "Current flow instability and nonlinear structures in dissipative two-fluid plasmas," *Physics of Plasmas*, vol. 25, no. 1, p. 011604, 2018.

[142] E. Ahedo, J. M. Gallardo, and M. Martinez-Sanches, "Model of the plasma discharge in a Hall thruster with heat conduction," *Physics of Plasmas*, vol. 9, no. 9, pp. 4061–4070, 2002.

[143] E. Ahedo and D. Escobar, "Influence of design and operation parameters on Hall thruster performances," *Journal of Applied Physics*, vol. 96, no. 2, pp. 983–992, 2004.

[144] S. Barral and E. Ahedo, "Low-frequency model of breathing oscillations in Hall discharges," *Physical Review E*, vol. 79, no. 4, 2009.

[145] L. Dorf, V. Semenov, and Y. Raitses, "Anode sheath in Hall thrusters," *Applied Physics Letters*, vol. 83, no. 13, pp. 2551–2553, 2003.

[146] N. Fisch and A. Fruchtman, "Modeling the Hall thruster," *PPPL reports*, 8 1998.

[147] A. Fruchtman, N. J. Fisch, and Y. Raitses, "Control of the electric-field profile in the Hall thruster," *Physics of Plasmas*, vol. 8, no. 3, pp. 1048–1056, 2001.

[148] E. Ahedo, P. Martinez-Cerezo, and M. Martinez-Sanchez, "One-dimensional model of the plasma flow in a Hall thruster," *Physics of Plasmas*, vol. 8, no. 6, pp. 3058–3068, 2001.

[149] A. Cohen-Zur, A. Fruchtman, J. Ashkenazy, and A. Gany, "Analysis of the steady-state axial flow in the Hall thruster," *Physics of Plasmas*, vol. 9, no. 10, pp. 4363–4374, 2002.

[150] S. Chable and F. Rogier, "Numerical investigation and modeling of stationary plasma thruster low frequency oscillations," *Physics of Plasmas*, vol. 12, no. 3, p. 033504, 2005.

[151] S. Barral, Z. Peradzynski, K. Makowski, and M. Dudeck, "Fluid model of Hall thruster - comparison with hybrid model," *High Temperature Material Processes: An International Quarterly of High-Technology Plasma Processes*, vol. 5, no. 2, 2001.

[152] G. N. Tilinin, "High-frequency plasma waves in a Hall accelerator with an extended acceleration zone," *Soviet Physics Technical Physics*, vol. 22, pp. 1684–1691, Aug. 1977.

[153] N. Yamamoto, K. Komurasaki, and Y. Arakawa, "Discharge current oscillation in Hall thrusters," *Journal of Propulsion and Power*, vol. 21, no. 5, pp. 870–876, 2005.

[154] J. M. Sankovic, J. A. Hamley, and T. W. Haag, "Performance evaluation of the Russian SPT-100 thruster at NASA LeRC," in *23rd IEPC Conference; 13-16 Sep. 1993; Seattle, WA; United States*, pp. IEPC–93–0947, 1994.

[155] T. Ito, N. Gascon, W. S. Crawford, and M. A. Cappelli, "Experimental characterization of a micro-Hall thruster," *Journal of Propulsion and Power*, vol. 23, no. 5, pp. 1068–1074, 2007.

[156] W. Liqiu, W. Chunsheng, H. Ke, and Y. Daren, "Effect of ionization distribution on the low frequency oscillations mode in Hall thrusters," *Physics of Plasmas*, vol. 19, no. 1, p. 012107, 2012.

[157] A. Smirnov, Y. Raitses, and N. J. Fisch, "Enhanced ionization in the cylindrical Hall thruster," *Journal of Applied Physics*, vol. 94, no. 2, pp. 852–857, 2003.

[158] A. Smirnov, Y. Raitses, and N. J. Fisch, "Controlling the plasma flow in the miniaturized cylindrical Hall thruster," *IEEE Transactions on Plasma Science*, vol. 36, pp. 1998–2003, Oct 2008.

[159] E. M. Granstedt, Y. Raitses, and N. J. Fisch, "Cathode effects in cylindrical Hall thrusters," *Journal of Applied Physics*, vol. 104, no. 10, p. 103302, 2008.

[160] K. D. Diamant, J. E. Pollard, Y. Raitses, and N. J. Fisch, "Ionization, plume properties, and performance of cylindrical Hall thrusters," *IEEE Transactions on Plasma Science*, vol. 38, pp. 1052–1057, April 2010.

[161] Y. Raitses, D. Staack, A. Dunaevsky, L. Dorf, and N. Fisch, "Measurements of plasma flow in a 2 kW segmented electrode Hall thruster," in *The proceedings of the 28th International Electric Propulsion Conference, Toulouse, France*, pp. 03–0139, 2003.

[162] A. Smolyakov, I. Romadanov, O. Chapurin, Y. Raitses, G. Hagelaar, and J. Boeuf, "Axial flow in Hall thruster," *Physics of Plasmas*, p. in preparation, 2018.

[163] B. Dudson, M. Umansky, X. Xu, P. Snyder, and H. Wilson, "BOUT++: A framework for parallel plasma fluid simulations," *Computer Physics Communications*, vol. 180, no. 9, pp. 1467 – 1480, 2009.

[164] B. D. Dudson, J. Madsen, J. Omotani, P. Hill, L. Easy, and M. Løiten, "Verification of BOUT++ by the method of manufactured solutions," *Physics of Plasmas*, vol. 23, no. 6, p. 062303, 2016.

[165] B. D. Dudson, A. Allen, G. Breyiannis, E. Brugger, J. Buchanan, L. Easy, S. Farley, I. Joseph, M. Kim, A. D. McGann, and et al., "BOUT : Recent and current developments," *Journal of Plasma Physics*, vol. 81, no. 1, p. 365810104, 2015.

[166] K. Hara, S. Keller, and Y. Raitses, "Measurements and theory of driven breathing oscillations in a Hall effect thruster," in *52nd AIAA/SAE/ASEE Joint Propulsion Conference*, p. 4532, 2016.

[167] S. Purves, "Phase and the Hilbert transform," *The Leading Edge*, vol. 33, no. 10, pp. 1164–1166, 2014.

[168] W. Liqiu, L. Wenbo, D. Yongjie, and Y. Daren, "Effect of low-frequency oscillation on performance of Hall thrusters," *Plasma Science and Technology*, vol. 20, no. 7, p. 075502, 2018.

[169] A. I. Morozov, "The conceptual development of stationary plasma thrusters," *Plasma Physics Reports*, vol. 29, pp. 235–250, Mar 2003.

[170] A. Morozov, *Physics and application of plasma accelerators*. Minsk: Nauka i Tekhnika), 1974.

[171] A. I. Morozov, *Fizicheskie osnovy kosmicheskikh elektroreaktivnykh dvigatelei*. Atomizdat (in Russian), 1978.

[172] A. Morozov, "Stationary plasma thruster (SPT) development steps and future perspectives," in *Proceedings of the 23rd International Electric Propulsion Conference*, pp. 13–16, 1993.

[173] C. Ellison, Y. Raitses, and N. Fisch, "Fast camera imaging of Hall thruster ignition," *IEEE Transactions on Plasma Science*, vol. 39, no. 11, pp. 2950–2951, 2011.

[174] S. Barral, J. Kaczmarczyk, J. Kurzyna, and M. Dudeck, "Closed-loop control of ionization oscillations in Hall accelerators," *Physics of Plasmas*, vol. 18, no. 8, 2011.

[175] V. V. Arsenin, "Possibility of suppressing ionization instability of a magnetized weakly ionized nonisothermal plasma by means of a system of feedbacks.," tech. rep., Inst. of Atomic Energy, Moscow, 1970.

[176] J. B. Taylor and C. N. Lashmore-Davies, "1.5 plasma stabilization by feedback," *AIP Conference Proceedings*, vol. 1, no. 1, pp. 23–26, 1970.

[177] H. P. Furth and P. H. Rutherford, "2.5 feedback control problems in tokamaks," *AIP Conference Proceedings*, vol. 1, no. 1, pp. 74–79, 1970.

[178] V. V. Arsenin and V. A. Chuyanov, "Reviews of topical problems: Suppression of plasma instabilities by the feedback method," *Soviet Physics Uspekhi*, vol. 20, pp. 736–762, 09 1977.

[179] H. Lashinsky and E. M. Dewan, "5.1 dynamic stabilization of plasma instabilities," *AIP Conference Proceedings*, vol. 1, no. 1, pp. 199–205, 1970.

[180] A. Morozov, "Plasma accelerators(plasma accelerators design, discussing physical principles, acceleration techniques, plasma conductivity and optimization)," *Plasma accelerators. (A 73-37352 19-25) Moscow, Izdatel'stvo Mashinostroenie, 1973,*, pp. 5–15, 1973.

[181] J. Parker, Y. Raitses, and N. Fisch, "Transition in electron transport in a cylindrical Hall thruster," *Applied Physics Letters*, vol. 97, no. 9, p. 091501, 2010.

[182] J. Carlsson, I. Kaganovich, A. Powis, Y. Raitses, I. Romadanov, and A. Smolyakov, "Particle-in-cell simulations of anomalous transport in a Penning discharge," *Physics of Plasmas*, vol. 25, no. 6, p. 061201, 2018.

[183] V. A. Nevrovskii, *Hall thrusters*. PhD thesis, Kurchatov Instiute, 1971.

[184] Y. Shi, Y. Raitses, and A. Diallo, "Controlling azimuthal spoke modes in a cylindrical Hall thruster using a segmented anode," *Plasma Sources Science and Technology*, vol. 27, no. 10, p. 104006, 2018.

[185] M. S. McDonald and A. D. Gallimore, "Rotating spoke instabilities in Hall thrusters," *IEEE Transactions on Plasma Science*, vol. 39, no. 11, pp. 2952–2953, 2011.

Appendix A

Total ion current calculation

The total ion flux and its angular distribution in the plume were measured using a 1.3 cm diameter flat electrostatic probe with the guarding sleeve. The ion collection surface of the probe was at 14 cm from the thruster exit plane. Probe and sleeve were biased relative to the ground to -40 V. The probe current was measured across a 1 kOhm resistor (see Fig. 7.2). Probe measurements were taken while probe was rotated between to 0°, $\sim$ 20°, and $\sim$ 40° relative to the thruster axis. Measurements were conducted during the modulations of the thruster discharge voltage. These results were fitted into the distribution curve, which was taken from previous measurements, which were conducted at similar conditions, but at constant anode voltage, see Ref. 23. Results for two modulation amplitudes: 10 V and 30 V, are shown in Fig. A.1.

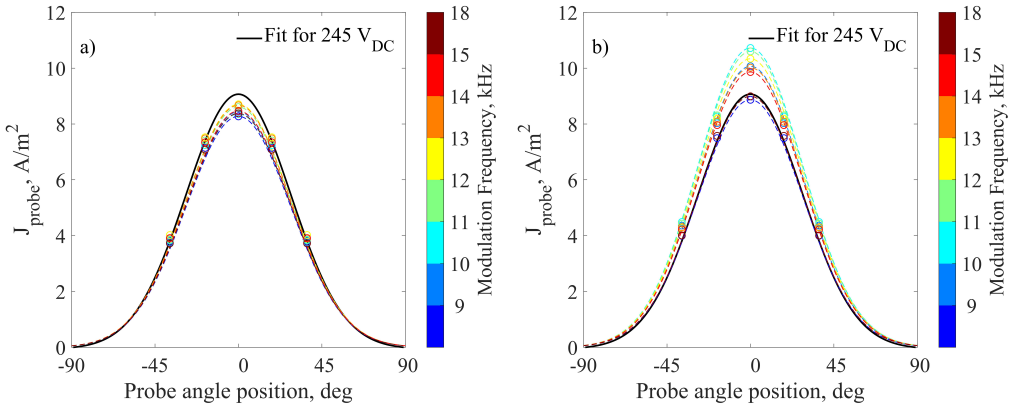

Figure A.1: Angular distribution of the ion flux at 10 V modulation amplitude (a), and at 30 V modulation amplitude (b). Different colors represent different driving frequencies. Black line – referenced ion flux distribution at constant discharge voltage.

The total ion current was estimated by using the following equation,

$$I_{ion} = 2\pi R^2 \int_0^{\pi/2} f \sin\theta d\theta,$$

where I_{ion} is the ion current.

Appendix B

Effect of the voltage modulations on the circuitry and probe

Because experiments involved modulations of the anode potential with high amplitudes, it was important to verify that there were no parasitic resonances or non-linear responses from the electric circuit itself. For this purpose, the electrical circuitry was checked for internal resonance frequencies separately from the thruster. The thruster was replaced by 100 Ohm 50 W resistor, which was installed between the anode and the cathode power supplies. External modulation with different frequencies and amplitudes was applied, and the discharge current traces were logged. From this data two parameters were determined: RMS values of the discharge current and its spectrum. As it is seen from Figure B.1a, RMS values of the current are uniform over a wide range of frequencies. With the increase of the modulation voltage, current response remains flat. Fourier transforms are shown in Figure B.1b. For this case, the modulation voltage amplitude was 30 V peak-to-peak. As one can see there are no additional harmonics. Even though, there is some broadening at 11 and 13 kHz, it did not affect our measurements.

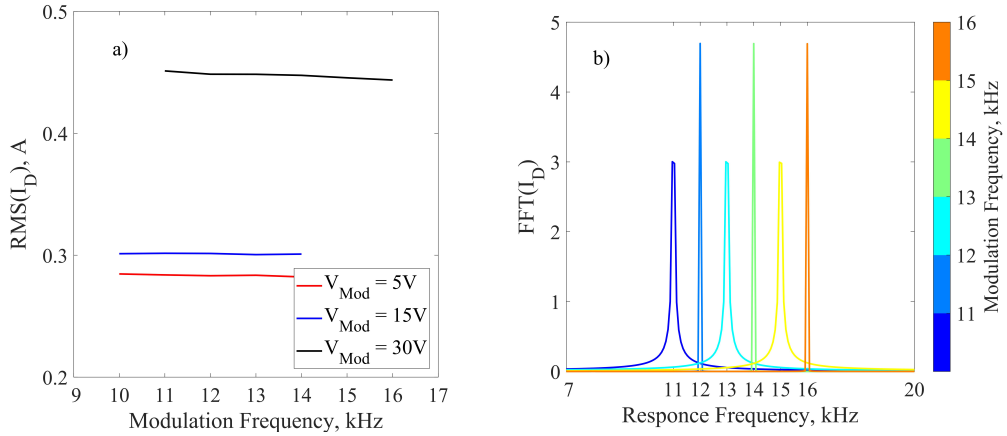

Figure B.1: a) RMS values of the discharge current at different modulation amplitudes; b) Fourier transforms of the discharge current traces at different modulation frequencies, and 30 V peak-to-peak amplitude. Each color represents different modulation frequency.

Appendix C

Details of the image processing techniques

Recorded video can be considered as a 3-dimensional matrix of image pixel brightness as a function of position and time

$$I = I(x, y, t),$$

where x and y are pixel column and row with correspondingly, and t is a time index. There are three main components of the video, which can be identified by looking at it. First, is the image from the thruster channel itself and the background plasma, which gives some DC level of intensity. Second, is the oscillations of the intensity of the whole image due to the breathing mode, or $m = 0$ mode. Third, is the rotating oscillations of the intensity due to the rotating spoke, or $m = 1$ mode, which are of the main interest. To filter these oscillations from the DC level and $m = 0$ mode several steps were done. Stages of image processing are shown in Fig. 14.

- Circle fitting to find external radius R_{ext} of the channel and the anode cup radius R_{int}. This is done by the MATLAB function "imfindcircles".
- Cut frames by the channel size.
- Calculate mean DC level of all frames over time to obtain the mean image M, defined as

$$M(x, y) = \frac{1}{N_t} \sum_t I(x, y, t).$$

- Subtract $M(x, y)$ matrix from each frame. Therefore, by subtracting it from each frame the background intensity is eliminated

$$I_{AC}(x, y, t) = I(x, y, t) - M(x, y).$$

- Apply circular mask on each frame by setting pixel values to zero within R_{int} and outside R_{ext}.
- Split each frame on circles C_{it} with radius r_i and width of 1 pixel, so $R_{int} < r_i < R_{ext}$, and obtain $R_{ext} - R_{int}$ arrays of pixels.
- Calculate average intensity of each circle as

$$c_i = \frac{1}{N_c} \sum_\theta C_{it}(\theta).$$

- Eliminate breathing oscillation effect from each circle by subtracting average intensity c_i from each C_{it} array.
- Transform each frame to polar coordinates

$$I(x, y, t) \to I(R, \theta, t).$$

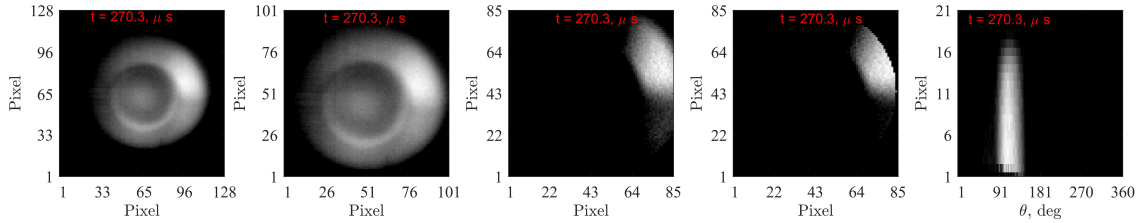

Figure C.1: Image processing stages at one time step. From the left to the right: raw image, cut by R_{ext}, removed background, applied mask and removed effect from the breathing mode, image in polar coordinates.

- Because our analysis is focused on identifying the rotational structures, the radial dependency will be neglected. This is accomplished by average pixel intensity along the radius. Therefore, the matrices $I_{avg}(\theta, t)$ are obtained

$$I_{avg}(\theta, t) = \frac{1}{R_{ext} - R_{int}} \sum_{r=R_{int}}^{R_{ext}} I(r, \theta, t).$$

- Such matrices can be combined in so called 2D "spoke surface". This surface represents variation of pixel intensity in angular direction θ and with time t.
- In order to determine characteristic frequencies of azimuthal modes the 2D Fourier transform was applied to it. The particular implementation is based on the built-in "fft" command in MATLAB. Results are shown in Fig. C.2

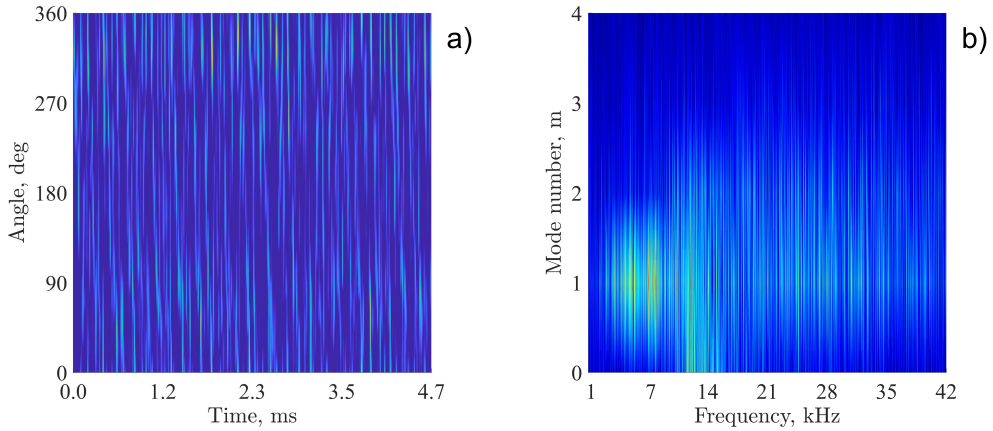

Figure C.2: a) Spoke surface. The angled lines correspond to the spoke propagating in azimuthal direction with time. b) 2D FFT matrix of the spoke surface. This matrix contains a discrete signal for each mode number. One can see that the $m = 0$ mode is still present even though it was cleaned out of the video. This happens because the breathing mode is much stronger compare to the azimuthal modes ($m = 1$).

- Breathing mode was identified through the Fourier transform of the signal, which was defined as follow

$$B(t) = \sum_{x,y} I(x, y, t).$$